City Research Online

City, University of London Institutional Repository

This is the accepted version of the paper.

This version of the publication may differ from the final published version.

Vortex Characteristics of Sharp and Round Step Cylinders at High Reynolds Numbers

Junxian Wang

Supervisor

Prof. Qingwei Ma

A thesis submitted for the degree of Doctor of Philosophy

School of Mathematics, Computer Science and Engineering

City, University of London

November, 2020

TABLE OF CONTENTS

LIST OF FIGURES

LIST OF TABLES

ACKNOWLEDGEMENT

DECLARATION

No portion of the work referred to in the thesis has been submitted in support of an application for other degree or qualification of this or any other university or other institute of learning.

I grant powers of discretion to the City, University of London's Library to allow this thesis to be copied in whole or in part without any reference to me. This permission covers only single copies made for study purpose subject to normal condition of acknowledgement.

Junxian Wang

ABSTRACT

'Flow around a uniform circular cylinder' being one of typical physical issues has been comprehensively investigated in the past few decades, the involved content of which includes but is not limited to surface pressure distribution, surface loading variation and vortex characteristics behind the cylinder. As for actual engineering practises, such a simple structure encounters geometrical variation along the span which gives rise to a series of non-uniform cylinders having circular cross-sections but varying the diameter along the span. Non-uniform cylinders significantly strengthen the complexity regarding fluid dynamics in the wake, which posts a vital threat to ensure service time of relevant engineering buildings and facilities.

A step cylinder consists of two circular cylinders with different diameters, by connecting with each other coaxially. This special shape has a wide range of applications, one of which is to compose 'buoys-risers' system in ocean engineering field. The addition of buoys gives rise to geometrical changing along the span, furthermore, causing complicated three-dimensional flow structures in the wake zone and vortex-induced vibration (VIV) of the riser, thereby is greatly worth investigation. It should be borne in mind that the majority of step cylinder models which have been investigated are sharp step cylinders, i.e., sharp corner near the step junction. The present study tests a modified step cylinder (viz. round step cylinder) by replacing the sharp edge with a round corner. Besides, most part of previous research regarding sharp step cylinders successfully and reliably discussed complex vortex interaction in the wake under lower Reynolds numbers, indicating that there can be some improvement for experimental / numerical study on corresponding vortex interaction under higher Reynolds numbers. As a result, this thesis focuses on comparative study on turbulent flow properties (e.g., vortex characteristics) behind sharp step cylinder and round step cylinder under moderate high Reynolds numbers (1.6e+4, 3.3e+4), which can help gain a deep insight on vortex behaver in turbulent state, as well as the impact of shape of step junction.

More specifically, the present study carries out a series of experiments in terms of the aforementioned two types of step cylinder (viz. sharp step and round step) at Re = 1.6e+4, 3.3e+4 by applying particle image velocimetry (PIV) technique. Velocity fluctuation in streamwise and spanwise along two measuring planes parallel to the model axial in the wake is captured and investigated. Different types of vortex shedding, as well as vortex interaction, are quantitatively characterised by investigating flow fields, corresponding spectra, local frequency variation, spatial energy distribution and primary 'ingredients' of flow fields. Considering the fact that flow structures near step junctions display strong three-dimensionality which cannot be fully depicted based on the present experimental data, i.e., planar velocity fields, corresponding numerical simulations are performed using the open source CFD (computation fluid dynamics) software namely OpenFOAM, with the emphasis on time-averaged content near sharp step junction and round step junction, streamwise vortices, velocity contours along multi-planes, surface pressure distribution and loading variation. Besides, during the numerical simulation, a hybrid mesh strategy is introduced and utilized, with the combination of structured grid and 'Cartesian grid', to achieve reduction of cell numbers.

Chapter 1
INTRODUCTION

1.1 Background

Turbulence (turbulent flow) widely exists in the great nature, e.g., the perturbation due to the collision between water and rocks, which can be observed and reproduced via physical experiments. One representative observation from Taylor in 1923 is to fill the gap between two concentric cylinders with water and subsequently rotate the inner cylinder while keeping the outer one stable, the expectation of which is that the water would become chaotic if the spinning speed of inner cylinder is high enough (P. A. Davidson, 2015). A proper definition in terms of turbulence in fluid dynamics is that a typical flow state featuring randomness, chaos and diffusivity (Falkovich & Sreenivasan, 2006). It should be noted that two notable features of turbulence depict its unique activity, one of which is the 'unpredictability'. For a given time series of velocity fluctuation in turbulent state, a tiny changing at a certain instant of time will significantly cause unpredictable alteration in the subsequent moments, making corresponding instantaneous results seem not reliable (P. A. Davidson, 2015). Nevertheless, the corresponding statistical outcome from enough amount of data, e.g., the time-averaged / phase-averaged value, keeps stable and robust, normally being treated as reliable proofs for turbulence evaluation in publications (Roshko, 1961; Breuer, 2000; Catalano, et al., 2003).
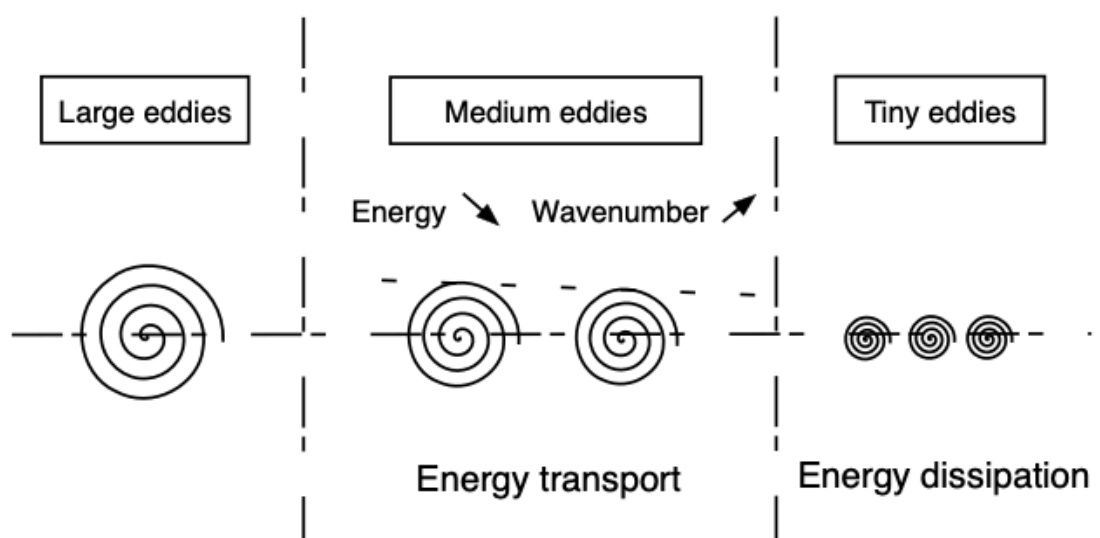
Figure 1.1 Schematic sketch about turbulence energy cascade.

For its spatial 'ingredients' at a certain instant of time, turbulent flow comprises a wide range of vortices equipped with various length scales with corresponding energy variation against the wave number shown in the above graph (see figure 1.1), where large eddies being highly energetic correspond to low wave number. At 'Energy dissipation' stage, vortices isotopically stay at tiny scales, normally called as Kolmogorov scales. The 'Energy transport' in between displays a significantly decrease trend where energy conveyance takes place from large scales to small scales (Aseyev, 2015; P. A. Davidson, 2015).

Unlike the turbulent flow, the laminar flow characterises smooth travelling with no perturbation along the flow direction. Normally, there are two types of transition from laminar state to turbulence. Turbulence near boundary layers (Saric, et al., 2002), starts from tiny initial instability, which gradually merges with other vortices in the subsequent activities and eventually induces the fully turbulent flow. It should be borne in mind that the surface quality can significantly affect the aforementioned transition process, e.g., high surface roughness remarkably accelerating the turbulence growth. Another type is to transit at the flow state approaching certain thresholds, the first stage of which is to transfer from the original laminar state to another more complicated laminar state. As its further evolvement reaches another threshold, tiny perturbation emerges and grows, giving rise to the transition (P. A. Davidson, 2015). The physical process in terms of flow around a uniform circular cylinder attracts plenty of research in the last few decades (Berger & Wille, 1972; Williamson, 1996), the schematic sketch (streamlines) of which is plotted in figure 1.2 where two types of 'laminar-turbulence' transition take place at different position if the proper incident flow is given.
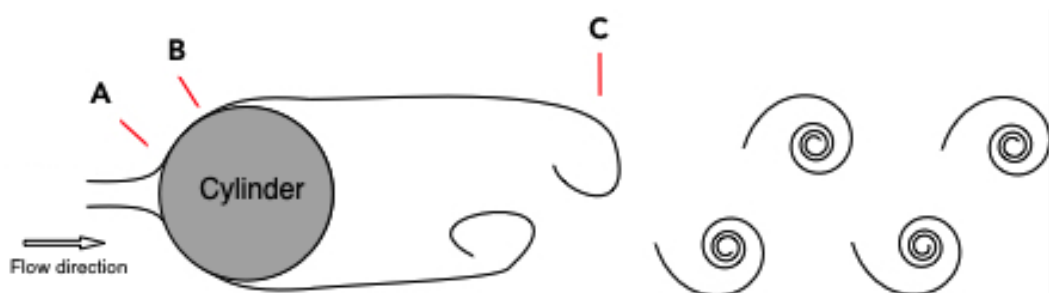
Figure 1.2 Schematic sketch about vortex shedding behind a circular cylinder.

The incoming flow hitting the front side of cylinder, subsequently goes along the cylinder surface where boundary layers (marked as 'AB' in figure 1.2) emerge. With the conflict between inertia force and viscous force, inverse pressure profile occurs near the cylinder surface. Meanwhile, the boundary layer separates from the cylinder surface at the separation point which is noted as 'B' in figure 1.2, resulting in separated shear layers

(marked as 'BC' in figure 1.2). Due to the negative pressure right behind the cylinder, the shear layer rolls up towards the central plane. Tiny perturbation in the near wake breaks the stability, giving rise to periodical and alternative vortex shedding from the cylinder. A non-dimensional term is introduced and used for judging the flow state, say Reynolds number (Re), representing the ratio of inertia force to viscous force. Transition from laminar state to turbulent state takes place successively at three different positions during the whole process, i.e., in the wake, in separated shear layer and in the boundary layer, corresponding to three different phases and three different Reynolds number ranges (Zdravkovich, 1997). Periodic and steady vortex shedding occurs at purely laminar state at the regime of [30 to 48 < Re < 180 to 200]. Subsequently, flow structures in the wake zone start to switch into turbulent state at the Reynolds number range from 180 to 400. Furthermore, the continuous growth of Reynolds number promotes the development of turbulence taking place at shear layer till forming a fully turbulent wake. If the Reynolds number reaches 3.5e+6 to 6e+6 (i.e., the post-critical regime), the above-mentioned transition starts to occur in the boundary layer (Zdravkovich, 1997).

Uniform cylinder-shaped structures are quite prevalent in practical engineering, for instance, chimneys and tall buildings, wind turbine supports, components of aircrafts, as well as spar platforms and risers in ocean engineering industry. Plentiful previous research focuses on load variation and pressure distribution on cylinder surface due to the exertion of incident flow, as well as periodic vortex shedding from the cylinder. On the one hand, the asymmetrical vortices detaching from the cylinder can give rise to structure vibration (vortex-induced vibration, VIV) which induces the fatigue damage being a significant impact on the service life. On the other hand, structure vibration and highly disordered flow in the wake release substantial energy during its process, which can be treated as useful renewable energy sources. It is no wonder that cylinder-shaped structures play an important role in practical engineering. Countless relevant researches have taken place in the last few decades by mitigating (Rashidi, et al., 2016) or enhancing (Ding, et al., 2015) the vortex shedding phenomenon.

However, cylinder-shaped structures for industrial use seem to be more complicated, one branch of which features geometrical variation along the spanwise direction. For instance, the foundation and mast of wind turbine (Stickland, et al., 2013) change the cross-section dramatically at the interface in between. For the purpose of wind loading suppression, there are some skyscrapers varying the geometrical shape towards the top end (Kim & You, 2002). Buoyancy Catenary Risers (Hatton, 1995; Alderton & Thethi, 1998), which

are widely used at deep / ultra-deep water environment for oil exploitation, rely on buoyant configurations to resist huge self-weight. The concept of 'geometrical variation' greatly benefits engineering industries, while the complicated surface loading and fully three-dimensional flow in the wake expose the structure stability and service life to danger resulting in a sequence of simplified models being experimentally and numerically investigated, for instance, the cantilevered cylinders, the tapered cylinders, and the stepped cylinders (Demartino & Ricciardelli, 2017). To be specific, studies regarding the cantilevered cylinders greatly contribute to characterise vortex shedding activity near free ends and near grounds, meanwhile the observation of flow behind tapered cylinders is to identify multi-cellular vortex shedding and corresponding vortex interaction in between.

(a): side view;   (b): top view;
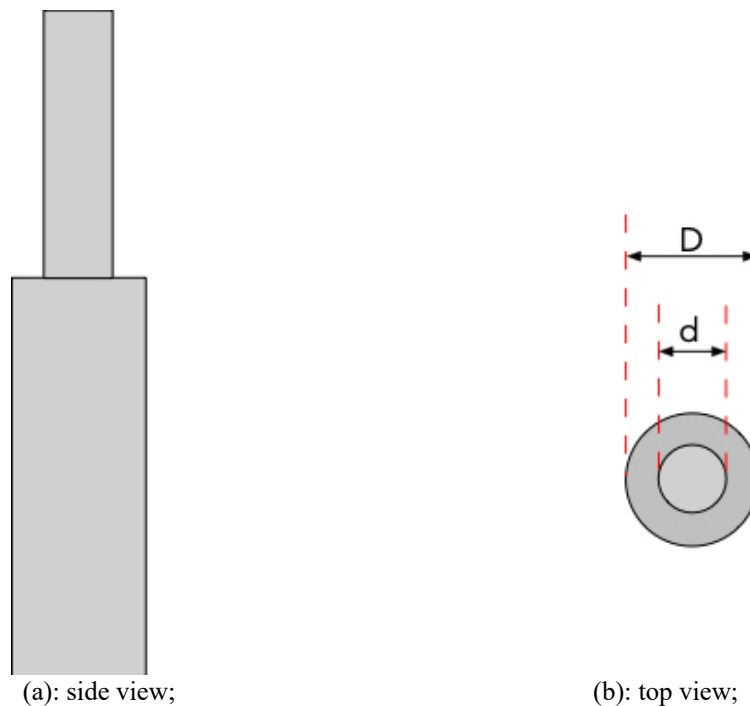
Figure 1.3 Schematic sketch of a single step cylinder.

A normal description about step cylinders is a cylindrical structure which connects a large-diameter cylinder and a small-diameter cylinder co-axially together, as shown in figure 1.3. The emphasis regarding stepped cylinder studies is placed on the area near step junction which unites features from 'cantilevered cylinders' and 'tapered cylinders', i.e., 'free-end', 'ground impact' and 'spanwise geometrical variation', which leads to the complicated vortex shedding as well as surface loading. In addition, the corresponding research will be a valuable reference for industries.

1.2 Motivation

As it is mentioned in section 1.1, structures with geometrical variation along the span show remarkable weightiness in the industrial field as well as the academic field,

indicating the pressing requirement of investigation. As a result, the single step cylinder is selected as a typical structure for further investigation in the present study. According to a succession of research achievements accomplished in previous publications (Lewis & Gharib, 1992; Dunn & Tavoularis, 2006), issues under lower Reynolds number have already been fully studied by launching relevant experiments, with the emphasis on vortex shedding cells' properties and vortex interaction. At higher Reynolds numbers, limited experimental contributions have been made by several previous publications (Ko, et al., 1982; Yagita, et al., 1984; Norberg, 1992; Ko & Chan, 1984, 1990, 1992; Chua, et al. 1998; Dunn & Tavoularis, 2006, 2011; Morton & Yarusevych, 2010a, 2014a; Rafati, 2014; Teutsch, 2012). In the early stage, researchers mainly focused on qualitative observation on flow structures in the wake with the assistance of flow visualization technique, such as smoke wire or hydrogen bubbles. As for PIV-based studies (Rafati, 2014; Teutsch, 2012), on account of the size limitation of 'field of view' (FOV), measurement on velocity fields only concentrates at a small region behind the step junction, inducing that vortex interaction which occurs behind the large-diameter cylinder cannot be entirely captured. Considering turbulence randomness, there comes a prediction that the vortex interaction could show discrepancy between the laminar state and turbulent state, which needs more quantitative experimental support for study about turbulent flow structures behind step cylinders. As a result, more PIV-based experiments under high Reynolds numbers are greatly needed, as well as more corresponding quantitative analysis. Furthermore, a suitable size of 'field of view' should be selected, to help capture more details regarding dynamic vortex interaction behind the large-diameter cylinder.

Studies on single step cylinders have witnessed strong three-dimensional flow structures in the wake, as well as notable surface pressure variation near the step junction. And a question came out, i.e., '*is there a solution to ease the flow motion after the step junction*'. All of this brings about the structure optimization in terms of the step junction. The present study tests another type of step cylinder, which is also prevalent around us, and can be called as 'round step junction' (see figure 1.4), in contrast to the typical step junction (viz. 'sharp step junction'). The only discrepancy between these two step cylinders is to round the step edge in 'round step junction' to produce a relaxed transition from large-diameter cylinder to small-diameter cylinder. Consequently, this thesis puts 'sharp step cylinder' and 'round step cylinder' together and launches corresponding comparative study experimentally on the impact of shape of step junction, i.e., 'sharp step' versus 'round step', concentrating on vortex characteristics and vortex interaction in the wake.

(a): side view;   (b): top view;
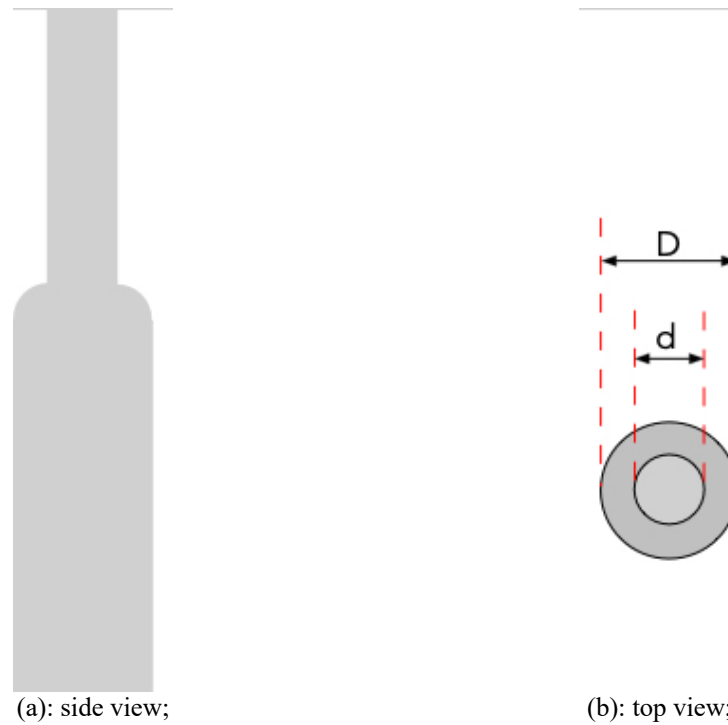
Figure 1.4 Schematic sketch of a round step cylinder.

With respect to the numerical simulation regarding single step cylinders, limited studies have already been done and are sumarrized in table 2.3. Recently, Tian et al. (2021) studied flow fields near sharp step junction at $Re = 3900$ via directly numerical simulation, revealing more detailed vortices near the step junction. For much higher Reynolds number (viz. $Re > 1.3e +4$), corresponding numerical simulation is needed. More details about research gap regarding numerical simulation is given via discussion about table 2.3. Due to the structure complexity, proper mesh arrangement near the step junction seems to be a challenge. Besides, mesh resolution in the wake should be extremely fine enough for resolving small-scale eddies, which is a distinct difference from that in laminar state. DES (detached eddy simulation) turbulence solution was employed to carry out the present numerical simulations. According to previous publications in terms of numerical configuration strategy (Nishino, et al., 2008; D'Alessandro, et al., 2016), mesh resolution for DES along spanwise direction is much higher than that for RANS turbulence solution. As DES is a hybrid model, there is a high-resolution demand for meshing near the cylinder surface, to allow adequate grid nodes within the boundary layer. Besides, the present thesis adopts a hybrid mesh strategy by allowing structured grids round the step cylinder and filling the outer region with Cartesian grids, for the reason that structured grids round the step cylinder can fulfil a smooth adjustment from the cylinder surface to the outside and Cartesian grids can greatly reduce cell consumption.

1.3 Objectives

The present thesis experimentally investigates complex flow structures (especially vortex characteristics) in the wake of sharp and round step cylinders under higher Reynolds numbers (1.6e+4, 3.3e+4) using planar PIV methodology, followed by the implement on numerical simulations using an open source CFD software, i.e., OpenFOAM (v5.x). The obtained numerical results show great consistency with corresponding experimental results. Meanwhile, numerical results in terms of three-dimensional flow fields and vortex information near the step junction could be the supplement for the present experimental investigation. Besides, during the numerical simulation process, a hybrid mesh strategy is designed and adopted, indicating the significant grid cell reduction. All the objectives in detail can be listed as follows:

1. Investigate vortex characteristics in the wake of sharp step cylinder under high Reynolds number experimentally, some quantitative results of which have never been done by previous publications before.
2. Investigate flow around a round step cylinder under high Reynolds numbers experimentally, to reveal the impact of shape of step junction.
3. Launch relevant numerical simulations by applying a new hybrid mesh strategy, to gain a comparative study on three-dimensional flow structures near two types of step junction.

1.4 Thesis Outline

The current thesis consists of nine chapters, with more details being given as follows. First of all, project background is briefly introduced in Chapter 1, involving turbulence characteristics, the application and importance of non-uniform cylinders, followed by the motivation of the present experimental and numerical study about the comparison of vortex shedding from sharp / round step cylinders under high Reynolds numbers. Chapter 2 gives a comprehensive introduction about related literature, i.e., basic knowledge on vortex shedding behind uniform cylinders and previous investigations in terms of several forms of cylinder with geometric variation along the span. Subsequently, Chapter 3 narrates experimental information in detail, covering the wind tunnel, testing models, PIV measuring system, as well as data processing methods, followed by the introduction on related CFD technique content. The subsequent three chapters namely Chapter 4, Chapter 5, Chapter 6, present experimental results and analysis with respect to the comparison of vortex shedding from two types of step cylinder, focusing on vortex identification,

spectra-based features and vortex interaction dynamics. After that, this thesis turns to the numerical part (Chapter 7 and Chapter 8), with the emphasis on the comparison of three-dimensional flow and vortices near the step junction between two types of step cylinder, as well as the surface pressure distribution and loading variation on the step junction. In the last chapter (Chapter 9), the obtained achievement from the current study and the potential work which could be done in the future are summarized.

Chapter 2
LITERATURE REVIEW

This chapter systematically introduces related literature regarding vortex shedding from plain cylinders and non-uniform cylinders. As for plain cylinders, the general vortex shedding process, together with the definition of corresponding normalized variables, are presented, followed by the introduction about the occurrence of turbulence transition against the Reynolds number. The next stage is to characterise vortex shedding from non-uniform cylinders, involving linear tapered cylinders, wavy cylinders, finite length cylinders, single step cylinders and dual step cylinders. The last part of this chapter summaries the previous achievements in relation to single step cylinders, i.e., 'what has been done', and highlights the corresponding research gap namely, 'what hasn't been done', as well as the present work.

2.1 Vortex Shedding behind Plain Cylinders

It is the wide existence in the great nature and the significant impact in industrial field regarding vortex shedding behind bluff bodies that promote corresponding research progress during the last one hundred years (Weiselsberger, 1921; Roshko, 1961; Gerrard, 1978; Williamson, 1996; Norberg, 2003). Its general process starts with the incident flow (the corresponding Reynolds number should be over a critical value) hitting the front side of the cylinder, subsequently resulting in the increase of pressure at the stagnation point, the fluid moving along cylinder surface and the development of boundary layers at both sides. Furthermore, flow separation takes place at a certain surface location, together with the formation of two shear layers due to the combination action of viscous force and the pressure force. The negative pressure in the near wake causes the shear layers rolling up towards the central plane, which eventually gives rise to the periodical vortex shedding.

Reynolds number, defined as the ratio of inertial force to viscous force, is introduced to quantify and identify the fluid state, which can be expressed via formula as:

$$Re = \frac{U_0 \times D}{\nu} \qquad (2.1)$$

where U_0, D, ν denote the free stream velocity, the cylinder diameter and the kinematic viscosity respectively. The Strouhal number is a non-dimensional variable related to vortex shedding frequency, which is expressed via the equation as:

$$St = \frac{f \times D}{U_0} \tag{2.2}$$

where f, U_0, D denote the vortex shedding frequency, the free stream velocity and the cylinder diameter respectively. The periodic vortex shedding gives rise to surface pressure variation, which furthermore causes the applied loading on cylinder surface changing cyclically. The corresponding force coefficient is given as:

$$C = \frac{2F}{\rho U_0^2 A} \tag{2.3}$$

where F, ρ, U_0, A represent forces exerted on the cylinder, the density of ambient fluid, the velocity of the incident flow and the projecting area of the structure in the flow direction. The exerted force normally consists of two components namely drag force (in the streamwise direction) and lift force (in the transverse direction), corresponding to drag coefficient (C_d) and lift coefficient (C_l), the mean and rms (root-mean-square) value of which are useful and reliable to evaluate the loading dynamics. The pressure distribution along the cylinder surface can be written as a non-dimensional form namely the pressure coefficient (C_p):

$$C_p = \frac{P - P_\infty}{0.5\rho U_0^2} \tag{2.4}$$

where P, P_∞, ρ, U_0 stand for the pressure on the cylinder surface, the reference pressure, the density of the fluid and the velocity of the incident flow.

As it is mentioned in Chapter 1, fluid near the cylinder and in the wake switches from laminar state to turbulence gradually in response to the Reynolds number increase. Consequently, Williamson (1996) studied the turbulent vortex shedding from cylinders and the position where turbulence transition takes place, finally sorted out several Reynolds ranges to identify diverse vortex shedding states. It is believed that the fluid keeps a laminar steady state at lower Reynolds number, forming the separated flow near the cylinder, as well as two symmetric stationary recirculating vortices in the near-wake zone till the Reynolds number approximately reaching 49 when the typical periodic vortex shedding occurs (Williamson, 1996). It should be noted that this 'near-wake' zone gradually elongates itself in the streamwise, and two-dimensional vortices detach from two sides of circular periodically and alternatively under laminar state at $49 \leqslant Re \leqslant 140 \; to \; 194$ (Williamson, 1996). At the Reynolds number range of 190 ~ 260, turbulence transition happens in the wake zone, displaying two distinctive secondary instabilities namely Mode A at $Re = 180 \sim 194$ and Mode B at $Re = 230 \sim 250$ (Williamson,

1996). The original vortex shedding exhibits significant deformation along its spanwise direction, which gives rise to the formation of streamwise vortices. As for Mode B instability, the streamwise vortices become finer, with the spanwise gap between neighbouring ones by approximate one diameter. The continuous increase of Reynolds number enables the gradual development in terms of turbulence in the wake till the Reynolds number reaching 1000, when the flow in the wake becomes fully turbulent. At the range of *Re* from 1e+3 to 2e+5, transition to turbulence emerges at shear layers, and the location where the transition takes place slowly moves towards the cylinder as the Reynolds number increases. When the Reynolds number reaches post-critical regime, boundary layer along the cylinder surface starts to transit to turbulent state (Williamson, 1996).

2.2 Vortex Shedding behind Non-uniform Cylinders

The above section (Section 2.1) gives a fundamental introduction on vortex shedding phenomenon behind plain cylinders, as well as its evolution towards three-dimensional activity by altering the Reynolds number. Apart from the adjustment about the Reynolds number, changing some other parameters can also give rise to the three-dimensional vortex shedding, for instance, applying the linear shear incident flow or tuning the cross-section along the span. Consequently, this section mainly focuses on complicated three-dimensional vortex shedding from non-uniform cylinders. The summary about non-uniform cylinders is listed in figure 2.1, including the linear tapered cylinder, the wavy cylinder, the finite length cylinder, the single step cylinder, and the dual step cylinder.

(a): side view

(b): top view
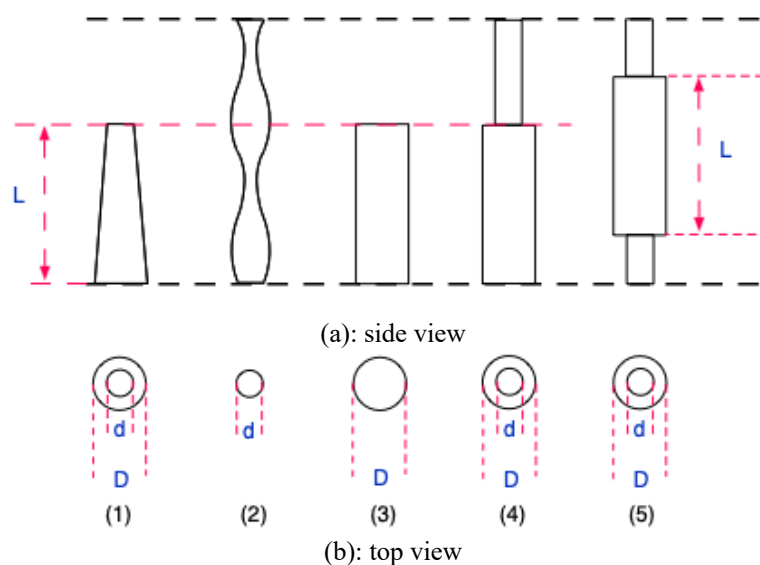
Figure 2.1 Schematic sketch about non-uniform cylinders.

Note: (1): Linear tapered cylinder; (2): Wavy cylinder; (3): Finite length cylinder; (4): Single step cylinder; (5): Dual step cylinder.

<u>Linear tapered cylinders</u>

The definition of a linear tapered circular cylinder is a certain height ('L' marked in the figure 2.1) of structure with big circular surface ('D') on the base and small circular surface ('d') on the top. Vortex shedding from tapered cylinders is in relationship with the Reynolds numbers and the taper. There are two different forms of Reynolds number, one of which is local Reynolds number (Re_{loc}), corresponding to Reynolds numbers at a certain cross-section; another one is maximum Reynolds number (Re_{max}), corresponding to Reynolds number at the base section. Besides, the taper ratio denotes the ratio of diameter difference ($D - d$) between the top end and the base to the height ('L'). Plenty of previous research in terms of linear tapered cylinders mainly focuses on investigation about cellular vortex shedding, velocity modulation, vortex interaction dynamics, the details of which are given as follows.

Cellular vortex shedding

A vortex shedding cell denotes vortices detach from the cylinder in the identical frequency and phase, which visually forms one piece. In general, the diameter discrepancy along the span alters the vortex shedding activity behind different portions of span, giving rise to the cellular vortex shedding. Gaster (1969, 1971) conducted the investigation about tapered cylinders, with the emphasis on the variation of velocity fluctuation over time along the spanwise direction in the wake obtained by assigning hot-wire probes vertically located at different cross-sections in the wake. Results reveal the existence of multi-cellular vortex shedding behind the tapered cylinder. Papangelou (1992) confirmed the shedding frequency keeps constant along a certain portion of the span and subsequently jumps to another value at the neighbouring portion, suggesting the occurrence of cellular vortex shedding. The cellular vortex shedding is found to depend on the Reynolds number (calculated based on the wider end), resulting in three distinct regions namely, the 'pre-cellular' region, the 'cellular' region and the 'post cellular' region. Besides, Cellular vortex shedding from tapered cylinders is dependent on the taper ratio. Experimental results (Jagadeesh, 2009) prove that a certain number of cells with fixed 'discontinuity' locations are observed behind cones with large taper ratios, in contrast to that behind small taper ratio cones, that is, the vortex cells moving along the spanwise direction.

Each vortex-shedding cell corresponds to a specific frequency, resulting in the frequency difference between the neighbouring cells, and furthermore, the frequency difference keeps stable along the spanwise direction depending on free stream velocity, the taper

angle and kinematic viscosity (Papangelou, 1992). The amplitude modulation can be clearly detected in velocity fluctuation over time. It should be noted that the velocity modulation is different behind large / small taper ratio cones. The entire span of small taper ratio cones is seen to have the vortex shedding with a gradual changing frequency and the modulated velocity signal with a constant modulation frequency, the latter of which is believed to be 'a global process' (Jagadeesh, 2009). In addition, Piccirillo & Van Atta (1993) decomposed the flow along two directions (normal to the front surface, parallel to the front surface), the component of which is parallel to the front surface dominates the modulation frequency.

In the early stage of investigation towards tapered cylinders, a major part of researchers focused on experiments at relative low Reynolds numbers. Later on, Hsiao & Chiang (1998) carried out tapered cylinder experiments at high Reynolds numbers ($4000 < Re < 14000$), figuring out two types of transition in relation to the Strouhal number. The Strouhal number experiences a sudden jumper at lower Reynolds number regime, whilst a smooth change at higher Reynolds number regime. Recently, Chen & Martinuzzi (2018) experimentally studied turbulent flow structure behind the cone with low aspect ratio; the vortices with counter-rotation directions were observed from phased-averaged velocity fields, indicating significant difference with that behind cantilevered cylinders.

Vortex interaction

A typical vortex interaction behind cones can be explained as shown in figure 2.2. The vortex shedding activity is different near small-diameter end and large-diameter end owing to different shedding rates, which gives rise to the occurrence of 'vortex kink' behind the cone (see vortex *d*, *d'*, *e*, *f*). With vortices gradually moving downstream, vortex *f* and vortex *e* form a so-called 'vortex loop'; vortex *d*, vortex *d'* and its extension form the typical 'vortex split'. A general description about the growth of 'vortex split' is following. Initially, vortex shedding cells are parallel to the cone axis till 'vortex split' taking place near the small end of the cone. Subsequently, 'vortex split' enlarges it scale, and gently moves from the small end to the large end. After the presence of the largest vortex split, the entire vortex cell detaching from the cone is in parallel to the cone again, suggesting the starter of the next loop (Piccirillo & Van Atta, 1993).

Note: lines (a, b, c, …, g) are vortex-shedding cells near small-diameter end; lines (a', b', c', …, e') are vortex-shedding cells near large-diameter end; blue solid lines and red dash lines stand for two sides of vortex street.
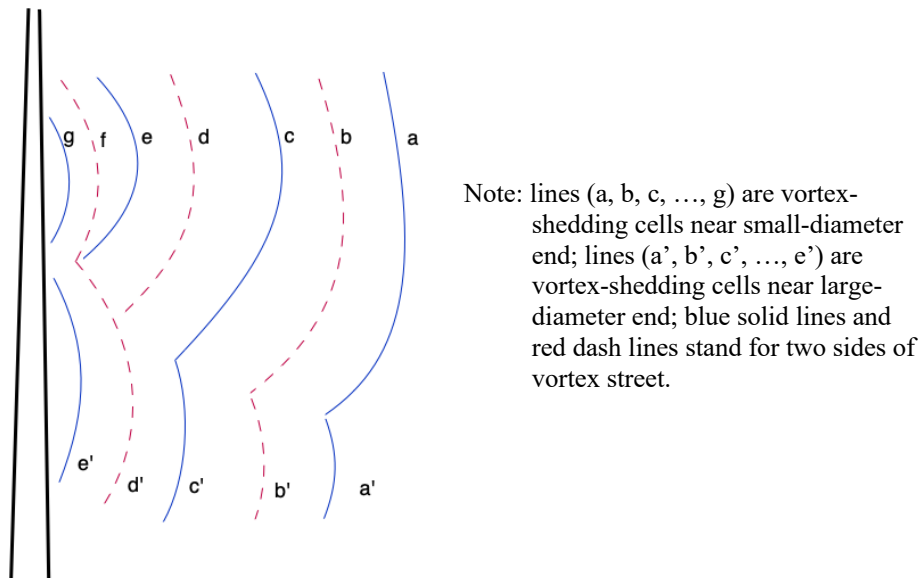
Figure 2.2 Explanation about vortex splitting, adapted from Piccirillo & Van Atta (1993).

Numerical simulation

The published achievements regarding numerical simulation on tapered cylinders mainly focus on the validation with previous experimental results as well as the exploration of corresponding mechanism. Vallès, et al. (2002a) did the numerical simulation on linearly tapered circular cylinders with the Reynolds number range from 130 to 180 by solving 3D N-S equations. The corresponding simulation results reveal a successive of typical behaviours, including the vortex dislocation, which shows great consistence with experimental results published from Piccirillo & Van Atta (1993). Reinders, et al. (2002) put forward to a new application technique to identify vortex cells in the wake of tapered cylinders. De & Sarkar (2020) implemented DNS simulations in terms of the tapered cylinder at *Re* = 300 (calculated by using the averaged diameter) to investigate flow structure at the transition region from two-dimension to three-dimension; corresponding results presented more detailed information about vortex interactions.

Wavy cylinders

The wavy cylinder features a sine wave-shaped span as shown in figure 2.1. A series of relevant experiments have proved that the separation line as well as pressure-induced drag force on cylinder surface is not symmetrical, although the structure shape is symmetrical (Ahmed & Bays-Muchmore, 1992). This special structure can help reduce the drag loading, with at least 30% reduction (Bearman & Owen, 1998). Lam, et al. (2004a, 2004b) validated the suppression of mean drag force, lift force fluctuation, as well as discovered the relationship between the drag force reduction and the spanwise waviness. Comparing to the flow state near the nodal region, the formation length is longer and the secondary

flow in the wake is stronger near the saddle region. Besides, strong three-dimensional vortex behaviour is formed due to the geometrical variation surface.

Finite length cylinders

In general, there are two types of finite length cylinder, which can be interpreted as follows. The finite length cylinder with one free end can be supported as a cantilever and totally immersed in the flow. A certain amount of previous literature (Ayoub & Karamcheti, 1982; Farivar, 1981) has already proved that flow structures in the wake after the free end and near the base, together with the corresponding surface pressure and force coefficients, display strong three-dimensionality. Another type is the finite length cylinder with two free ends, which eliminates the 'ground effect'.

The flow evolution near ends can be interpreted to start with the incident fluid hitting the free end, subsequently a portion of the fluid going along the side surface. The rest part flow moves over the free end towards the mid span, eventually, melting into the recirculation zone in the near wake due to the negative pressure (Baban & So, 1991). The inverse flow takes place near the front face of the base, resulting in the occurrence of 'horseshoe' vortex which furthermore merges with the inverse flow and the separation flow. Meanwhile, a pair of counter-rotating vortex emanate from the edge of the free end owing to the impact of downwash flow (viz. the above mentioned 'the rest part flow'). The complicated interaction among counter-rotating vortices, the secondary flow and the Karman vortex shedding significantly affects the vortex formation, surface pressure distribution and the force coefficients (Park & Lee, 2000). The normal Karman vortex shedding displays strong three-dimensionality, which is apparently suppressed near both ends (Etzold & Fiedler, 1976). With the location gradually approaching the free end, the vortex formation region is decreased (Park & Lee, 2000). The separation line near ends seems to bend backward, indicating the delay of boundary layer's separation (Sykes, 1962), which results in the slanting vortex shedding.

The aspect ratio (*L/D*), namely the ratio of the height to diameter, determines characteristics of vortex shedding from finite length cylinders. A total of three regions distribute along the span namely one near the top free end, one covering the central portion, one near the base, and furthermore, the aspect ratio affects the portion near top free end if *L/D* is below 4 (Sykes, 1962). A further investigation is to figure out several distinct regions to characterise the cellular vortex shedding in the wake by varying the aspect ratio, for instance, the 'over three cells' region, the 'two cells' region, the 'one cell' region (Summer, et al., 2004). Besides, with the continuous reduction of the aspect ratio

till the critical value, the normal Karman vortex shedding featuring antisymmetric characteristic changes into the symmetric version (Tanaka & Murata, 1999). Table 2.1 makes a summary on the critical aspect ratio for recognising the transition to symmetric vortex shedding. It could be found that the critical aspect ratio in terms of the occurrence of the symmetric version differs in previous publications. Zdravkovich, et al. (1989) believe the corresponding discrepancy on critical aspect ratios is due to diverse boundary-layer thickness.

Table 2.1 Summary of achievements about vortex cells behind finite length cylinders.

	critical aspect ratio (L/D) for the transition to symmetric vortex shedding
Gould, et al., 1968	5
Sykes, 1962 three regions	4
Sakamoto & Arie, 1983	2.5
Okamoto & Sunabashiri, 1992	2 ~ 4
Fox & West, 1993	7

The total drag coefficient, together with total the lift coefficient fluctuation, is smaller than that from a uniform cylinder under the same Reynolds number (Luo, et al., 1996; Farivar, 1981; Sarode, et al., 1981; Fox & West, 1993). Besides, the total drag coefficient decreases with the reduction of the aspect ratio but keeps nearly constant when the aspect ratio is below a critical value (Uematsu & Yamada, 1994), due to the impact of viscous force exerting on the free end. Especially for the finite length cylinder with two free ends, it is believed that the free end dominates the total drag coefficient when the aspect ratio is under 6 (Zdravkovich, et al., 1989). The mean local drag coefficient keeps constant at the location away from the free end and declines towards both ends. Surface pressure at the front side is relatively independent from the aspect ratio and the location (Luo, et al., 1996; Sykes, 1962). However, the base pressure keeps steady at region where normal Karman vortex shedding takes place and decreases its absolute value towards free ends.

Single step cylinders

A single step cylinder (see figure 2.1) consists of a large-diameter cylinder and a small-diameter cylinder, connecting with each other co-axially. It is the discontinuity at the step junction that gives rise to complicated vortex shedding and vortex interaction in the wake. It should be noted that the Reynolds number for step cylinders in the present study is calculated based on large cylinder diameter ('D').

Direct mode / indirect mode

It has been proved that it is the diameter ratio (ratio (r) of large cylinder diameter to small cylinder diameter) and the Reynolds number that characterise the complicated three-

dimensional vortex shedding behind step cylinders. More specifically, three distinct regimes in terms of flow structures in the wake were put forward namely 'direct mode', 'indirect mode' and a transition stage, corresponding to three different diameter ratio ranges, i.e., r < 1.25, r > 1.55 and 1.25< *r* <1.55 (Lewis & Gharib, 1992). Schematic sketches about 'direct mode' and 'indirect mode' are presented in figure 2.3. It should be noted that for each mode in figure 2.3, only one side of the cellular vortex street is exhibited. For 'direct model', two types of vortex shedding take place from the step cylinder, marked as 'cell A' and 'cell C' in figure 2.3(a). Meanwhile, a narrow region (entitled 'step interface') behind the step junction turns up, allowing the occurrence of vortex interaction between 'cell A' and 'cell C'. The discrepancy of two shedding frequencies gives rise to the alternative presence of out-of-phase shedding and in-phase shedding (Lewis & Gharib, 1992).
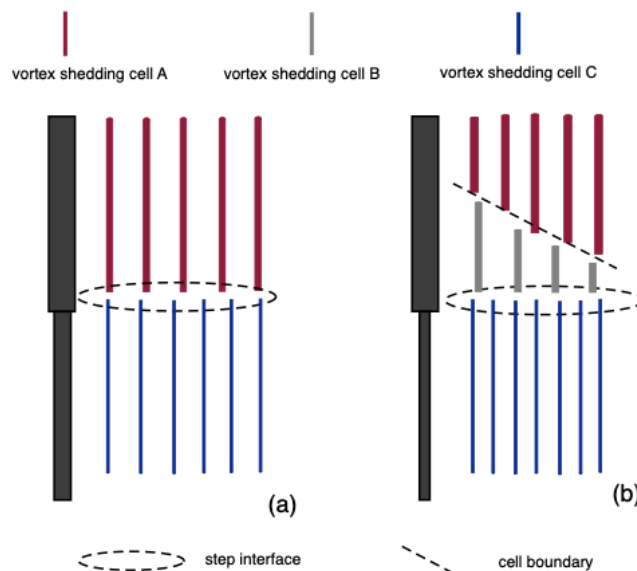
Figure 2.3 Schematic diagrams of direct mode (a) and indirect mode (b), adapted from Lewis & Gharib (1992), Dunn & Tavoularis (2006).

The most significant symbol for 'indirect mode' is the occurrence of a new-born vortex cell marked as 'cell B' in figure 2.3(b), behind the large-diameter cylinder near the step junction, which breaks the direct connection between Large cylinder vortex cell and small cylinder vortex cell. The three types of cellular vortex shedding have different shedding frequencies, which directly gives rise to in-phase and out-of-phase vortex interactions, as well as two boundary areas in between, namely the 'step interface' and 'cell boundary' (see figure 2.3(b)). The cell boundary between 'cell A' and 'cell B' is proved to periodically emerge and is found to be slanting to the cylinder axis (Lewis & Gharib, 1992). The mechanism of 'cell B' evolution is believed and proved to be related to the 'downwash' originated from the step junction (Dunn & Tavoularis, 2006; Morton &

Yarusevych, 2010b). For the turbulent state, the duration of the 'B-C cell boundary' is radomly fluctuated, the possible explanation of which is about the fluctuated shedding frequency regarding turbulence (Morton & Yarusevych, 2010a, 2014a). In addition, three cells namely 'cell A', 'cell B' and 'cell C' were first termed as 'L-cell', 'N-cell' and 'S-cell' by Dunn & Tavoularis (2006), corresponding to the 'Large cell', the 'New cell' and the 'Small cell' respectively.

Vortex characteristics

The 'Y-shape' vortex connection is experimentally observed behind single step cylinders for high Reynolds numbers by applying 'the black ink' (Yagita, et al.,1984) and the 'smoke-wire' (Norberg, 1992) flow visualization techniques. Considering the fact that different vortex shedding cells have different vortex strength, the vortex connection at near the boundary would definitely allow the third or more vortex filaments to join (Dunn & Tavoularis, 2006). Consequently, the vortex interaction near the 'step interface' and the 'cell boundary' seems to be complicated in figure 2.3. In addition, Yagita, et al. (1984) found that the Strouhal number is related to the Reynolds number, diameter ratio and aspect ratio. Ko & Chan (1992) carried out related experiments at the Reynolds number of 8e+4, focusing on the velocity fluctuation in the wake, and figured out the recirculation zone extend is 1*D* in streamwise behind the small-diameter cylinder and is 3*D* behind the large-diameter cylinder.

Numerical achievement

Vallès, et al. (2002b) numerically reproduced vortex shedding and vortex interaction behind the single step cylinder which was published by Lewis & Ghari (1992). Morton together with his colleagues (Morton, et al., 2009; Morton & Yarusevych, 2010a; Morton & Yarusevych, 2010b) numerically investigated vortex shedding from the single step cylinder at different Reynolds numbers (*Re* = 150, 300, 1050 and 2000), the obtained numerical results of which not only show consistency with corresponding experimental results, but also promote deep insight into N-cell evolution. Dunn & Tavoularis (2006) suggest that the N-cell evolution was experimentally observed to be cyclical, with discontinuance between two neighbouring loops. Whilst, Morton & Yarusevych (2010b) numerically detected the abrupt reduction of N-cell extent between two successive loops, eliminating the 'breaking off'. Besides, Morton & Yarusevych (2010b) successfully established the link between the N-cell cycle and the 'downwash' by figuring out the identical periodicity in terms of N-cell variation and the spanwise velocity variation near the step. Shin et al. (2018) did numerical study on the rotating step cylinder. Bjørkli

(2012) numerically investigated velocity fields and pressure variation regarding single step cylinders with diverse diameter ratio (D/d= 1.11 ~3.33) at Re = 150 ~ 600. Recently, Tian et al. (2017a, 2017b, 2019, 2020a and 2020b) numerically investigated flow around single step cylinders with diverse diameter ratios under low Reynolds number by means of DNS simulation, and made manifest progress in phase difference variation between N-cell and L-cell over time. Apart from that, Tian et al. (2021) focused on three-dimensional flow structures near the step junction at Re = 3900 by means of direct numerical simulations; corresponding results, e.g., time-mean / instantaneous flow fields, revealing more details about vortices near the step surface.

<u>Dual step cylinders</u>

A typical dual step cylinder is made up of three cylinders (see figure 2.1), by connecting two small-diameter cylinders to one finite large-diameter cylinder at both ends co-axially. Besides, the aspect ratio (L/D), the diameter ratio (D/d) and the Reynolds number (Re), govern complicated three-dimensional flow structures in the wake. Morton together with his colleagues (Morton & Yarusevych, 2011; Morton & Yarusevych, 2012a; Morton & Yarusevych, 2012b; Morton & Yarusevych, 2014b; Morton & Yarusevych, 2014c; McClure, et al., 2015) implemented related experimental studies and numerical studies, characterising complicated vortex shedding from dual step cylinders with the variation of aspect ratio and diameter ratio, and sorted out two sets of regions by fixing the diameter ratio and aspect ratio respectively. Subsequently, Wang, et al. (2018, 2019) implemented numerical simulations on flow around dual stepped cylinders with diverse diameter ratios (D/d) as a supplementary study; results reveals the relationship between secondary flow (spanwise velocity) and vortex interaction.

With the constrain of D/d = 2, the impact of aspect ratio (L/D) towards cellular vortex shedding behind dual step cylinders can be summarized as follows. For L/D >= 17, three vortex cells co-exist behind the large-diameter cylinder, with the L-cell detaching from the mid-span, and two N-cells near both ends. For $7 < L/D <= 14$, there is only one vortex cell parallel to the cylinder axis behind the large-diameter cylinder. A new shape of vortex (hairpin-like) occurs in the range of $2 <= L/D < 7$. If the aspect ratio is small enough (viz. $0.2 <= L/D <= 1$), no distinct vortex-shedding cell can be observed behind the large-diameter cylinder (Morton & Yarusevych, 2011; Morton & Yarusevych, 2014b; Morton & Yarusevych, 2014c; Morton & Yarusevych, 2015). Similarly, by fixing the aspect ratio at 5, the variation of diameter ratio from 1.1 to 4 was found to significantly affects the vortex shedding from dual step cylinders (McClure, et al., 2015; Morton & Yarusevych,

2020). At D/d = 4, strong hairpin-like vortices detach from the rear side of large-diameter cylinder. With the continuous decrease of diameter ratio (D/d), the impact of step junctions towards vortex shedding behind large-diameter cylinder gradually becomes weak. Morton and his colleagues (Morton & Yarusevych, 2016; Morton, et al., 2016) also did relevant investigation on dual step cylinders to reconstruct three-dimensional wake by using advanced PIV methodology. Recently, Ji et al. (2019, 2020) numerically study fixed / moving dual step cylinders with diverse diameter ratios by means of direct numerical simulations. Yan et al. (2020) carried out direct numerical simulations regarding a pair of dual-stepped cylinders and characterised two 'flip-flopping flow' regions in the wake zone.

2.3 Existing Problems and Objectives

This chapter mainly narrates the background about flow around cylinders, involving plain cylinders, and non-uniform cylinders. Discussion regarding the plain cylinders promotes a deep insight into vortex shedding mechanism and its relationship with the Reynolds number. Subsequently, several typical models with geometrical variation (viz. non-uniform cylinders) are introduced, such as the tapered cylinder, the wavy cylinder, the finite length cylinder, the single step cylinder and the dual step cylinder, all of which share common traits, i.e., strong three-dimensional vortex shedding and complicated vortex interaction in the wake. Although plenty of research achievements regarding the single step cylinder have been done in the last few decades, there are still much room for the improvement.

Table 2.2 Summary of experiments about single-step cylinders having been done.

researches	D/d	Re	Methods	Spanwise size
Ko, et al. (1982)	2	8e+4	P* Probes in the wake	/
Yagita, et al. (1984)	1.25 ~ 5	8e+2 ~ 1e+4	HW* probes/FV	/
Lewis & Gharib (1992)	1.14 ~ 1.76	35 ~ 200	HW probes / FV	/
Norberg (1992)	1.25 ~ 2	3e+3 ~ 1.3e+4	HW probes / FV	/
Ko & Chan (1984, 1990, 1992)	2	8e+4	HW probes / FV	/
Chua, et al.(1998)	3	4.72e+3	HW probes / Pitot tubes	/
Dunn & Tavoularis (2006)	1.92	62 ~ 1230	LDV / FV	/
Morton & Yarusevych (2010a, 2014a)	2	1050	LDV/ FV	/
Dunn & Tavoularis (2011)	1.92	152 ~ 674	LDV/ FV	/
Teutsch (2012)	1.2, 2	2.2e+3 ~ 5.1e+4	STEREO PIV	$-2D ~ 2D$
Rafati (2014)	1.14 ~ 2.67	2e+3 ~ 5.1e+3	TOMO PIV	$-2.5D~ 4.5D$

*HW probes represent hot-wire probes; P probes represent pressure probes.

Note: FV is short for flow visualization; LDV is short for laser-doppler velocimetry; PIV is short for particle image velocimetry.

It is highly appreciated that large amounts of experimental research in terms of single step cylinders with diverse diameter ratios and Reynolds numbers have been carried out since 1982. All the relevant achievements can be summarized in table 2.2, the major part of which observed three-dimensional vortex shedding and vortex interaction in the wake under a wide range of Reynolds number by means of flow visualization technique, i.e., black ink, smoke wire, hydrogen bubble and dye system, to provide with straightforward and qualitative observation. Although limited quantitative analysis has already been carried out, such as velocity fluctuation at finite positions in the wake zone (achieved via Hot-wire probes or LDV system), it is still not enough for determining instantaneous vortices. Consequently, there can be a significant improvement if one can quantify characteristics regarding diverse types of vortex as well as vortex interactions in between, for instance obtaining the velocity field for each instant of time from the wake zone.

Subsequently, with the utilization of PIV methodology, instantaneous flow field around the step junction and in the wake was quantitatively captured (Teutsch, 2012; Rafati, 2014). After 2014, some researchers gradually placed the emphasis on more complicated structures, such as dual step cylinders and finned cylinders, whereas the author believes more experimental studies in terms of single step cylinders by means of PIV technique are still needed, especially for higher Reynolds numbers. Besides, due to the size limitation of field of view, relevant previous PIV experiments (Teutsch, 2012; Rafati, 2014) didn't manage the capture of the instantaneous vortex interaction between N-cell and L-cell existing behind the large-diameter cylinder, neither the evaluation of N-cell extent for high Reynolds numbers. More specifically, N-cell characteristics regarding the frequency and its dynamic extent against the time at $Re > 1.3e+4$ need to be revealed. As a result, PIV experiments regarding traditional single step cylinders at higher Reynolds number ($Re > 1.3e+4$) with suitable measurement zone coving the dynamic N-L vortex interaction are greatly needed.

Considering the fact that the traditional single step cylinders namely 'sharp step cylinders', have been investigated and demonstrated in previous literature (see table 2.2), the step junction plays a vital role in determining three-dimensional flow structures in the wake. For instance, the mechanism of 'N-cell' vortex shedding is investigated by several previous researchers, including Dunn & Tavoularis (2006) who established the link between the 'N-cell' activity to the spanwise flow emanating from the step junction (viz. the 'downwash'). Relevant perspectives were approved and validated by Morton & Yarusevych (2010a, 2014a). Aiming at controlling the 'downwash', limited experimental

studies on step junction modification (Teutsch, 2012; Rafati, 2014) are launched by varying the diameter ratio (D/d). As a result, deeper insight on the impact of shape of the step junction can be gained, if more kinds of shape can be put forward and evaluated experimentally, for instance switching the sharp corner to round corner.

Table 2.3 Summary of numerical simulations about single-step cylinders having been done.

researches	D/d	Re	Method
Vallès et al. (2002b)	1.34	99	DNS-based
Morton et al. (2009)	2	2000	URANS-based
Morton & Yarusevych (2009, 2010b)	2	150, 300	Finite-volume based (ANSYS CFX)
Morton & Yarusevych (2010a)	2	1050	DES-based
Bjørkli (2012)	$1.11 \sim 3.33$	$150 \sim 600$	Fluent 13.0
Tian et al. (2017a, 2017b, 2019)	2	150	DNS-based
Tian et al. (2020a)	2, 2.4	150	DNS-based
Tian et al. (2020b)	$2 \sim 3$	150	DNS-based
Tian et al. (2021)	2	3900	DNS-based

In contrast to experimental research progress, limited numerical studies have been done and are summarized in table 2.3. In the early stage, relevant numerical simulations were implemented (Vallès, et al., 2002b; Morton, et al., 2009; Morton & Yarusevych, 2009; Morton & Yarusevych, 2010a; Morton & Yarusevych, 2010b), with the main purpose of reproducing the experimental phenomenon. Recently, several related papers in relation to numerical work were published, by revealing more basic physical phenomenon which cannot be obtained from experiments or need more convinced proofs under lower Reynolds numbers (Bjørkli, 2012; Tian, et al., 2017a; Tian, et al., 2017b; Tian, et al., 2019; Tian, et al., 2020a; Tian, et al., 2020b; Tian, et al., 2021), such as, the impact of diameter ratio (D/d), and surface pressure distribution near the step junction, and the phase difference accumulation between N-cell and L-cell. However, there are still much potential in modelling flow around single step cylinders at higher Reynolds number, especially when Re is above 1.3e+4. With the continuous increase of Reynolds number, much more chaos is involved in the wake, which directly affects the corresponding primary vortex shedding. Apart from that, the limitation on experiment facilities, such as the size and the position of field of view (FOV), makes it difficult for capturing three-dimensional flow structures within a larger region. The implement of corresponding numerical simulations can help make a supplement to observe flow activities which are out of the experimental field of view (FOV), furthermore, can help explain some physical observations which cannot be illustrated via experimental studies.

In a summary, fluid properties (especially vortex characteristics) behind single step cylinders were investigated experimentally and numerically. For the sharp step cylinder (D/d = 2), relevant experiment tests were designed and carried out with the Reynolds

number of 1.6e+4, by means of Planar PIV testing system. Vortex-shedding cells, as well as vortex interactions, under high Reynolds number can be quantitatively studied. Apart from that, the entire dynamic N-cell features can be obtained within a suitable field of view (FOV). For study on various shapes of step junction, a round step cylinder model is introduced and experimentally tested. In contrast to the sharp step cylinder, this model changes its step edge into round corner (see figure 1.3 & 1.4). By launching relevant experimental tests, vortex shedding properties behind the round step cylinder is investigated; the outcome is compared with that behind the sharp step cylinder, indicating the impact of shape of step junction, furthermore, building a connection with the 'downwash'. For the numerical contribution of the present study, considering the limited experimental data, numerical simulations aiming at the comparative study between the sharp step cylinder and round step cylinder are employed, with the emphasis on flow structures near step junctions, as well as surface pressure and loading variation.

Chapter 3
METHODOLOGY

3.1 Experimental Setup

Experiments were carried out in a closed loop wind tunnel situated at the Handley Page laboratory at City, University of London, with schematic explanation in figure 3.1. The incident velocity range from 10m/s to 45m/s is appropriate, to maintain the turbulence intensity at approximately 1% (Šidlof, et al., 2017). During the entire experimental process, the target Reynolds number is guaranteed by means of 'temperature control'. More specifically, the environment temperature is monitored all the time and allowed to cool down between two adjacent tests, to maintain the air density around 1.2kg/m^3. Taking a look at previous PIV-related experiments (see table 2.2), the corresponding Reynolds number from 2e+3 to 5.1e+4 is covered, where transition from laminar state to turbulence takes place at shear layer. However, the size of measuring zone is not large enough to capture the complicated vortex interaction behind large-diameter cylinder, which motivates the author to conduct the following tests, as well as to determine the Reynolds number within that range. Consequently, step cylinders with two Reynolds numbers (*Re*) are studied namely, 1.6e+4 and 3.3e+4. As it is mentioned in Chapter 2, the Reynolds number (*Re*) for step cylinders in the present study is calculated based on large cylinder diameter ('*D*').
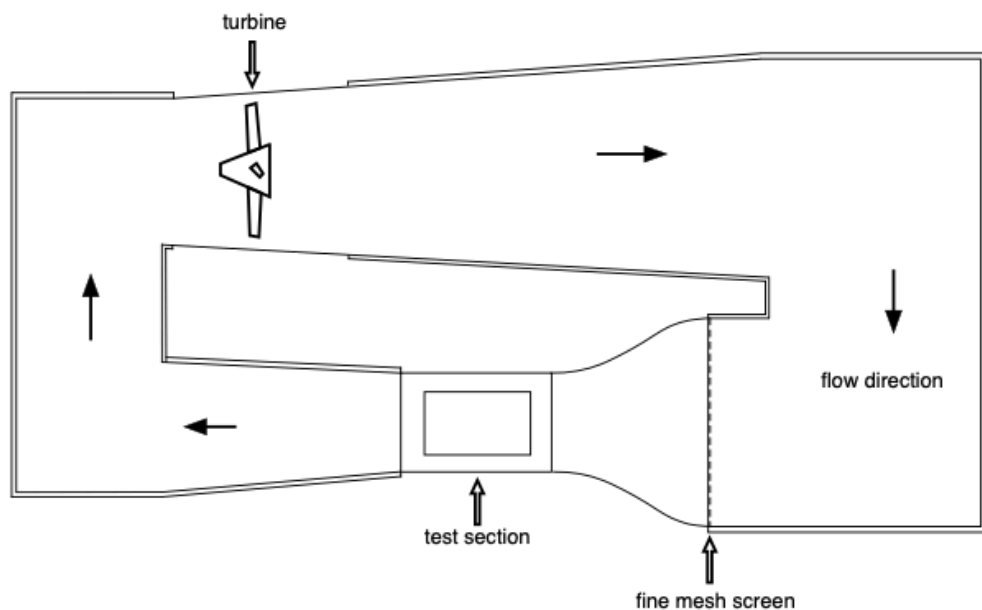
Figure 3.1 Schematic sketch of the wind tunnel.

<div align="center">(a)   (b)</div>
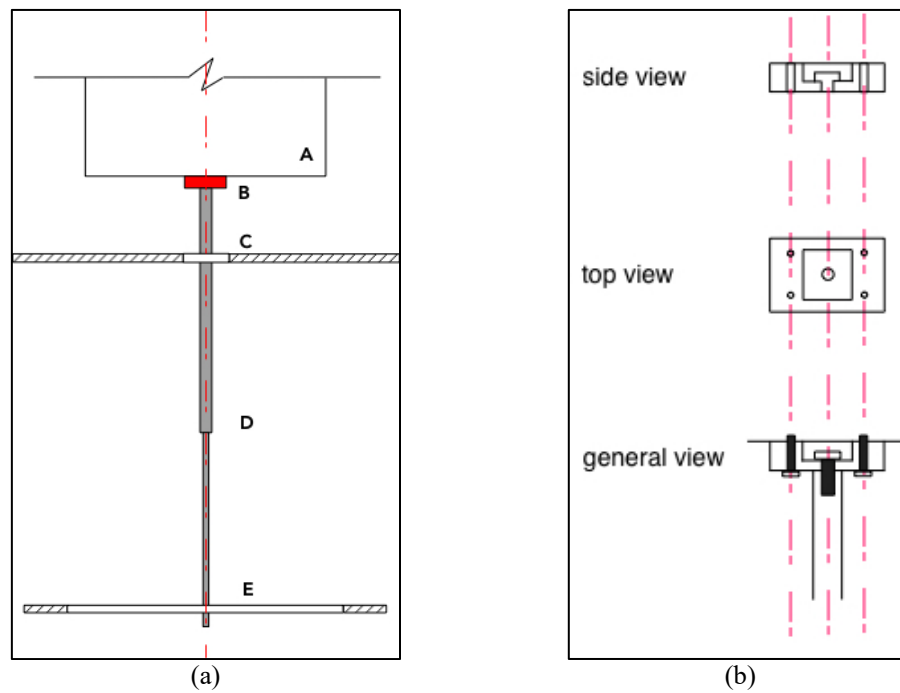
Figure 3.2 Schematic sketch of test section (a) and connecter (b).

Note: A: Top support (six-component aerodynamic force balance); B: Connecter; C: Acrylic ring; D: Testing model; E: Acrylic disc (optical window).

The test section where all experiments take place is located in the middle part of the wind tunnel, featuring the dimension of $1.78m \times 0.81m \times 1.22m$. Large rectangle glass window (optical window) is mounted along each side, to allow the visualization from outside, the model installation and replacement. The step cylinder model is vertically placed at the centre of the test section (see figure 3.2(a)). Its two ends extend past the top wall and bottom wall, ensuring the test model take up the entire span. The large-diameter end passing through an Acrylic ring, eventually fixed with the top support using the connecter. There is an optical window at its bottom, covered by an acrylic disc at the diameter of $0.32m$, which can let laser light get through and provide with a smooth boundary condition. There is a six-component aerodynamic force balance located above the test section. In the present experimental study, a special connecter is fabricated and installed on the force balance to achieve the joint between the top support to testing models. To avoid the potential vibration, the connector is well designed as shown in figure 3.2(b). Four screws combine the connector with the top support, and another one big central screw is used to mount the testing model.

<u>Testing model details</u>

In the present research, a total of three experimental models are designed and fabricated, one of which is the plain cylinder, and the other two of which are step cylinders with different step junctions. It should be noted that every testing model is made in one piece, to avoid errors near the junction due to the assembly of multi-parts. If high precision can be guaranteed, the large cylinder part and small cylinder part can be made separated, and the 'screw system' is used to complete the combination (Rafati, 2014). The corresponding schematic sketch in figure 3.3 depicts general features of these three models. As for Model 1 and Model 2, step cylinders are made up of two co-axial circular cylinders with different diameters, namely large cylinder (L-cylinder) and small cylinder (S-cylinder). The diameter of L-cylinder (D) and S-cylinder (d) keeps the same dimension between Model 1 and Mode 2. The key difference between Model 1 and Model 2 is the shape of the step junction, which is highlighted using red dash circle in figure 3.3. The step junction of Model 1 is equipped with sharp corner, whilst that in Model 2 is round corner. Model 3 (viz. the plain cylinder) can be regarded as a reference model, whose diameter is the same as L-cylinder of Model 1 and Model 2. Table 3.1 presents the description of all models, and table 3.2 summarizes all relevant technical parameters.
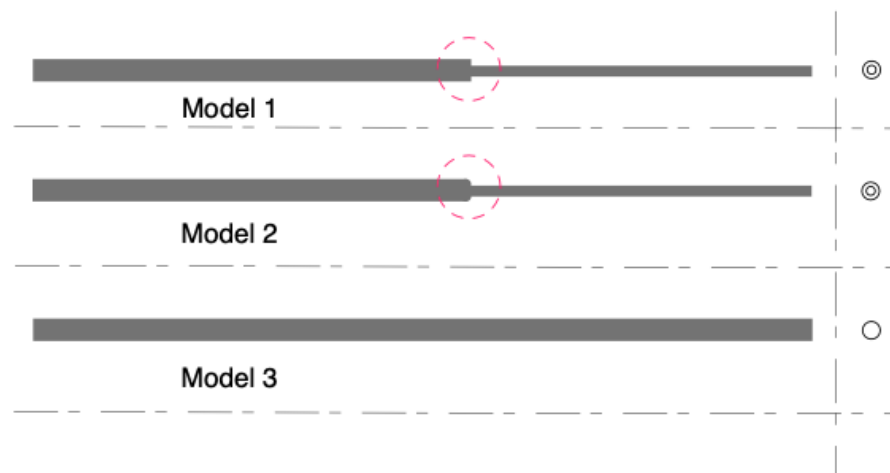
Figure 3.3 Schematic diagram of three experimental models.

Table 3.1 Summary of details about experimental models.

	Description	For short	Component
Model 1	sharp step cylinder	sharp step (*S step*)	Large cylinder (D), Small cylinder (d)
Model 2	round step cylinder	round step (*R step*)	Large cylinder (D), Small cylinder (d)
Model 3	Plain cylinder	/	Large cylinder (D)

Table 3.2 Summary of experimental model dimensions.

	Component	Diameter ratio (D/d)	Aspect ratio	Shape of step junction
Model 1	Large cylinder	2	16.2	sharp corner
	Small cylinder		32.4	
Model 2	Large cylinder	2	16.2	round corner
	Small cylinder		32.4	
Model 3	Plain cylinder	1	16.2	/

There is a short supplement to be added in terms of the design of such a big aspect ratio. Previous research has proved that vortex shedding from a uniform circular cylinder can be affected near both ends, with a spanwise range of 3.5D (Mair & Stansby, 1975). Besides, Morton & Yarusevych (2010a) successfully discerned special vortex shedding with a spanwise region of 3D near two sides (endplates) of single step cylinder. Consequently, the big aspect ratio can help mitigate the 'end effect' towards flow fields near the step junction.

Planar PIV measurements

Two-dimensional particle image velocimetry (PIV) technique is an effective method for evaluating and measuring instantaneous flow state along pre-assigned planes (Willert & Gharib, 1991; Grant, 1997). Its general procedure can be summarized as follows. Moving tracer particles along a plane are illuminated by the high-power laser. One image pair (raw data) is captured via a digital camera equipped with CCD (charged couple device) component. The time interval of this image pair is at the order of microsecond (μs), determined by two neighbouring exposures of the laser. The raw data is converted to the post-processing software, to extract the displacement of tracer particles using 2D cross-correlation technique, further determine the instantaneous velocity vector field. Consequently, the velocity vector field ensemble can be obtained provided that large numbers of pairs of images are captured. Some other techniques must be mentioned namely how to link the distance on the image to the physical length and how to utilize 2D cross-correlation methodology, both of which together with specific information in terms of relevant devices for the current experiments are given in the following part.

(a): side view   (b): top view
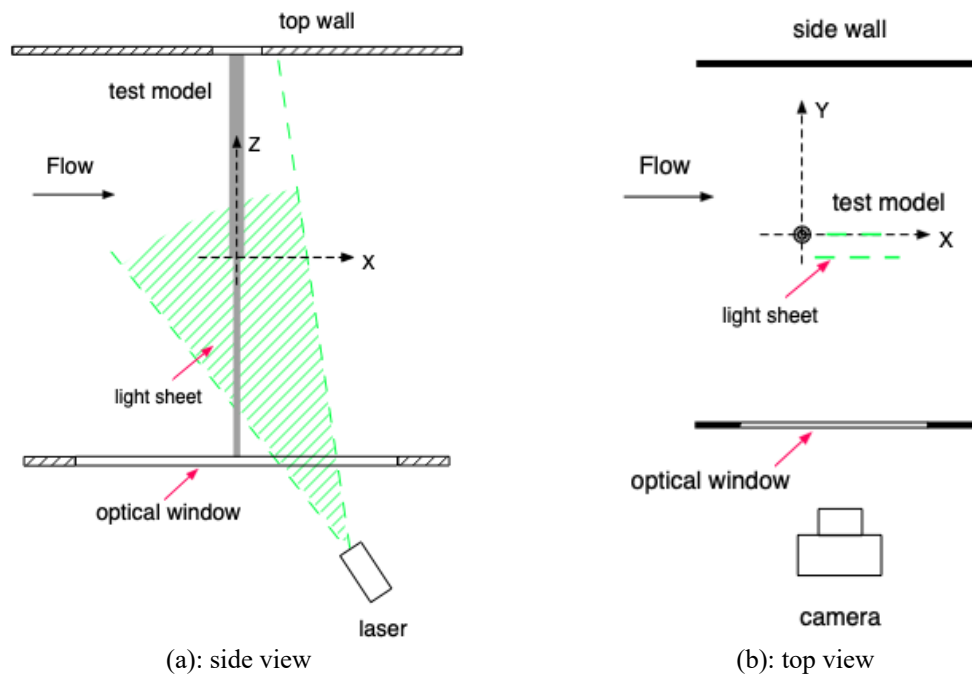
Figure 3.4 Schematic sketch of PIV measuring system.

The schematic sketch of the PIV measuring system for the present experiments is shown in figure 3.4. Two measuring planes are vertical located behind step cylinders namely Plane Y = 0D, -0.6D. The laser emanates from a cylinder-shaped lens apparatus underneath the wind tunnel, which goes through the bottom Acrylic disc (optical window) and lightens the measuring area in the wake. The cylinder-shaped lens apparatus is connected to a double-pulsed Nd: YLF laser through long flexible mental arms. A high-speed digital camera (Phantom Miro M310) equipped with a 100mm focal length Tokina macro-lens is utilized and mounted on a mental frame at one side of the wind tunnel. It can monitor flow activity behind the step cylinders through the side glass window (optical window). The entire process consists of three stages namely, the optical calibration, raw data obtainment and post-processing.

As per how to get raw data, olive oil seedings with approximate 1μm in diameter is adopted as tracer particles, to mix with the moving fluid. The 2mm thick laser light sheet (see 'green area' in figure 3.4) generated from the cylinder-shaped lens apparatus, is set to illuminate and overlap with the target measuring plane. Subsequently, moving olive oil seedings along the measure plane are illuminated. A 2mm thickness is assigned to mitigate or avoid potential errors result from particles stepping out of the measuring plane. With the assistance of the digital camera, one pair of image with specific time interval (10μs or 30μs) at the frames of 1280×800 pixels are captured to determine the instantaneous movement of these moving particles. As a result, 2000 to 3000 successive image pairs (raw images) are gathered at the sampling frequency of 1000Hz or 1500Hz, to give an

evaluation of the continuous displacement. The corresponding PIV parameters vary by altering light sheet location and Reynolds number, as shown in table 3.3.

Table 3.3 Summary of PIV related parameters.

Re	Light sheet	Sampling frequency	Pair of images	Time interval of each pair
1.6e+4	Plane Y = 0D	1000Hz	2000	30μs
1.6e+4	Plane Y = -0.6D	1000Hz	3000	30μs
3.3e+4	Plane Y = 0D	1500Hz	2000	10μs
3.3e+4	Plane Y = -0.6D	1500Hz	3000	10μs

The main content of post-processing is to transfer raw image pairs to TSI Insight 4G software. Within the TSI Insight 4G software, instantaneous velocity vector field can be calculated via 2D cross-correlation on each image pair. For the post-processing, particles within a virtual window are considered which is called as 'interrogation window'. As a general principle, smaller window contains a smaller number of particles as well as less area provided that the particle density is fixed, which gives rise to more accuracy at the particle positioning and to mitigate noise errors. However, a big interrogation window is proved to be more reliable in velocity vector generation (Fincham & Delerce, 2000). As a result, the strategy is to implement two interrogation windows with different sizes at two steps. An interrogation window (32×32 pixels) is employed for the first time and a smaller window (16×16 pixels) is utilized to do cross-correlation at the result from the first step, to help capture the particle displacement inside. Similar PIV operation and related parameter setting was used for other aerodynamic investigations (Talboys & Brücker, 2018; Teutsch, 2012).
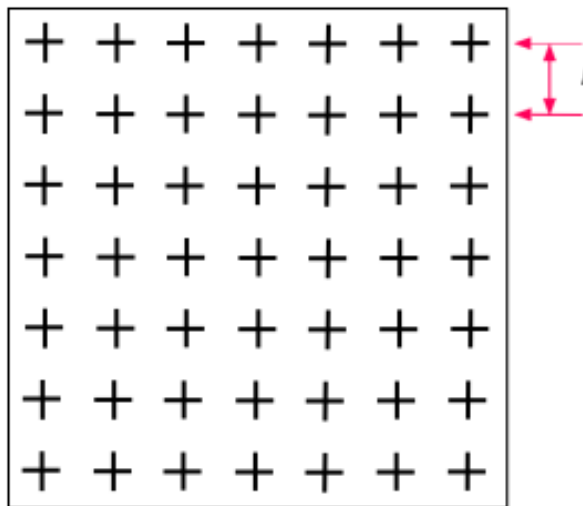
Figure 3.5 Schematic sketch of black board for calibration.

Considering the fact that particles move within each image pair in pixels, it is with high importance to establish a relationship between the pixel gap and the physical distance. Consequently, the optical calibration is implemented. A black board, comprising small and evenly distributed white crosses (see figure 3.5), is vertically placed, letting its

surface coinciding with the laser light sheet. From figure 3.5, the physical distance between crosses keeps constant, given as 'l_P'. One can observe the black board with crosses from the images, where the gap between two neighbouring crosses can be measured in pixels, given as ''l_C'. Consequently, the relationship between the physical distance and pixel gap in the image can be established using the ratio of l_C/l_P. Eventually, the corresponding ratio in terms of two light sheets (Plane Y = 0D, -0.6D) can be achieved namely, 5.067px/mm and 5.095px/mm respectively.

3.2 Data Processing

This section mainly introduces a series of useful mathematical methods for processing PIV experimental data. In the very beginning, time-averaging related content is given, comprising the mean value and the root mean square value of velocity in three directions (u, v, w), followed by the definition of Reynolds decomposition, as well as its further application. Subsequently, proper orthogonal decomposition (POD) and its extension (viz. phase averaging) are expressed via corresponding equations, which can help identify coherent structures with diverse scales under turbulent state and do average on the basis of phase variation. Lastly, spectral analysis and wavelet analysis are introduced, for determining the averaged and instantaneous frequency of vortex shedding from testing models.

Mean, rms and Reynolds decomposition

The mean value and root mean square value being essential and useful statistic terms for evaluating velocity fluctuation are believed to be reliable for solving turbulence-related issues due to the impact of involved chaotic and random part in turbulent flow being significant. As a result, the corresponding equations are listed as:

$$\overline{u} = \frac{\sum_{j=1}^{M} u_j}{M} \ , \qquad \overline{v} = \frac{\sum_{j=1}^{M} v_j}{M} \ , \qquad \overline{w} = \frac{\sum_{j=1}^{M} w_j}{M} \ , \qquad (3.1)$$

$$u_{rms} = \sqrt{\overline{u'^2}} = \sqrt{\frac{\sum_{j=1}^{M} (u_j - \overline{u})^2}{M}} \qquad (3.2)$$

$$v_{rms} = \sqrt{\overline{v'^2}} = \sqrt{\frac{\sum_{j=1}^{M} (v_j - \overline{v})^2}{M}} \qquad (3.3)$$

$$w_{rms} = \sqrt{\overline{w'^2}} = \sqrt{\frac{\sum_{j=1}^{M} (w_j - \overline{w})^2}{M}} \qquad (3.4)$$

where u, v, w represent velocity at three directions namely streamwise, cross-streamwise and spanwise. The capital 'M' is the number of involved elements. The subscript of '*rms*' denotes root mean square.

In order to gain deep insight on turbulence, the original turbulent flow can be divided into two main components by applying the 'Reynolds decomposition' (Adrian, et al., 2000), thereby generating the mean flow part [$\overline{U}(x, y, z)$], the fluctuation part [$U'(x, y, z, t)$], as shown in the equation below.

$$U(x, y, z, t) = \overline{U}(x, y, z) + U'(x, y, z, t) \tag{3.5}$$

'Reynolds decomposition' presents one concept for solving Navier-Stokes equations by replacing the velocity with time-averaged part and the fluctuation part, corresponding content of which will be narrated in section 3.3.2.

The fluctuation part, consisting of entire instantaneous velocity variation, especially chaotic and random term for turbulent flow, which is hard to predict and describe. For the periodic flow, i.e., flow behind the cylinder, this fluctuation part (mentioned as [$U'(x, y, z, t)$]) can have another decomposition, to expose the dominant vortex shedding, to filter the random turbulence. As a result, the original 'Reynolds decomposition' can be rewritten in another form (Hussain & Reynolds, 1970):

$$U(x, y, z, t) = \overline{U}(x, y, z) + \widetilde{U}(x, y, z, t) + u'(x, y, z, t) \tag{3.6}$$

where $\widetilde{U}(x, y, z, t)$ is the dominant vortex shedding activity, indicating instantaneous periodic fluctuated velocity component; $u'(x, y, z, t)$ is the instantaneous random disturbance. This multi-decomposition method has a wide application, for instance, recognising dominant vortex shedding from the turbulent flow. Besides, the instantaneous velocity field reconstruction eliminating the disturbance can clearly characterise the vortex shedding activity, especially the occurrence of vortex interaction.

Proper orthogonal decomposition (POD)

On the basis of the concept of notable coherent structures (Hussain, 1986), turbulent flow could be estimated with quite high precision. Illustration about POD methodology in detail can be found in a series of literature, involving introduction papers and relevant applications (Liang, et al., 2002; Berkooz, et al., 1993; Meyer, et al., 2007). POD, a kind of data processing method for solving turbulence issues, shares similar concept with PCA (Principal Component Analysis). The theory of PCA (Jolliffe & Cadima, 2016) is to describe the dataset by creating a series of principal components. It should be noted that

all the principal components are linearly uncorrelated. Similarly, POD can help recognise coherent structures with diverse scales in turbulent flow and place an order to find primary coherent structures. Considering the two-dimensional situation, POD processing can be described to divide the fluctuation part $[U'(x, y, t)]$ into a series of un-associated parts with the equation form shown as (Morton, 2014):

$$U'(x, y, t) = \sum_{m=1}^{N} a_m(t) \vec{\theta}_m(x, y) \qquad (3.7)$$

$a_m(t)$: temporal part; $\qquad\qquad$ $\vec{\theta}_m(x, y)$: spatial part;

Each normalized base function $[\vec{\theta}_m(x, y)]$ is orthogonal with the others in terms of spatial scope. The mode coefficient $[a_m(t)]$, depending on time series, is obtained by projecting the fluctuation part $[U'(x, y, t)]$ onto the corresponding base function $[\vec{\theta}_m(x, y)]$. Considering the ensemble of velocity fields $[U'(x, y, t1), U'(x, y, t2), ..., U'(x, y, tn)]$, the corresponding mode coefficient series for each base function can be achieved in form of '$a_m(t1), a_m(t2), ..., a_m(tn)$'. It should be noted that each mode coefficient $[a_m(t)]$ is independent from the others in terms of temporal scope. Besides, the variance $[\lambda_m]$ of the mode coefficient series for each base function can be termed as eigenvalue, representing the 'weight' or 'contribution' of each base function. According to the eigenvalue magnitude, all the base functions can be placed in an order from the largest to the smallest, named as 1st, 2nd, ..., nth POD mode. It is obvious that the first several POD modes being dominant modes has larger contribution to the entire flow field.

As for the above mentioned periodic turbulent flow which contains only one type of vortex shedding (constant shedding frequency), the original flow field consists of three components namely, the mean flow field, the dominant vortex shedding activity and random turbulence. The dominant vortex shedding activity can be extracted using POD method, normally denoting the first pair of POD mode. It should be borne in mind that the rest POD modes can be treated as random turbulence part due to the contribution of first pair of mode being significantly far larger than that of other modes. Consequently, a new field $[U_{esti}(x, y, t)]$ can be reconstructed by superposing the first pair of mode on the mean flow, as shown in the forthcoming equation (Van Oudheusden, et al., 2005).

$$U_{esti}(x, y, t) = \overline{U}(x, y) + a_1(t) \vec{\theta}_1(x, y) + a_2(t) \vec{\theta}_2(x, y) \qquad (3.8)$$

For an instantaneous velocity field, it is believed that (Van Oudheusden, et al., 2005; Perrin, et al., 2006) mode coefficient of the first pair of POD mode determines the instantaneous shedding phase. A reasonable explanation is to treat the two orthogonal base functions namely, $\vec{\theta}_1(x,y)$ and $\vec{\theta}_2(x,y)$, as two orthogonal axes, corresponding mode coefficients of which form a set of coordinates namely $[a_1(t), a_2(t)]$, comprising instantaneous phase information. For the ensemble dataset $(t_1, t_2,..., t_n)$, normalized mode coefficients namely $a_1(t)/\sqrt{2\lambda_1}$ and $a_2(t)/\sqrt{2\lambda_2}$ are proved to have sinus / cosine relationship with corresponding phase degrees (Van Oudheusden, et al., 2005), which can be expressed in equations as:

$$a_1(t)\sqrt{2\lambda_1} = \cos(\gamma), \qquad\qquad a_2(t)\sqrt{2\lambda_2} = \sin(\gamma) \qquad (3.9)$$

where the γ is the specific shedding phase. The ensemble discrete normalized mode coefficients ($a_1(t)/\sqrt{2\lambda_1}$ and $a_2(t)/\sqrt{2\lambda_2}$) against shedding phase are plotted in figure 3.6. The involved discrete data covers the entire span from 0 degree to 360 degree, well concentrating near red curves, expressed as:

$$\cos(\gamma) = 1, \qquad\qquad sine(\gamma) = 1 \qquad (3.10)$$
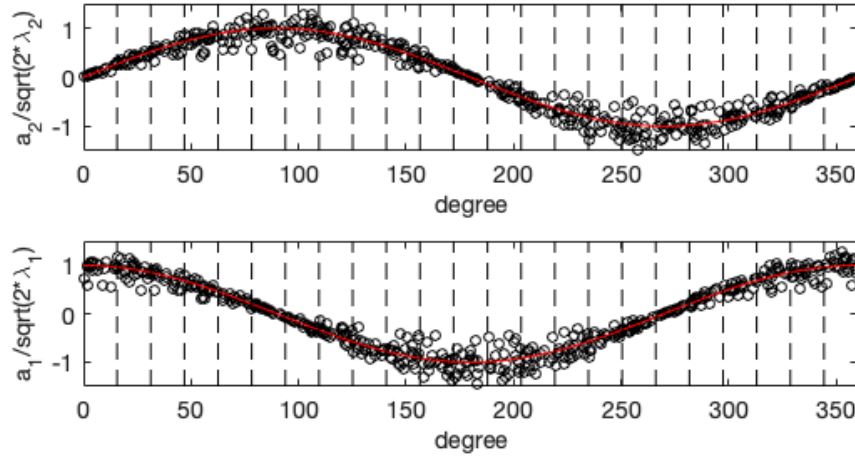
Figure 3.6 Explanation about identifying phases and dividing phases into bands.

Note: data from the present study (Plain cylinder, Plane Y = -0.6*D*, *Re* = 1.6e+4). the coordination of each circle stands for mode coefficient of the first pair of POD mode at a certain instant of time.

Figure 3.6 successfully establishes relationship between the instantaneous vortex shedding and the shedding phase, inspiring a conditional averaging approach on the basis of phase variation. Considering the entire phase range namely from 0 degrees to 360 degrees, 24 bands (Rafati, 2014) with the identical width can be obtained with borders marked as dash line shown in figure 3.6. Subsequently, the entire dataset is divided into

24 parts namely 24 phases. The averaged flow in terms of a specific phase can be achieved by averaging the discrete data involved into the same band.

The aforementioned POD-related content only presents the general concept and key equations in terms of POD and phase averaging. More details in terms of POD processing will be given in section 4.3.

Spectral and Wavelet analysis

In the present thesis, spectral analysis in terms of velocity signal is implemented using discrete Fourier transform (DFT), a method for extracting frequency component from a certain length of signal. DFT-related calculation and operation is achieved using Welch's method within the frame of MATLAB. Welch's method is an advanced option for estimating the power spectral density (PSD) and obtaining the frequency content. During its processing, the entire signal is divided into several same length parts with overlapping setting (50% or 0%). Each individual portion of signal is windowed separately to mitigate the spectral leakage (Harris, 1978). The frequency resolution is determined by the sampling frequency and the length of each portion. For the present study, the window function of Hanning window is selected.

According to a preliminary estimation on involved vortex shedding activities, the shedding frequency is below $200Hz$, of the order of $10Hz$ and $100Hz$, which is believed that a processing frequency resolution of $1Hz$ is appropriate to spotlight dominant frequencies and gaps in between. Consequently, parameters regarding Welch's method can be determined, for instance the 50% overlapping. It should be noted that two sampling frequencies namely $1000Hz$ and $1500Hz$, are used for recording velocity fluctuation for different cases, which determines the width of 'Hanning window' as 500 and 750.

Wavelet analysis (wavelet transform, short for WT, (Farge, 1992)) is proved to be a robust methodology for obtaining frequency information from time-series signal and detecting frequency dynamics. Unlike the other two methods namely FT (Fourier transform) and STFT (shout-time Fourier transform), WT exhibits excellent performance in processing unstable signal which consists of multi-frequencies. Its emphasis is placed on the 'local' parts of target signal, which allows frequency variation over time exposed. However, FT, a classical time-frequency analysis tool, is believed to do a good job in finding frequency information from stationary signal. STFT, with the utilization of window functions, can localise frequency over time, whilst exposes tricky issues in terms of time and frequency relationship (Kıymık, et al., 2005). The key concept of Wavelet transform is to use a single wavelet, that is, a little wave with small oscillation, starting from '0' magnitude

and ending up with '0' magnitude. By convolving the single wavelet with the target signal, the occurrence of this single wavelet over the entire target signal can be obtained. The current study employs the complex Morlet wavelet which defines of a complex sine function substituting into the Gaussian (Torrence & Compo, 1998; Dunn & Tavoularis, 2006; Cohen, 2019). The following equation provides one expression adopted in MATLAB:

$$\psi\left(x\right) = \left(fb \times \pi\right)^{-1/2} e^{2\pi i \times fc \times x} e^{-x^2/fb} \tag{3.11}$$

where x is the time centred at '0' and 'i' denotes the imaginary operator. 'fb' and 'fc' are the bandwidth and central frequency, being assigned as 2 and 1 respectively for the present study.

On the basis of the initial wavelet ($\psi\left(x\right)$, also known as mother wavelet), equation 3.12 is used to create a group of wavelets (Sinha, et al., 2005):

$$\psi_{b,x^*}\left(x\right) = \frac{1}{\sqrt{b}}\psi\left(\frac{x - x^*}{b}\right) \tag{3.12}$$

where 'b' is the scale to adjust the width of mother wavelet, and the application of normalized time 'x' is to give the displacement along time axis. It should be noted that the present study employs the continuous wavelet transform (CWT) by convoluting the wavelet function ψ with the continuous signal $h(x)$; its formula expression is given as follows (Daubechies, 1992; Sinha, et al., 2005):

$$C_{b,x^*} = \int_{-\infty}^{\infty} h\left(x\right) \frac{1}{\sqrt{b}}\widetilde{\psi}\left(\frac{x - x^*}{b}\right) dx \tag{3.13}$$

where the $\widetilde{\psi}$ is the ensemble wavelet. The scale (b) range and gap of two neighbouring scale elements quantify the ultimate frequency domain and resolution (Mallat, 1999). The left side of the above equation (C_{b,x^*}) is CWT result, corresponding to the scale range (b_1, b_2, b_3, ..., b_m) and the time range (x_1, x_2, x_3, ..., x_n). As the scale range can be converted to frequency range, the ultimate CWT result can be displayed as a three-dimensional surface graph, with the vertical axis of the coefficient (C_1, C_2, C_3, ..., C_{m*n}), the horizontal axis and transverse axis being frequency and time. The utilization of CWT for the current study extracts peaks of surface graph at each instant of time which indicates instantaneous frequency variation over the time.

3.3 Computational Methods

This section makes a brief introduction about background knowledge of CFD (computational fluid dynamics) in relation to the present numerical study, starting with basic equations for fluid dynamics. In order to investigate the turbulent flow, several turbulence models are systematically presented namely RANS, LES and DES respectively. RANS solution (Reynolds-averaged Navier-Stokes) provides a simplified concept for solving Navier-Stokes equations, by decomposing the instantaneous flow into two components, i.e., the time-averaged part and fluctuation part. By setting the appropriate filter, LES solution (large eddy simulation) enables turbulence with large length scales numerically solved via Navier-Stokes equations, and the smaller scale portion modelled using sub-grid scale (SGS) models. The DES solution (detached eddy simulation) being a hybrid model with the combination of RANS and LES employs RANS mode to solve flow within boundary layer and LES mode for regions outside.

<u>Governing equations</u>

The continuity equation is used to interpret the conservation of mass. Assuming an element in fluid flow, the mass of the element might vary against time due to the flow in and out. In another word, the mass increase rate of the element equals to the difference of net rate of the flow in and out, the ultimate equation of which is given in equation 3.14. For incompressible flow, the rate that the fluid enters the element equals to the rate that the fluid leaves the element owing to the constant density (ρ). The continuity equation can be made a simplification and rewritten in the form of equation 3.15.

$$\frac{\partial \rho}{\partial t} + \nabla \bullet (\rho \mathbf{U}) = 0 \tag{3.14}$$

$$\nabla \bullet \mathbf{U} = 0, \qquad\qquad \frac{\partial u}{\partial x} + \frac{\partial v}{\partial y} + \frac{\partial w}{\partial z} = 0 \tag{3.15}$$

Assuming a small control volume containing a certain number of particles, the variation of particles' momentum equals to forces that particles encounter (viz. surface forces and body forces) on the basis of Newton's second law. In incompressible flow, the simplified momentum equations can be given as:

$$\frac{\partial \rho u}{\partial t} + \nabla \bullet (\rho u \mathbf{U}) = \nabla \bullet (\mu \nabla u) - \frac{\partial p}{\partial x} + \rho f_x \tag{3.16}$$

$$\frac{\partial \rho v}{\partial t} + \nabla \bullet (\rho v \mathbf{U}) = \nabla \bullet (\mu \nabla v) - \frac{\partial p}{\partial y} + \rho f_y \tag{3.17}$$

$$\frac{\partial \rho w}{\partial t} + \nabla \bullet (\rho w \mathbf{U}) = \nabla \bullet (\mu \nabla w) - \frac{\partial p}{\partial z} + \rho f_z \tag{3.18}$$

Turbulence models

For resolving turbulence issue, three different turbulence models are raised in this subsection namely RANS, LES and DES. Considering the fact that the hybrid method, i.e., DES, exhibits more reliable performance in resolving separated flows than RANS and LES (Spalart, 2009), $k - w$ SST DES is eventually determined for this thesis.

Reynolds-averaged Navier-Stokes

The Reynolds-averaged Navier-Stokes (RANS) equations can be derived from the original Navier-Stokes equations by means of time averaging (L. Davidson, 2015). The derivation processing is briefly introduced below. Equation 3.19 interprets the original Navier-Stokes equation:

$$\frac{\partial u_i}{\partial t} + \frac{\partial(u_i u_j)}{\partial x_j} = \nu \frac{\partial^2 u_i}{\partial x_j \partial x_j} - \frac{1}{\rho} \frac{\partial p}{\partial x_i} + f_i \tag{3.19}$$

The key principle for RANS is to do Reynolds decomposition, as mentions in section 3.2, by dividing the instantaneous flow into time-averaged part and fluctuating part. The flow properties (*u* and *p*) can be decomposed as:

$$u_i = \overline{u}_i + u'_i, \qquad\qquad p = \overline{p} + p' \tag{3.20}$$

where the 'upper bar' represents time-averaged term and the prime symbol represents fluctuating term. Substitute equation 3.20 into the Navier-Stokes equation and do averaging on both hands, we can have the following two equations:

$$\overline{\frac{\partial (\overline{u}_i + u'_i)}{\partial t}} + \overline{\frac{\partial \left[(\overline{u}_i + u'_i)(\overline{u}_j + u'_j) \right]}{\partial x_j}} = \nu \overline{\frac{\partial^2 (\overline{u}_i + u'_i)}{\partial x_j x_j}} - \frac{1}{\rho} \overline{\frac{\partial (\overline{p} + p')}{\partial x_i}} + f_i \tag{3.21}$$

$$\frac{\partial \overline{u}_i}{\partial t} + \frac{\partial(\overline{u}_i \overline{u}_j)}{\partial x_j} = \frac{\partial}{\partial x_j} \left[\nu \frac{\partial \overline{u}_i}{\partial x_j} - \overline{u'_i u'_j} \right] - \frac{1}{\rho} \frac{\partial \overline{p}}{\partial x_i} + f_i \tag{3.22}$$

where $\overline{u'_i u'_j}$ is the Reynolds stress tensor (viz. τ_{ij}) consisting of six independent elements. Including the original four terms into consideration namely, velocity components at three directions and the pressure, we have a total of ten unknowns. However, the original four equations are not enough to close the system. In 1877, Boussinesq put forward to the approximation (Schmitt, 2007), that is, the Reynolds stress is in proportion to the mean rate of strain, which can be described as equation 3.23. Besides, the definition regarding turbulence kinetic energy (k) is given as equation 3.24.

$$-\rho \overline{u'_i u'_j} = \mu_T \left(\frac{\partial \overline{u}_i}{\partial x_j} + \frac{\partial \overline{u}_j}{\partial x_i} \right) - \frac{2}{3} \rho k \delta_{ij} \tag{3.23}$$

$$k = \frac{\overline{u'_j u'_j}}{2} \tag{3.24}$$

where μ_T represents the eddy viscosity. The significance of Boussinesq approximation is that it solves turbulence closure problem with great simplification and introduces the eddy viscosity to sort out micro flow fluctuation.

The $k - \omega$ SST model is a two-equation turbulence model, which has been widely used since it was put forward by Menter (1994). It successfully unites the advantages of $k - \omega$ model and $k - \varepsilon$ model using shear stress transport (SST) formulation. At the near-wall region, the $k - \omega$ model is applied within the boundary layer, which can be treated as a Low-Re turbulence model. Whilst the $k - \varepsilon$ mode is active in the free stream, which can avoid the sensitivity of the inlet turbulence condition.

Large Eddy Simulation

Large eddy simulation (LES) (Smagorinsky, 1963; Deardorff, 1970) is widely used in commercial and academic simulations. Its main principle is to economically solve Navier-Stokes equations by discarding turbulence with smaller scales. As for OpenFOAM (v5.x) software, the corresponding fulfilment in numerical way is to employ a spatial filter which defines a filter width 'Δ_F' to allow the direct solving of the eddies with length scale larger than the filter width. For OpenFOAM (v5.x) software, the common strategy for assigning the filter width 'Δ_F' for LES is '*cubeRootVol*'. The principle of filter width used for LES can be explained via the following equation:

$$\Delta_F = (dx \times dy \times dz)^{1/3} \tag{3.25}$$

where the '*dx*', '*dy*', '*dz*' on the right hand denote the dimension of the grid element. As a result, turbulence with smaller length scale would be modelled via sub-grid scale models (SGS models). Besides, if more turbulence details can be directly solved, the filter width 'Δ_F' must be small enough. It could be obviously deduced that high simulation precision requires high grid resolution, especially for simulating separated flows. Large eddy simulation (LES) has a wide application in investigating turbulent flow around a circular cylinder (Lysenko, et al., 2012; Parnaudeau, et al., 2008; Franke & Frank, 2002).

Detached Eddy Simulation

Detached eddy simulation (DES) is a hybrid solution, aiming to combining the advantages of RANS and LES together (Spalart, 2009). First of all, two key terms are introduced namely the grid spacing 'Δ_G' and the DES length scale ($\widetilde{l}$). The so-called grid

spacing is similar with the filter width in LES solution. However, 'Δ_G' for $k - \omega$ SST DES in OpenFOAM (v5.x) is commonly given via the term '*maxDeltaxyz*'. The general description of the grid spacing is given as:

$$\Delta_G = max\,(dx, dy, dz) \tag{3.26}$$

As for hexahedron-shaped grids, the right hand of equation 3.26 interprets the largest edge of a grid element. By making a comparison between the filter width 'Δ_F' for LES and the grid spacing 'Δ_G' for DES, it is easy to perceive that the former is dominated by cell size in three directions, whilst the latter is only determined by the maximum edge of the cell. Consequently, one might infer that DES solution doesn't need high grid resolution as that for LES solution.

$$\widetilde{l} = min\left(C_{DES}\Delta_G, \frac{k^{1/2}}{\beta^* w}\right) \tag{3.27}$$

The DES length scale ($\widetilde{l}$) for $k - \omega$ SST DES model is given in equation 3.27, which is introduced for determining the switch between 'RANS mode' and 'LES mode' in turbulent flow (Strelets, 2001). For simulating separated flows, considering the grid spacing near the surface being smaller enough, the DES length scale is chosen as $k^{1/2}/\beta^* w$ to ensure $k - \omega$ SST model being applied within boundary layer. For the region away from the surface, the DES length scale being governed by the grid size indicates the implement of 'LES mode'. It should be noted that the grid dimension (viz. $dx \approx dz$, $dx \gg dy$) near surface for DES application is specified on the basis of the grid spacing 'Δ_G', directly evidencing the less computing cost near surface than that for LES application.

Chapter 4
EXPERIMENTAL RESULTS -PRELIMINARIES

Ahead of investigation in terms of single step cylinders, a preliminary experimental study about plain circular cylinders is presented in Chapter 4, corresponding results involving instantaneous / time-averaged velocity fields, POD-based outcome and related spectrum. Two different incident velocities are considered, corresponding to the Reynolds number of 1.6e+4 and 3.3e+4 respectively. For each Reynolds number, velocity measurement after the cylinder is carried out along two different planes (see figure 4.1), one of which is vertically located right behind the cylinder along its axis (viz. 0D offset). The placement of the other measuring plane, 0.6D offset to the cylinder axis, is to highlight one side of the vortex street.
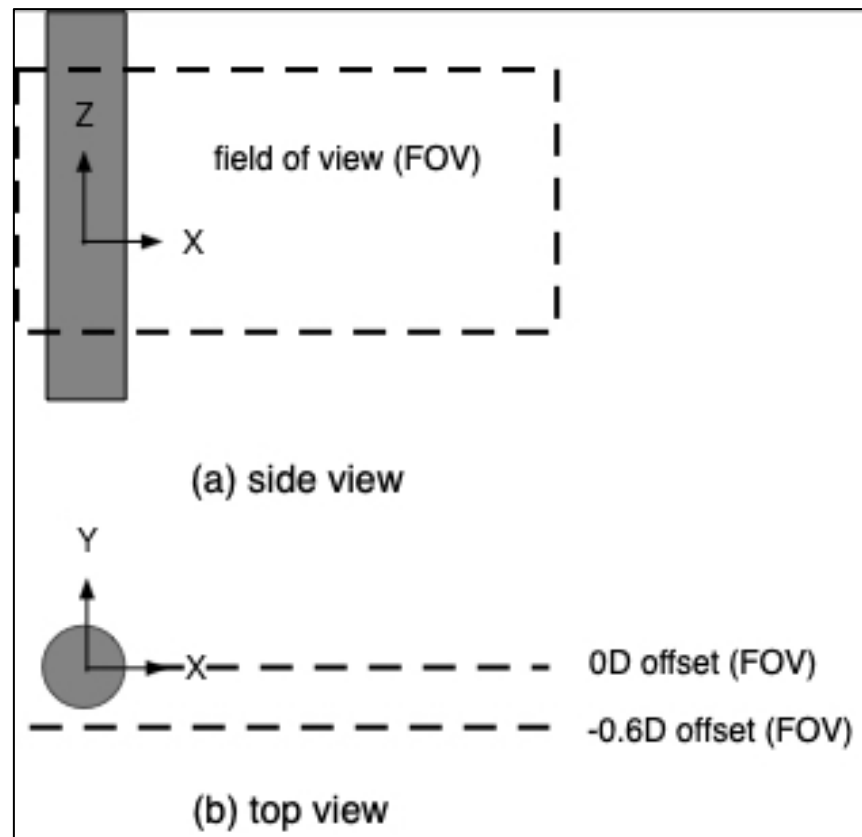
Figure 4.1 Position of field of view (FOV, dash lines) behind the plain cylinder.

4.1 Vortex Identification behind Plain Cylinders

Although velocity components in streamwise direction and spanwise direction along two planes (Plane Y = 0D, -0.6D) were experimentally recorded under each Reynolds number (1.6e+4, 3.3e+4) with the assistance of PIV-based facilities, the obtained data still seems to be too limited to reflect characteristics of three-dimensional vortices detaching from

both sides of the cylinder. As a result, section 4.1 quotes numerical results from case c9 (viz. flow around uniform large-diameter cylinder under Re = 1.6e+4) from Chapter 7, consisting of instantaneous normalized vorticity (Z direction), iso-surface contours and streamwise velocity contents at planes (Plane Y = 0.6D, -0.6D), to establish the relationship between vortex identification and streamwise velocity fields. Relevant numerical results can be sorted out and exhibited in figure 4.2.

(f)
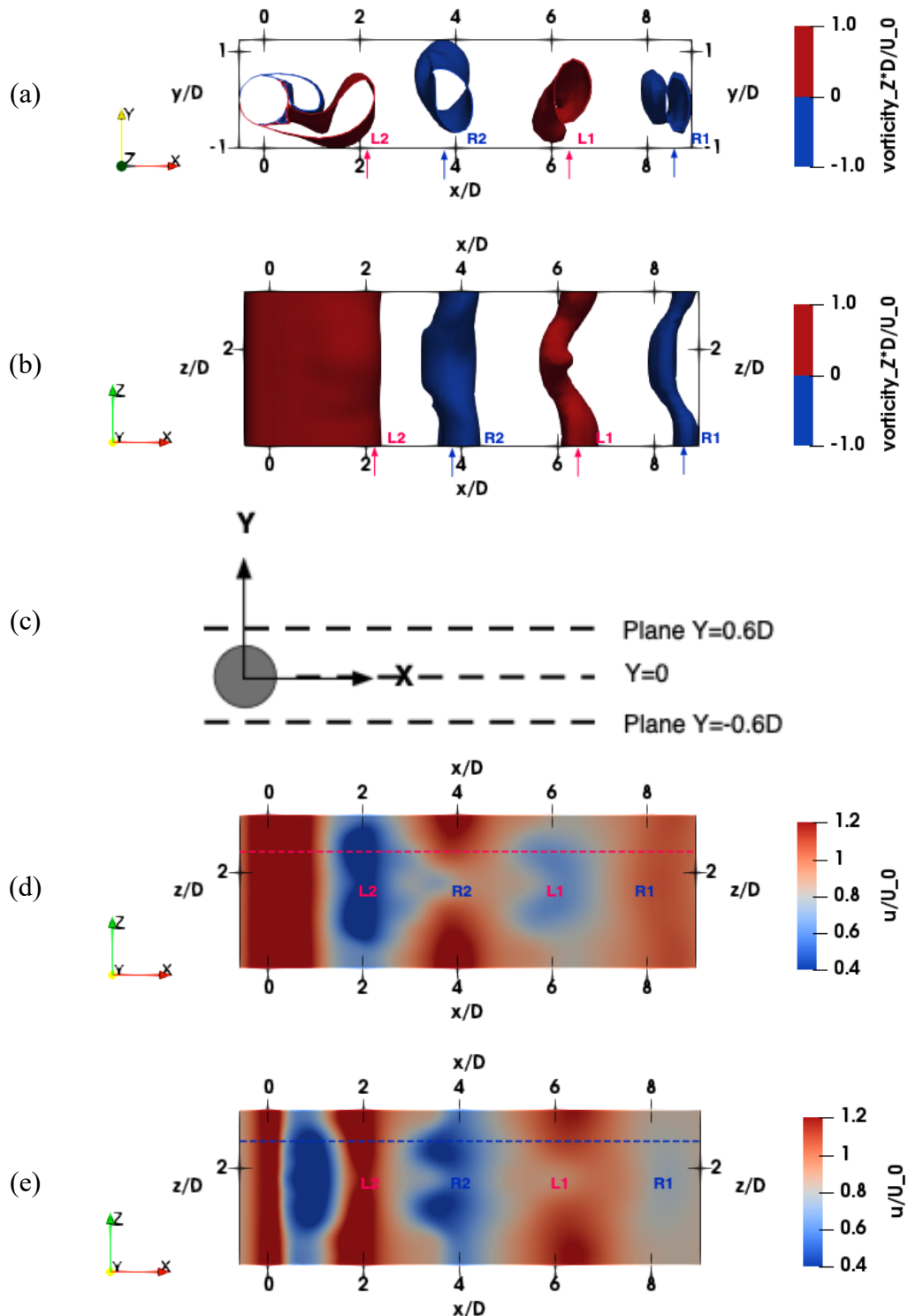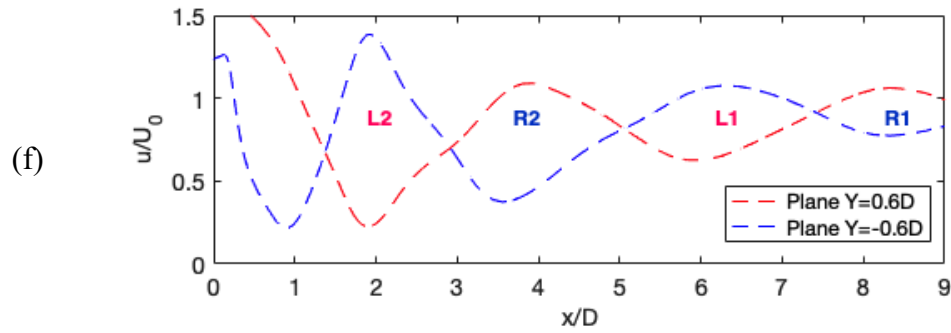
Figure 4.2 Explanation about vortex identification.

Note: (a),(b): vorticity isosurface (*vorticity_z*D/U_0* = 1, -1) from top view (a) and side view (b).

(c): placement of reference planes for instantaneous streamwise velocity fields.

(d),(e): instantane streamwise velocity fields at Plane $Y = 0.6D$ (d) and Plane $Y = -0.6D$ (e).

(f): streamwise velocity variation over Ref. Line A / B.

Red / blue dash lines in (d) / (e): Ref. Line A / B for extracting velocities.

L1 / L2: 1st / 2nd vortex shed from left side; R1 / R2: 1st / 2nd vortex shed from right side.

From figure 4.2(a) & (b), one can clearly observe the Karman vortex street behind the uniform circular cylinder, consisting of several swirling vortices which can be recognised and coloured via normalized vorticity (Z direction). A total of four typical vortices, namely L2, L1 (coloured by red) and R2, R1 (coloured by blue), are evenly distributed along X axis, symbolizing vortices shed from left side and right side of the uniform cylinder. Meanwhile, two reference planes at $Y = 0.6D$, $-0.6D$ are targeted, and shown in figure 4.2(c). The purpose of $0.6D$ offset is to highlight the discrepancy of vortex shedding from two sides of cylinder. The corresponding instantaneous streamwise velocity fields at Plane $Y = 0.6D$, $-0.6D$ are presented at figure 4.2(d), (e), where the colormap represents non-dimensional streamwise velocity. It could be easily found that velocity fluctuates along X axis, giving rise to a series of 'valleys' and 'peaks' which correspond to vortex L1, R1, L2 and R2. A comparison between figure 4.2(d) and figure 4.2(e) exposes the significant difference, that the 'valleys' and 'peaks' in figure 4.2(d) stand for vortices shed from left side (L1, L2) and right side (R1, R2) respectively, whilst they denote right vortices (R1, R2) and left vortices (L1, L2) respectively in figure 4.2(e). Subsequently, extract velocity content from the fields (figure 4.2(d), (e)) along reference lines, namely Ref. Line A ($z/D = 2.4$, red dash line in (d)) and Ref. Line B ($z/D = 2.4$, blue dash line in (e)), and plot them in figure 4.2(f) to reveal more details. The 'valleys' and 'peaks' of velocity variation are completely reversed at Ref. Line A and Ref. Line B, but both successfully identify vortices. In summary, velocity fields along Plane $Y = 0.6D$, $-0.6D$ can be used to identify vortex street behind circular cylinders. The velocity 'valleys' at the plane ($Y = -0.6D$) denote vortices shed from the other side of circular cylinder. For

the present experimental study, vortices shedding from one side are focused, and the velocity 'valleys' are adopted to determine the occurrence of vortices.

4.2 Flow Fields behind Plain Cylinders

Instantaneous velocity fields

Figure 4.3(a) and figure 4.3(b) illustrate two instantaneous streamwise velocity contours ($t^* = t \times U_0/D = $ *793.6, 1065.6*) at Plane Y = -0.6*D* behind a plain cylinder under two Reynolds numbers (1.6e+4, 3.3e+4). The black block shown in figure stands for the rear part of plain cylinder. The horizontal axis represents nondimensional horizontal distance away from the cylinder and the vertical axis represents nondimensional spanwise location along the cylinder. The colourmap stands for the ratio of streamwise velocity component to incident velocity (u/U_0). High speed flow (bright colour) is observed to depart from the rear of cylinder, whilst most part of the two figures is occupied by low speed region (deep colour). One notable discrepancy between figure 4.3(a) and figure 4.3(b) is that velocity contour in the wake under a higher Reynolds number (3.3e+4) features more distinctive turbulence, thereby displaying more chaos.

(a): *Re* = 1.6e+4   (b): *Re* = 3.3e+4
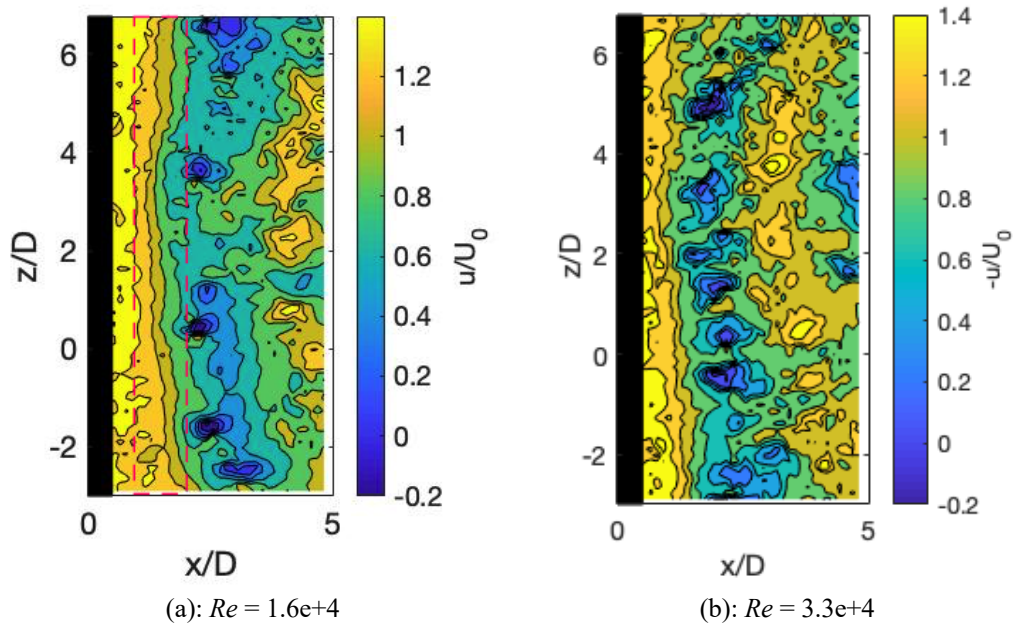
Figure 4.3 Instantaneous streamwise velocity contour along Plane Y = -0.6*D*.
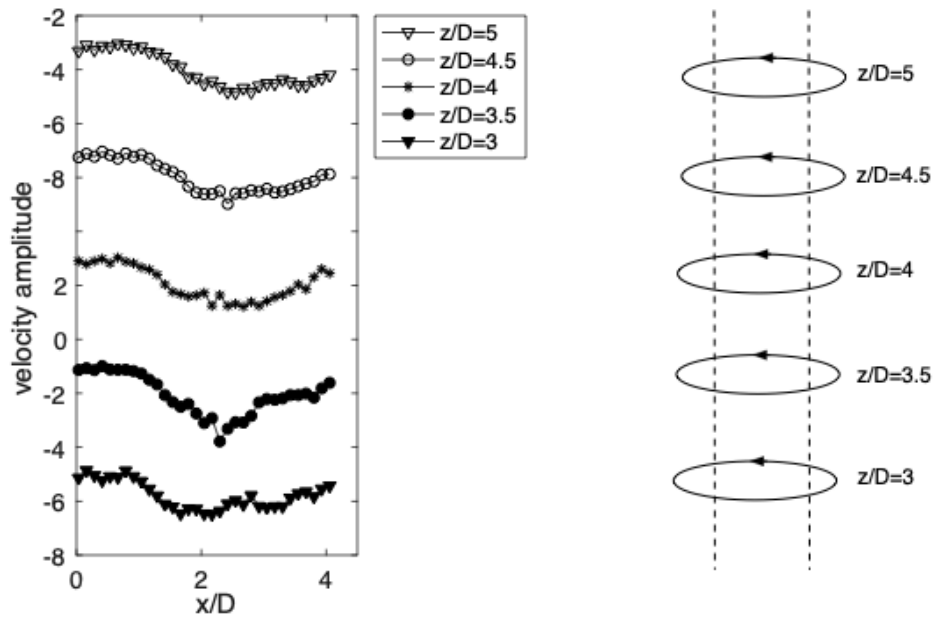
(a): Velocity trends at different cross-sections   (b): Vortex tube concept

Figure 4.4 Illustration about vortex tube in the wake zone (Re = 1.6e+4).

Following the aforementioned vortex identification principle, the streamwise velocity variation in downstream at different cross-sections (z/D = 5, 4.5, 4, 3.5 and 3) in figure 4.3(a) are picked out and shown in figure 4.4(a). The vertical axis stands for normalized relative velocity amplitude. In order to make a separate exhibition, normalized velocities of 'z/D = 4.5, 4, 3.5, 3' are reduced by 2, 4, 6, 8. Obviously, the 'valley' shown in each cross-section represents the occurrence of vortex. Considering the fact that all the 'valleys' take place with a similar phase, it can be deduced that vortex shedding at neighbouring cross-sections is united, resulting in a complete vortex tube parallel to the cylinder axis (see figure 4.4(b)). If we consider the three-dimensionality of vortex shedding, the contour enclosed in red dash frame in figure 4.3(a) varies at high decrease rate in downstream direction, suggesting the occurrence of strong roll-up flow at the transverse.

Figure 4.3 and figure 4.4 provide us with a brief view about instantaneous vortex shedding behind the plain cylinder, by recognising the vortex tube out of multiple aligned velocity 'valleys'. The forthcoming sequence of velocity contours could describe the general movement of vortex tubes, that is, detaching from the rear part of cylinder and moving downwards. Equivalently, vortex shedding phenomenon in the wake of step cylinders can also be evaluated by spotting different types of 'velocity valley' in terms of amplitudes and phases, all of which will be narrated in detail in Chapter 5.

Time-averaged velocity fields

In order to statistically evaluate velocity information in the wake, successive velocity contours along planes (Y = 0D, -0.6D) are averaged in time domain, the number of which is 2000 snapshots for the central plane (Y = 0D), 3000 snapshots for 0.6D offset plane (Y = -0.6D). It should be borne in mind that one 'snapshot' denotes the processed instantaneous velocity field within field of view (FOV) at an instant of time. The time interval between neighbouring snapshots is 1/1000s for Re = 1.6e+4 and 1/1500s for Re = 3.3e+4. As a result, mean value and fluctuating value in terms of streamwise velocity component at different planes (Y = 0D, -0.6D) and different Reynolds numbers (1.6e+4, 3.3e+4) are summarized and presented in figure 4.6(a) -(d) and figure 4.7(a) -(d).
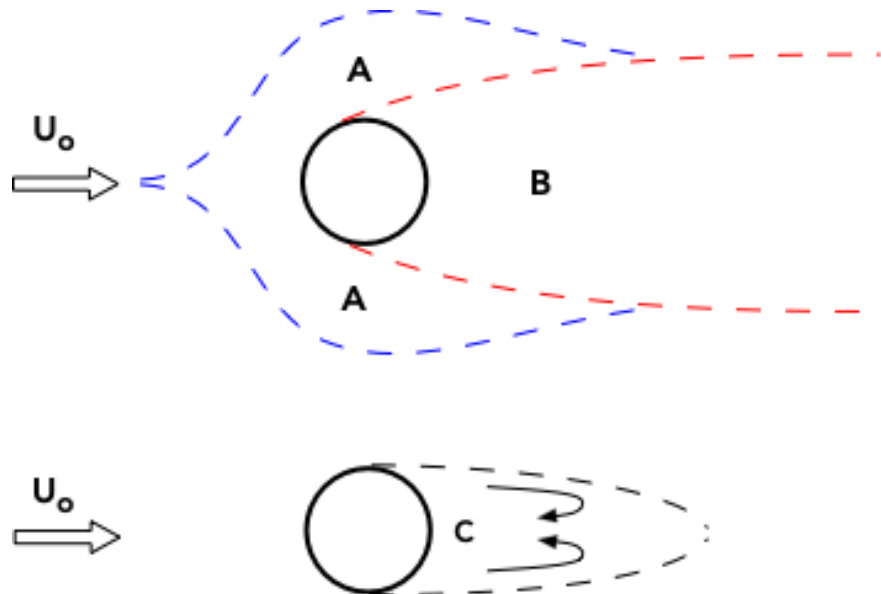
Figure 4.5 Steady velocity at different regions around the circular cylinder.

Note: A: region of displaced flow ($U > U_0$); B: wake region ($U < U_0$) (Zdravkovich, 1997); C: recirculation region ($U < 0$) (Williamson, 1996).

With respect to the two-dimensional steady state of flow around circular cylinder, several flow regions are announced as shown in figure 4.5, i.e., flow region A, flow region B (Zdravkovich, 1997) and flow region C (Williamson, 1996). The incident flow (U_0) approaches the front side of circular cylinder, subsequently moving along the surface towards both sides, eventually resulting in the occurrence of displaced flow region (enveloped by blue dash line), i.e., flow region A, where the absolute velocity (U) surpasses the original U_0. At most area behind the circular cylinder (flow region B, bordered with red dash lines), the absolute velocity is significantly reduced owning to the blockage of circular cylinder. Two shear layers induced by flow separation on boundary layers are located in flow region B, meeting with each other at the location downstream, furthermore, forming the near wake region (flow region C, surrounded by black dash

lines). The reserve flow (displayed as black solid lines with arrows) causes negative velocity in near wake region, suggesting two stationary vortices permanently stay symmetrically along the central line. As a result, it can be obviously found that the steady fluid property in the near wake is remarkably affected with the existence of circular cylinder, and the velocity variation downstream right after the cylinder differs from that near one side of the cylinder.

(a)   (b)

(c)   (d)
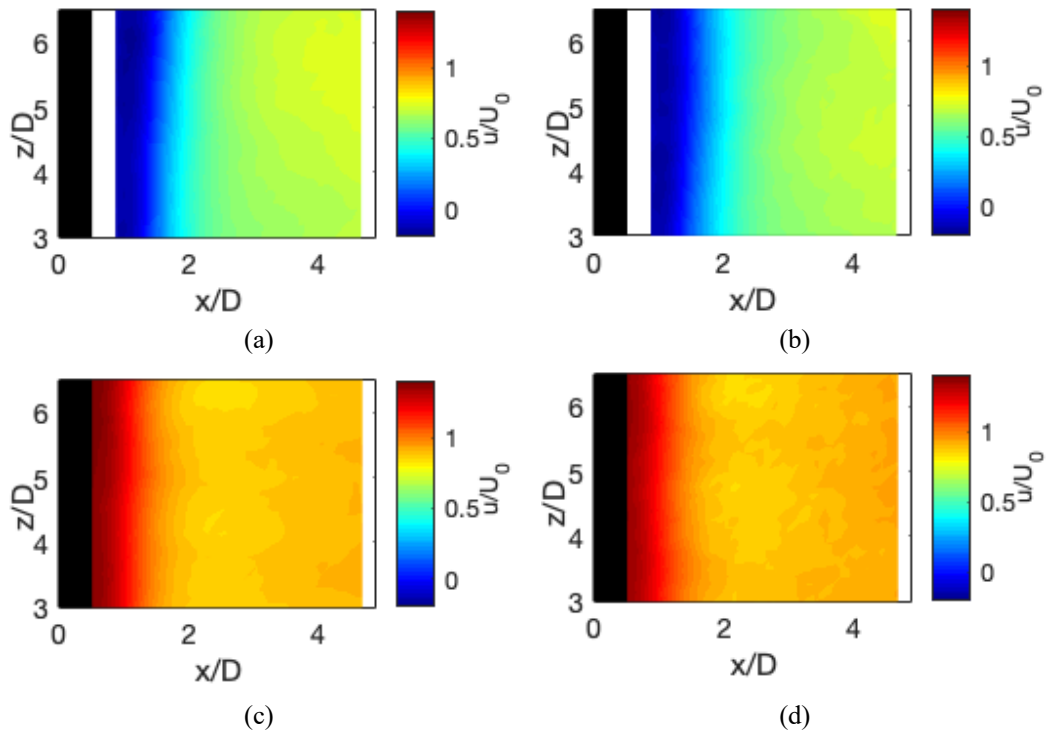
Figure 4.6 Mean planar streamwise velocity fields varying the plane and *Re*.

Note: (a): Plane Y = 0*D*, *Re* = 1.6e+4; (b): Plane Y = 0*D*, *Re* = 3.3e+4;
      (c): Plane Y = -0.6*D*, *Re* = 1.6e+4; (d): Plane Y = -0.6*D*, *Re* = 3.3e+4.

As for the plain cylinder, figure 4.6(a) -(d) exhibits mean streamwise velocity fields behind a portion of span at planes (Y = 0*D*, -0.6*D*) under the Reynolds number of 1.6e+4, 3.3e+4. The horizontal axis and vertical axis denote normalized horizontal distance behind the circular cylinder and normalized distance along the span respectively. The colormap denotes ratio of mean streamwise velocity ($\overline{u}$) to free stream velocity (U_0), and the black rectangle block indicates rear part of circular cylinder. For each velocity contour in figure 4.6, one can easily perceive the significant discrepancy between the near wake region (approximately $0.5 < x/D < 2$) and the outside. For the identical Reynolds number, this discrepancy varies at different planes (Y = 0*D*, -0.6*D*). Specifically, the streamwise velocity becomes negative within the entire near wake region along Plane Y = 0*D*, and it displays a trend to recover and approach but not reach the free stream velocity with the flow moving downwards. However, extremely strong current excessing U_0 is observed at

near wake region along Plane Y = -0.6*D*. The current gradually decreases towards U_0 in downstream. With the assistance of figure 4.5, different velocity contours along Plane Y = 0*D* and -0.6*D* can be explained as follows. The near wake region of Plane Y = 0*D* is fully immersed in flow region C, where the streamwise velocity is reverse, whilst half of the near wake region of Plane Y = -0.6*D* is located in flow region A and the other half is in flow region B, velocity within the former of which is higher than the incident velocity (U_0).

(a)   (b)

(c)   (d)
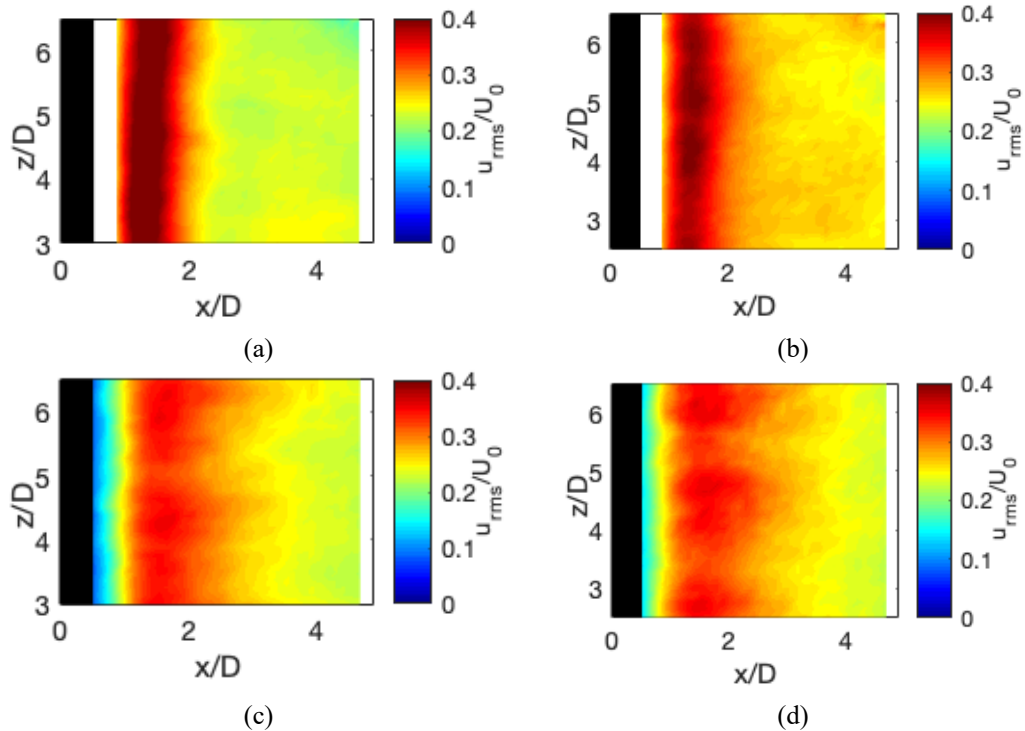
Figure 4.7 Root-mean-square (rms) planar streamwise velocity fields varying the plane and *Re*.

Note: (a): Plane Y = 0*D*, *Re* = 1.6e+4; (b): Plane Y = 0*D*, *Re* = 3.3e+4;
    (c): Plane Y = -0.6*D*, *Re* = 1.6e+4; (d): Plane Y = -0.6*D*, *Re* = 3.3e+4.

Similarly, figure 4.7(a) -(d) interpret the root-mean-square (rms) streamwise velocity fields, suggesting the trend that a notable area with high rms value emerges in the near wake zone followed by the rms value gradually decaying downstream. The comparison about rms value between two planes shows a qualitative evaluation that high rms value region at Plane Y = -0.6*D* is wider than that at Plane Y = 0*D*, meanwhile the former decrease rate is much lower, which can be quantitatively studied via the variation of averaged mean value / rms value against the normalized horizontal distance in figure 4.8 and figure 4.9.
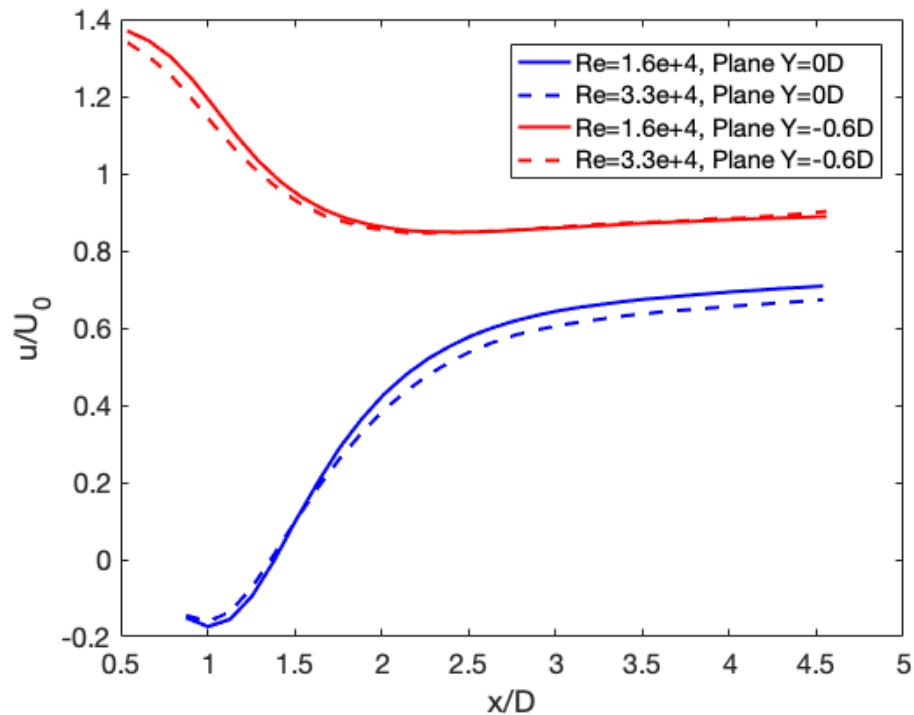
Figure 4.8 Mean streamwise velocity variation against downstream distance.
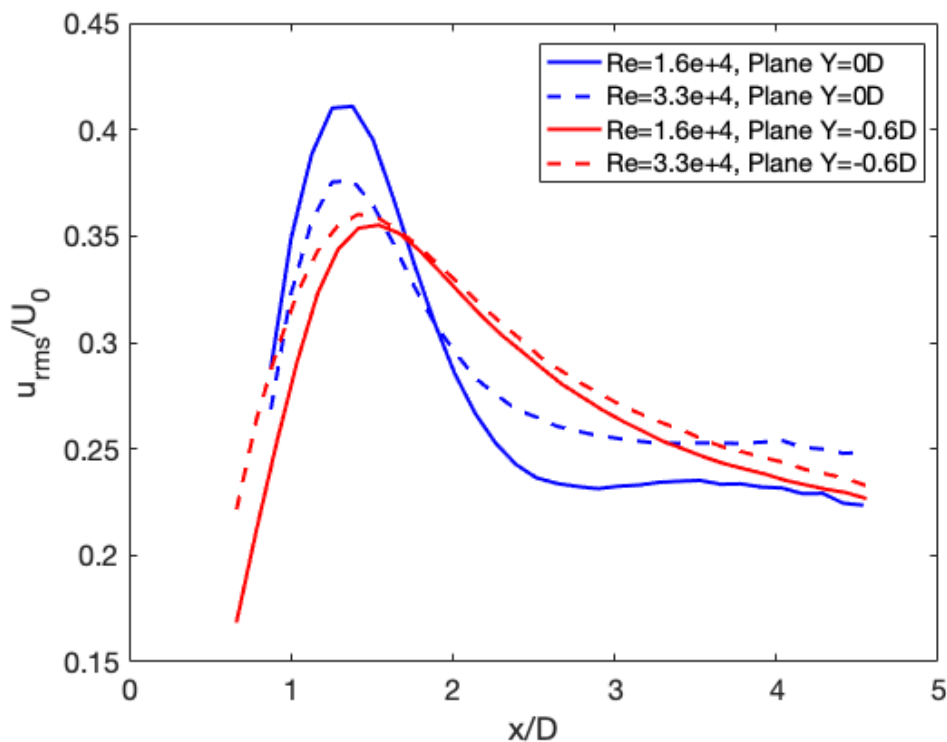
Figure 4.9 Root-mean-square (rms) streamwise velocity variation against downstream distance.

Figure 4.8 and figure 4.9 quantify time-averaged streamwise velocity variation (mean / rms) against the downstream distance at two planes (Y = 0D, -0.6D) at the Reynolds number of 1.6e+4 and 3.3e+4. The corresponding averaged curves are obtained by averaging results in relation to figure 4.6 & 4.7 along the entire span. In figure 4.8, one can observe similar trend from different Reynolds numbers (comparing the dash line to

the solid line with identical colour). Aside from that, negative velocity and extremely high velocity at near wake region are outstanding at Plane Y = 0D and -0.6D respectively, revealing the fact that different flow region near the circular cylinder have different flow properties as shows in figure 4.5 (Zdravkovich,1997; Williamson,1996). As for the value at the steady stage (x/D > 4), the velocity at Plane Y = -0.6D is higher than that at Plane Y = -0.6D, indicating a larger velocity deficit at the central plane (Y = 0D). In figure 4.9, the above mentioned high rms value area can be decerned in the near wake for all involved cases. The decrease rate behind the maximum rms value at Plane Y = 0D is larger than that at Plane Y = -0.6D.

4.3 POD-based and Spectral Analysis

POD (proper orthogonal decomposition) being a useful signal processing tool shares the similar concept with PCA (principal component analysis), that is, to describe dataset with the assistance of a group of linearly uncorrelated principal components. As for fluid dynamics, the turbulent flow can also be equivalent to the union of many 'principal components', for instance, eddies or coherent structures with a wide range of scales. It should be noted that the term of 'coherent structures' being another description about the 'interior ingredients' of turbulent flow is defined as a part of flow mass with phase-correlated (Hussain, 1986). Consequently, POD-based processing is employed to identify coherent structures in turbulent flow in the present study.

As POD theoretical introduction has already been discussed in section 3.2, the following part exhibits corresponding operation procedures in detail, accompanied with an assistant flow chart (see figure 4.10). Considering the two-dimensional flow, fluctuating velocity components $[U'(x, y, t)]$ are extracted from the original velocity dataset $[U(x, y, t)]$ using Reynolds decomposition, followed by the establishment of autocovariance matrix $[C(t)]$. Applying 'Eigen decomposition' to the autocovariance matrix, we can get the corresponding Eigenvectors $[\vec{\theta}_m(x, y)]$, as well as Eigenvalues $[e_m]$. In fluid dynamics, the obtained eigenvectors being ordered based on eigenvalues can be equivalent to a group of normalized POD mode $[\vec{\theta}_m(x, y)]$, that is, the 'coherent structures' in turbulent flow. Subsequently, we can project the fluctuating velocity components to each normalized POD mode and get the corresponding mode coefficients $[a_m(t)]$. For a specific mode coefficient, its physical meaning is to reveal the instantaneous weight of its corresponding normalized POD mode, suggesting that the variation of mode coefficient over time directly reflects the 'strength' variation of the corresponding normalized POD mode. Furthermore, the spectral analysis on mode coefficients can be used to characterise normalized POD modes. In addition, the variance $[\lambda_m]$ of mode coefficients $[a_m(t)]$ for a certain normalized POD mode $[\vec{\theta}_m(x, y)]$ denotes the mode weight, indicating 'energy percentage' within the entire time.
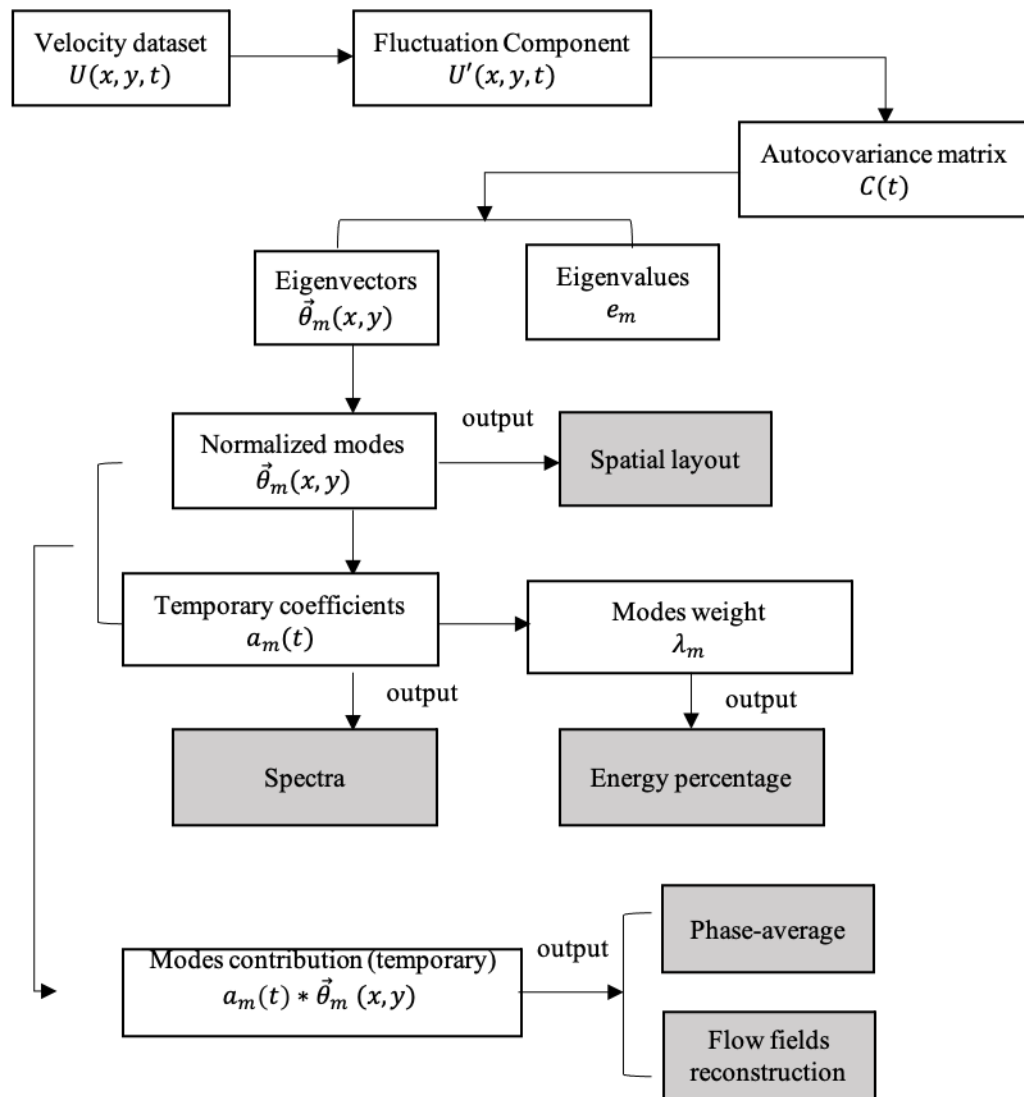
Figure 4.10 Flow chart of POD-based processing.

Followed by the above-mentioned operation guidance, this subsection exhibits analysis about velocity fields behind the plain cylinder along the measuring plane ($Y = -0.6D$) at the Reynolds number of 1.6e+4, 3.3e+4 using POD. In order to ensure that the involved data is enough for a reliable result, figure 4.11 shows the convergence test outcome by varying the sample capacity from $N = 600$ successive snapshots to $N = 3000$ successive snapshots. It should be noted that one 'snapshot' refers to the velocity data in the 'view of field' at an instant of time. The horizontal axis is the order of POD mode, starting with the dominant modes with higher mode weight (energy, contribution or proportion); meanwhile the vertical axis stands for the energy percentage, indicating the proportion of each mode in the entire flow field. The energy variation against the POD mode at different sample capacity shares the same trend that dominant modes have high energy percentage, whilst displays a clear scatter between small sample capacities. With the increase of sample capacity, the discrepancy between neighbouring curves gradually become acceptable, for instance, within 5% between $N = 3000$ and 2800.
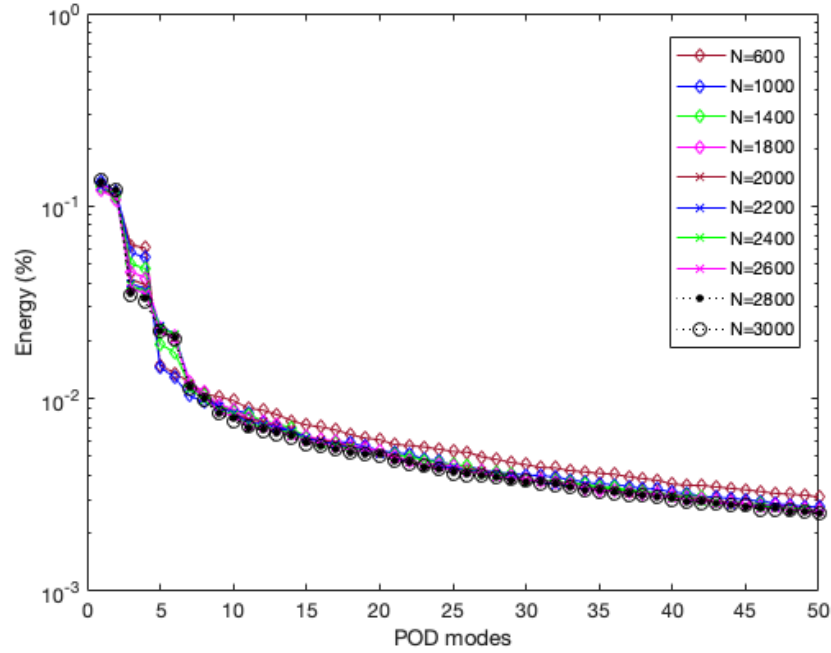
Figure 4.11 Convergence tests of dataset capacity (*N*).

As '*N* = 3000' is proved to be enough to provide us with reliable POD analysis, the corresponding comparison of energy percentage of first ten POD modes between the Reynolds number of 1.6e+4 and 3.3e+4 is presented in figure 4.12(a). It could be found in figure 4.12(a), that the energy percentage variation against the mode order between two Reynolds numbers show great consistency with each other beyond 5th mode. As for the first four modes, a significant energy reduction takes place between 2nd mode and 3rd mode at *Re* = 1.6e+4, whilst the decrease becomes smooth for *Re* = 3.3e+4. It is obvious that the first pair of mode namely 1st mode and 2nd mode are dominant in the original flow, which displays higher and more concentrative energy under Reynolds number of 1.6e+4. For higher Reynolds number (3.3e+4), it could be inferred that more energy of first pair of mode is transferred to the flow, thus exhibits smooth transition to the successive higher order modes. The related cumulative energy variation versus the order of POD mode is presented in figure 4.12(b), where each scattered data represents the sum of energy percentage from first mode to the target mode. More specifically, the cumulative energy percentage at 10th mode is 40.4% under the Reynolds number of 1.6e+4, followed by the continuous growth enabling the percentage reach 46.3% at 20th mode. In other words, the sum energy from 1st mode to 10th mode is 40.4%, and the sum energy from 11th to 20th is 5.9%.

63
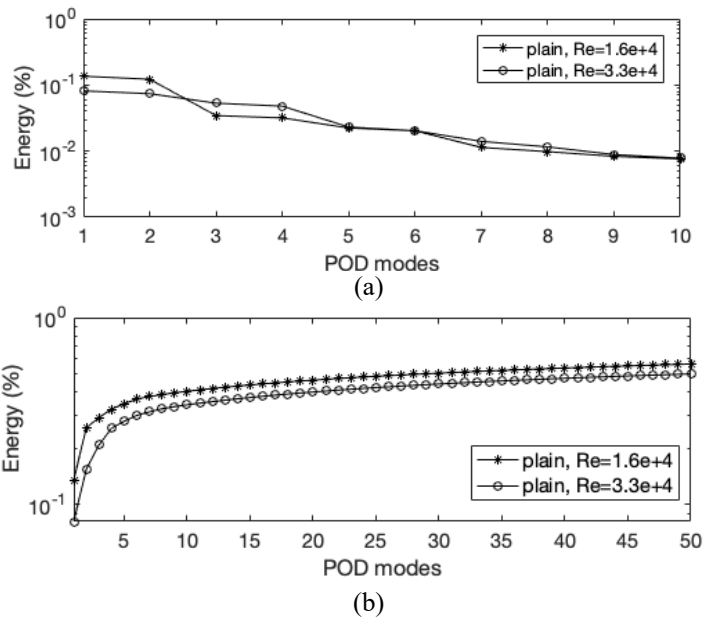
Figure 4.12 Variation of single(a) / cumulative(b) energy against POD modes.

Table 4.1 Summary of energy and spectral analysis (plain cylinder).

		1st mode	2nd mode	3rd mode	4th mode	5th mode	6th mode
Re=1.6e+4	Energy	13.6%	12.2%	3.4%	3.2%	2.2%	2.0%
	fD/U_0	0.1975	0.1975	0.195	0.195	0.2	0.2
Re=3.3e+4	Energy	8.1%	7.4%	5.3%	4.8%	2.3%	2.0%
	fD/U_0	0.1913	0.19	0.1913	0.1913	0.1925	0.1925

Energy percentage together with the frequency of each POD mode fluctuating over time, are summarized in table 4.1. For the Reynolds number of 1.6e+4, the above-mentioned significant energy percentage difference between 2nd mode and 3rd mode is 8.8%. Meanwhile, energy percentage is gently changing against the order of mode under higher Reynolds number (3.3e+4), with that of the first four modes being 8.1%, 7.4%, 5.3% and 4.8% respectively. As for the spectral analysis, it seems that all the modes have the comparable frequency, suggesting that coherent structures with small scales detaching from the cylinder share the same frequency with the primary vortex shedding, i.e., the Karman vortex shedding. It should be noted that the energy percentage of the first pair of POD mode is 25% and 15%, corresponding to Re = 1.6e+4 and 3.3e+4. However, previous achievements (Van Oudheusden, et al., 2005) concluded that of the first pair should be approximate 60% to 70%. The discrepancy might be due to turbulence, especially along the spanwise direction. Conventional relevant POD-based studies in terms of plain cylinders mainly focus on results at cross-sections, where significant and outstanding Karman vortex shedding takes place. As the present study implements POD processing towards velocity fields along the planes parallel to cylinder axis, the addition of flow information along the span gives rise to the occurrence that the first pair of POD mode seems to be weaker than that in the literature.

(a): 1st mode

(b): 2nd mode
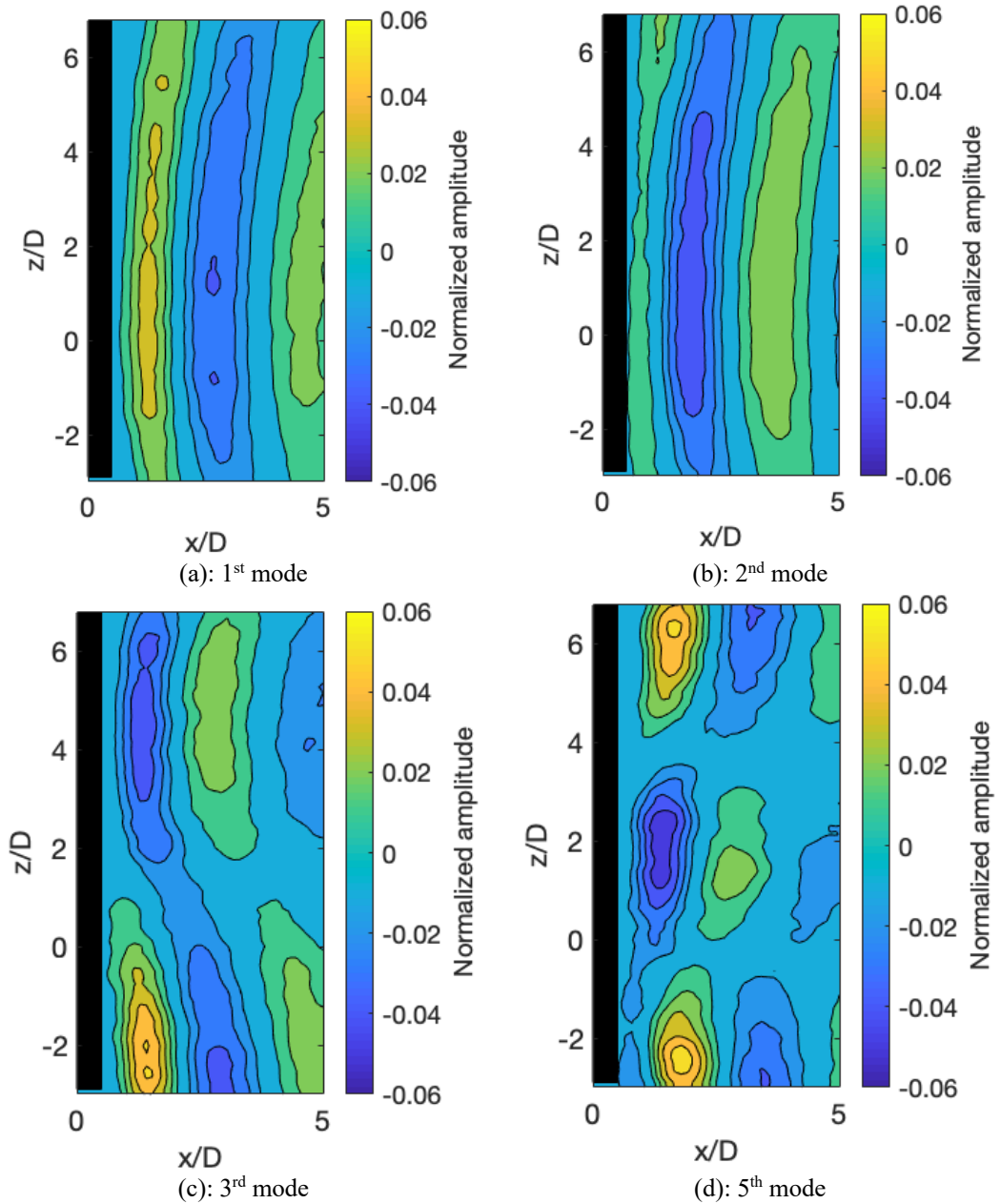
(c): 3rd mode

(d): 5th mode

Figure 4.13 POD mode contours (based on streamwise velocity component) at Re = 1.6e+4.

The normalized POD modes, i.e., 1st mode, 2nd mode, 3rd mode and 5th mode, are presented in figure 4.13(a) -(d). Compared to the original instantaneous velocity field (see figure 4.3(a)), it could be inferred that the first pair of POD mode (1st mode and 2nd mode) in figure 4.3(a), (b) represent the dominant vortex shedding, which exhibits large-scale coherent structure parallel to the cylinder axis. In addition, the first pair (1st mode and 2nd mode) are orthogonal with other, displaying similar content, and so on for the pair of 3rd, 4th mode, and 5th, 6th mode. The subsequent POD modes namely 3rd mode, 4th mode, 5th mode, etc., characterise coherent structures with smaller scales, the 3rd and the 5th of which are shown in figure 4.13(c), (d). Comparing figure 4.13(a) with figure 4.13(c), (d), it could be found that the coherent structure gradually reduces its scale towards higher order.

Phase averaging

As it is mentioned above, the first pair of normalized POD mode (1st mode, 2nd mode) resemble the original flow field (see figure 4.3(a)), suggesting that the evaluation on the primary vortex shedding can be obtained by monitoring the combined activity of the first pair of mode. The contribution of each mode towards the original instantaneous flow field is calculated by multiplying the mode coefficient and the normalized POD mode as shown in figure 4.10. Eventually, the instantaneous reconstructed velocity field can be obtained by superposing the contribution of the first two modes on the mean flow field (more details in section 3.2). In addition, the mode coefficient of the first two modes can be used to define the vortex shedding phase.
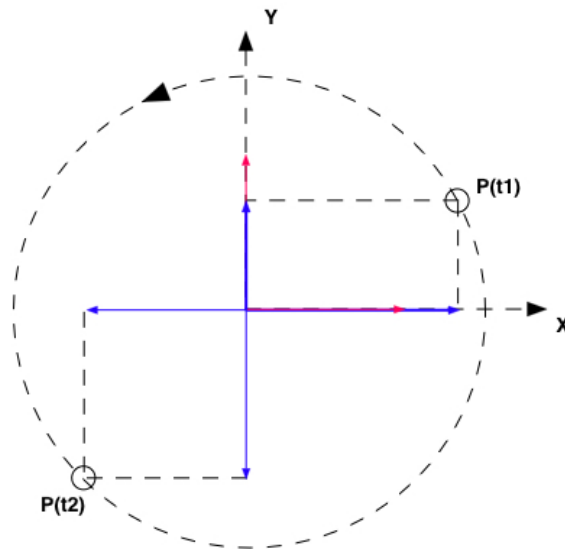
Figure 4.14 Explanation about phase identification using a periodical event.

Note: P(*t1*) and P(*t2*): periodic instantaneous behaviour at moment *t1* and *t2*, Red arrows: normalized orthogonal bases, $\vec{\theta}_1(x,y)$ and $\vec{\theta}_2(x,y)$, Blue arrows: P(*t1*) $[a_1(t1) * \vec{\theta}_1(x,y) + a_2(t1) * \vec{\theta}_2(x,y)]$, P(*t2*) $[a_1(t2) * \vec{\theta}_1(x,y) + a_2(t2) * \vec{\theta}_2(x,y)]$.

The corresponding phase identification can be proved via figure 4.14. Consider a two-dimensional periodical activity, for instance, a movement along the dash circle. P(*t1*) and P(*t2*) represent the periodic instantaneous behaviour at moment *t1* and *t2*. The red arrows stand for a pair of normalized orthogonal base which can be equivalent to normalized POD modes for the current study, and the blue arrows represent the projection of P(*t1*) and P(*t2*) on these two bases. Consequently, the pair of mode coefficients, i.e., $(a_1(t1), a_2(t1))$ and $(a_1(t2), a_2(t2))$ can help determine the accurate activity at each instant of time, including the corresponding phase. Furthermore, this periodical activity can be averaged according to phase properties.
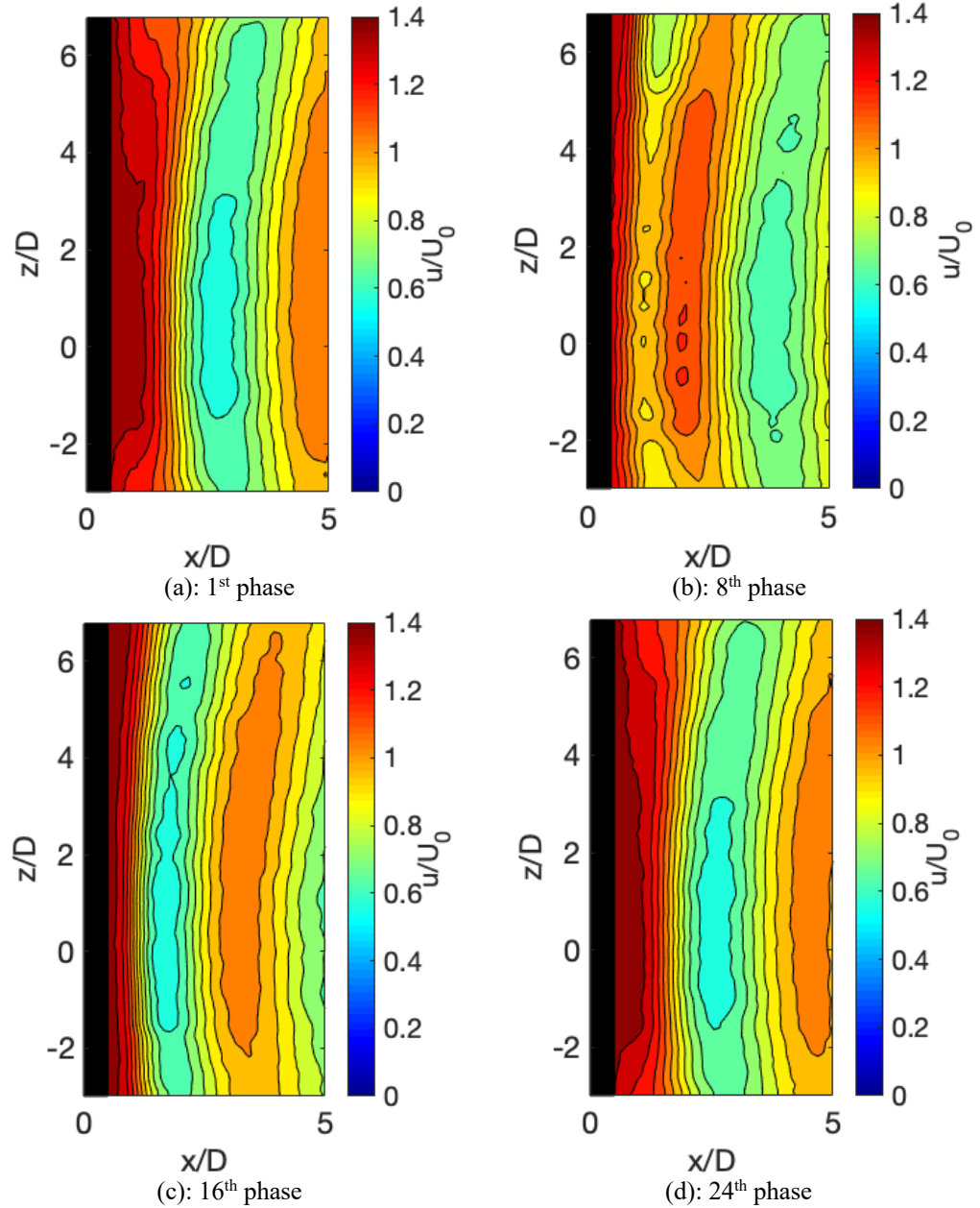
Figure 4.15 Phase-averaged streamwise velocity fields (Plane Y = -0.6D, Re = 1.6e+4).

Similarly, the vortex shedding phase for each instant of time can be obtained from the related mode coefficients. Divide the phase ensemble, i.e., $[0, 2\pi]$ into to 24 portions with equal width. Meanwhile, the reconstructed velocity field ensemble can be split into 24 portions based on their phases. Eventually, a total of 24 phase-averaged reconstructed velocity fields can be achieved by averaging the velocity fields within each portion. Figure 4.15(a) -(d) exhibits four typical phase-averaged reconstructed velocity contours (1st, 8th, 16th and 24th phase) behind the plain cylinder for the Reynolds number of 1.6e+4. Clear velocity 'valleys' in the wake region could be observed from figure 4.15, as well as, the development of these velocity 'valleys' in downstream.

Ratio of propagation to phase (PPR)

Considering the downstream propagation in terms of the specific velocity 'valley' in a sequence of velocity contours in figure 4.15, this subsection attempts to quantify this visible propagation via 'spatial correlation (equation 4.1)' inspired by PIV methodology. Besides, a new term namely, ratio of propagation to phase (short for 'PPR'), is put forward to describe this propagation. And more specifically, the 'PPR' can be defined as the distance of the vortex propagating downwards between neighbouring shedding phases. The key concept of the proposed method is to capture two parts with high similarity in the neighbouring phase-averaged velocity contours, indicating the identical content moving from one location to another location in between, which can be illustrated by comparing corresponding results regarding the 10th phase and 14th phase (see figure 4.16(a), (b)). It might need more explanation about how to obtain figure 4.16(a), (b). A sequence of phase-averaged streamwise velocity contours from 1st phase to 24th phase have been created, four of which are plotted in figure 4.15. Consider another two phases namely 10th phase, 14th phase, and convert corresponding velocity contours into three-dimensional iso-surfaces, and eventually one could observe the clear velocity 'valley' from side view as shown in figure 4.16. The horizontal axis represents normalized streamwise distance, and the vertical axis stands for normalized streamwise velocity. The specified part of the velocity iso-surface is enveloped within the grey box where one could observe high similarity between that of 10th and 14th phase, as well as a significant shift from x/D = 2 to 2.5. Consequently, the movement of the grey box can be used to evaluate the vortex propagation.

(a): 10th phase   (b): 14th phase
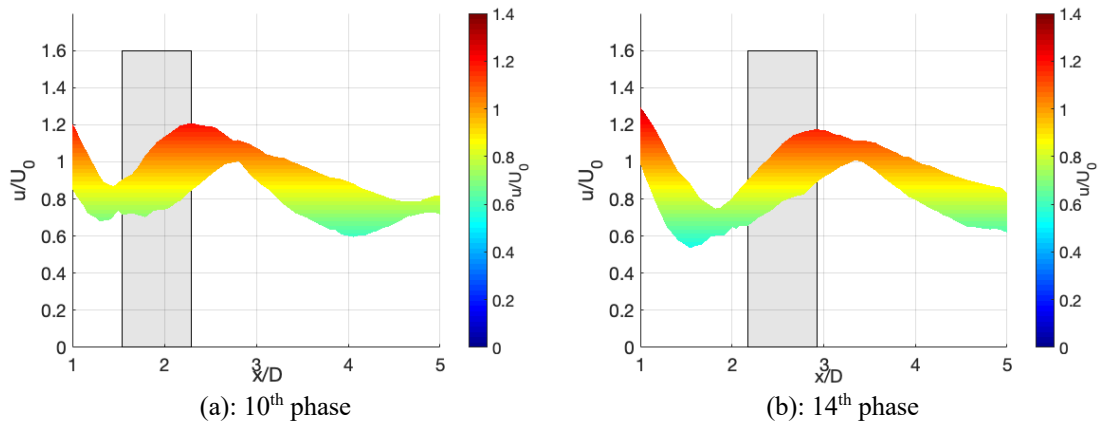
Figure 4.16 Similarity between two phase-averaged flow fields (Plane Y = -0.6D, Re = 1.6e+4).

$$r_{xy} = \frac{\sum_{m=1}^{c}, \sum_{n=1}^{d} \left(U_{mn}^{a} - \overline{U^{a}}\right)\left(U_{mn}^{b} - \overline{U^{b}}\right)}{\sqrt{\sum_{m=1}^{c}, \sum_{n=1}^{d} \left(U_{mn}^{a} - \overline{U^{a}}\right)^{2}} \sqrt{\sum_{m=1}^{c}, \sum_{n=1}^{d} \left(U_{mn}^{b} - \overline{U^{b}}\right)^{2}}} \quad (4.1)$$

Systematic description in terms of quantifying the aforementioned propagation is given as follows, accompanied by the schematic sketch in figure 4.17. The entire process can be divided into two parts namely, to figure out the grey box moving between two phases and to apply the 'two-phase' theory to the 'multi-phase' situation. It should be noted that the grey box could be two-dimensional or three-dimensional, corresponding to the two-dimension velocity contour and the three-dimensional velocity iso-surface respectively. The forthcoming explanation is on the basis of two-dimensional velocity contours, thereby using the two-dimensional grey box. In figure 4.17, consider the phase-averaged streamwise velocity contour at a certain phase (viz. the reference phase), e.g., phase 'a' (P(a)), then fix the grey box, enveloping part of the velocity contour (marked as a 'star' in figure 4.17) and marking the initial location of the grey box, i.e., L(a). Subsequently, pay attention to another consequent phase (P(b)) where one can figure out the new position of the 'star' identified by the new grey box position, i.e., L(b)$_a$. The subscript 'a' stands for its reference phase. Analysis about 'spatial correlation' is utilized to figure out the identical part of velocity contour enveloped in the grey box (i.e., the 'star') between two phases and to determine L(b)$_a$, with its two-dimensional equation being given in equation 4.1. Consequently, the movement in terms of grey box between P(a) and P(b) can be obtained, as L(b)$_a$ – L(a).

Option A : L(t0), L(t1)$_{t0}$, L(t2)$_{t0}$, L(t3)$_{t0}$, L(t4)$_{t0}$, ...
Option B : L(t0), L(t1)$_{t0}$, L(t2)$_{t1}$, L(t3)$_{t2}$, L(t4)$_{t3}$, ...
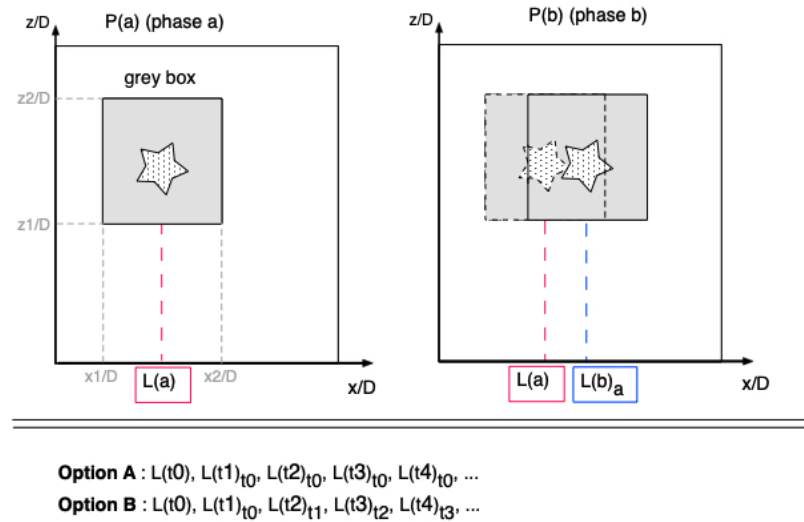
Figure 4.17 Schematic sketch of identifying 'grey box' movement.

As for the 'multi-phase' situation, two strategies are put forward, namely Option A and Option B as shown in figure 4.17, to figure out all the positions of the identical 'star' in all phases. The corresponding discrepancy in between is how to determine the reference phase. First of all, Option A and Option B share the identical initial reference phase, i.e., phase '$t0$' (P($t0$)). For Option A, the successive phases, i.e., $t1$, $t2$, $t3$, $t4$, …, have the same reference phase, i.e., P($t0$). Nevertheless, the successive phases for Option B chose

their neighbouring phases as reference phases. More precisely, the reference phase of *t1*, *t2*, *t3*, *t4* are *t0*, *t1*, *t2*, *t3* respectively. Option A seems to be quite stable due to the fixed reference phase, while Option B seems to be more accurate due to a stronger correlation between neighbouring phases, which needs further investigation. Besides, the grey box size, as well as the initial reference phase (P(*t0*)) might also affect the eventual result. As a result, the following part will do relevant tests to check the impact of the grey box and to compare these two strategies.

Table 4.2 Summary of configurations regarding all testing cases.

Re = 1.6e+4					
	Option A			Option B	
	P(*t0*)	Grey box position in P(*t0*) [x1/*D*, x2/*D*] [z1/*D*, z2/*D*]		P(*t0*)	Grey box position in P(*t0*) [x1/*D*, x2/*D*] [z1/*D*, z2/*D*]
Case1	10th	[1.54, 1.92] [1.88, 4.39]	Case2	10th	[1.54, 1.92] [1.88, 4.39]
Case3	10th	[1.54, 2.17] [1.88, 4.39]	Case4	10th	[1.54, 2.17] [1.88, 4.39]
Case5	10th	[1.54, 1.92] [-0.63, 4.39]	Case6	10th	[1.54, 1.92] [-0.63, 4.39]
Case7	13th	[1.79, 2.17] [1.88, 4.39]	Case8	13th	[1.79, 2.17] [1.88, 4.39]
Case9	15th	[1.92, 2.30] [1.88, 4.39]	Case10	15th	[1.92, 2.30] [1.88, 4.39]
Note:	Case1&3, Case2&4: variation on box size (X direction); Case1&5, Case2&6: variation on box size (Z direction); Case1, 7&9, Case2, 8&10: variation on the initial reference phase (10th, 15th, 17th)				

Table 4.2 makes a short summary about a total of ten testing cases focusing on the impact of box size (Case1&3; Case2&4; Case1&5; Case2&6), the initial reference phase (Case1, 7&9; Case2, 8&10) and the comparison between Option A and Option B. The grey box is designed to cover part of the back side of the velocity 'valley', the initial coordinates of which, namely [x1/*D*, x2/*D*], [z1/*D*, z2/*D*], can be explained via figure 4.17. It should be noted that the grey box in Case1, 7&9 (Case2, 8&10) keeps the same size but varies in its initial absolute position due to the fact that the velocity 'valley' moves downstream between diverse phases. The following part of this subsection takes Case1 and Case2 as examples, focusing on result exhibition in terms of the comparison between Option A and Option B. After that, results about the other eight cases will be presented, accompanied with corresponding PPR equations.

A group of graphs in figure 4.18 exhibit related outcome in terms of Case1 and Case2, indicating the significant difference between Option A and Option B. The corresponding outcome consists of the correlation coefficient iso-surface, the linear fit of iso-surface peaks and the residual plots. The correlation coefficient iso-surface is believed to be the key outcome. According to the above-mentioned methodology, for each phase-averaged contour, allow the grey box to move along the X axis, thereby obtaining a group of contour portion. Subsequently, do 'spatial correlation' between each contour portion and the original contour portion in corresponding reference phase-averaged contour. We can get a group of correlation coefficient, the biggest of which reveals the location of 'high

similarity'. Consider the fact that each phase-averaged contour corresponds to a group of correlation coefficient and plot the iso-surface to contain all correlation coefficients in terms of all phase-averaged contours as shown in figure 4.18(a), (b). The horizontal axis stands for normalized streamwise distance away from the cylinder, and the vertical axis stands for correlation coefficient value. As for the transverse axis, it represents the phase angle (γ) defined as the middle degree of each phase; for instance, the phase angle of the 10th phase is 142.5° or 0.79π. It is obvious that each phase angle corresponds to a significant peak, for instance a black circle within the red box, which reveals the highest correlation coefficient, furthermore the position of 'high similarity'. As a result, all the black circles in each iso-surface form the trend, suggesting the movement of that 'high similarity', i.e., the vortex propagation in the present study.

(a): correlation iso-surface (Case1)   (b): correlation iso-surface (Case2)

(c): linear fit (Case1)   (d): linear fit (Case2)

(e): residual plot (Case1)   (f): residual plot (Case2)
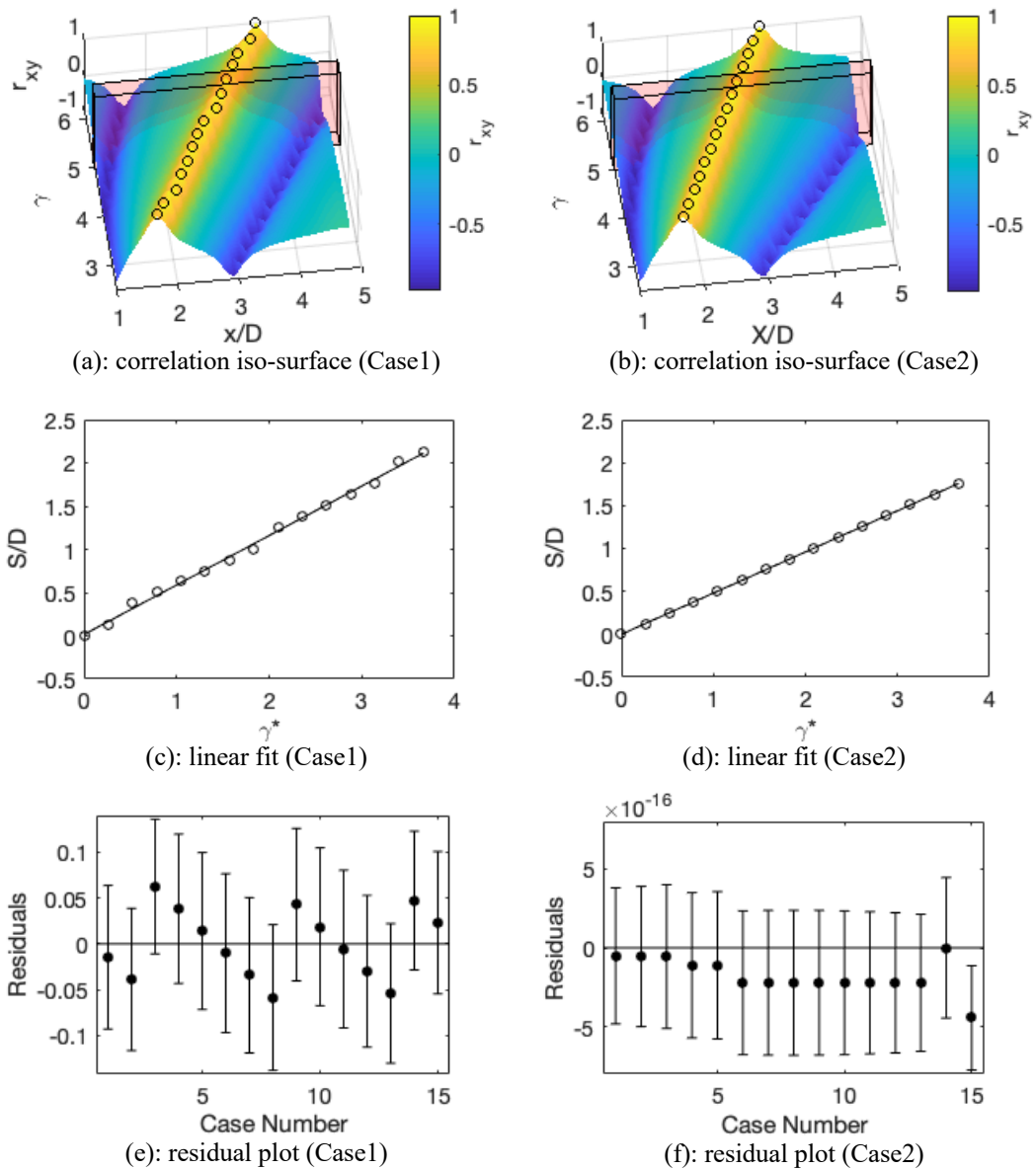
Figure 4.18 Comparison of results between Case1 and Case2.

The above-mentioned black circles can be extracted and presented in two-dimensional form as shown in figure 4.18(c), (d), accompanied with lines of linear fit. The horizontal axis is the relative phase angle (γ^*) against the initial phase angle. And the vertical axis is the normalized distance. With the comparison between figure 4.18(c) and (d), the remarkable linear trend is observed in both figures, suggesting a steady movement. However, black circles seem to be more scattered in figure 4.18(c) and to be smoothly changing in figure 4.18(d), which indicates the better performance of Option B. As for lines of linear fit, the slope of each line represents PPR (the ratio of propagation to phase), with the value of 0.4798 in Option B and 0.5724 in Option A. Figure 4.18(e), (f) display residual plots of corresponding linear fit. The residual of Option A is found to be much bigger than that of Option B.

Table 4.3 Summary of slopes and residuals of all testing cases.

Re=1.6e+4					
	Option A			Option B	
	Slope	variance of residual		Slope	variance of residual
Case1	0.5724	1.49e-03	Case2	0.4798	1.23e-32
Case3	0.5981	1.57e-03	Case4	0.4798	1.23e-32
Case5	0.5724	1.49e-03	Case6	0.4798	1.23e-32
Case7	0.5385	1.11e-03	Case8	0.4798	6.75e-33
Case9	0.4798	2.19e-33	Case10	0.4798	2.19e-33

Table 4.4 Summary of PPR equation for two Reynolds numbers.

$Re = 1.6e+4$	$\dfrac{S}{D} = 0.4798 \times \gamma^*$

Similarly, the other 8 testing cases (Case3, Case4..., Case10) can be processed in the same procedures, and all relevant obtained results are summarized in table 4.3. All testing cases in Option B have the identical slope and keep the residual at extremely low level. Meanwhile, the slope data in Option A significantly fluctuates and the corresponding residual is much bigger than that in Option B. In addition, normalized PPR equation for the Reynolds number of 1.6e+4 is presented in table 4.4. In summary, Option A can make more errors leading to the uncertainty of identifying the target motion. Option B exhibits a reliable performance, and its result is independent from the size of the grey box as well as the initial reference phase. The purpose of introducing PPR is to provide a term to uncover more details about vortex shedding; its mathematics expression might inspire other academic researches.

Spectral analysis

This subsection focuses on spectra information of vortex shedding from the plain cylinder by processing streamwise velocity time series obtained from a line parallel to the cylinder axis at 2.5D downstream and 0.6D offset of the cylinder axis. Each velocity signal has a capacity of 3000 samples; its sampling frequency is 1000Hz for Re = 1.6e+4 and 1500Hz for Re = 3.3e+4. As the related methodology has been discussed in section 3.2, this subsection will give a brief description about setting key parameters, followed by corresponding result analysis. The flexible 'Hanning window' is employed, which can move along the sequence of velocity signal with the 'overlap' being 50%. Relevant key parameters regarding two Reynolds numbers (1.6e+4, 3.3e+4) are summarised in table 4.5 and related spectra are presented in figure 4.19(a), (b) where axis in three directions is the normalized frequency (viz. the Strouhal number fD/U_0), the normalized location along the span (z/D) and the ratio of power spectral density (PSD) to the incident velocity (U_0) respectively. In figure 4.19, it is obvious that single identical peak exists at all spanwise locations, with the value of 0.1975 for Re = 1.6e+4 and 0.19 for Re = 3.3+4. The present results are comparable to reference values in the literature (Norberg, 2003), namely 0.196 for Re = 1.6e+4 and 0.190 for Re = 3.3e+4.

Table 4.5 Summary of spectral analysis parameters.

Reynolds number	Samples	Sampling frequency	Hanning window width	overlap
1.6e+4	3000	1000	500	50%
3.3e+4	3000	1500	750	50%
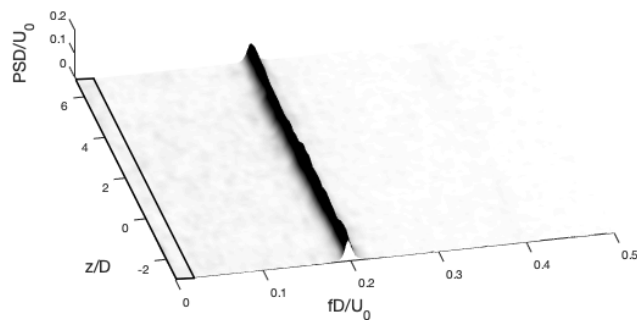
(a): Re = 1.6e+4
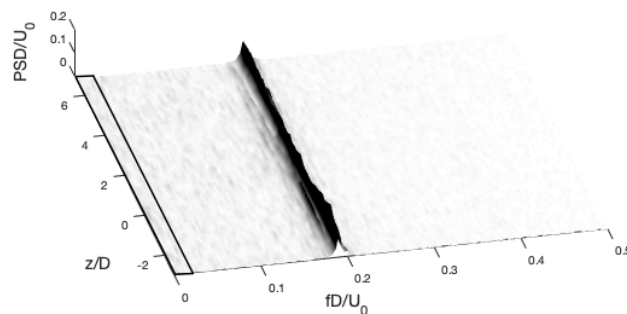
(b): Re = 3.3e+4

Figure 4.19 Velocity spectra behind plain cylinder along reference line (x/D = 2.5, y/D = -0.6).

4.4 Brief Summary for Plain Cylinders

This chapter performs a comprehensive study on flow properties in the wake of plain cylinders by processing and analysing streamwise / spanwise velocity fields along two measuring planes ($Y = 0D$, $-0.6D$) under Reynolds number of 1.6e+4 and 3.3e+4. Results cover a wide range of aspects, i.e., instantaneous / time-averaged velocity contours, vortex identification, POD-based discussion, phase-averaged velocity contours and spectral analysis. As a preliminary study, the obtained deep insight on vortex shedding behind plain cylinders could be the useful benchmark and the contrast content for step cylinders which would be exposed in the coming chapters. Apart from that, as a 'trailer', this part also exhibits applications in terms of several data processing methods, all of which shows great reliability and can be directly applied to the following step cylinders.

Chapter 5
VORTEX BEHIND STEP CYLINDERS

This chapter places the emphasis on characteristics of vortex shedding from the sharp step cylinder and the round step cylinder at the Reynolds number of 1.6e+4 and 3.3e+4. Relevant results are obtained by processing the original velocity fields along planes (Y = 0D, -0.6D) in the wake. Different types of vortex being recognised in the wake zone are proved to be more complicated than that behind plain cylinders. Spectral analysis and frequency fluctuation over time (wavelet transform) are used to quantify properties of vortices behind two types of step cylinder, some results of which are compared to that from previous publications.

A total of six experimental cases are designed and implemented, by taking the impact of shape of step junction, Reynolds number (1.6e+4, 3.3e+4), and the position of FOV (field of view) into consideration, all of which are summarised in table 5.1. Figure 5.1 provides us with a schematic sketch for illustrating the discrepancy of experimental models and exact positions of FOV. Two types of step cylinder are concerned, i.e., *S step* (sharp step cylinder) and *R step* (round step cylinder). These two types of step cylinder share the identical cylinder diameter in terms of large cylinder (*D*) and small cylinder (*d*) but differ in the shape of step junction. In figure 5.1, one could observe that step junction has the sharp edge in *S step*, whilst the round corner is in *R step*. FOV, namely the measuring plane is placed parallel to the cylinder axis, covering the region near the step junction. Its exact dimensions can be found in table 5.1. Two measuring planes are employed, namely one being directly behind the cylinder axis and the other one having a 0.6D offset from the cylinder axis.

Table 5.1 Summary of configurations regarding all experimental cases.

No.	Model*	*Re***	FOV location	Effective FOV dimension
1st case	*S step*	1.6e+4	Y = 0D	[x/D, z/D] = [(0.75, 5), (-3, 6.8)]
2nd case	*S step*	1.6e+4	Y = -0.6D	[x/D, z/D] = [(0.50, 5), (-3, 6.7)]
3rd case	*R step*	1.6e+4	Y = 0D	[x/D, z/D] = [(0.88, 5), (-3, 6.8)]
4th case	*R step*	1.6e+4	Y = -0.6D	[x/D, z/D] = [(0.50, 5), (-3, 6.7)]
5th case	*R step*	3.3e+4	Y = 0D	[x/D, z/D] = [(0.88, 5), (-3, 6.8)]
6th case	*R step*	3.3e+4	Y = -0.6D	[x/D, z/D] = [(0.50, 5), (-3, 6.7)]

Note: * : '*S step*' represents sharp step cylinder; '*R step*' represents round step cylinder.
       **: Reynolds number (*Re*) is determined by the diameter of large cylinder (*D*).
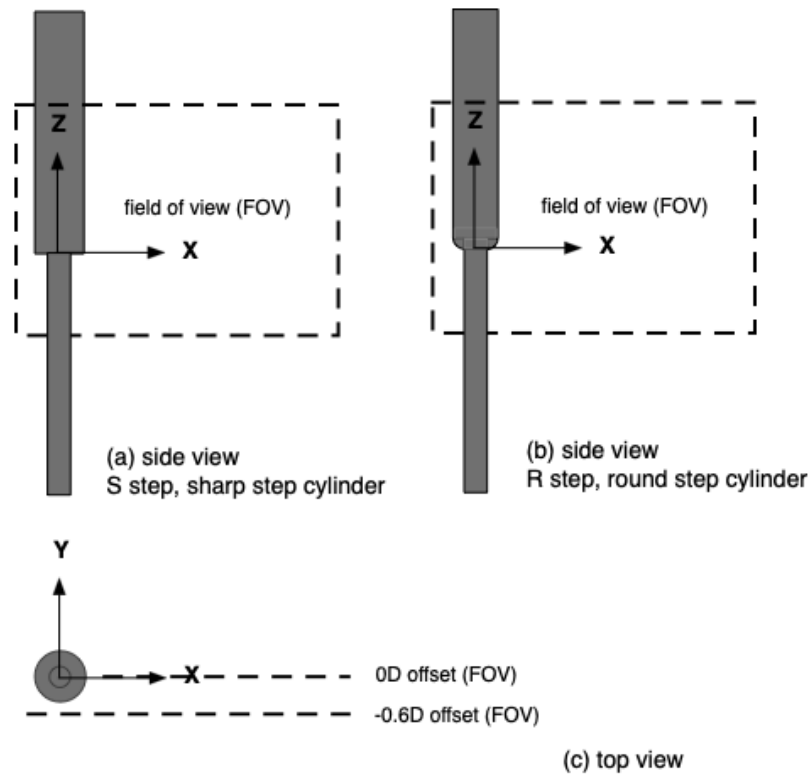
Figure 5.1 Schematic sketch of experiment models and field of view (FOV).

5.1 Vortex Identification behind Step Cylinders

As it has been introduced in section 4.1, vortices can be identified in the wake zone by recognising the 'velocity valley' in streamwise velocity contours. Besides, the introduction of 'vortex tube' in section 4.2 is to describe the ensemble of aligned 'vortex valleys' with identical phase and constant frequency, which is equivalent to the concept of 'vortex cell' when cellular vortex shedding takes place (Gaster, 1969). As for step cylinders, Dunn & Tavoularis (2006) launched experiments regarding sharp step cylinder under the Reynolds number range from 62 to 1230, and observed three different types of vortex shedding in the wake, corresponding to L-cell (detach from the large-diameter cylinder away from the step junction), S-cell (behind the small-diameter cylinder) and N-cell (behind the large-diameter cylinder near the step junction). Subsequently, three vortex cells behind sharp step cylinders were experimentally and numerically proved by Morton together with his colleagues (Morton, et al., 2009; Morton & Yarusevych, 2009; Morton & Yarusevych, 2010a; Morton & Yarusevych, 2010b; Morton & Yarusevych, 2014a). For the present study, this subsection attempts to identify vortex shedding cells by figuring out 'velocity valleys' in the wake of the sharp step cylinder, as well as the round step cylinder, at Reynolds number of 1.6e+4 and 3.3e+4.
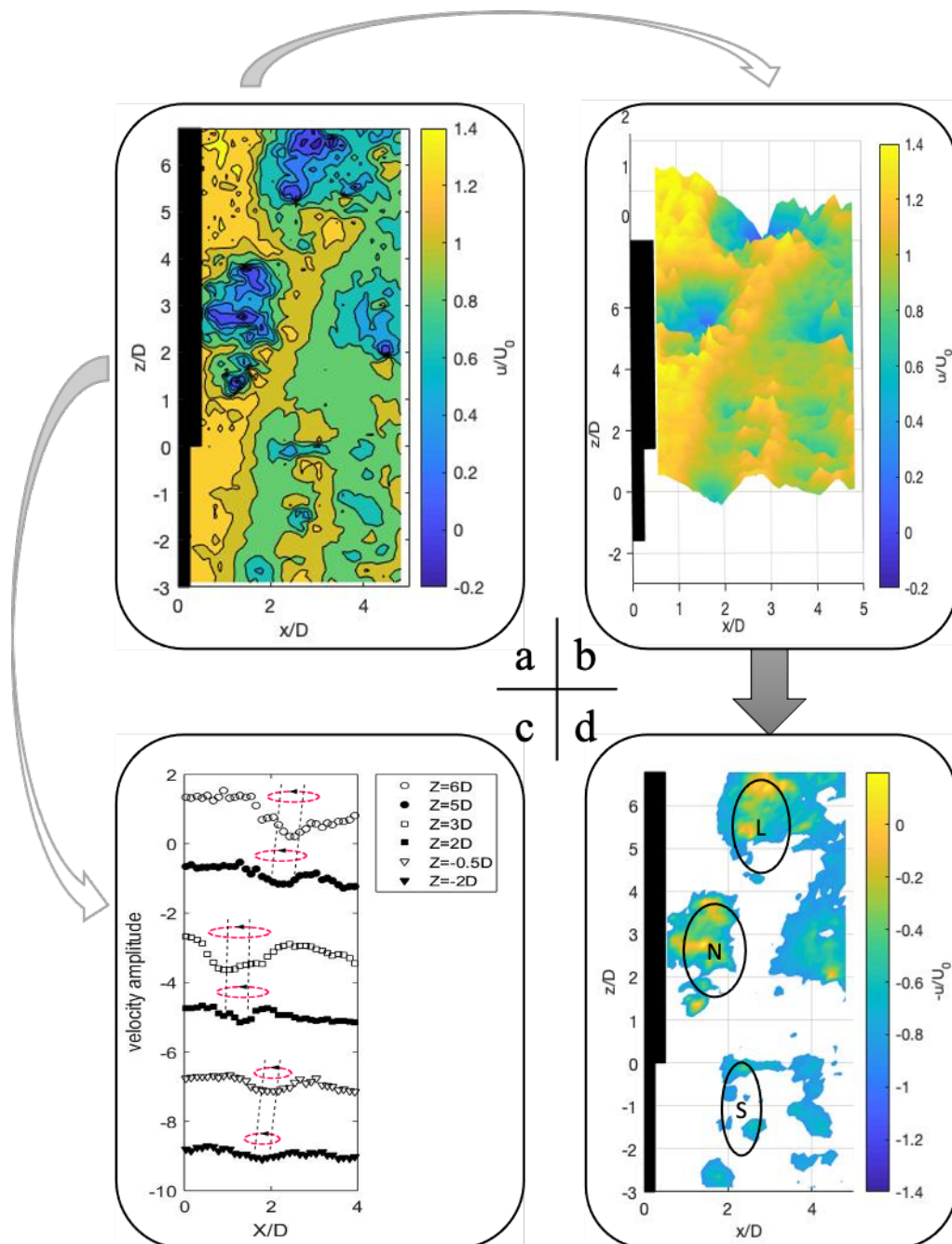
Figure 5.2 Vortex identification procedures (1st case, *S step*, *Re* = 1.6e+4).

Note: (a): instantaneous streamwise velocity contour (flat version); (b): three-dimensional version;
(c): streamwise velocity varies downstream; (d): inversed three-dimensional version.

Taking 2nd case as the example, the streamwise velocity contour along plane (Y = -0.6*D*) at a certain instant of time is considered and processed, with four relevant graphs exposed in figure 5.2(a) –(d). Figure 5.2(a) displays the corresponding two-dimensional contour (flat version), where contour lines behind the small-diameter cylinder roughly parallel to the cylinder axis. However, velocity variation (u/U_0) against the horizontal axis at diverse cross-sections of large-diameter cylinder, e.g., z/D=*3, 4, 5*, changes drastically, indicating the occurrence of the complicated vortex shedding. Subsequently, streamwise velocity distributions (u/U_0) in terms of several cross-sections (z/D = 6, 5, 3, 2, -0.5, -2) are plotted

and shown in figure 5.2(c). It should be noted that the velocity amplitudes at z/*D* = *5, 3, 2, -0.5, -2* are reduced by 2, 4, 6, 8, 10 respectively. Several typical 'velocity valleys' are picked out and marked with red oval circulars, evidencing the emergence of vortices. Consequently, vortices with similar phase form 'vortex cell' highlighted by dash lines in figure 5.2(c), which suggests that a total of three different vortex cells co-exist behind the sharp step cylinder. In order to spot the complete vortex cells in the wake, velocity contour in figure 5.2(a) is converted to a three-dimensional version as shown in figure 5.2(b). One can easily observe complete 'real' three dimensional 'velocity valleys' from figure 5.2(b), and their relative positions agree with that shown in figure 5.2(c). Furthermore, to make a clear exhibition about the above-mentioned vortex cells, flip the velocity contour in figure 5.2(b) over and display the contour portion with the value being below -0.87 in figure 5.2(d) where three distinct vortex cells are clearly marked.

According to the definition towards vortex shedding cells after step circular cylinder (Dunn & Tavoularis, 2006), i.e., L-cell, N-cell, S-cell. A reliable assumption about full names of L-cell, S-cell, and N-cell (Dunn & Tavoularis, 2006) is vortices from the **L**arge cylinder, from the **S**mall cylinder, and the third (**N**ew) type of vortices. Three diverse vortex cells can be discerned in figure 5.2(d) and marked as L-cell, N-cell, S-cell, respectively. S-cell takes up the entire span of small-diameter cylinder, with its top end extending into the wake of large-diameter cylinder. The other two vortex shedding cells, namely L-cell and N-cell, exist behind the large-diameter cylinder, with approximate spanwise range of z/*D* > 4 and 1 < z/*D* < 4. As 'N-cell' is a new-born or an additional vortex cell, the reason for the 'N-cell' formation arises researchers' interest, which gives rise to corresponding explanations. Actually, the occurrence of the additional vortex shedding is prevalent near ends of finite length cylinders, for instance, near free ends (Zdravkovich, et al., 1989) or near endplates (Williamson, 1989; Morton & Yarusevych, 2010b). It can be attributed to the increase of base pressure (surface pressure coefficient at the rear of circular cylinder), and the enlargement of the formation length. Eventually, the vortex shedding delays near ends, giving rise to a new vortex cell differing with the primary one (Zdravkovich, et al., 1989).

(a)   (b)

(c)   (d)
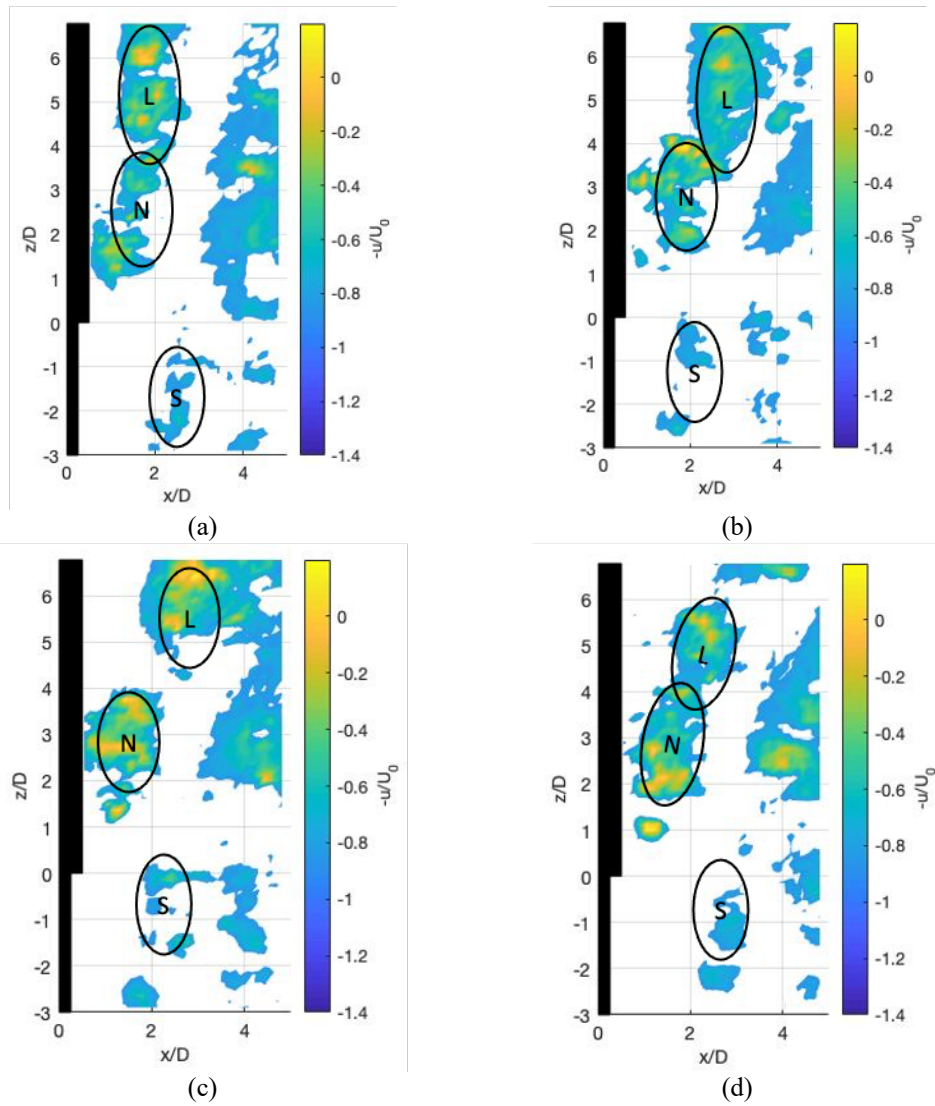
Figure 5.3 Diverse patterns of co-existence of vortex cells at four instants of time (1st case, *S step*, *Re* = 1.6e+4).

It has also been found that the co-existence of three vortex cells behind step cylinders has different patterns at different instants of time. Consequently, considering the velocity contours at the other three typical instants of time, corresponding vortex cells together with that in figure 5.2(d) are presented in figure 5.3(a) –(d). It is obvious that three vortex cells namely, L-cell, N-cell and S-cell co-exist in all the above-mentioned instants of time in figure 5.3 but differ in their relative positions. As for figure 5.3(a), N-cell and L-cell are detaching from large-diameter cylinder in phase, and subsequently melting into one piece parallel to the cylinder axis. A clear phase difference appears in figure 5.3(b) where these two vortex cells (viz. L-cell, N-cell) are still struggling to maintain the one-piece state. In figure 5.3(c), the significant displacement between N-cell and L-cell is observed due to the notable phase difference in between, which clearly indicates two distinct different types of vortex shedding (N-cell and L-cell). Besides, at some instants of time,

e.g., in figure 5.3(d), N-cell and L-cell form one piece which inclines against the cylinder axis.

<table>
<tr><td>(a): 4th case, Re = 1.6e+4</td><td>(b): 6th case, Re = 3.3e+4</td></tr>
</table>

(a): 4th case, *Re* = 1.6e+4 (b): 6th case, *Re* = 3.3e+4
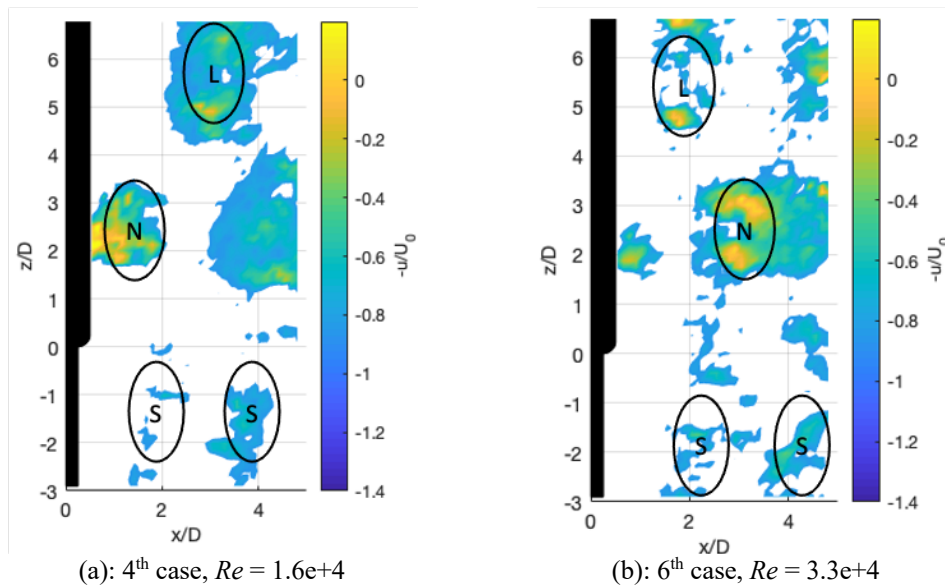
Figure 5.4 The co-existence of vortex cells behind round step cylinder.

S-cell can be recognised in all instants of time in figure 5.3(a) -(d) but its scale cannot be comparable to the other two vortex cells owning to the measuring plane offset from the cylinder axis being 0.6 times of the large diameter and 1.2 times of the small diameter. Consequently, the velocity fluctuation along Plane Y = -0.6*D* behind the span of small-diameter cylinder is weaker. Lastly, following the same procedures, these three vortex-shedding cells can also be clearly distinguished in the wake of *R step* (round step cylinder) at Reynolds number of 1.6e+4 (see figure 5.4(a)) and 3.3e+4 (see figure 5.4(b)).

5.2 Properties of Vortex-shedding Cells

According to the discussion in section 5.1, three vortex-shedding cells are successfully recognised in the wake zone for the 2nd case, 4th case and 6th case. For this section, deeper insight on characteristics of vortex-shedding cells behind *S step* and *R step* can be gained, on the basis of spectral analysis and dynamic frequency analysis. For *S step* (sharp step cylinder), related results are in good agreement with those in previous publications (Norberg, 1992), i.e., frequency of L-cell and N-cell. In line with guidance from Dunn & Tavoularis (2006), averaged cell boundaries can be well determined at Reynolds number of 1.6e+4. As a supplementary discussion of Morton & Yarusevych (2010a, 2014a), frequency ratio (f_L/f_N) and the averaged N-cell extent (the length of N-cell) are studied to a great extent, and relevant empirical formulas are proposed. Lastly, study on frequency variation against the time provides us with more reliable information in terms of local frequency fluctuation at different cross-sections. For *R step* (round step cylinder), vortex characteristics in the wake are well studied and presented by applying the identical methodology. Furthermore, the impact of shape of step junction, i.e., sharp step junction vs. round step junction, on vortex characteristics is revealed.

Spectral distribution along the span

Considering the 2nd case, 4th case and 6th case, spectral analysis regarding streamwise velocity along a reference line parallel to the cylinder axis, i.e., x/*D* = 2.5, y/*D* = -0.6, is implemented, yielding frequency variation along the span as shown in figure 5.5. The corresponding spectral setting keeps the same as that for the plain circular cylinder (see table 4.5). The horizontal axis stands for nondimensional frequency, namely *fD/U₀*, and the axis parallel to the cylinder span stands for the spanwise location (z/*D*). Besides, heigh of all peaks denotes the ratio of PSD (power spectral density) to the incident velocity (*U₀*). For each case, images from two views are provided, namely a front view and a side view, the former of which can help display a clear layout of frequency peaks and the latter of which can demonstrate the energy information (equivalent to PSD/*U₀*) variation along the span.
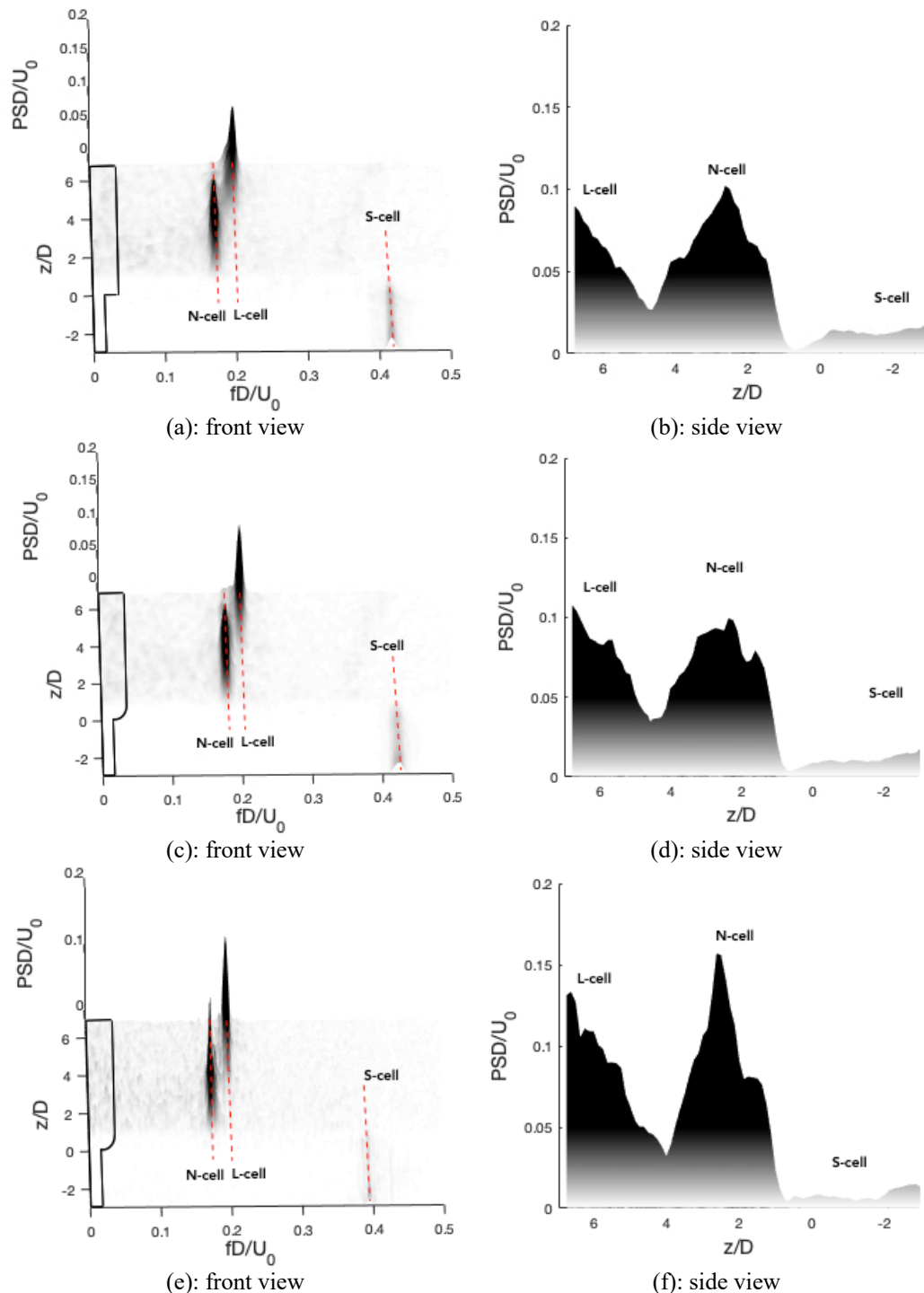
Figure 5.5 Streamwise velocity spectra along the reference line ($x/D = 2.5$, $y/D = -0.6$).

Note: (a), (b): 2nd case, *S step*, $Re = 1.6e+4$; (c), (d): 4th case, *R step*, $Re = 1.6e+4$;
(e), (f): 6th case, *R step*, $Re = 3.3e+4$.

By observing a group of graphs in figure 5.5, a total of three apparent frequency peaks co-exist in the wake of these three cases, two of which are in charge of area behind the large-diameter cylinder, and the other one mainly distributes behind the small-diameter cylinder. It should be borne in mind that the amplitude of frequency peak after the small-diameter cylinder cannot be comparable to that of the other two frequencies; because the measuring plane (Plane $Y = -0.6D$) is further away from the small-diameter cylinder

surface than from the larger-diameter cylinder surface. It has been demonstrated that each vortex-shedding cell corresponds to a constant frequency and three vortex-shedding cells co-exist behind step cylinders. Consequently, the aforementioned three frequencies can be linked with corresponding three vortex-shedding cells namely L-cell, N-cell and S-cell, which are marked and labelled in figure 5.5(a), (c), (e). The frequency distribution in figure 5.5 directly indicates that the co-existence of three vortex cells behind the sharp step cylinder happens under the high Reynolds number (1.6e+4) in agreement with that in lower Reynolds numbers (Dunn & Tavoularis, 2006; Morton & Yarusevych, 2010a, 2010b, 2014a). Besides, these three vortex cells being observed behind the round step cylinder at $Re = 1.6e+4$, $3.3e+4$ suggests that its occurrence is independent from the shape of step junction (*S step*, *R step*) and the continuous increase of Reynolds number. With respect to the frequency variation along the span, each dominant frequency corresponding to a certain vortex-shedding cell is in charge of a certain portion of the span, which is in agreement with the relative position of three vortex cells shown in figure 5.3 & 5.4. And meanwhile, the overlap of L-cell frequency and N-cell frequency can be found near z/D = 4 where the amplitude of L-cell frequency and N-cell frequency experiences significant drop (see figure 5.5(b), (d), (f)) due to cell boundaries' location being fluctuating against time (Morton & Yarusevych, 2014a). The corresponding normalized frequencies in terms of three vortex-shedding cells of these three cases (2nd case, 4th case, and 6th case) are summarized in table 5.2. For a better comparison with relevant results in the literature, quantitative studies on frequency relationship between L-cell and N-cell are presented in the coming part of this section.

Table 5.2 Summary of vortex-shedding frequencies.

Original frequency			
No.	$f_L D/U_0$	$f_N D/U_0$	$f_S D/U_0$
2nd case	0.2025	0.1725	0.4150
4th case	0.2025	0.1800	0.4225
6th case	0.1988	0.1738	0.3937

Note: 2nd case: sharp step cylinder, $Re = 1.6e+4$; 4th case: round step cylinder, $Re = 1.6e+4$;
6th case: round step cylinder, $Re = 3.3e+4$.

A clear discrepancy regarding N-cell frequency can be observed at 4.2% between that in 2nd case and 4th case. And meanwhile, L-cell frequency keeps constant. It could be inferred that the step junction (sharp step junction and round step junction) affects the N-cell frequency to some extent. By comparing 6th case with 4th case, L-cell frequency and N-cell frequency give a distinct decrease subject to the increase of Reynolds number. Compare L-cell frequency and N-cell frequency of 2nd case with related experimental data under lower Reynolds numbers in the literature (Norberg, 1992); the corresponding outcome is presented in figure 5.6. One could observe both N-cell frequency and L-cell

frequency obtained from Norberg (1992) smoothly decrease with the growth of Reynolds number, both of which perfectly match with lines of linear fit (marked as red and blue dash lines in figure 5.6). Besides, As for the present result from 2nd case, L-cell frequency and N-cell frequency are located at the extension of two fitted lines, indicating that the present experimental data is reliable and acceptable.
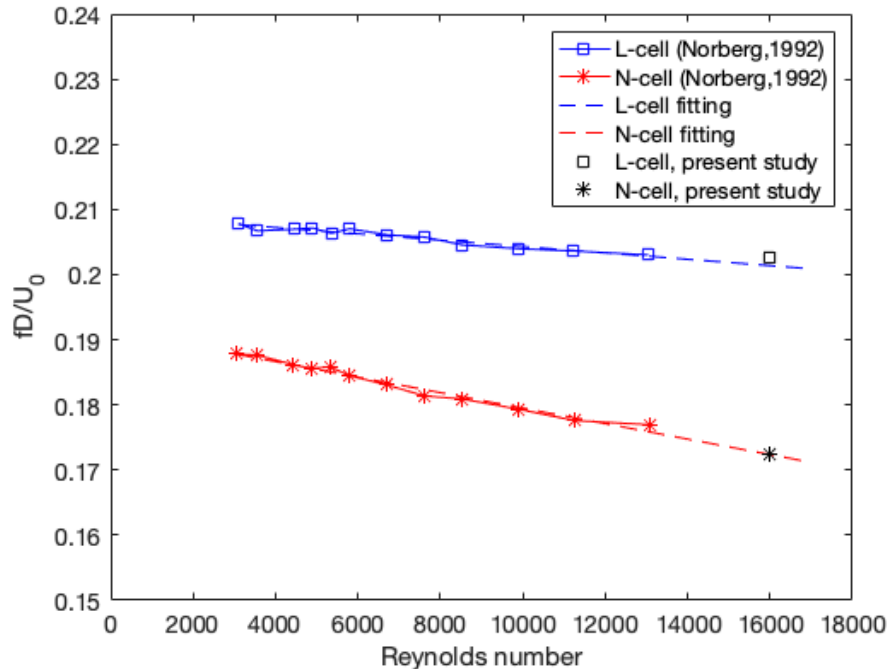
Figure 5.6 Normalized frequency of N-cell and L-cell vs. Reynolds number. (*S step*, *D/d* = 2).
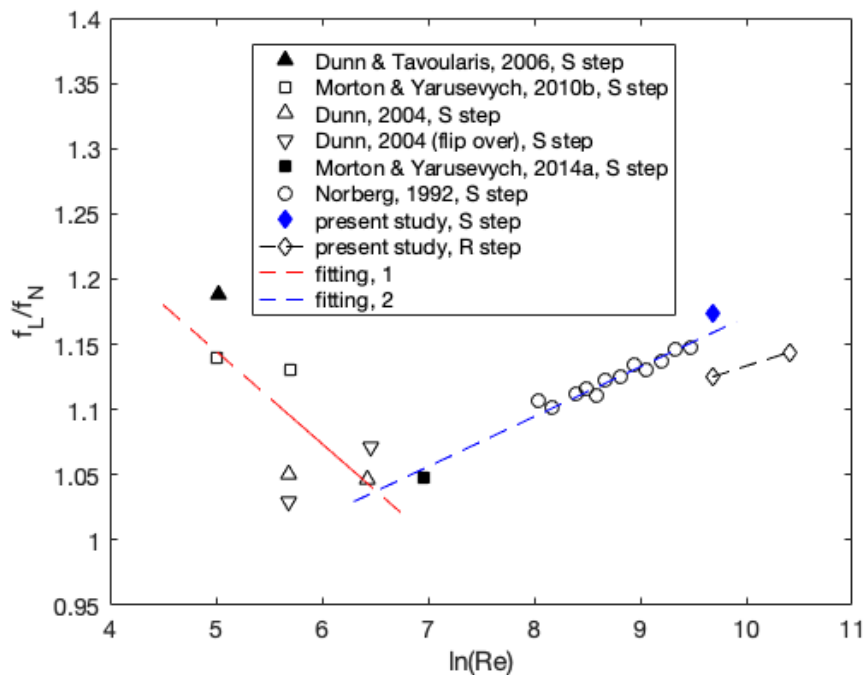
Figure 5.7 Frequency ratio vs. Reynolds number (*D/d* = 2).

The frequency ratio (f_L/f_N) being a useful term to evaluate the united feature of L-cell and N-cell in table 5.2 is seen to vary among different testing cases. In order to investigate

the relationship between frequency ratio (f_L/f_N) and the Reynolds number, Results from previous publications (Dunn, 2004; Dunn & Tavoularis, 2006; Morton & Yarusevych, 2010b; Morton & Yarusevych, 2014a; Norberg, 1992), together with that from the present study (2nd case, 4th case, 6th case), are summarized and presented in figure 5.7. Morton & Yarusevych (2014a) made the similar summary of the ratio of f_N/f_L, and concluded its trend against the Reynolds number from related scattered data, that is, f_N/f_L exhibits a growth trend at $Re < 400$ and subsequently decreases when the Reynolds number is beyond 400. In figure 5.7, one could find that the present results from sharp step cylinder and round step cylinder follow the similar trend put forward by Morton & Yarusevych (2014a). In order to expose more details about this trend, two lines of linear fit (see red / bule dash lines in figure 5.7) indicating two branches of this trend are obtained, together with the black dash line connecting the present results of *R step*. According to the equations regarding these two fitted lines (eq. 5.1 and eq. 5.2), the present study deduces the turning point between two branches should be roughly at Reynolds number of 672.

$$\frac{f_L}{f_N} = 1.4999 - 0.0710 \times \ln(Re) \qquad \qquad Re < 672 \qquad (5.1)$$

$$\frac{f_L}{f_N} = 0.7883 + 0.0383 \times \ln(Re) \qquad \qquad Re > 672 \qquad (5.2)$$

More explanation regarding the comparison of two turning points ($Re = 400$ and 672) is given as follows. The turning point of 672 can provide with a perfect linear fit for the high Reynolds number branch, and the option of 400 seems to be a trade-off, which can induce to acceptable linear fits for both at low Reynolds number and at high Reynolds number. Pay attention to results from *R step*, and one can find drastic reduction of the frequency ratio, compared with that obtained from *S step* at the same Reynolds number (1.6e+4). Besides, the increase trend for *R step* against Reynolds number is in good agreement with the blue fitted line indicating that the increase trend is independent from shape of step junction validating the reliability of experimental results from *R step*.

Identification of averaged cell boundaries

The aforementioned three dominant frequencies being staggered along the cylinder span gives rise to a question, that is, '*how can they switch from one dominant frequency to the other?*' One might speculate that a frequency disappears completely before the successive one coming or a sudden jump takes place in between. However, results at low Reynolds numbers from previous publications (Dunn & Tavoularis, 2006; Morton & Yarusevych, 2010b; Morton & Yarusevych, 2014a) proved that the alternation from one frequency to another is a gentle process, accompanied by the amplitude fluctuation. Consequently, in order to make a supplement for frequency transition behind *S step* under high Reynolds number and to explore frequency transition behind *R step*, spectral analysis at eight cross-sections behind the sharp step cylinder (2nd case) and behind the round step cylinder (4th case, 6th case) is performed, to investigate the impact of Reynolds number and shape of step junction towards the frequency transition.
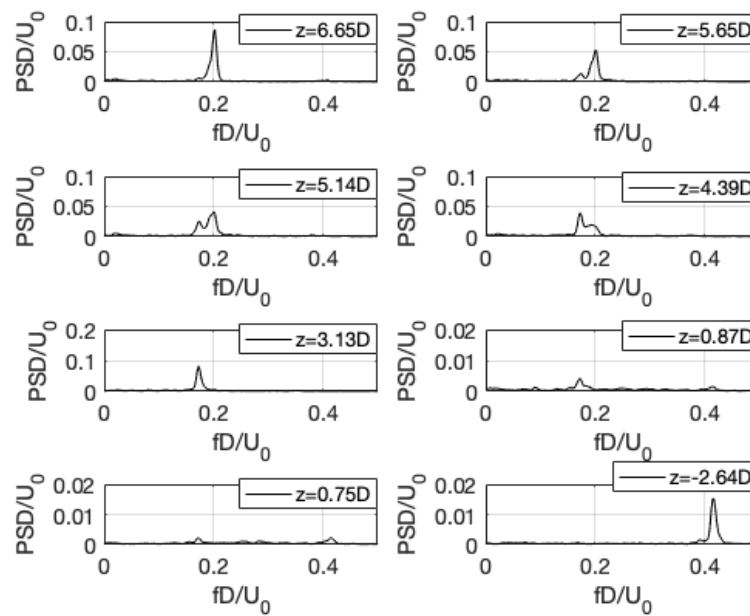
Figure 5.8 Streamwise velocity spectra along the reference line ($x/D = 2.5$, $y/D = -0.6$) in the wake of *S step* (2nd case, $Re = 1.6+4$).

Figure 5.8 presents spectral analysis along a reference line ($x/D = 2.5$, $Y/D = -0.6$) behind sharp step cylinder (*S step*) under Reynolds number of 1.6e+4, where eight representative spanwise locations are chosen, i.e., $z/D = 6.65$, 5.65, 5.14, 4.39, 3.13, 0.87, 0.75 and -2.64. The horizontal axis stands for normalized frequency (fD/U_0), and the vertical axis stands for ratio of PSD (power spectral density) to the incident velocity(U_0). At $z/D = -2.64$, single notable frequency peak with a value of 0.4150, can be detected, corresponding to S-cell. With it gradually approaching the step junction, this identical frequency peak (0.4150) decreases it amplitude gradually till a very low level at $z/D = 0.75$. After that, the second peak (0.1725) exceeds the first peak (0.4150) in amplitude,

suggesting the complete of changeover in dominant frequency between $z/D = 0.75$ and $z/D = 0.87$. As it is mentioned in table 5.2, the frequency peak of 0.1725 corresponding to N-cell reveals that N-cell starts to be outstanding after the changeover. Similarly, the dominant frequency switch from 0.1725 to 0.2025 takes place between $z/D = 4.39$ and $z/D = 5.14$. It should be noted that the real critical neighbouring positions for the transition between 0.1725 and 0.2025 are closer namely $z/D = 4.64$ and $z/D = 4.77$ where the amplitude difference is small and is hard to visually recognise from a similar spectral plot. From $z/D = 5.14$ to $z/D = 6.65$, it can be easily observed that the frequency peak (0.2025) corresponding to L-cell gradually increases the amplitude, and meanwhile the N-cell frequency peak (0.1725) gradually weakens.
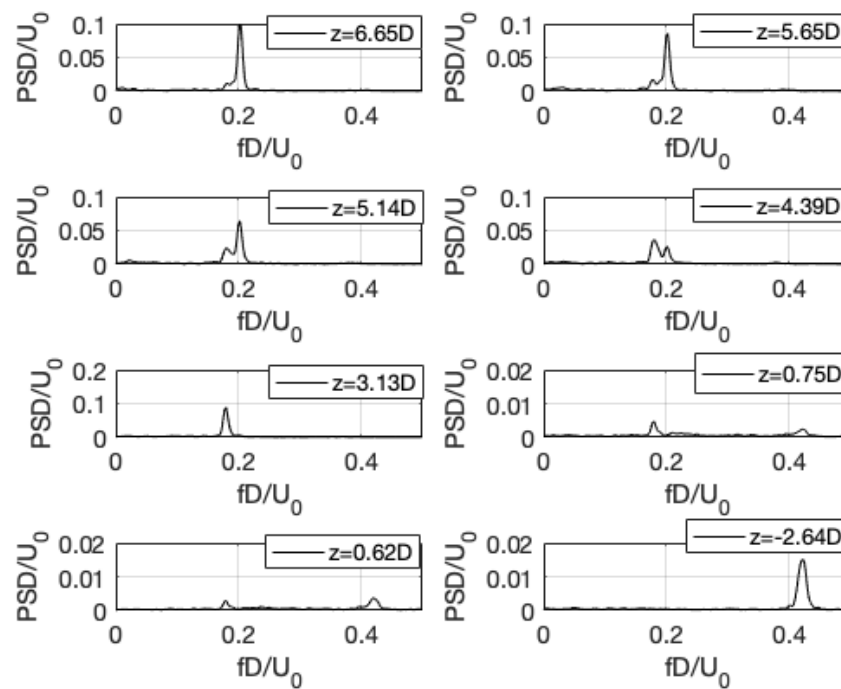
Figure 5.9 Streamwise velocity spectra along the reference line ($x/D = 2.5$, $y/D = -0.6$) in the wake of *R step* (4th case, $Re = 1.6+4$).
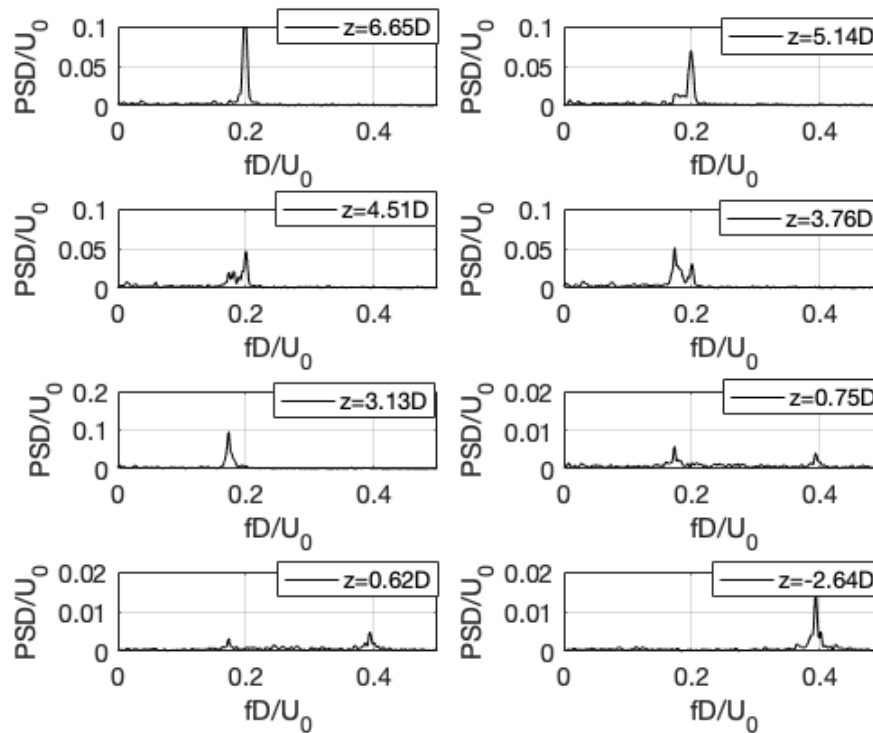
Figure 5.10 Streamwise velocity spectra along the reference line (x/D = 2.5, y/D = -0.6) in the wake of *R step* (6th case, *Re* = 3.3+4).

Subsequently, streamwise velocity spectra behind *R step* at *Re* = 1.6e+4 and 3.3e+4 are obtained following the same procedures; corresponding results presented in figure 5.9 and figure 5.10 suggest that the smooth frequency transition among L-cell, N-cell and S-cell also takes place in the wake of the round step cylinder. However, some further meaningful phenomena can still be revealed by comparing three cases namely 4th case (figure 5.9), 6th case (figure 5.10) and 2nd case (figure 5.8). The comparison between figure 5.9 and figure 5.8 exposes the impact of shape of step junction. More specifically, for 4th case in figure 5.9, L-N frequency transition and N-S frequency transition occur at the region of [4.64*D*, 4.52*D*] and [0.75*D*, 0.62*D*] respectively, which displays a downward shift (0.125*D*) approaching the step junction. Besides, the spectrum near *z/D* = 0.75 behind *R step* (see figure 5.9) displays stronger amplitude than that behind *S step* (see figure 5.8). As for the impact of Reynolds number, one can observe the frequency transition in terms of L-N and N-S in figure 5.10 happens at [4.14*D*, 4.01*D*] and [0.75*D*, 0.62*D*] respectively. The L-N frequency transition significantly differs from that under lower Reynolds number , corresponding discussion being given in the forthcoming part.

(a)   (b)
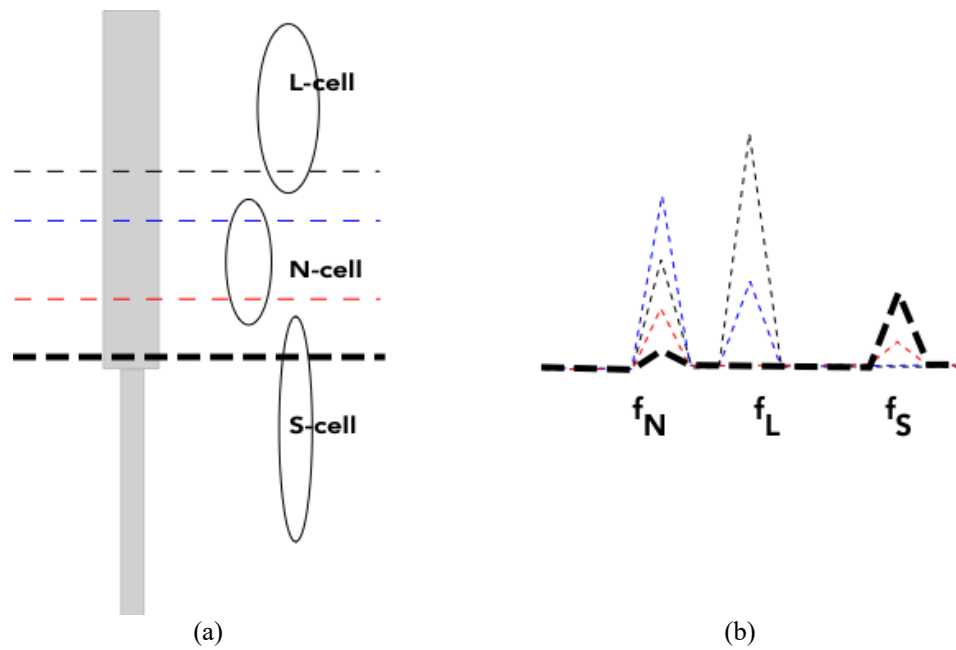
Figure 5.11 Schematic sketch of delimiting averaged cell boundaries.

Note: (a): spatial layout of L-cell, N-cell and S-cell and four cross-sections (colour dash lines);
    (b): sketch of spectrum at four cross-sections;
    f_N, f_L and f_S denote frequencies of N-cell, L-cell and S-cell.

(a)   (b)   (c)
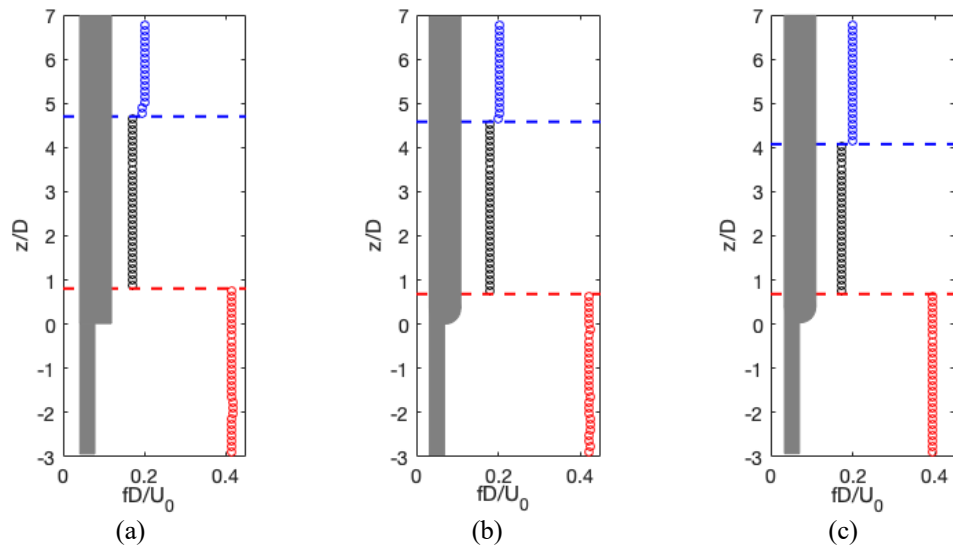
Figure 5.12 Exhibition of dominant frequencies and averaged cell boundaries.

Note: (a): 2nd case, S step, Re = 1.6e+4; (b): 4th case, R step, Re = 1.6e+4; (c): 6th case, R step, Re = 3.3e+4.
    Red circle: S-cell frequency; Black circle: N-cell frequency; Blue circle: L-cell frequency.
    Red dash line: N-S boundary; Blue dash line: L-N boundary.

The smooth frequency transition among L-cell, N-cell and S-cell have been demonstrated via figure 5.8 to 5.10, which reveals such a prevalent phenomenon not only takes place behind the sharp step cylinder (S step), but also the round step cylinder (R step). Besides, the Reynolds number plays a vital role in determining the transition location. On the basis of frequency transition outcome, the averaged cell boundary can be defined as the

spanwise position where the switch of dominant frequency between two neighbouring cells takes place (Dunn & Tavoularis, 2006). The identification of averaged cell boundaries can be illustrated via figure 5.11. Figure 5.11(a) interprets the spatial distribution of three vortex-shedding cells (L-cell, N-cell, S-cell), as well as four representative cross-sections (marked as colour dash lines) which are assigned near the ends of these three cells. And meanwhile, figure 5.11(b) depicts velocity spectra at corresponding four cross-sections in the wake. Consequently, the averaged cell boundary can be precisely located if the dominant frequency switches between neighbouring cross-sections. For instance, L-N cell boundary can be determined between black dash line and blue dash line if a switch between f_L and f_N takes place at these two dash lines. Similarly, the N-S cell boundary can be recognised between red dash line and the black bold dash line.

As a result, the spanwise layout of dominant frequencies (L-cell, N-cell, S-cell) for 2nd case, 4th case and 6th case can be summarized in figure 5.12, together with locations of averaged cell boundaries. Results in figure 5.12(a) –(c) display similar spanwise location of N-S boundary (red dash line) for all the three cases namely, being $z/D = 0.81$ for 2nd case, $z/D = 0.685$ for 4th case and $z/D = 0.685$ for 6th case, which indicates that the N-S boundary is independent from shape of step junction and the Reynolds number. It is comparable to result obtained from Morton & Yarusevych (2014a) under the Reynolds number of 1050, i.e., $0.5D$ away from the step junction ($z/D = 0$). With regard to the L-N boundary location, one can observe a huge difference between 6th case and the other two cases (2nd case, 4th case), suggesting the notable impact of Reynolds number on the L-N boundary location. Exact locations of L-N boundary for the three cases can be given as $4.705D$ (2nd case), $4.58D$ (4th case) and $4.075D$ (6th case).

Subsequently, the averaged N-cell extent along the span of step cylinders can be deduced from the gap between N-L cell boundary and N-S cell boundary. According to related results from previous publications, figure 5.13 summarizes N-cell extent variation against the Reynolds number, accompanied by the present results in terms of *S step* and *R step*. Considering the present results at $Re = 1.6e+4$, i.e., $\ln(Re) = 9.68$, one could observe the N-cell extent behind S step and R step keeps the same, suggesting the averaged N-cell extent is independent from the shape of step junction. Consequently, one could infer that the averaged N-cell extent for *S step* at higher Reynolds number ($3.3e+4$), i.e., $\ln(Re) = 10.4$, should be roughly the same as that obtained from *R step*.
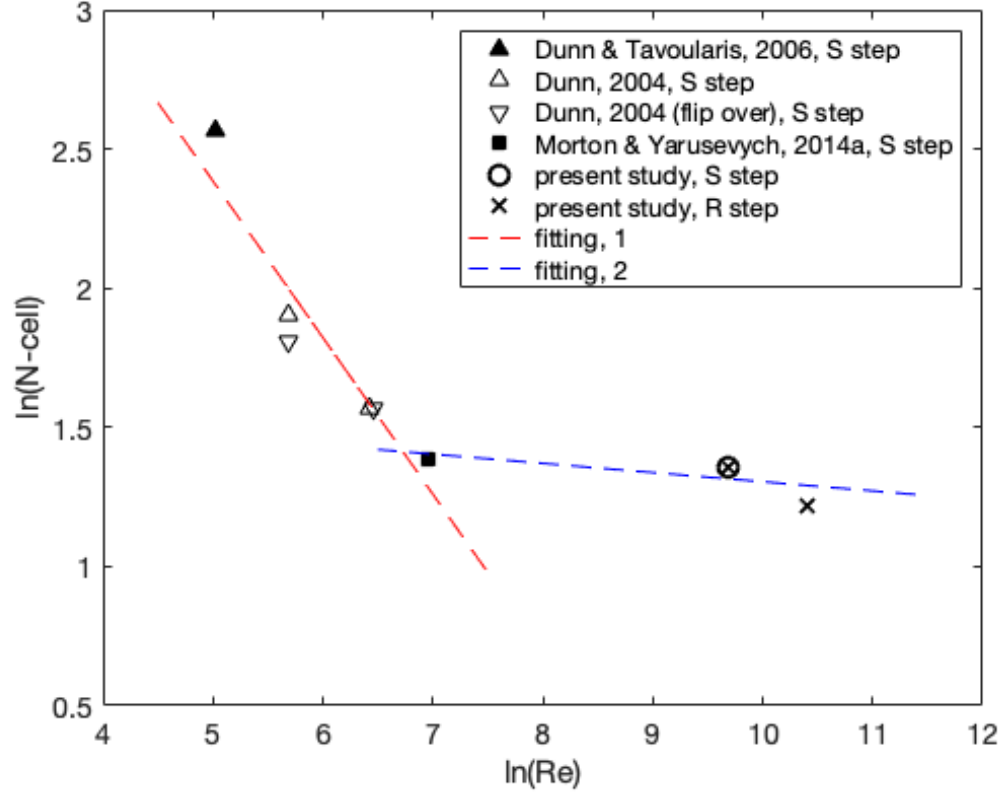
Figure 5.13 Averaged N-cell extent vs. Reynolds number.

$$\ln\left(N - cell\right) = 5.1982 - 0.5626 \times \ln(Re), \qquad Re < 836 \quad (5.3)$$

$$\ln\left(N - cell\right) = 1.6346 - 0.0330 \times \ln(Re), \qquad Re > 836 \quad (5.4)$$

Besides, one could also observe the trend of N-cell extent variation against the Reynolds number, which is split into two branches. Initially, N-cell extend decreases sharply with the growth of Reynolds number till the turning point, subsequently starts to decrease at a mild rate. Two fitted lines corresponding to two branches are plotted in figure 5.13; the empirical formulas for two fitted lines are given in eq. 5.3 and eq. 5.4. The emergence of another turning point namely at Reynolds number of 836, is of interest to the present study, because it quite approaches the turning point ($Re = 672$) obtained from frequency ratio analysis in figure 5.7. As a result, the present study attempts to put forward a united summary regarding the relationship among frequency ratio (f_L / f_N), N-cell extend and the Reynolds number, that is, a critical Reynolds number region can be obtained, i.e., 672 < Re < 836, which allows significant different trends in terms of frequency ratio and N-cell extend before and after this Reynolds number region.

Local frequency fluctuation

Followed by related analysis regarding velocity spectral, i.e., frequency ratio and N-cell extent, this subsection focuses on local frequency variation over time to gain deeper insight on how frequency of different vortex cells fluctuates against the time. For all experimental cases (2nd case, 4th case, 6th case), six probes are distributed along the reference line (x/D = 2.5, y/D = -0.6) in the wake zone, more details being summarised in table 5.3. The ensemble (3000 samples) of streamwise velocity data at each probe is processed using continuous wavelet transform (CWT). Subsequently, local frequency variation over time for all involved velocity signal from 2nd case, 4th case and 6th case is presented in figure 5.14 to 5.16. The horizontal axis denotes non-dimensional time, i.e., t* ($t^* = t \times U_0/D$), comparably, the vertical axis represents non-dimensional frequency, i.e., *fD/U_0*.

Table 5.3 Summary of properties of all relevant probes.

	2nd case (*S step*) Re = 1.6e+4	4th case (*R step*) Re = 1.6e+4	6th case (*R step*) Re = 3.3e+4	Comments
Probe1	z/D = 6.77	z/D = 6.77	z/D = 6.77	L-cell
Probe2	z/D = 4.64	z/D = 4.52	z/D = 4.01	One end of N-cell *(near L-cell)*
Probe3	z/D = 2.25	z/D = 2.25	z/D = 2.25	N-cell
Probe4	z/D = 0.75	z/D = 0.62	z/D = 0.62	One end of S-cell *(near N-cell)*
Probe5	z/D = -3.0	z/D = -3.0	z/D = -3.0	S-cell
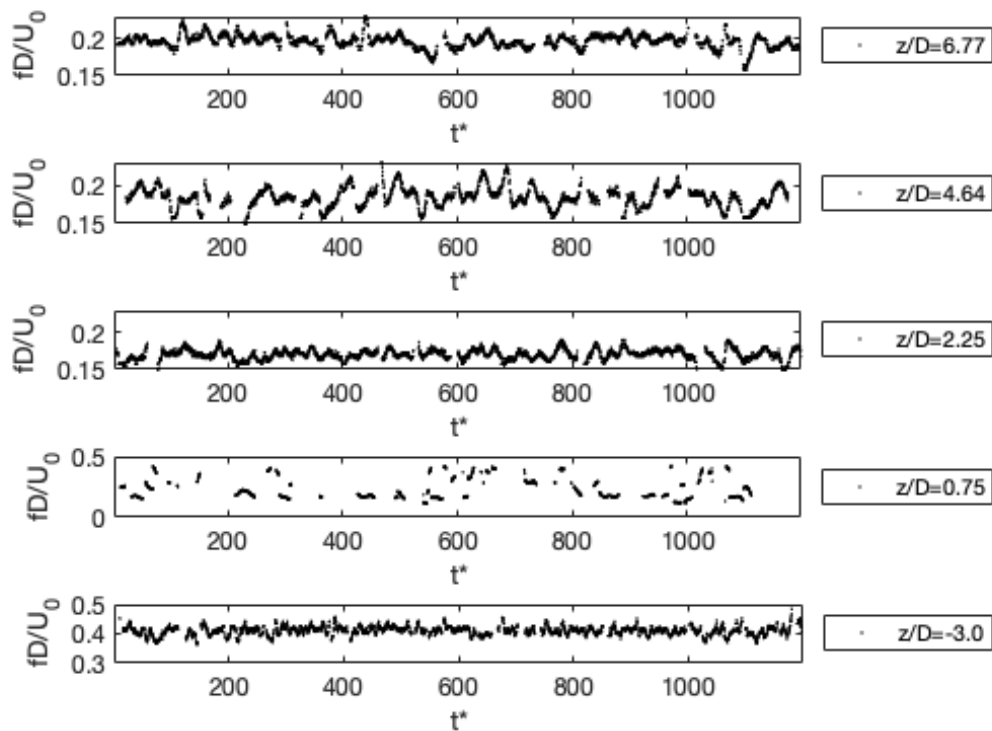
Figure 5.14 Time series of local frequency fluctuation (based on streamwise velocity) along the reference line (x/D = 2.5, y/D = -0.6, 2nd case, *S step*, Re = 1.6e+4).

Results in figure 5.14 interprets local frequency variation against time for diverse probes for 2nd case, indicating a larger frequency fluctuation than that under low Reynolds numbers (Dunn & Tavoularis, 2006; Morton & Yarusevych, 2014a). One can observe frequency variation over time for L-cell ($z/D = 6.77$), N-cell ($z/D = 2.25$) and S-cell ($z/D = -3.0$) keeps steady and concentrated, which reveals the significant typical periodical flow. When it comes to the location near N-L cell boundary ($z/D = 4.64$), strong frequency fluctuation can be discerned, and the local frequency keeps switching between L-cell frequency and N-cell frequency from time to time. The time series near N-S cell boundary ($z/D = 0.75$) being weak exhibits discrete points distribute with significant interval along the frequency and along the time. According to the fact of significant frequency fluctuation over time occurring at two cell boundaries, it can be inferred that cell boundaries change the location from time to time. The fluctuation of cell boundaries over time was also been confirmed (Dunn & Tavoularis, 2006; Morton & Yarusevych, 2014a) by perform similar experiments under lower Reynolds numbers.

Similarly, consider the impact of shape of step junction and Reynolds number, and subsequently process transient local frequency variation over time from 4th case and 6th case. The relevant results are shown in figure 5.15 and figure 5.16. It should be noted that the location of some probes for a specified case might differ with that from the other two cases due to the discrepancy of averaged cell boundaries. Results in figure 5.15 expose similar phenomenon with that from 2nd case in figure 5.14, i.e., local frequency variation for L-cell, N-cell, and S-cell being stable and concentrated, as well as the significant frequency fluctuation near cell boundaries. The comparison between 2nd case (figure 5.14) and 4th case (figure 5.15) reveals the notable difference taking place near N-S boundary where the signal after round step cylinder (*R step*) being stronger displays stable and continuous frequency variation. By comparing results between 4th case (figure 5.15) and 6th case (figure 5.16), it could be found the enhancement of frequency fluctuation is observed for all probes with the increase of Reynolds number due to the disturbance in the wake.
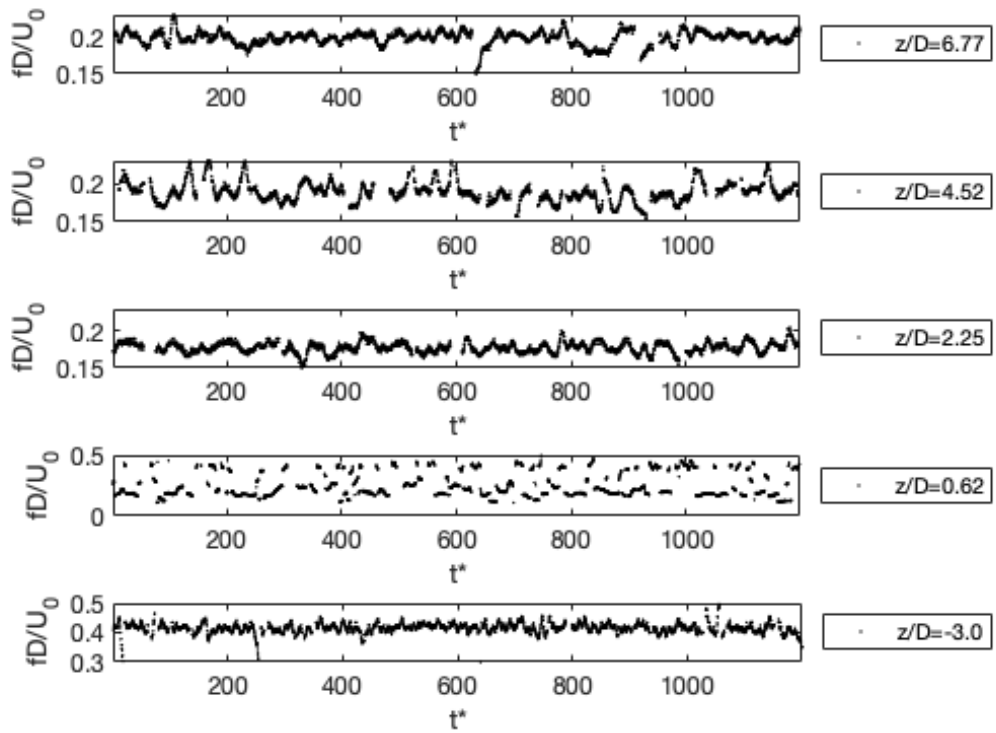
Figure 5.15 Time series of local frequency fluctuation (based on streamwise velocity) along the reference line ($x/D = 2.5$, $y/D = -0.6$, 4th case, *R step*, *Re* = 1.6e+4).
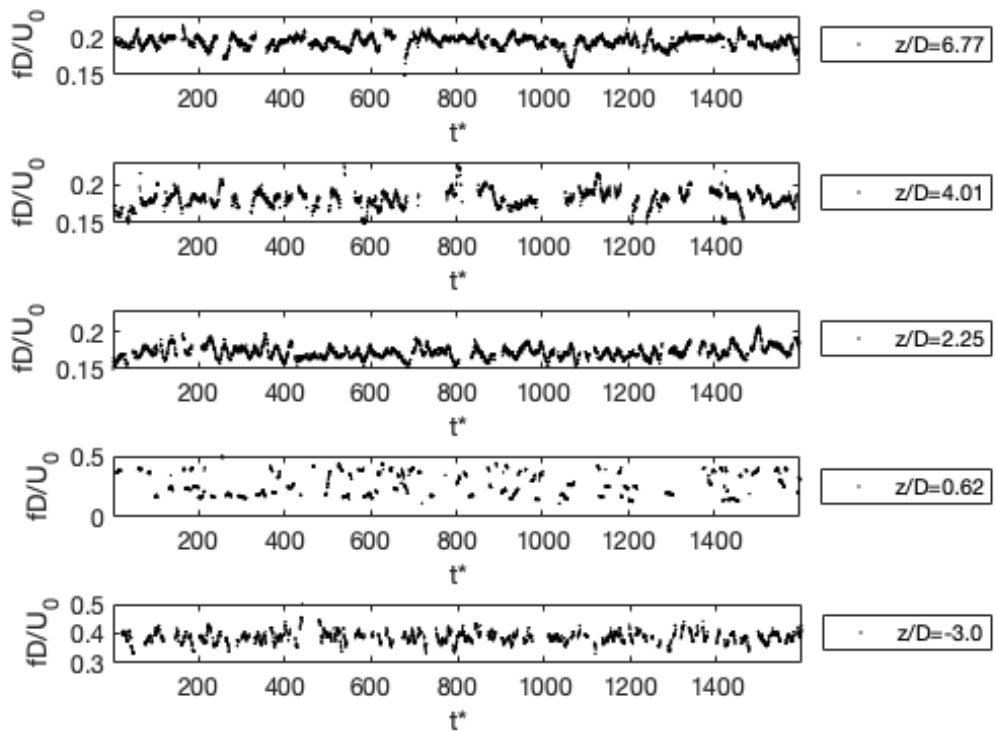
Figure 5.16 Time series of local frequency fluctuation (based on streamwise velocity) along the reference line ($x/D = 2.5$, $y/D = -0.6$, 6th case, *R step*, *Re* = 3.3e+4).

5.3 Brief Summary for Vortex Properties

This chapter mainly focuses on characteristics of vortex-shedding cells behind a sharp step cylinder and a round step cylinder under high Reynolds numbers. By applying the above-mentioned 'velocity valleys' identification, a total of three vortex-shedding cells are successfully recognised, namely the L-cell, the N-cell and the S-cell. Based on velocity spectral analysis, properties of three vortex cells are comprehensive studied. For the sharp step cylinder, f_L and f_N at Reynolds number of 1.6e+4 are in good agreement with trends (3e+3 < Re < 1.3e+4) published by Norberg (1992) as shown in figure 5.6. Trends about the variation of frequency ratio and N-cell spanwise extent against the Reynolds number are summarized by associating with results from previous publications, and subsequently, a critical Reynolds number region is put forward namely from 672 to 836, to highlight the different trends of frequency ratio and N-cell extent at different Reynolds number range namely Re < 672 and Re > 836. Smooth frequency transition between neighbouring vortex cells are detected, and the local frequency fluctuation over time shows more significant amplitude than that under smaller Reynolds numbers. For the round step cylinder, apart from similar vortex characteristics, it possesses a higher N-cell frequency, and the averaged N-cell extent displays a slight spanwise displacement towards the step. The averaged frequency and local frequency fluctuation over time near the round step show significant enhancement, compared to that behind the sharp step cylinder.

Chapter 6
FLOW FIELDS BEHIND STEP CYLINDERS

6.1 Time-averaged Velocity Fields

Results about three experimental cases (2nd case, 4th case and 6th case) are investigated in Chapter 5, with the emphasis on frequency-based characteristics of three different vortex-shedding cells. Time-averaged velocity fields in the wake of sharp step cylinders (*S step*) have ever been investigated in pervious researches under diverse Reynolds numbers by means of PIV experiments (Rafati, 2014; Teutsch, 2012). However, the area near N-L cell boundary cannot be well captured due to the size limit of field of view (FOV). Consequently, this section will pay attention to averaged velocity fields within bigger area behind *S step*, especially the area near N-L cell boundary, part result of which can be validated with that from previous publications (Rafati, 2014; Teutsch, 2012).

Apart from that, with the introduction of round step cylinder (*R step*), the impact of shape of step junction, together with different Reynolds number, are investigated. In summary, considering three experimental cases (1st case, 3rd case and 5th case), time-averaged velocity fields along the central plane (Plane Y = 0*D*) is studied in this section, to gain deeper insight on fluid state in the near-wake region right behind the cylinder axis. By averaging streamwise / spanwise velocity towards the entire dataset with 2000 samples, results about mean / rms value are plotted and analysed. It should be noted that the reflection being detected near the step junction significantly affects velocity fields close to small-diameter cylinder. As a result, part velocity field close to the cylinder is removed during data processing.
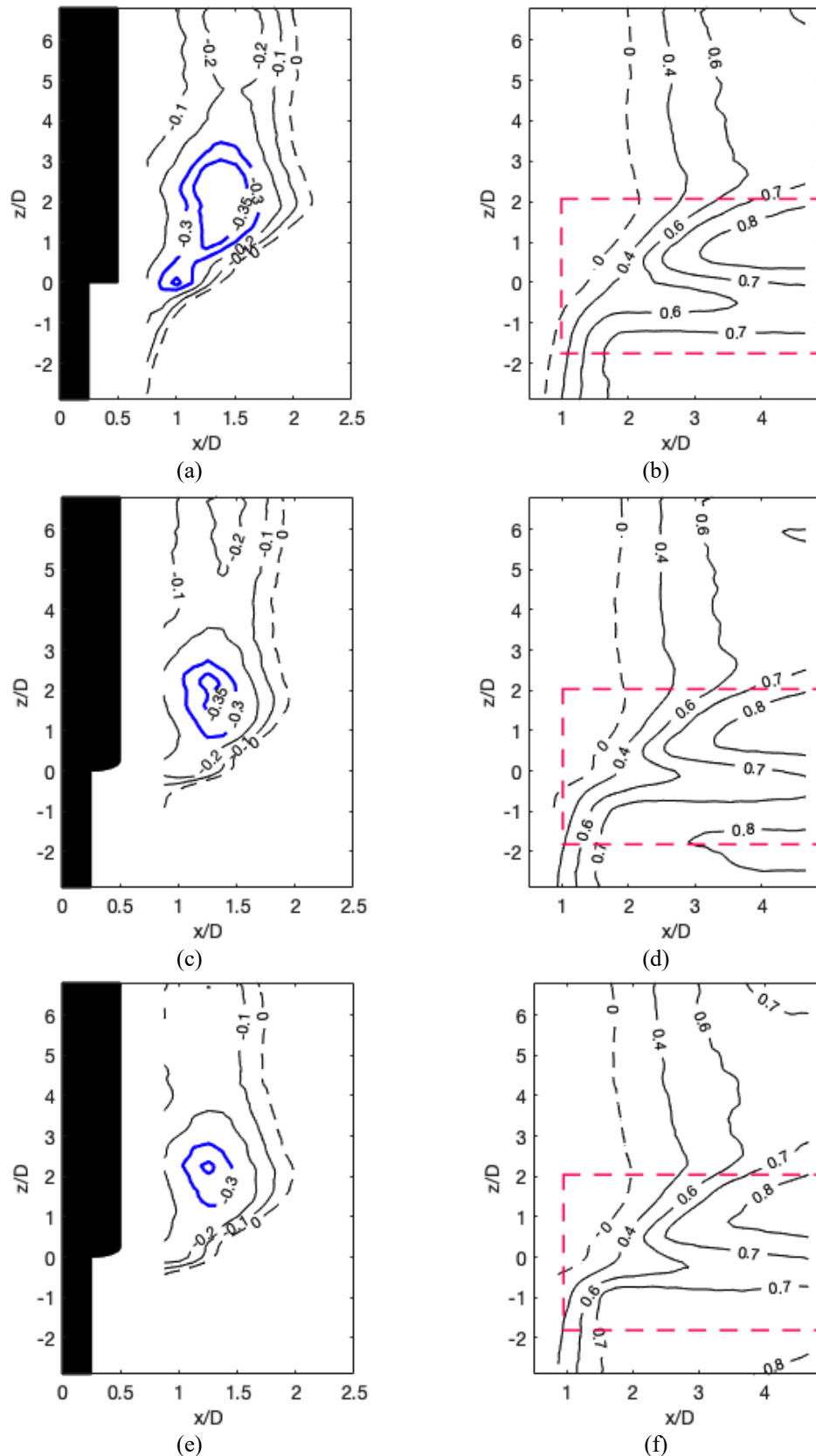
Figure 6.1 Contours of mean streamwise velocity behind step cylinders (Plane Y = 0*D*).

Note: (a), (b): 1st case, *S step*, *Re* = 1.6e+4; (c), (d): 3rd case, *R step*, *Re* = 1.6e+4;
(e), (f): 5th case, *R step*, *Re* = 3.3e+4.

Figure 6.1 focuses on three experimental cases namely, 1st case, 3rd case, 5th case, to interpret mean streamwise velocity contours along the plane (Plane Y = 0*D*) in the wake.

Horizontal axis and vertical axis stand for normalized distance along the streamwise and spanwise direction respectively. The contour value refers to normalized streamwise velocity (u/U_0). The discussion at section 4.2 about averaged velocity fields after plain cylinder depicts a negative velocity region behind the cylinder termed as 'near-wake region', or 'the recirculation zone', comprising two symmetrical stable vortices. Consequently, the meaningful contour line '0' successfully divided the entire field into two parts, namely near-wake region in figure 6.1(a), (c), (e) and behind near-wake region in figure 6.1(b), (d), (f).

Results of three experimental cases in figure 6.1 share similar characteristics as follows. The streamwise extent of recirculation zone behind the large-diameter cylinder is wider than that behind the plain cylinder (see figure 4.8). For a specific step cylinder testing case, the variation of recirculation zone shows a smooth decrease near the step which does not follow the geometrical variation. At the span portion away from the step ($z/D > 4$), the velocity contour keeps roughly uniform along the spanwise direction resembling that behind the plain cylinder. As it gradually approaches the step, the reverse velocity become more negative forming the notable 'negative streamwise velocity' region marked with blue lines in figure 6.1 (hereinafter referred to as 'NSV' region). This so-called 'NSV' region being observed in three cases but varies contour line values and sizes. Downstream flow behind near-wake region in figure 6.1(b), (d), (f) gradually rises its streamwise velocity but at different rates at different cross-sections. A significant high rate can be found at $0.5 < z/D < 1.5$, displaying denser contour lines in figures. Besides, several contour lines behind the step junction ($-1 < z/D < 1$) bend downstream highlighted within dash red rectangles in figures.

However, the above-mentioned bending contour lines show different characteristics in three experimental cases. For instance, the contour line '0.6' within the red dash rectangle bends downstream with larger extent in figure 6.1(b) than that in figure 6.1(d), suggesting the notable impact of shape of step junction. Consequently, it can be reckoned that the 'round shape' contributes to mitigating velocity variation near the step junction. Besides, the bending appearance in figure 6.1(f) is more significant than that in figure 6.1(d) due to the increase of Reynolds number.
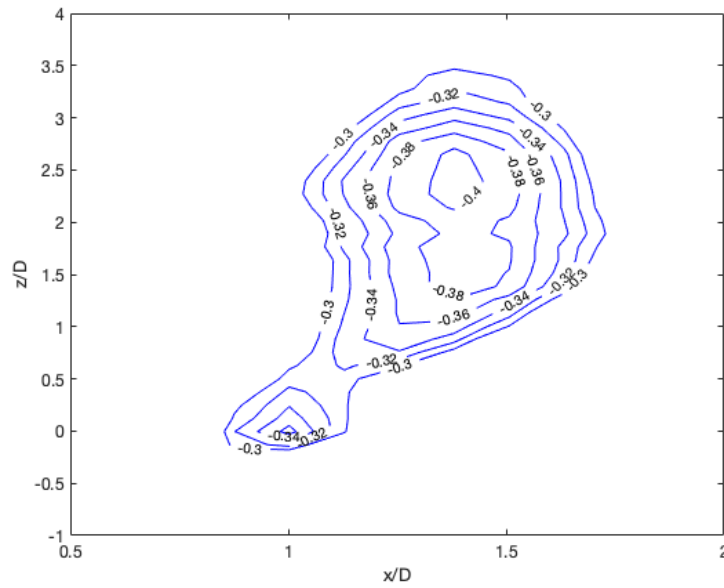
(a): 1st case, *S step*, *Re* = 1.6e+4;
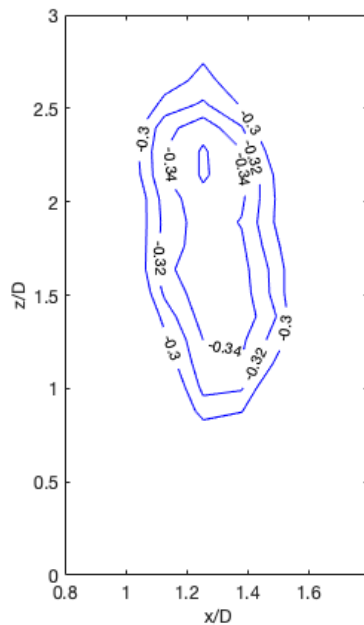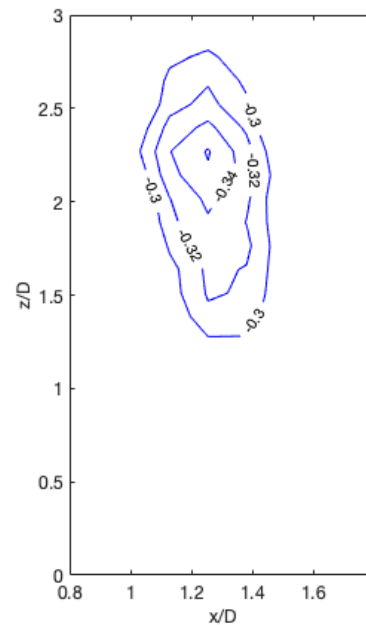
(b): 3rd case, *R step*, *Re* = 1.6e+4;　　　　(c): 5th case, *R step*, *Re* = 3.3e+4;

Figure 6.2 Layout of 'NSV' region (negative streamwise velocity).

The 'NSV' region in figure 6.1(a), (c), (e) is taken out and compared in figure 6.2. Treating the contour line '-0.3' as the benchmark, one can observe the significant larger area of 'NSV' region behind '*S step*' in figure 6.2(a) than that from the other two '*R step*' related cases (see figure 6.2(b), (c)). Besides, the contour line value near the centre in figure 6.2(a), i.e., '-0.4', is more negative, compared to that from the other two cases (see figure 6.2(b), (c)), i.e., '-0.36' and '-0.36'. The notable difference between result in figure 6.2(a) and results of the other two cases in figure 6.2(b), (c) can be directly attributed to the impact of shape of step junction, that is to say, the round step junction can help mitigate reverse velocity near the step on large cylinder side. In addition, the mild difference between 3rd case and 5th case in figure 6.2(b), (c) is believed to be related to

the Reynolds number impact. In order to make a quantitative comparison among three testing cases, we extract useful parameters from relevant contour lines from figure 6.2(a), (b), (c) and establish the relationship between the area enveloped by a specified contour line and the corresponding contour line value as shown in figure 6.3.
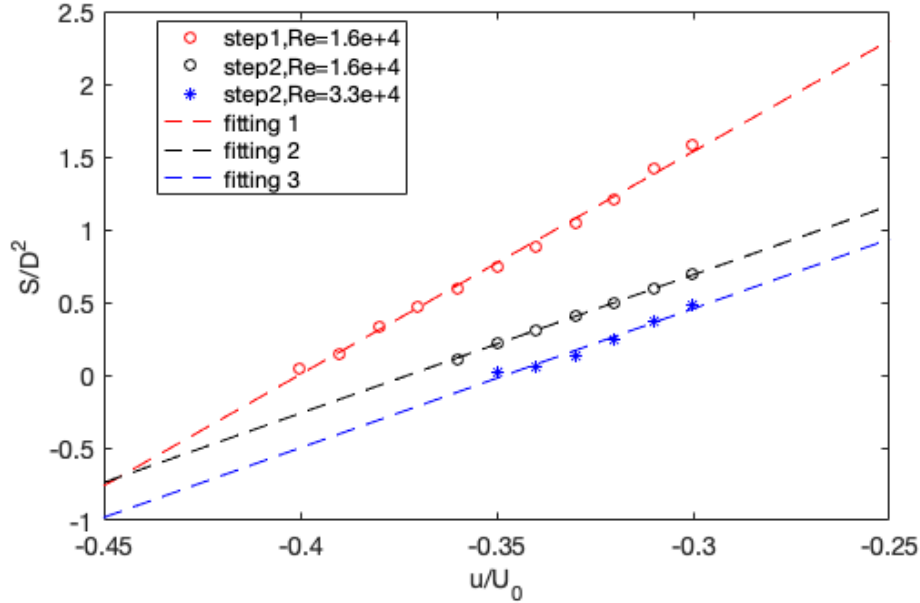
Figure 6.3 Normalized area (S/D^2) of 'negative velocity rings' vs. 'contour line value' (u/U_0).

Table 6.1 Summary of fitted lines.

Fitted line (1st case)	Fitted line (3rd case)	Fitted line (5th case)
$\dfrac{S}{D^2} = 6.13 + 15.31 \times \dfrac{u}{U_0}$	$\dfrac{S}{D^2} = 3.54 + 9.52 \times \dfrac{u}{U_0}$	$\dfrac{S}{D^2} = 3.33 + 9.57 \times \dfrac{u}{U_0}$

In figure 6.3, the horizontal axis stands for contour line value (u/U_0) and the vertical axis represents the normalized area (S/D^2). The normalized area shows a clear linear growth trend with the increase of contour line value. Besides, linear fit for three cases are processed and exhibited in figure 6.3, followed by the present of corresponding empirical formulas in table 6.1. Considering the comparison of slopes of fitted lines, the slope for 1st case is the largest, i.e., 15.31. Whilst, slopes for the other two cases (3rd case and 5th case) are comparable to each other, i.e., 9.52 and 9.57 respectively. Corresponding results indicate that the slope is dependent on shape of step junction (*S step* or *R step*), rather than the Reynolds number. Besides, a deduction can be given that the slope corresponds to velocity variation, revealing a more sensitive velocity behind sharp step junction (*S step*) than that behind round step junction (*R step*).

(a): 1st case, *S step*, *Re* = 1.6e+4;

(b): 3rd case, *R step*, *Re* = 1.6e+4;

(c): 5th case, *R step*, *Re* = 3.3e+4;

(d)
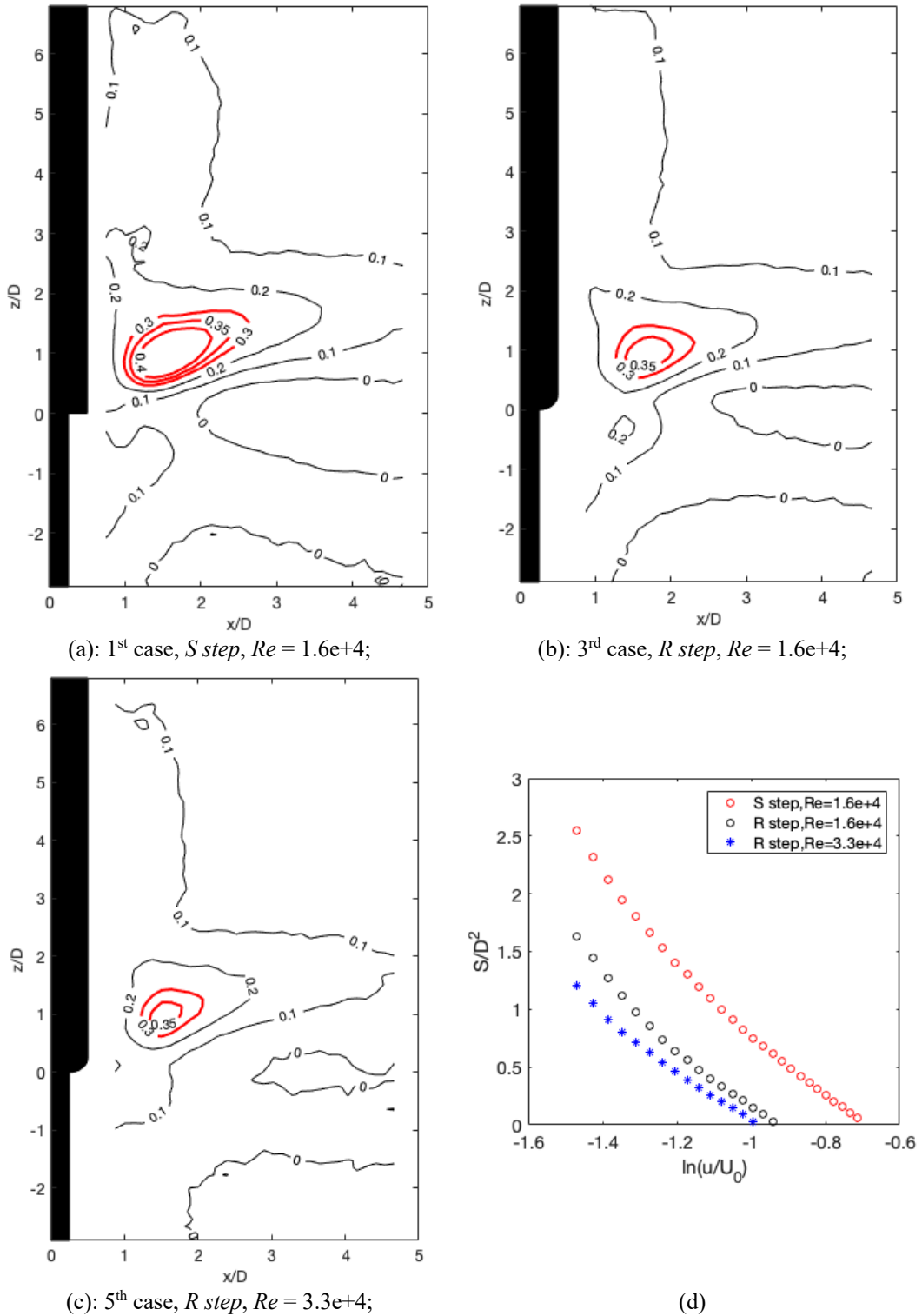
Figure 6.4 Contours of mean spanwise velocity along Plane Y = 0*D* (a, b, c) and normalized area (S/D^2) of 'PSV' region (positive spanwise velocity) vs. 'contour line value ($\ln(u/U_0)$)' (d).

Mean spanwise velocity contours for three cases can be summarized in figure 6.4(a) -(c). The positive spanwise velocity region significantly turns up behind the step junction (Hereinafter referred to as 'PSV' region) as marked in figure 6.4(a) –(c) with red contour lines. This 'PSV' region gradually decreases its value meanwhile splits into two branches, one of which climbing along the rear side of large-diameter cylinder affects the recirculation zone, another of which goes downstream. Focus on the comparison of 'PSV'

region area in figure 6.4(a) –(c) and set the contour line of '0.3' as the benchmark. The significant different size of the area enveloped by the contour line of '0.3' in figure 6.4(a) and figure 6.4(b) indicate the impact of shape of step junction. Besides, the impact of Reynolds number can also be perceived from figure 6.4(b) and figure 6.4(c), but not comparable to that of shape of step junction. In line with the guidance from figure 6.3, the relationship between the contour line value and the corresponding area size can be quantitatively studied as shown in figure 6.4(d). The horizontal axis stands for contour line value ($\ln(u/U_0)$), and the vertical axis stands for the corresponding normalized area (S/D^2). The result behind S $step$ (1st case) has the higher size at all the selected contour line values, and the maximum contour line value for 1st case is bigger than the other two cases. As for the impact of Reynolds number, it could be studied by comparing 3rd case with 5th case, that results of these two cases share the similar trend, but with a small displacement regarding 'S/D^2'.

(a)   (b)   (c)
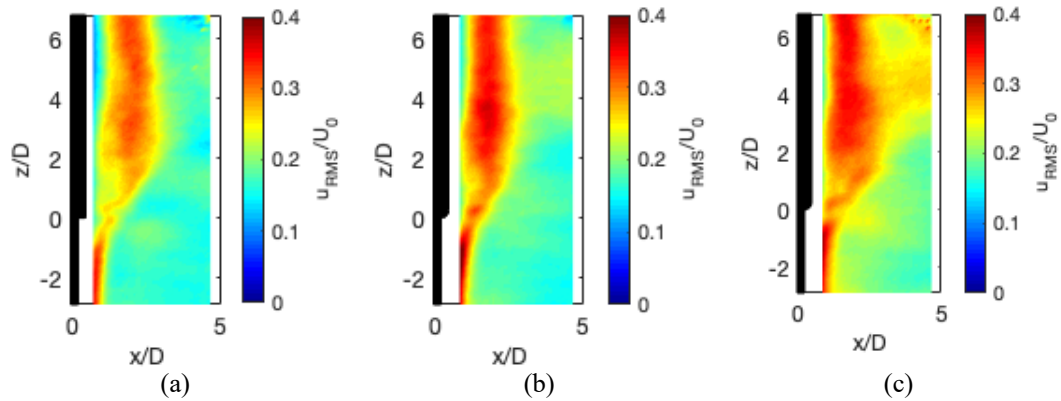
Figure 6.5 Contours of streamwise velocity (rms) in the wake (Plane Y = 0D).

Note: (a): 1st case, S $step$, Re = 1.6e+4; (b): 3rd case, R $step$, Re = 1.6e+4; (c): 5th case, R $step$, Re = 3.3e+4.

(a)   (b)   (c)
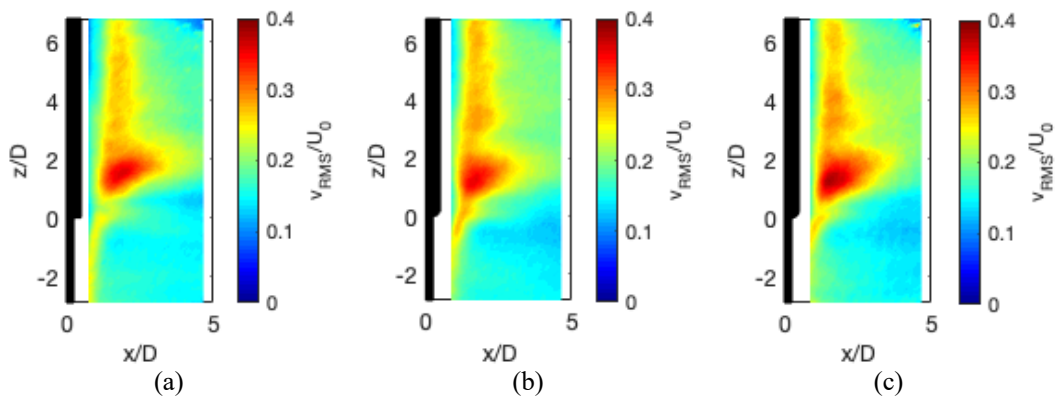
Figure 6.6 Contours of spanwise velocity (rms) in the wake (Plane Y = 0D).

Note: (a): 1st case, S $step$, Re = 1.6e+4; (b): 3rd case, R $step$, Re = 1.6e+4; (c): 5th case, R $step$, Re = 3.3e+4.

Figure 6.5 and figure 6.6 depict contours of rms value of streamwise / spanwise velocity fields from three involved cases. Obviously, streamwise velocity contours in figure 6.5 share similar characteristics, that the reduction of rms value near step junctions, as well as the enhancement away from the junctions. When it comes to the spanwise velocity (see figure 6.6), it could be found among the three graphs, that high rms value region exists behind step junctions at the large-diameter cylinder's side.

This section gives a comprehensive discussion on averaged velocity field at the central plane (Plane Y = 0D) behind step cylinders, involving three cases (1st case, 3rd case, 5th case). Impact of shape of step junction, as well as the Reynolds number, are concerned. It has been proved that the addition of step junction can significantly affect averaged flow fields right behind step cylinders (Rafati, 2014; Teutsch, 2012). For instance, the recirculation zone behind large cylinder is enlarged. 'Negative streamwise velocity (NSV)' region and 'positive spanwise velocity (PSV)' region can be well discerned behind step junctions, the former of which was called as 'back flow region' by Teutsch (2012). In addition, the rms value of spanwise velocity displays a significant increase behind step junctions. The discrepancy of results from 1st case and 3rd case reveals the impact of shape of step junction. Size of 'NSV' region and 'PSV' region being significantly reduced behind the round step junction (*R step*) indicates that round step junction contributes to relieving velocity disorder behind the step.
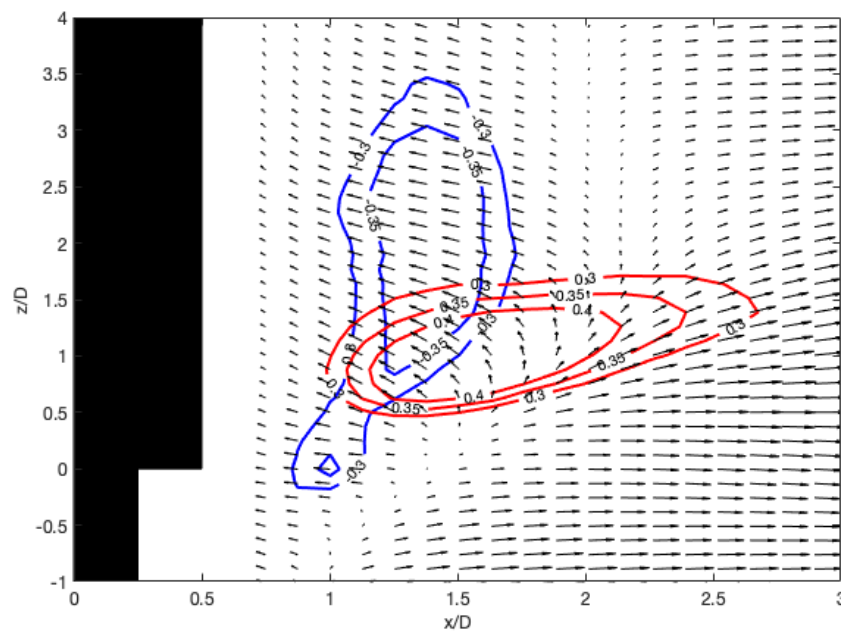
Figure 6.7 Relation among 'NSV' region (Blue solid lines), 'PSV' region (Red solid lines) and the velocity vector fields (1st case, *S step*, *Re* = 1.6e+4).

Lastly, an important term is mentioned, namely 'downwash', which goes over the step junction and into the near wake of large cylinder. It can also be observed near ends of finite length cylinders with free ends (Zdravkovich, et al., 1989). According to previous publications (Dunn & Tavoularis, 2006), the 'downwash' can be used to explain the formation of 'N-cell' for step cylinders. For the current part, the 'NSV' region and 'PSV' region can also be linked with 'downwash'. Figure 6.7 depicts the averaged velocity vector field behind the step junction (1st case, *S step*, *Re* = 1.6e+4), together with the relevant 'NSV' region (marked with blue lines) and 'PSV' region (marked with red lines). From the velocity vector field, one can clearly observe the spanwise flow (equivalent to 'downwash') behind the step, which is outstanding at the region enveloped by red contour line '0.4'. This spanwise flow is comparable to the so-called 'inflow' which was narrated by Zdravkovich, et al. (1989). This spanwise flow goes through 'PSV' region and 'NSV' region successively, indicating a strong relationship. If the 'downwash' directly gives rise to the formation of 'NSV' region and 'PSV' region, we can infer that the size of these two regions is determined by the strength of 'downwash'. Consequently, a conclusion can be made that 'downwash' behind round step junction (*R step*) is weaker than that after sharp step junction (*S step*).

6.2 Spatial Energy Fields

Analysis on streamwise velocity spectra is under fully discussion in Chapter 5, to characterise different types of vortex shedding in the wake of step cylinders, for instance, the constant frequency of vortex-shedding cells (viz. L-cell, N-cell, S-cell), averaged cell boundaries, etc. This section continues to investigate streamwise velocity spectrum with the emphasis on spectral amplitude. As the amplitude of the velocity spectrum can be processed into diverse forms, for instance, energy information, power information, PSD (power spectral density), etc., this section choses the energy amplitude (E_{uu}), to represent the energy contribution of a given streamwise velocity signal.
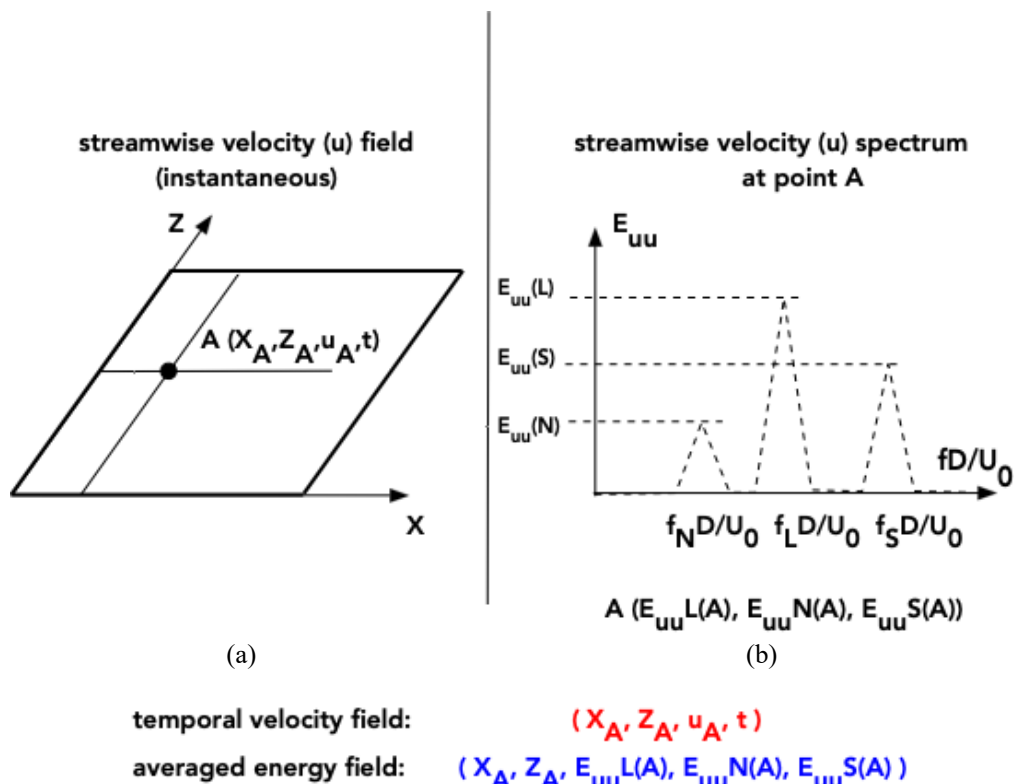
Figure 6.8 Schematic sketch of the construction of spatial energy field.

Subsequently, the averaged energy field (based on streamwise velocity) is constructed by extracting the energy information from relevant spectrum and associating it with its spatial location, all of which can be explained with the assistance of schematic sketches shown in figure 6.8. Providing that we have the ensemble of instantaneous streamwise velocity field (such as 3000 samples), the velocity at point A at a certain instant of time (see figure 6.8(a)) can be expressed as (x_A, z_A, u_A, t), and meanwhile, the streamwise velocity spectrum at point A can be obtained (see figure 6.8(b)). Consider the fact that three dominant frequencies corresponding to L-cell, N-cell and S-cell co-exist in the wake of step cylinders. We can figure out and mark these three dominant frequencies from the

streamwise velocity spectrum at Point A in figure 6.8(b), namely $f_L D/U_0$, $f_N D/U_0$, $f_S D/U_0$. The amplitude of three frequency peaks, namely $E_{uu}(L)$, $E_{uu}(N)$ and $E_{uu}(S)$, can be picked out and specified as the averaged energy at Point A. Consequently, the averaged energy field can be constructed by associating with coordination of point A; the corresponding mathematic expression is (x_A, x_A, $E_{uu}L(A)$, $E_{uu}N(A)$, $E_{uu}S(A)$).

(a): Re = 1.6e+4;

(b): Re = 3.3e+4;
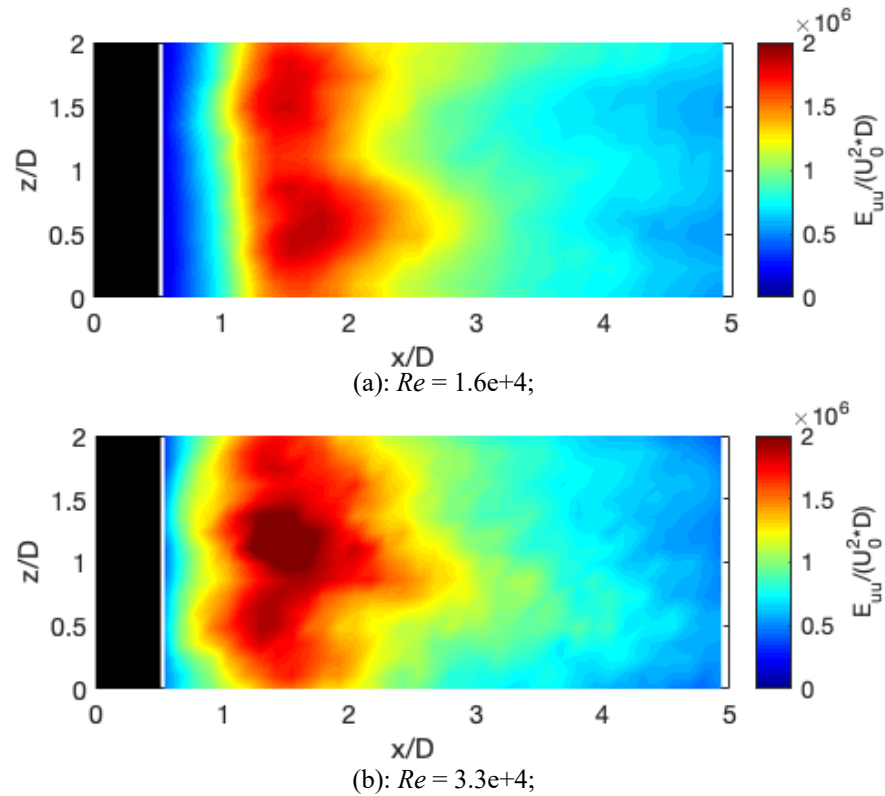
Figure 6.9 E_{uu} contours behind the plain cylinder at Plane Y = -0.6D.

Averaged energy contour associated with single dominant shedding frequency behind the plain cylinder at the Reynolds number of 1.6e+4 and 3.3e+4 is presented in figure 6.9. The horizontal axis and vertical axis denote streamwise normalized distance and the location along the span respectively. The colormap stands for the normalized energy amplitude. In figure 6.9(a), (b), the trend of energy varying downstream at the Reynolds number of 1.6e+4 and 3.3e+4 is similar, being evenly distributed along the span. For a certain cross-section, the energy trend reaches the peak approximately at x/D = 1.5, followed by it decaying downstream. Consequently, the energy layout behind step cylinders can be processed using the same method. It should be noted that three dominant frequencies co-exist in the wake, resulting in three different energy contours for each experimental case namely $E_{uu}(L)/(U_0^2 * D)$, $E_{uu}(N)/(U_0^2 * D)$, $E_{uu}(S)/(U_0^2 * D)$, corresponding to three vortex cells (L-cell, N-cell and S-cell).

(a): L-cell   (b): N-cell   (c): S-cell
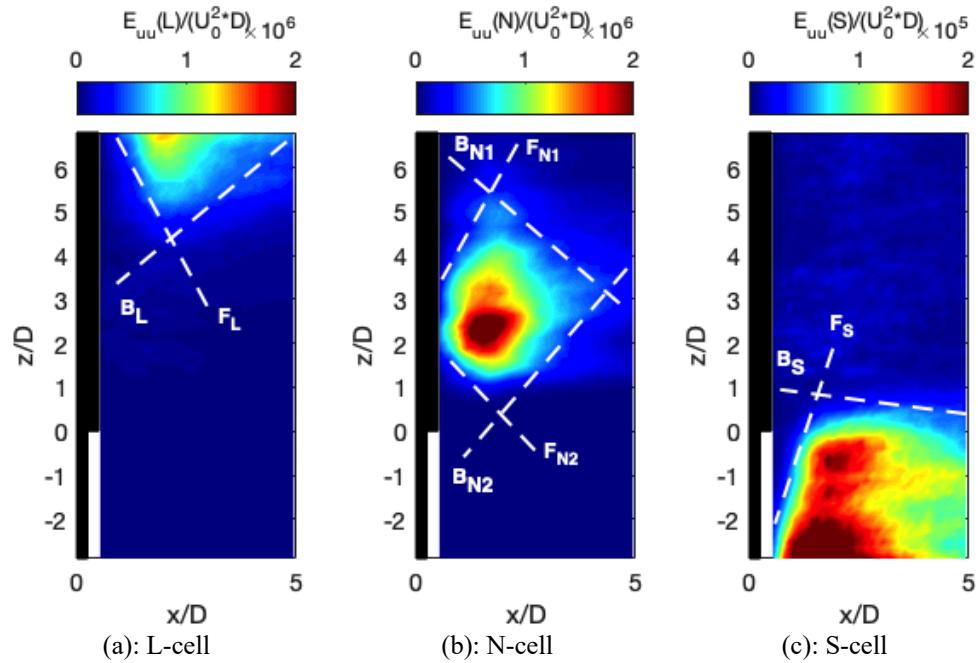
Figure 6.10 Energy contours behind sharp step cylinder at Plane Y = -0.6D (2nd case, *S step*, *Re* = 1.6e+4).

Figure 6.10 depicts the averaged energy contour regarding three vortex cells from 2nd case (*S step*, *Re* = 1.6e+4), and corresponding results from 4th case and 6th case are presented in figure 6.11. It is obvious that averaged energy distribution show similar trend for three cases. The bright colour part (red, yellow, green) in figure 6.10, 6.11 highlights high energy region, i.e., the area where vortex-shedding cell is strongly active, suggesting that the N-cell ($E_{uu}(N)$) is the most active along this plane. It could also be found that three regions with high energy are staggered along the span, in agreement with velocity spectral analysis results in figure 5.5. Apart from that, one could decern the outline of three 'high energy region' in figure 6.10 differs with each other, as well as that in figure 6.11. In order to clearly interpret, six white dash lines are manually added in figure 6.10 where the capital letters ('F', 'B') and subscripts ('L', 'N1', 'N2', 'S') denote front / back board and three vortex cells (L, N, S). $E_{uu}(S)$ nearly takes up the entire span of small-diameter cylinder, and its left border (F_S) is inclined against the cylinder axis suggesting a slanting vortex shedding phenomenon. Besides, its non-uniform distribution along the span reveals (see the border B_S) the energy defect near the step junction. $E_{uu}(N)$ is behind the large-diameter cylinder near the step junction, i.e., at the region of 2 < z/D < 3, 1 < x/D < 3. the left border of $E_{uu}(N)$ bends away from the cylinder at both sides (see the border F_{N1} and F_{N2}), and both ends of the right side (see the border B_{N1} and B_{N2}) indicate the occurrence of significant energy defect roughly at z/D = 1.5, z/D = 3.5. The bending left border of $E_{uu}(L)$, together with its non-uniform energy layout along the span, can also be recognized. In summary, the inclined left border for each cell and the 'energy defect' can be inferred to relate to the interaction between neighbouring cells.
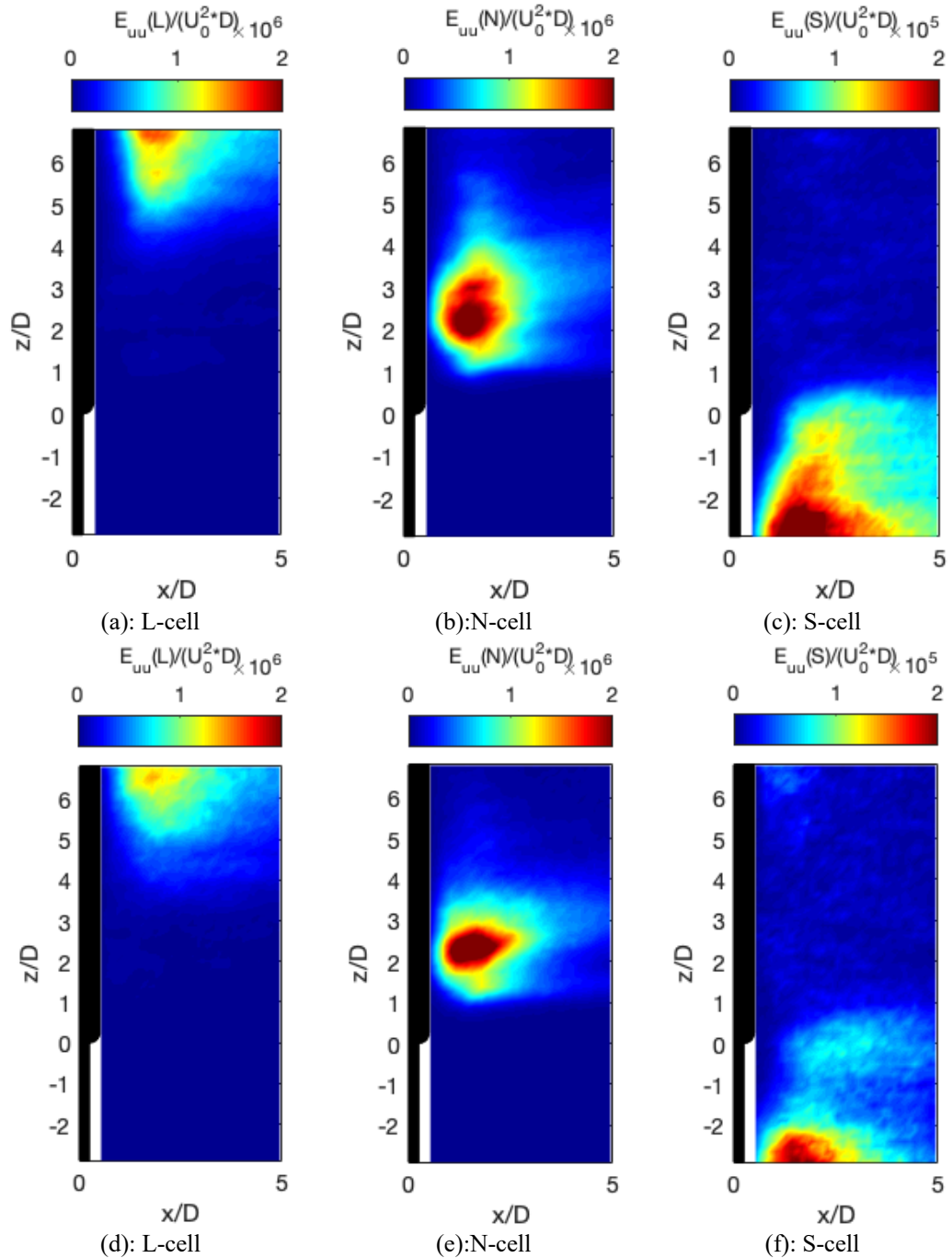
Figure 6.11 Energy contours behind round step cylinders at Plane Y = -0.6*D*. (a), (b), (c): 4th case, *R step*, *Re* = 1.6e+4; (d), (e), (f): 6th case, *R step*, *Re* = 3.3e+4.

The spatial energy layout behind round step cylinders is processed in the same method and shown in figure 6.11. Comparing with that behind sharp step cylinder, one could perceive similar phenomenon, for instance the staggered spanwise distribution, slanting front boarder and back boarder, and energy defect. The extent of $E_{uu}(N)$ along the span is shorter in 6th case than the other two, which is in agreement with the discussion about N-cell extent variation (see figure 5.13). In order to quantify the difference of 'energy region' regarding different vortex cells in different testing cases, the term of averaged energy decay is introduced, and presented via figure 6.12.

(a)   (b)
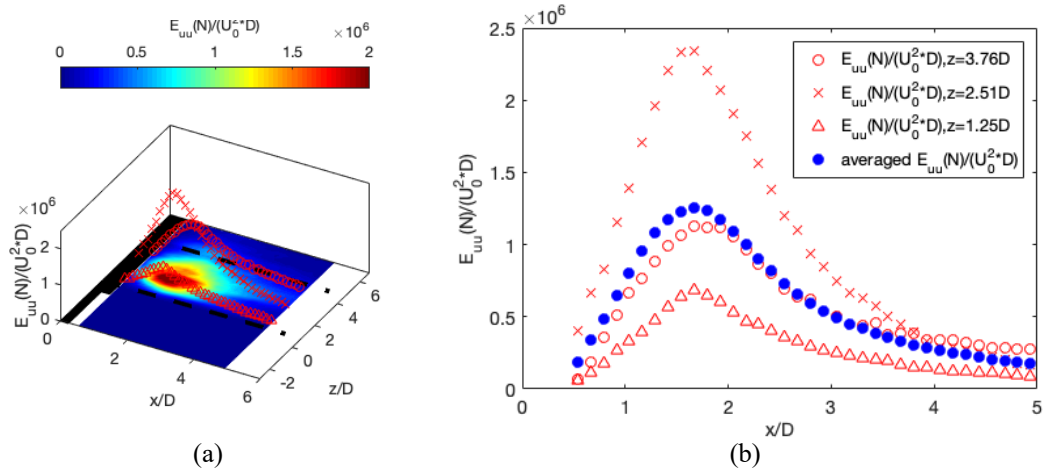
Figure 6.12 Explanation about averaged energy decay.

Note: (a): $E_{uu}(N)$ contour behind step cylinder (Plain $Y = -0.6D$); Black dash line: N-cell boundary; Red circles / Red crosses / Red triangles: $E_{uu}(N)$ variation at cross-sections ($z/D = 3.76, 2.51, 1.25$); (b): $E_{uu}(N)$ variation at selected cross-sections, and averaged $E_{uu}(N)$ variation.

Table 6.2 Summary of averaged cell location.

	2nd case (S step, Re = 1.6e+4)	4th case (R step, Re = 1.6e+4)	6th case (R step, Re = 3.3e+4)
L-cell	$4.77 < z/D < 6.77$	$4.64 < z/D < 6.77$	$4.14 < z/D < 6.77$
N-cell	$0.87 < z/D < 4.64$	$0.75 < z/D < 4.52$	$0.75 < z/D < 4.01$
S-cell	$-3.0 < z/D < 0.75$	$-3.0 < z/D < 0.62$	$-3.0 < z/D < 0.62$

For the averaged energy decay, take figure 6.10(b) as an example and place the emphasis on $E_{uu}(N)$ variation along the streamwise direction. At a certain spanwise location (e.g., $z/D = 2.51$), $E_{uu}(N)$ rises downstream dramatically till reaching its maximum value at x/D = 1.668 ($E_{uu}/U_0^2*D = 2.345e+6$); subsequently, it presents a gentle decrease. The energy variation at three cross-sections, i.e., $z/D = 3.76, 2.51, 1.25$, is plotted in figure 6.12(a), suggesting the maximum value as well as the decrease rate is different for each cross-section. Consequently, the new term namely 'averaged energy variation', can be obtained by averaging all the streamwise energy variation between two cell boundaries. Thus, we can have the mean energy variation of $E_{uu}(N)$ from figure 6.12(a) by averaging all relevant curves between cell boundaries (black dash lines), and present it in figure 6.12(b), marking as blue solid spots.
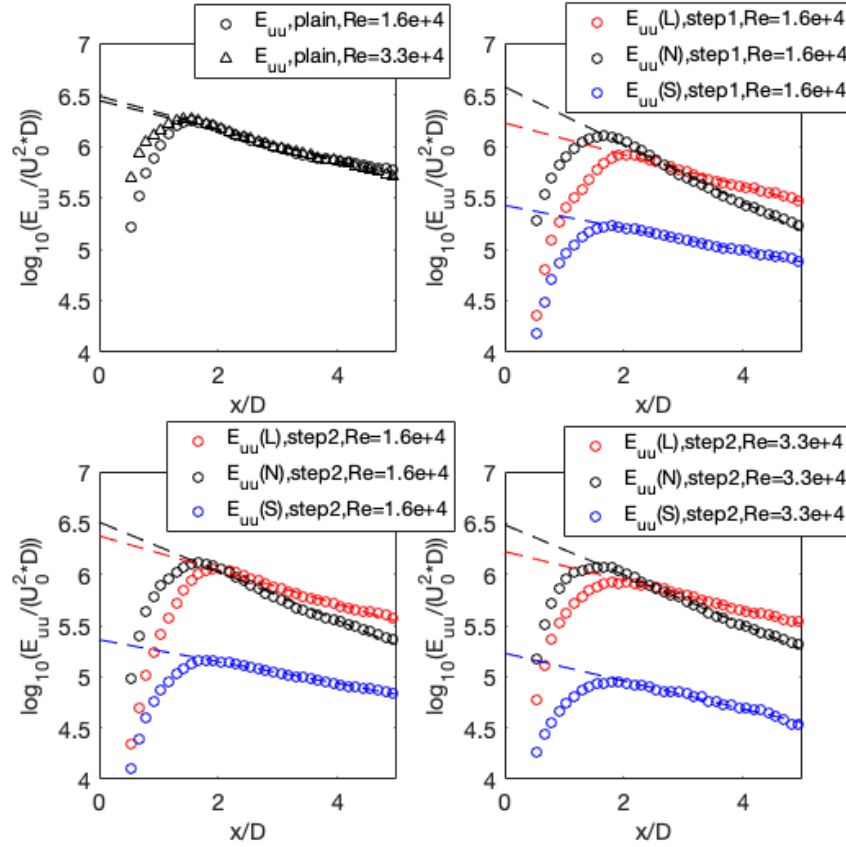
Figure 6.13 Averaged Energy decay comparison.

Note: (a): Plain cylinder, Plane Y = -0.6D; (b): 2nd case, $S step$, Plane Y = -0.6D;
(c): 4th case, $R step$, Plane Y = -0.6D; (d): 6th case, $R step$, Plane Y = -0.6D.

Table 6.3 Summary of energy peak properties*.

	Model	Re	$E_{uu}(L)$ [X, Y]	$E_{uu}(N)$ [X, Y]	$E_{uu}(S)$ [X, Y]	E_{uu} [X, Y]
2nd case	$S step$	1.6e+4	[2.05, 5.91]	[1.67, 6.1]	[1.79, 5.22]	
4th case	$R step$	1.6e+4	[2.05, 6.05]	[1.67, 6.1]	[1.79, 5.16]	
6th case	$R step$	3.3e+4	[2.05, 5.92]	[1.67, 6.1]	[1.92, 4.95]	
Reference	Plain cylinder	1.6e+4				[1.54, 6.24]
Reference	Plain cylinder	3.3e+4				[1.42, 6.27]
Note:			* the peak properties include the normalized location (*X*) where highest energy takes place, and the highest value (*Y*), i.e., $log_{10}E_{uu}/(U^2_0*D)$.			

The averaged energy variation for all cases can be obtained in the same way and summarized in figure 6.13. It should be noted that the vertical axis is converted to logarithmic form in figure 6.13, for better fit performance. Firstly, all involved cases share the similar trend, that is, the energy increases downstream and reaches the peak before decreasing at nearly constant rate. Information about the corresponding peaks, i.e., the position and its vertical value, varies at different vortex-shedding cells of different cases, all of which are summarized in table 6.3. For the reference cylinder, i.e., the plain cylinder, the maximum energy roughly being 6.25 happens at approximately x/D = 1.5. Peak of N-cell of the other three cases takes place at the nearest location (x/D = 1.67), followed by

that of the L-cell occurring at the furthest location ($x/D = 2.05$). The peak of S-cell being located at $x/D \approx 1.85$ has the weakest energy value at roughly 5.1.

In order to quantitatively interpret the energy decay after peaks, the samples after the peak of each trend is used to do linear fit. All corresponding fitted lines are added to figure 6.13. It should be noted that linear fit for the current study based on 'the samples after the peak' may show slight difference from that based on less samples (for instance 20 samples), but still keep similar trend for further evaluation. It can be inferred that the similar trend of all fitted lines reveals the inherent characteristic of vortex shedding from cylinders. Besides, another two terms namely the 'energy decay rate' (short for EDR) and the 'energy decay shift' (short for EDS), are introduced, the former of which is defined as the absolute slope of fitted lines and the latter of which is the intersection of fitted lines and the vertical axis. EDR and EDS extracted from the above-mentioned fitted lines is believed to present better physical description; corresponding useful data is summarized in table 6.4 and table 6.5.

Table 6.4 Summary of energy decay rate (EDR)*.

	Model	*Re*	EDR(L)	EDR(N)	EDR(S)	EDR (**)
2nd case	*S step*	1.6e+4	0.153	0.280	0.109	
4th case	*R step*	1.6e+4	0.166	0.240	0.106	
6th case	*R step*	3.3e+4	0.141	0.243	0.136	
Reference	Plain cylinder	1.6e+4				0.145
Reference	Plain cylinder	3.3e+4				0.159

Note:　　　* EDR: the absolute slope of fitted lines shown in figure 6.13.
　　　　　　**: based on the only one dominant frequency after uniform cylinder

Table 6.5 Summary of energy decay shift (EDS)*.

	Model	*Re*	EDS(L)	EDS(N)	EDS(S)	EDS (**)
2nd case	*S step*	1.6e+4	6.224	6.575	5.424	
4th case	*R step*	1.6e+4	6.373	6.508	5.360	
6th case	*R step*	3.3e+4	6.220	6.482	5.229	
Reference	Plain cylinder	1.6e+4				6.443
Reference	Plain cylinder	3.3e+4				6.485

Note:　　　* EDS: the intersection of fitted lines and the vertical axis shown in figure 6.13.
　　　　　　**: based on the only one dominant frequency behind the plain cylinder

Considering the EDR in table 6.4, one can find that EDR of L-cell and S-cell for all cases (2nd case, 4th case, 6th case), as well as EDR for reference cases, keeps stable; the median of all involved EDR is 0.143. However, the EDR of N-cell of three cases is 0.280, 0.240 and 0.243 respectively, which outstandingly surpasses the others. Explanation about results of EDR is following. Vortex shedding in terms of L-cell and S-cell takes place quite away from step junctions, which can be equivalent to that from plain cylinders. Consequently, the EDR of L-cell and S-cell behind step cylinders are quite comparable to that of plain cylinders. However, the 'N-cell' being a 'new-born' vortex-shedding cell behind the large-diameter cylinder near the step junction is a different vortex-shedding

cell from normal ones (i.e., L-cell, S-cell and that behind uniform cylinders), indicating a different EDR with higher amplitude and higher energy decay.

The EDS in table 6.5 seems to be linked with the evaluation of entire energy of a certain vortex-shedding cell in the wake. One can find EDS value behind large-diameter cylinders (L-cell, N-cell) and that behind reference cylinder is close, the median of which is 6.4625, higher than that of S-cells. An acceptable explanation can be given by considering the distance between the plane (Plane Y = -0.6D) and the models. It is true that all data are collected at Plane Y = -0.6D. However, the normalized value based on large diameter (D) and small diameter (d) is different, which is equivalent to Plane Y = -1.2d. Consequently, a relevant far distance for small cylinder give rises to the lower energy of S-cells, i.e., a lower EDS.

6.3 Dynamic Velocity Fields

This section implements POD-based analysis to gain deep insight upon velocity fields behind sharp step cylinder and round step cylinder to expose more characteristics of vortex-shedding cells (L-cell, N-cell and S-cell). During the process, instantaneous velocity fields in the wake are reconstructed by only taking three above-mentioned vortex cells into consideration, to present clear vortex interaction. Investigation on dynamic vortex interaction from three testing cases namely 2nd case, 4th case, 6th case, reveals the difference from that at laminar state, as well as the impact of shape of step junction.

POD-based analysis

Methodology in terms of POD has been comprehensively introduced in Chapter 3 and has been successfully applied to plain cylinders in section 4.3. Consequently, this part directly applies POD to velocity fields behind step cylinders to figure out more information about the fluid 'ingredients' namely, bases of the original velocity fields. The obtained bases corresponding coherent structures in turbulent flow can also be termed as POD modes ordered by the weight or the energy (Morton, 2014). Figure 6.14 makes a summary of POD results about the first 10 POD modes from three experimental cases. Each case employs a total of 3000 snapshots along Plane $Y = -0.6D$ to do POD processing in the same way as that for the plain cylinder. One can observe the first 4 POD modes (1st mode, 2nd mode, 3rd mode and 4th mode) for three cases are higher in energy contribution than that after 4th mode. The comparison between 2nd case and 4th case shows the sum of first 4 modes for 4th case has more energy contribution. In other words, the energy of velocity fields for 4th case is more concentrated within lower order of POD mode, concluding that round step junction in 4th case successfully mitigates the perturbation behind the step junction. Besides, according to the significant reduction of energy contribution of first 4 modes for 6th case, it can be deduced that more energy transfers from lower POD modes to higher POD modes subject to the increase of Reynolds number.
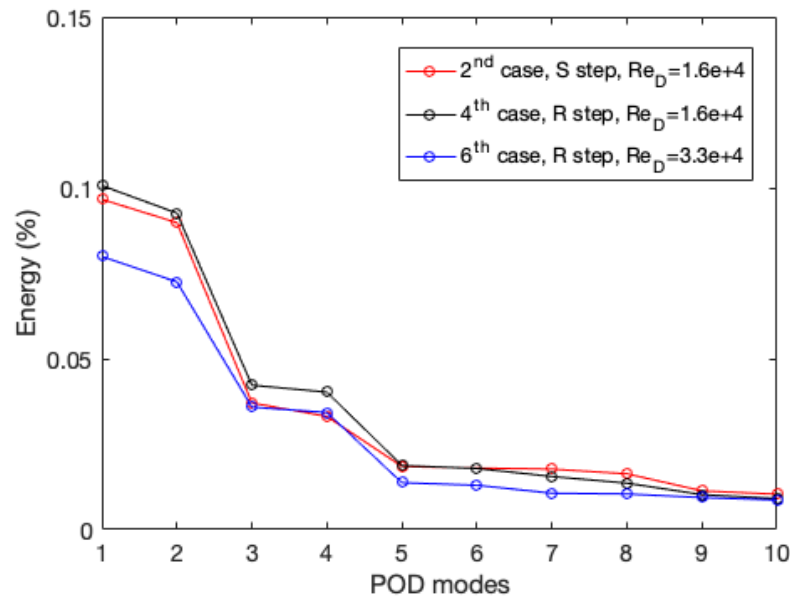
Figure 6.14 Relationship between energy percentage and POD modes.

Table 6.6 Summary of energy and spectral analysis (step cylinders).

		1st mode	2nd mode	3rd mode	4th mode	5th mode	6th mode	7th mode	8th mode
2nd case	Energy	9.66%	8.98%	3.71%	3.31%	1.85%	\	1.77%	\
	fD/U_0	0.1725	0.1725	0.2025	0.2025	0.415	\	0.415	\
4th case	Energy	10.1%	9.26%	4.23%	4.02%	1.87%	1.79%	\	\
	fD/U_0	0.18	0.18	0.2025	0.2025	0.4225	0.4225	\	\
6th case	Energy	8%	7.25%	3.6%	3.4%	\	\	1.1%	1%
	fD/U_0	0.1738	0.1738	0.1988	0.1988	\	\	0.3937	0.3937

Table 6.6 makes a short summary about the energy distribution of each mode, as well as the normalized frequency which is calculated based on time series of mode coefficient. The normalized frequency shown in table 6.6 can be used to establish a link between POD modes and vortex-shedding cells. More specifically, vortex-shedding cells having constant frequencies can be related to POD modes with identical frequencies. A combined study on table 5.2 and table 6.6 confirms that L-cell is in relation to 3rd mode, 4th mode for all three cases, and N-cell to 1st mode, 2nd mode. The POD modes regarding S-cell is different for 2nd case, 4th case, and 6th case, namely 5th / 7th modes, 5th / 6th modes and 7th / 8th modes respectively. The discrepancy in S-cell POD modes is due to energy contribution of 5th mode, 6th mode, 7th mode and 8th mode being comparable to each other. The forthcoming part presents graphs (figure 6.15 –figure 6.23) of POD results for three vortex cells from three cases, regarding contours of normalized POD modes, time series of mode coefficient and spectral analysis.

(a): 1st mode   (b): 3rd mode   (c): 5th mode

(d): 2nd mode   (e): 4th mode   (f): 7th mode
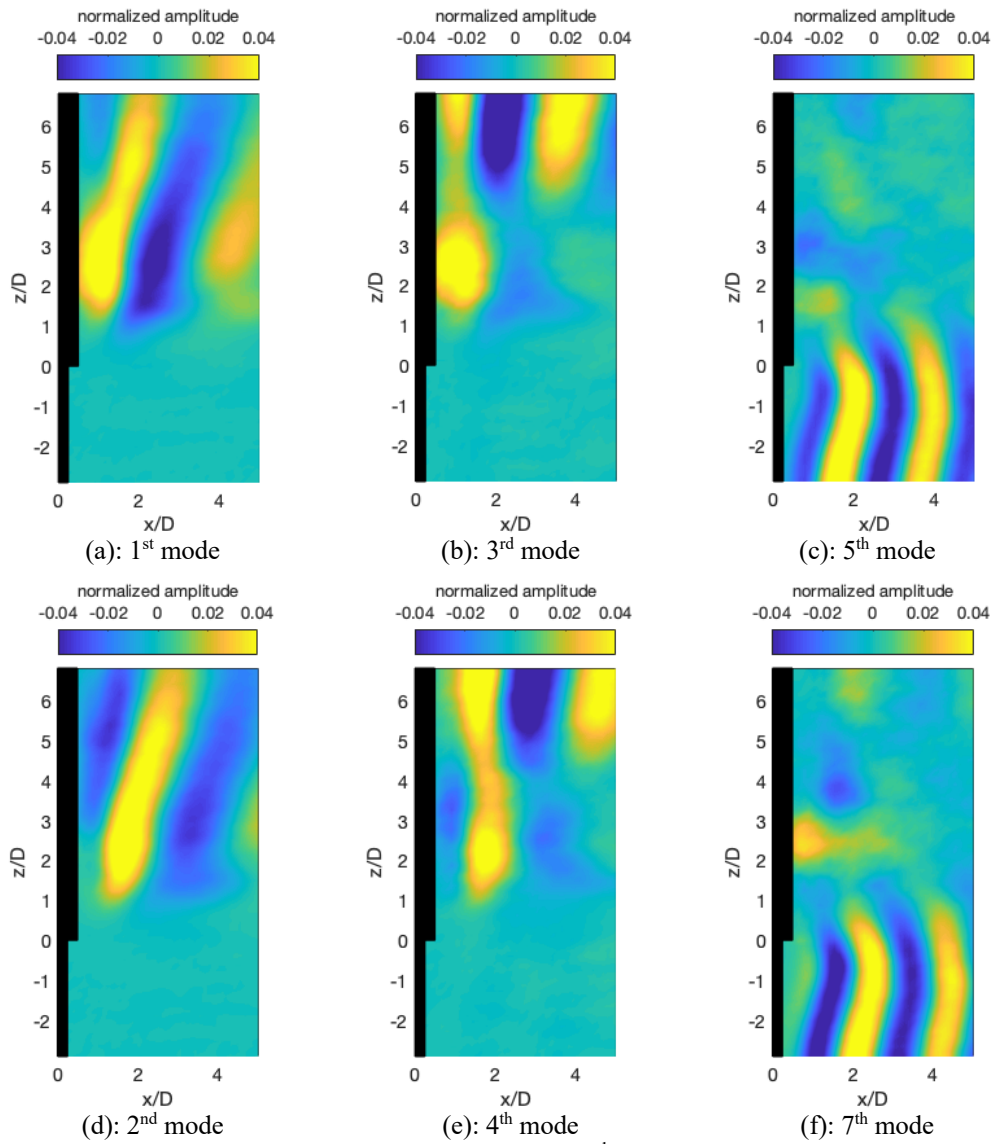
Figure 6.15 Contours of three pairs of POD mode for 2nd case.

(a): 1st mode   (b): 3rd mode   (c): 5th mode

(d): 2nd mode   (e): 4th mode   (f): 7th mode
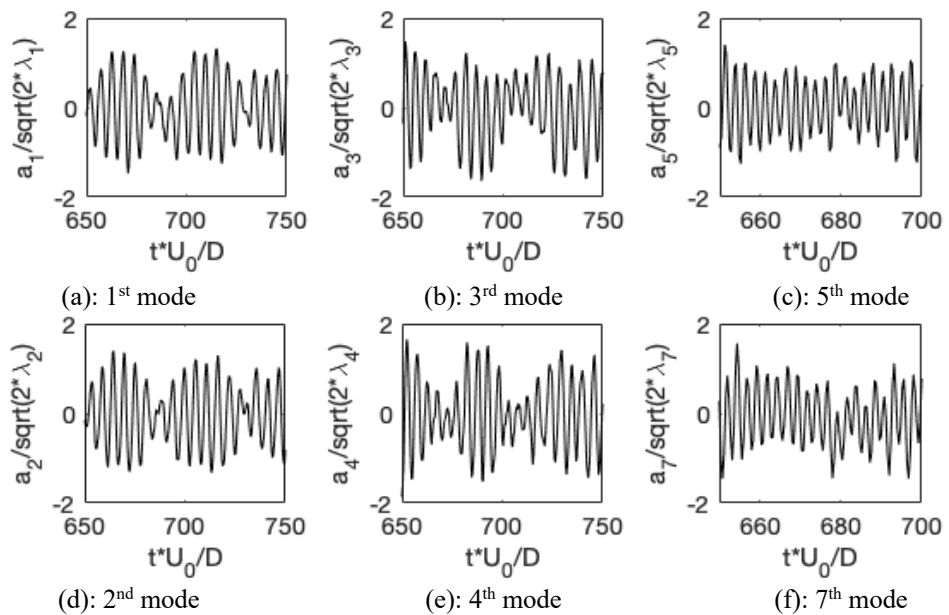
Figure 6.16 Time series of mode coefficients for 2nd case.
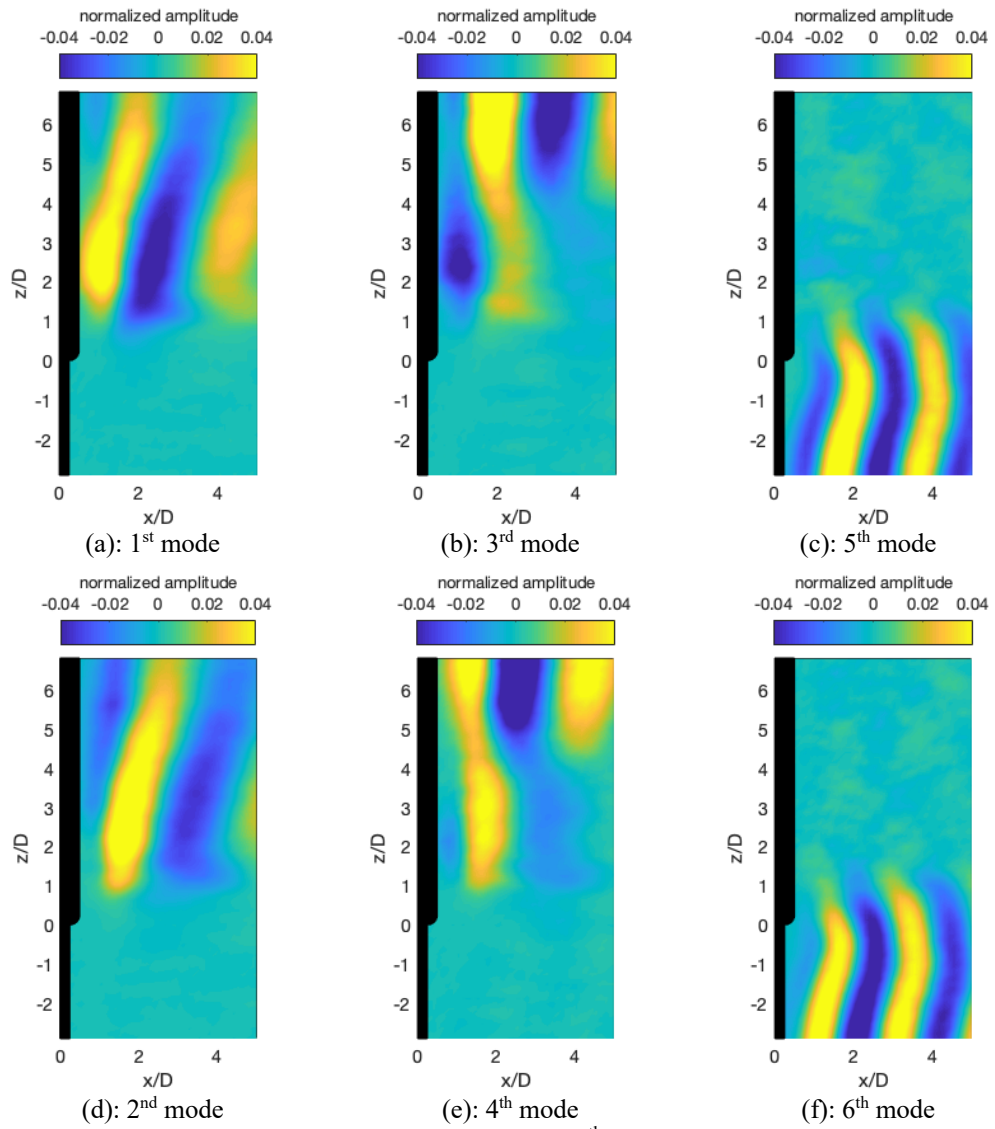
Figure 6.17 Contours of three pairs of POD mode for 4th case.
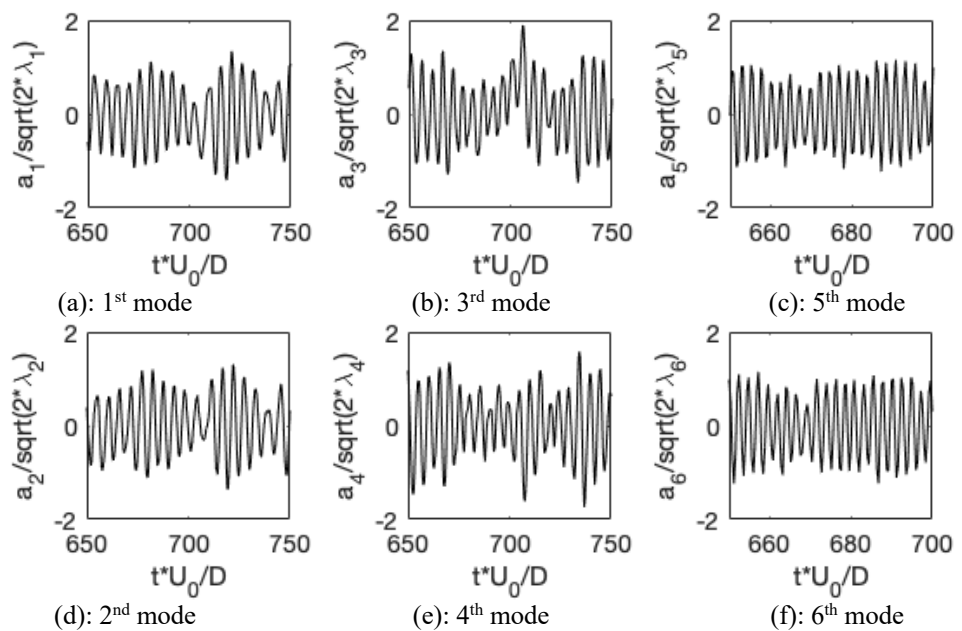
Figure 6.18 Time series of mode coefficients for 4th case.

(a): 1st mode   (b): 3rd mode   (c): 7th mode

(d): 2nd mode   (e): 4th mode   (f): 8th mode
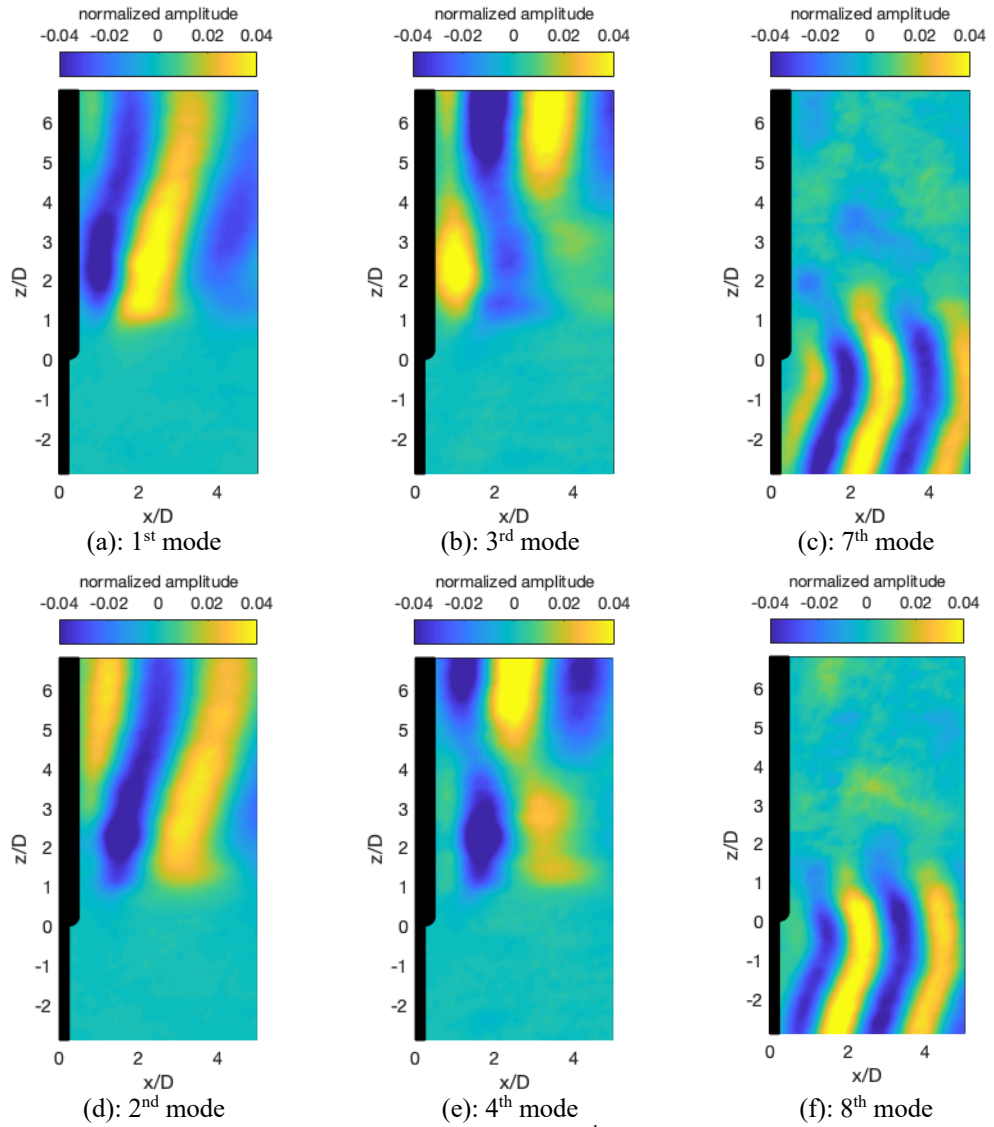
Figure 6.19 Contours of three pairs of POD mode for 6th case.

(a): 1st mode   (b): 3rd mode   (c): 7th mode

(d): 2nd mode   (e): 4th mode   (f): 8th mode
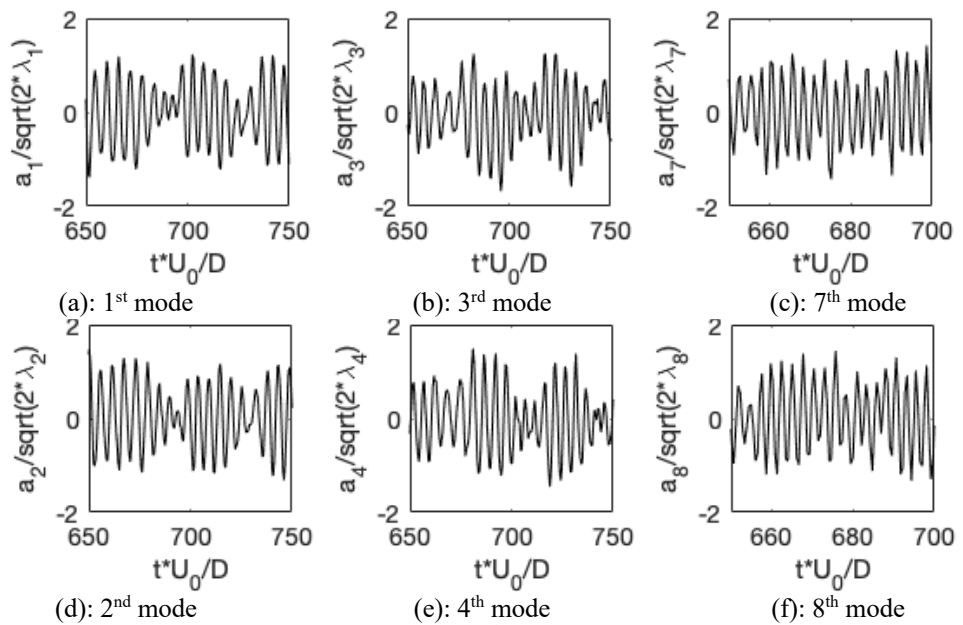
Figure 6.20 Time series of mode coefficients for 6th case.

(a): 1st mode   (b): 3rd mode   (c): 5th mode
(d): 2nd mode   (e): 4th mode   (f): 7th mode
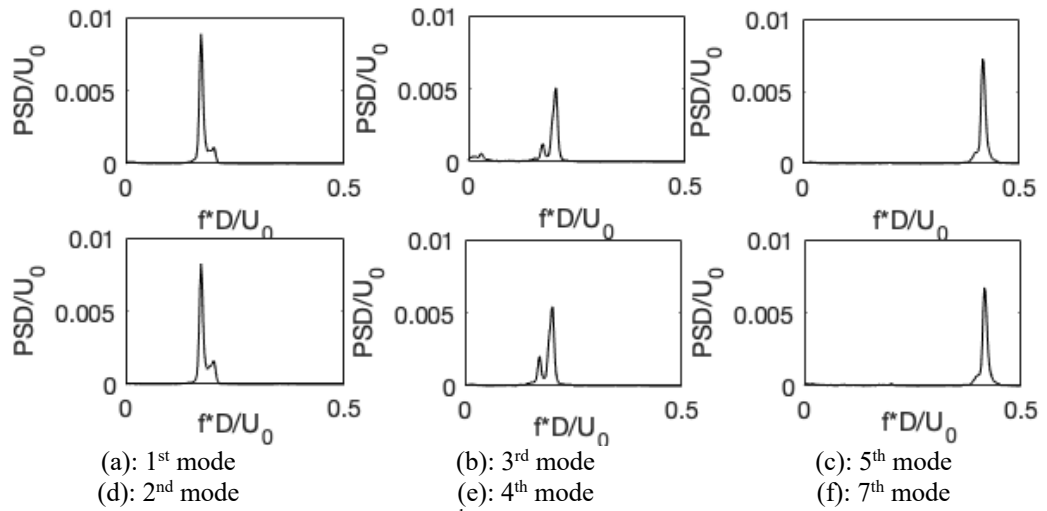
Figure 6.21 Normalized frequencies for 2nd case.

(a): 1st mode   (b): 3rd mode   (c): 5th mode
(d): 2nd mode   (e): 4th mode   (f): 6th mode
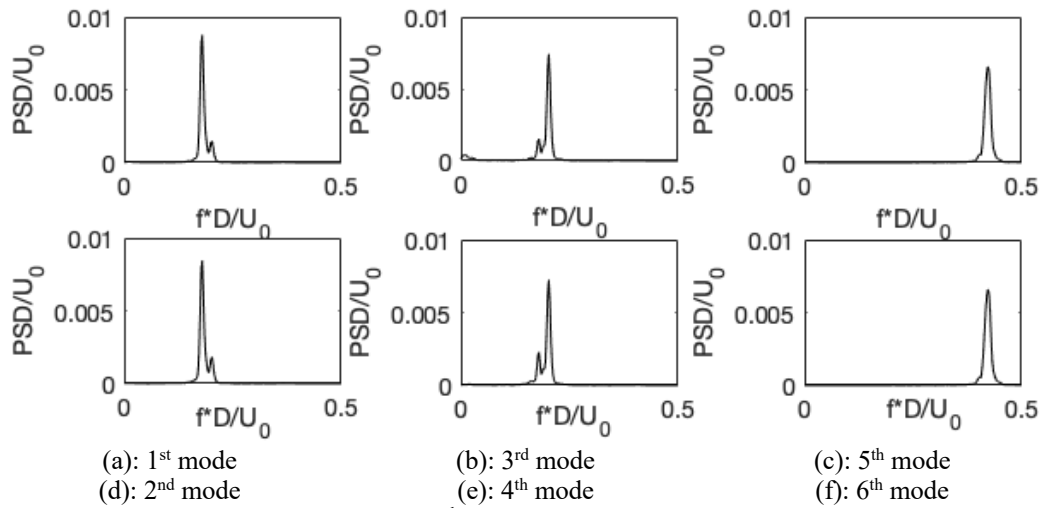
Figure 6.22 Normalized frequencies for 4th case.

(a): 1st mode   (b): 3rd mode   (c): 7th mode
(d): 2nd mode   (e): 4th mode   (f): 8th mode
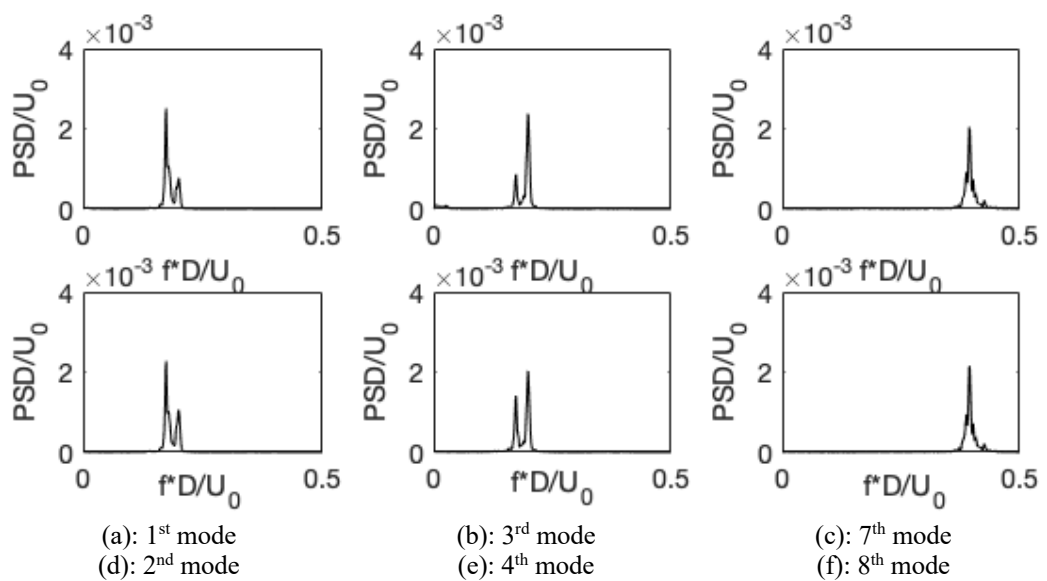
Figure 6.23 Normalized frequencies for 6th case.

Figure 6.15, 6.17, 6.19 exhibit contours of normalized POD modes in relation to three vortex cells of three cases. For each case, contours of the first two pairs of POD mode namely 1st mode / 2nd mode, 3rd mode / 4th mode, mainly spread behind the large-diameter cylinder, but differ in the spanwise continuity. It is obvious that the valid part of contours of the first pair takes up the entire span of large-diameter cylinder with good continuity, whilst that of the second pair break into two pieces approximately at $z/D = 4.5$. The valid part of contours of the last pair of POD mode mainly distributes behind small-diameter cylinder extending its one end into the wake zone of large-diameter cylinder. Figure 6.16, 6.18, 6.20 display the variation of mode coefficient over time indicating strong periodicity. Results about spectral analysis in terms of mode coefficient are shown in figure 6.21 - figure 6.23, to establish the relation between POD modes and vortex-shedding cells.

Considering spectral results in figure 6.21 -figure 6.23, the last pair of POD mode for three cases being single-frequency dominated can be directly associated with S-cell. However, spectra regarding the first two pairs present two frequency peaks co-existing in each graph, corresponding to L-cell shedding frequency and N-cell shedding frequency. Consequently, one can infer that L-cell and N-cell are not totally independent from each other in the wake though they are two distinct vortex cells with different shedding frequencies. They prefer to establish two types of vortex connection which form the related POD modes of velocity fields. In other words, the first two pairs of POD mode, should be regarded as two forms of vortex interaction between L-cell and N-cell, rather than directly linked to two vortex shedding cells respectively. For a clear illustration, these two typical and representative vortex connections can be termed as Type A and Type B as shown in figure 6.24. Type A depicts a complete in-phase connection, the moment when L-cell and N-cell detach from the cylinder with identical phase. Besides, N-cell is 'stronger' than L-cell at Type A connection. Similarly, Type B is a complete out of phase connection and L-cell dominates.
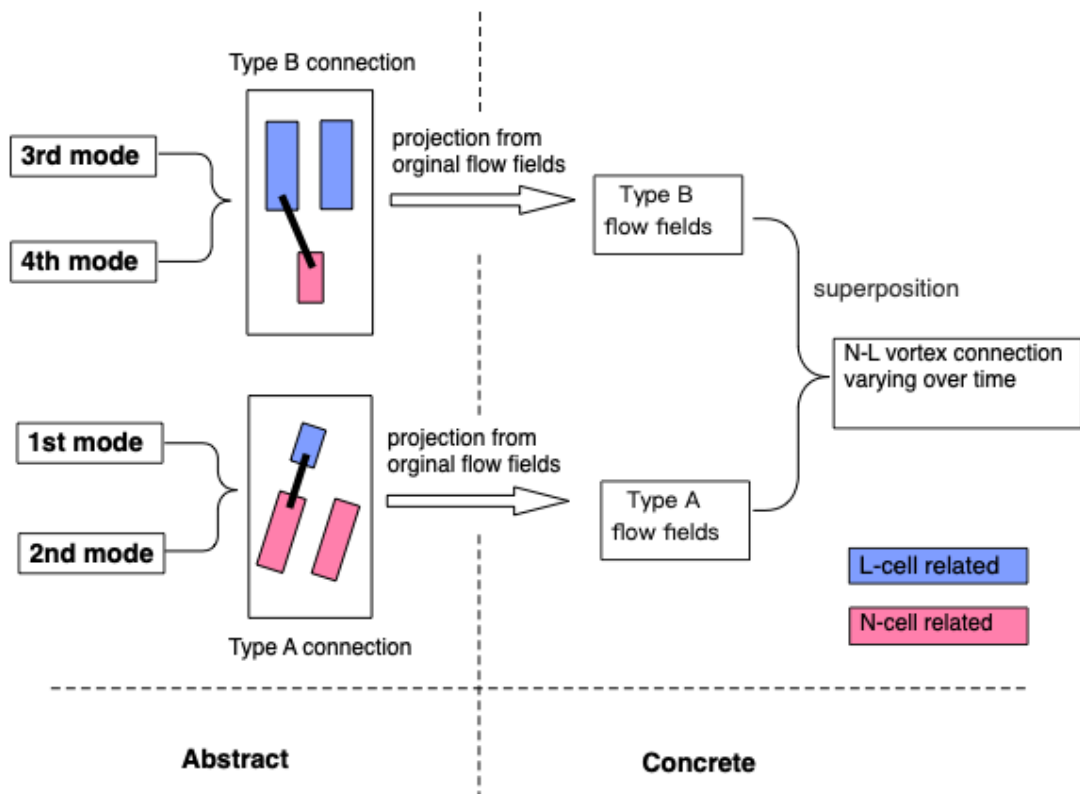
Figure 6.24 Schematic sketch of decomposition about N-L cell interaction.

On the basis of the above-mentioned two types of vortex connection, figure 6.24 gives a hypothesis about how to build the concrete connection between N-cell and L-cell. We normally agree that the complicated vortex connection between N-cell and L-cell varying over time is related to the direct composition of N-cell and L-cell. However, frequency co-existence regarding N-cell and L-cell in the first two pair of POD mode indicates that POD-based analysis cannot completely separate 'N-cell' from 'L-cell', in contrast to 'S-cell'. Consequently, this thesis guesses it is two types of vortex connection base that construct the complicated N-L vortex connection. As shown in figure 6.24, the first pair (1st mode, 2nd mode) and the second pair (3rd mode, 4th mode) successfully identify two types of vortex connection base namely Type A and Type B, standing for a completely in-phase status and a completely out of phase status. Subsequently, project original flow fields to two types of base, to get concrete flow components i.e., Type A flow fields and Type B flow fields. Considering the fact that Type A flow fields and Type B flow fields vary the 'strength' over time, the superposition of Type A flow fields and Type B flow fields describes the complication of N-L vortex connection.

Instantaneous vortex interaction

Methodology introduction in Chapter 3 has already demonstrated that the first pair of POD mode can be used to evaluate the state of periodic flow. More specifically, considering the situation of flow around the plain cylinder, the outcome about superposing flow components in relation to the first two POD modes on the original mean flow highlights the dominant vortex shedding, as well as eliminates the impact of coherent structures with small scales. However, the flow field behind step cylinders consists of three distinct vortex-shedding cells, corresponding to more complicated periodic flow than that behind plain cylinders. Similarly, reconstructed flow fields behind step cylinders can be obtained by adding flow components in terms of three vortex-shedding cells to the mean original flow. It should be noted that POD-based processing is used to recognise relevant POD modes, furthermore, to identify flow components regarding three vortex cells. Consequently, the reconstructed flow fields eliminating other flow portions clearly display the vortex interaction among three vortex cells, especially near the N-L cell boundary and the N-S boundary. The reconstruction processing can be expressed using equation 6.1.

It should be borne in mind that the subscript of '*k1*' and '*k2*' in equation 6.1 varies for these three cases, depending on the pair of POD mode that dominates S-cell. For a better illustration, the instantaneous velocity field at an instant of time from 2nd case is selected to demonstrate the flow field reconstruction process, and relevant graphs are summarized in figure 6.25. Initially, four important flow components are presented in figure 6.25(a) – (d), namely the mean original flow field (see figure 6.25(a)), flow components regarding three vortex cells (see figure 6.25(b) –(d)). Subsequently, the superposition of above-mentioned four flow components gives rise to the reconstructed velocity field as shown in figure 6.25(e). The smooth contour lines in figure 6.25(e) reveal that turbulence with small scales has been eliminated. Compared with the original flow field in figure 6.25(f), the reconstructed velocity field shows high similarity, featuring major characteristics of the original flow field. Besides, vortex cells identified by 'velocity valleys' show clear vortex interaction with each other.

$$U_{NLS}(x, y, t) = \overline{U}(x, y) + a_1(t)\vec{\theta}_1(x, y) + a_2(t)\vec{\theta}_2(x, y) + ...$$

$$+a_3(t)\vec{\theta}_3(x, y) + a_4(t)\vec{\theta}_4(x, y) + ... \qquad (6.1)$$

$$+a_{k1}(t)\vec{\theta}_{k1}(x, y) + a_{k2}(t)\vec{\theta}_{k2}(x, y)$$

Note: $\overline{U}(x, y)$ denotes the averaged velocity field;

$\vec{\theta}_m(x, y)$ (m = 1, 2, 3, 4) stands for the first four normalized POD modes;

$a_m(t)$ (m = 1, 2, 3, 4) represent for the mode coefficients.
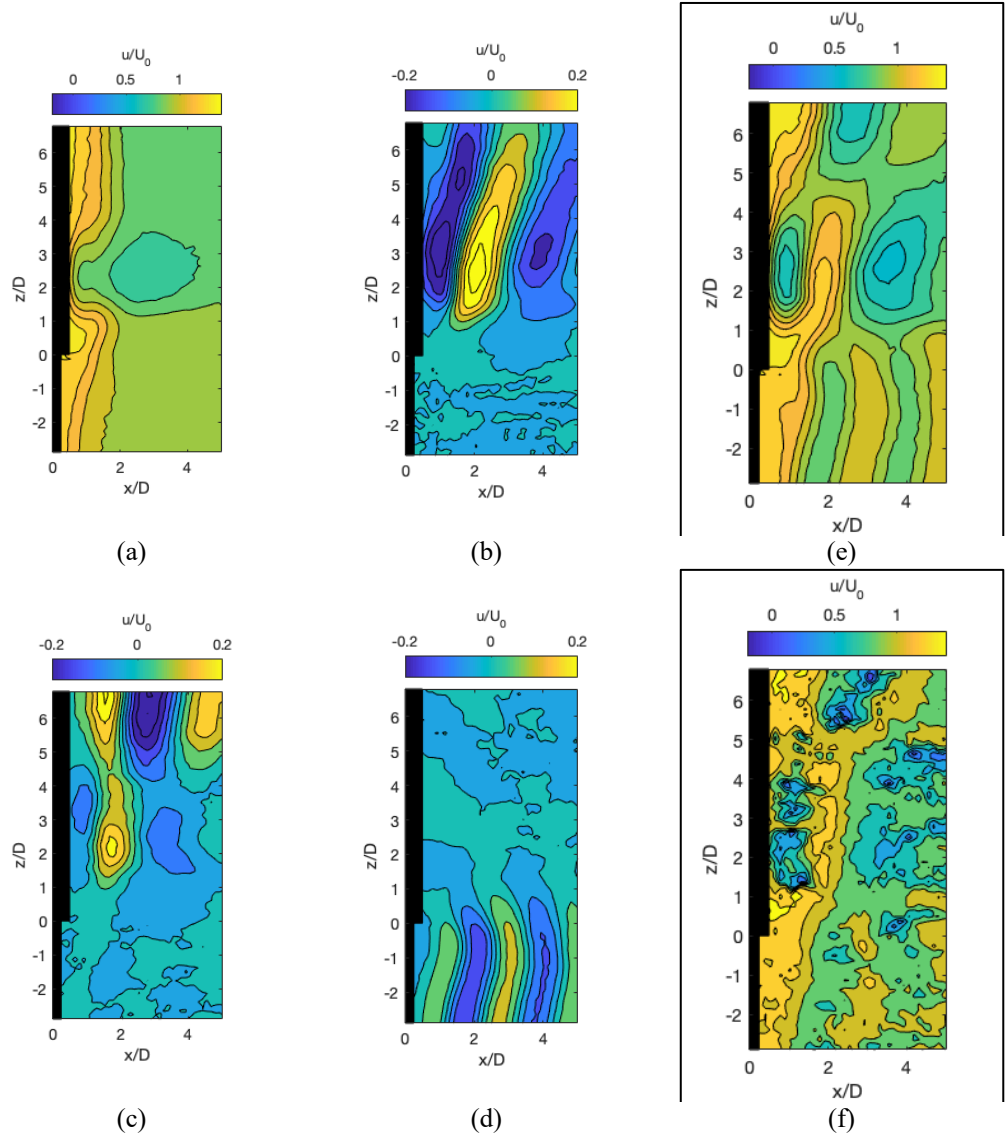
Figure 6.25 Explanation of velocity field reconstruction using a velocity field at an instant of time from 2nd case.

Note: (a): $\overline{U}(x, y)$; (b): $a_1(t)\vec{\theta}_1(x, y) + a_2(t)\vec{\theta}_2(x, y)$; (c): $a_3(t)\vec{\theta}_3(x, y) + a_4(t)\vec{\theta}_4(x, y)$;

(d): $a_{k1}(t)\vec{\theta}_{k1}(x, y) + a_{k2}(t)\vec{\theta}_{k2}(x, y)$; (e): $U_{NLS}(x, y, t)$;

(f): the original instantaneous velocity field.
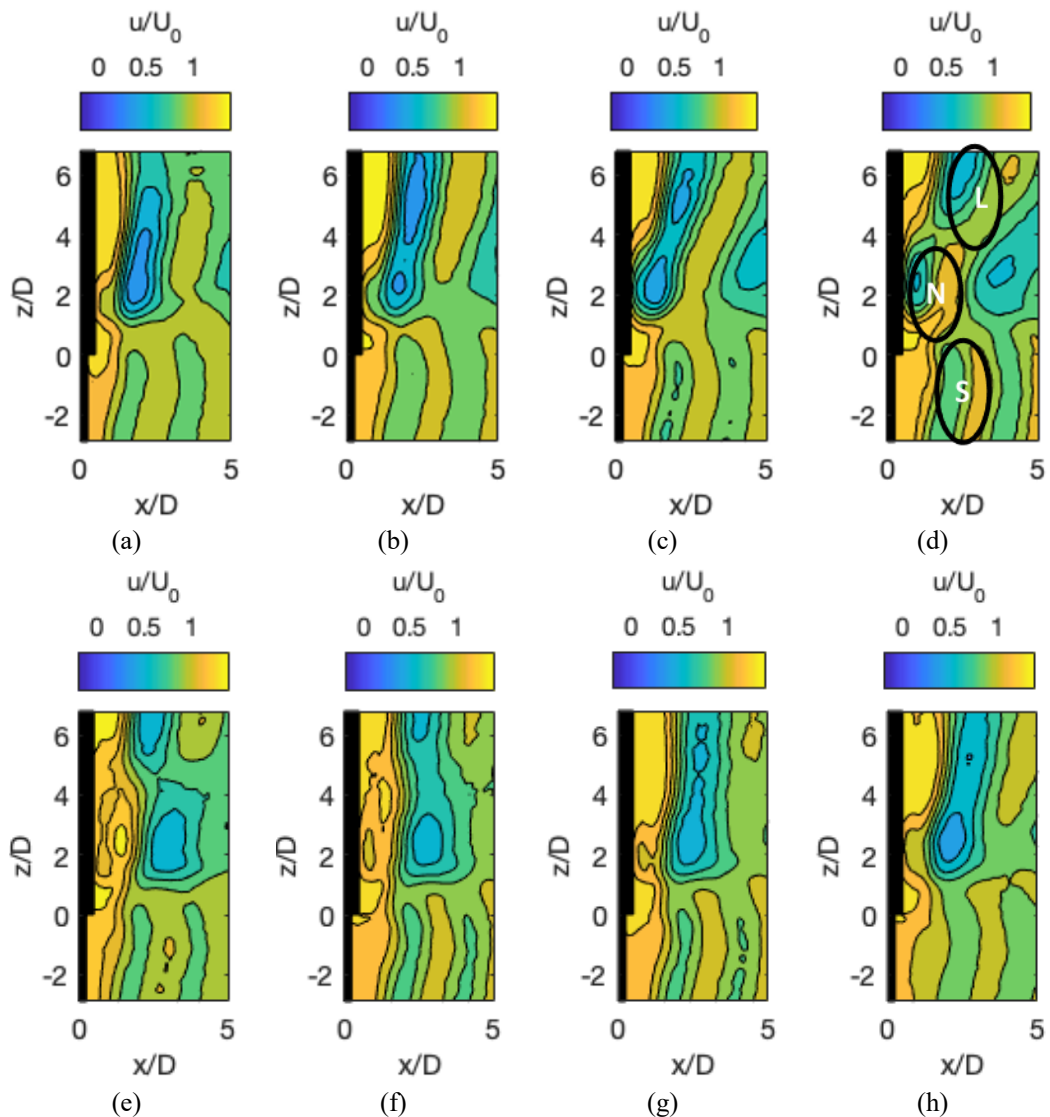
Figure 6.26 Instantaneous streamwise velocity fields. (2nd case, *S step*, *Re* = 1.6e+4). (a):t_0; (b): t_0+1T_L; (c): t_0+2T_L; (d): t_0+3T_L; (e): t_0+4T_L; (f): t_0+5T_L; (g): t_0+6T_L; (h): t_0+7T_L.

Reconstructed velocity fields for all cases are obtained in the same way as shown in figure 6.25, and a sequence of streamwise velocity fields (reconstructed) behind sharp step cylinders (*S step*, 2nd case) is presented in figure 6.26 to demonstrate the complete vortex interaction loop. The time interval for neighbouring captures is T_L (the period of L-cell). Initially, three vortex cells namely L-cell, N-cell and S-cell with diverse frequencies ($f_S > f_L > f_N$) are staggered along the span and marked in figure 6.26(d). L-cell detaches from the large-diameter cylinder in-phase / out of phase with N-cell periodically due to the frequency difference. A huge vortex tube parallel to the cylinder axis detaches from the large-diameter cylinder in figure 6.26(a), indicating that N-cell and L-cell melt with each other and form one piece. Subsequently, the vortex tube starts to slant in figure 6.26(b) - (c) due to the phase difference between L-cell and N-cell getting larger. Eventually in figure 6.26(d) -(f), the initial vortex connection between N-cell and L-cell cannot

maintain, and thereby the L-cell breaks its connection with previous N-cell and builds a new link with another N-cell. The new vortex connection gradually becomes firm in figure 6.26(f) -(h) and starts another loop. Similarly, reconstructed velocity fields behind *R step* round step cylinder (4th case, 6th case) can also be reconstructed and the N-cell, L-cell and S-cell vortex shedding, as well as the dynamic vortex interaction, can also be clearly highlighted.

Subsequently, aiming at reconstructed velocity fields, typical portions of streamwise velocity variation over time for three cases along the reference line (x/D = 2.5, y/D = -0.6) are presented in figure 6.28 to 6.30, which is similar to the work done by Jagadeesh (2009). The horizontal axis represents the normalized time and the vertical axis represents the spanwise location. It could be found that three distinct types of velocity fluctuation periodically vary over time at different frequency in figure 6.28 to 6.30.
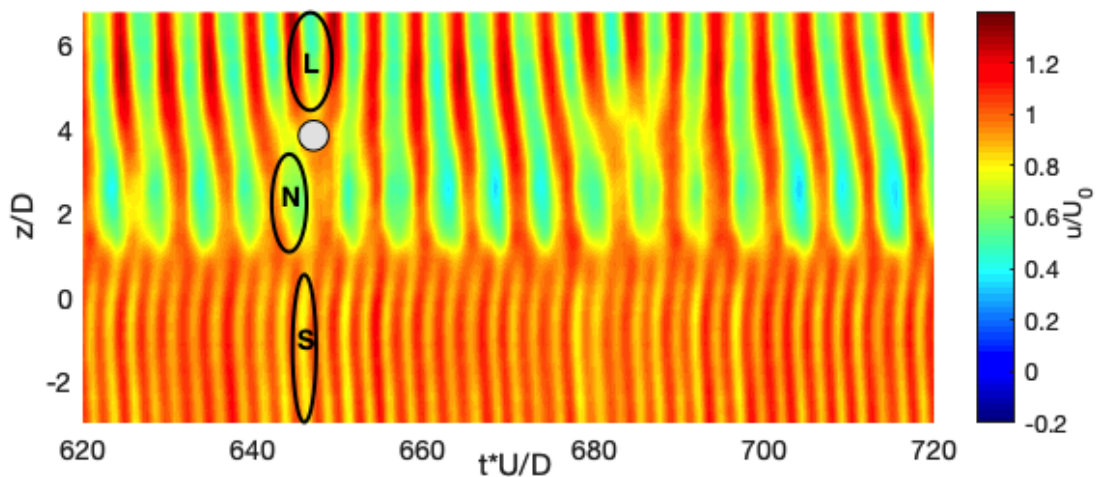
Figure 6.27 Identification of vortex-shedding cells and vortex dislocation. (2nd case, *S step*, *Re* = 1.6e+4).

More specifically, a certain type of velocity fluctuation is in charge of one portion of the span, corresponding to a certain vortex-shedding cell in figure 6.27. Due to the fixed frequency difference in between, velocity dislocations take place periodically marked via a grey round circle in figure 6.27. The occurrence of velocity dislocation between N-cell and L-cell corresponds to the out-of-phase shedding in between, indicating that the beat frequency $((f_L - f_N) \times D/U_0)$ characterises the vortex dislocation. Consequently, beat frequencies for 2nd case, 4th case and 6th case namely, 0.03, 0.0225, and 0.025, are used to do corresponding evaluation. For instance, the averaged normalized time interval $(t \times U_0/D)$ between neighbouring vortex dislocations can be calculated as 33, 44 and 40 respectively. It is obvious that beat frequency behind round step cylinder (4th case and 6th

case) is remarkably smaller than that behind the sharp step cylinder. Considering the fact that the time between two neighbouring vortex dislocations characterise a N-cell loop, the variation of N-cell loop over time behind sharp step cylinder and round step cylinder under high Reynolds numbers can be quantitatively investigated from figure 6.28 to 6.30. Obviously, the dynamic N-cell behaviour in figure 6.28 to 6.30 shows difference with that under lower Reynolds numbers (Dunn & Tavoularis, 2006; Morton & Yarusevych, 2010b). With respect to the situation at lower Reynolds numbers, N-cell loop is a stable and periodical activity, equipped with fixed N-cell duration and stable N-cell extent along the span. However, the N-cell duration between neighbouring vortex dislocations is not fixed in figure 6.28 to 6.30 and the N-cell spanwise extent changes at different vortex dislocations. Morton & Yarusevych (2014a) directly attribute the variation of N-cell duration to the frequency fluctuation over time behind large-diameter cylinder. However, the variation of unstable N-cell spanwise extent might not be fully illustrated via the above-mentioned explanation. Consequently, the present study attempts to explain the variation of N-cell duration and the unstable N-cell extension using the turbulence characteristics, i.e., the randomness. In turbulent flow, the energy transformation from large-scale eddies to small-scale eddies features significant random characteristic, resulting in the dominant eddies, i.e., L-cell, N-cell and S-cell, gaining the random characteristic. Consequently, the vortex interaction between three vortex cells, as well as the N-cell dynamic behaviour, characterises randomness.
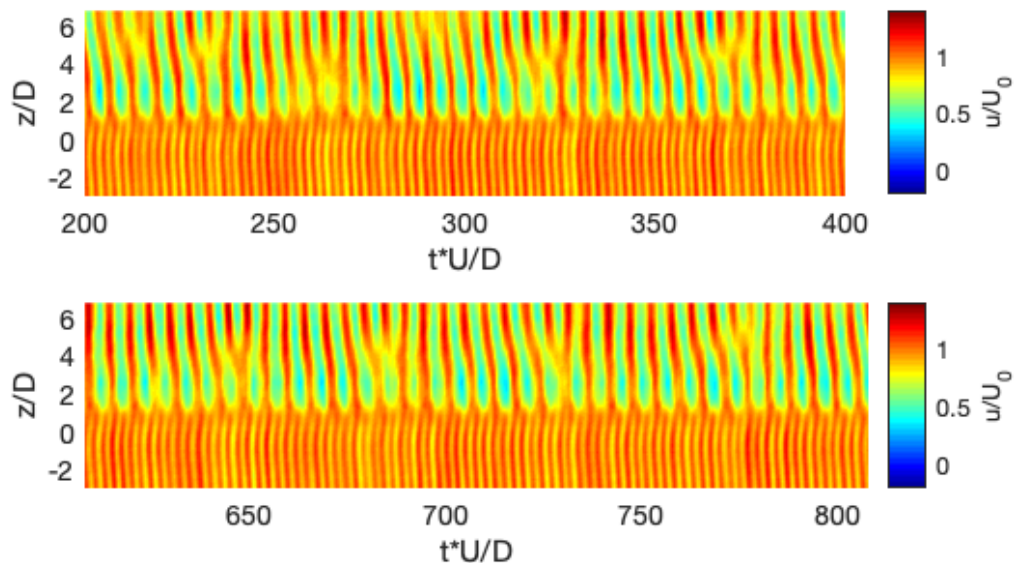
Figure 6.28 Streamwise velocity variation over time at the reference line ($x/D = 2.5$, $y/D = -0.6$), (2nd case, *S step*, $Re = 1.6e+4$).
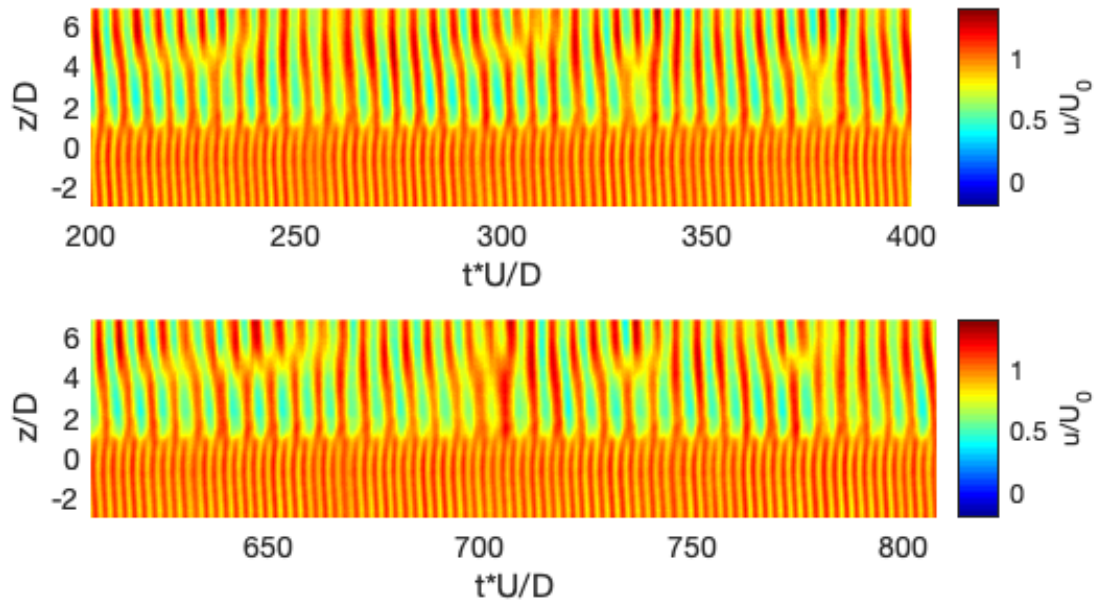
Figure 6.29 Streamwise velocity variation over time at the reference line (x/D = 2.5, y/D = -0.6), (4th case, *R step*, *Re* = 1.6e+4).
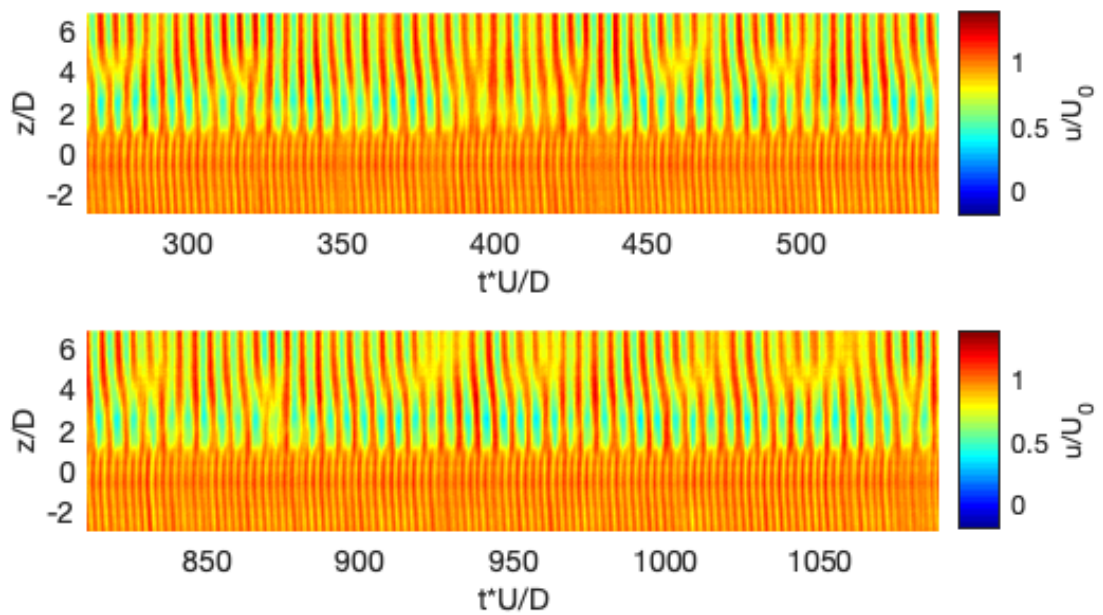
Figure 6.30 Streamwise velocity variation over time at the reference line (x/D = 2.5, y/D = -0.6), (6th case, *R step*, *Re* = 3.3e+4).

6.4 Brief Summary for Flow Fields

This chapter focuses on flow fields behind sharp step cylinder and round step cylinder, starting with analysis on time-averaged velocity fields along the Plane Y = 0D. Two notable velocity regions are detected behind the large-diameter cylinder near the step, termed as 'NSV' region (negative streamwise velocity) and 'PSV' region (positive spanwise velocity). Quantitative studies about 'NSV' region and 'PSV' region reveal significant impact of shape of step junction (sharp and round). Besides, the 'downwash' behind round step cylinder is weaker than that behind the sharp step cylinder. Energy content extracted from velocity spectrum for each position is used to construct the averaged energy field. Results indicate that energy field of a specific shedding frequency distributes unevenly along a certain portion of the span owning to vortex interaction between neighbouring cells. Linear fit is used to analyse average energy decay, giving rise to two terms namely EDR (energy decay rate) and EDS (energy decay shift). Associated with plain cylinders, EDR and EDS can be treated as inherent characteristics to recognise a certain type of vortex cells. Results show the significant higher EDR on N-cell than the other vortex cells. EDS, a term to evaluate the energy 'strength', is smaller for S-cell than the others vortex cells due to the larger relative offset of S-cell (the ratio of absolute offset to local diameter). POD-based analysis successfully identifies three pairs of 'components' behind sharp step cylinder and round step cylinder, the third pair of which can directly link with S-cell. The first and second pair of 'components' can be explained as two types (type A and type B) of vortex connection between N-cell and L-cell. Subsequently, reconstructed velocity fields emphasize three vortex-shedding cells, as well as vortex connections between neighbouring. N-cell duration and N-cell spanwise extent vary over time featuring the random characteristic.

Chapter 7
NUMERICAL SETUP AND VERIFICATION

In order to provide a supplement or extension for the experimental study above, Chapter 7 and Chapter 8 present numerical work with the emphasis on comparative study of three-dimensional flow fields near sharp step junction and round step junction. More specifically, Chapter 7 illustrates the numerical implementation regarding plain cylinders and step cylinders (*S step* and *R step*), for instance, defining the computation domain, assigning key parameters, grid topology design, convergence study and result validation.

7.1 Numerical Configurations
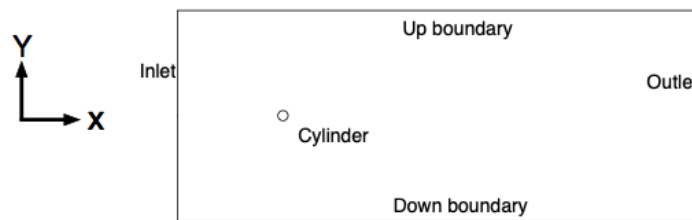
(a): domain at Plane X-Y for plain cylinders
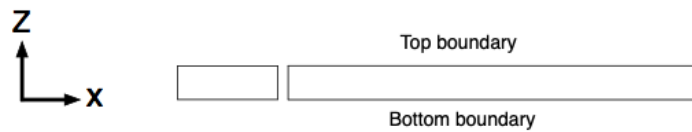
(b): domain at Plane X-Z for plain cylinders
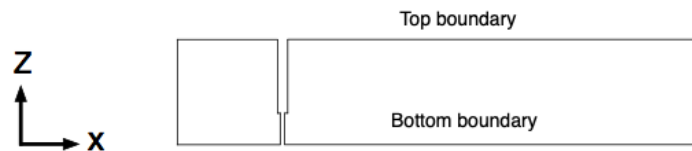
(c): domain at Plane X-Z for step cylinders

Figure 7.1 Schematic sketch of the computational domain.

The adopted computational domain layout for modelling plain cylinders is shown in figure 7.1. The length and width of the computational domain along X-Y plane are 50*D* and 20*D* (see figure 7.1(a)). The height of the computational domain along X-Z plane is *3.2D* for case of large-diameter cylinder and 1.6*D* for case of small-diameter cylinder (see figure 7.1(b)). The height slightly bigger than πD (πd) (D'Alessandro, et al., 2016) is determined to allow enough length span for observing entire vortex cell. The cylinder model is vertically placed at the location of x = 0, y = 0, where the distance between cylinder centre and the upstream boundary is the same as the distance between cylinder centre and side boundary, i.e., 10*D*. The domain dimension along X-Y plane keeps the same as that used by D'Alessandro, et al. (2016). The computational domain along X-Y

plane regarding step cylinders keeps similar with that for plain cylinders, but the height for step cylinders is larger, i.e., 10*D*. Details about boundary setting can be summarized in table 7.1. Only difference on boundary condition between modelling plain cylinders and modelling step cylinders is 'Top / Bottom', the former of which is defines as periodical boundary and the latter chooses symmetry boundary. When modelling step cylinders, the top boundary and bottom boundary cannot geometrically match each other owing to the cylinder diameter difference, which induces to the unsuitability of 'Periodical boundary'. A steady free flow with the velocity of $[U_0\ 0\ 0]$ and no perturbation is added to the inlet boundary. The pressure at the outlet boundary is set as 0 and the velocity at outlet boundary is set as zero gradient, which can be acceptable due to the long enough distance between the cylinder model and the outlet boundary. Two side boundaries (Up / down) are set as slip wall. The numerical simulation is carried out using an open source software namely OpenFOAM (version 5.x) and related numerical setting is presented in table 7.2. As for the comparison between DES solution and RANS solution, the significant difference is the discretization of the convection terms. The central difference scheme is used in DES solution and the upwind difference scheme is proved to be enough for RANS solution (Nishino, et al., 2008).

Table 7.1 Summary of boundary conditions.

Boundary condition	Modelling uniform cylinders	Modelling step cylinders
Reynolds number	1.6e+4 (Large cylinder), 0.8e+4 (Small cylinder)	1.6e+4 (*Re*)
Inlet	$U = [U_0\ 0\ 0]$, $\dfrac{\partial p}{\partial n} = 0$	$U = [U_0\ 0\ 0]$, $\dfrac{\partial p}{\partial n} = 0$
Outlet	$P = 0$, $\dfrac{\partial U}{\partial n} = 0$	$P = 0$, $\dfrac{\partial U}{\partial n} = 0$
Top/Bottom	Periodical boundary	Symmetry
Up/Down	Slip wall	Slip wall
Cylinder	No slip wall	No slip wall

Table 7.2 Summary of related numerical setting.

Simulation setting	DES	RANS (optional)
solver	pisoFoam (a transient solver for incompressible)	pisoFoam (a transient solver for incompressible)
Press-velocity coupling	PISO	PISO
Turbulence model	$k - \omega$ SST-DES	$k - \omega$ SST
The diffusive terms	2nd order accuracy	2nd order accuracy
The convection terms	2nd order central difference/ 2nd order limited central difference	2nd order upwind difference/ 1st order upwind difference
Pressure/Velocity Gradients	2nd order accuracy	2nd order accuracy
Temporal discretisation	Crank-Nicolson	2nd order implicit
Equation solvers	Stabilised preconditioned (bi-) conjugate gradient	Stabilised preconditioned (bi-) conjugate gradient

7.2 Grid Topology

The present numerical simulation adopts a type of hybrid grid method with the combination of Cartesian grids and normal structured grids. The key concept is to apply structured grids around the cylinder, and subsequently to fill the outside with Cartesian grids Structured grids featuring equal nodes at two opposite faces is widely used for computational mesh establishment, which exhibits superb performance in dealing with body-fitted grids near curve surface. However, its refinement method normally gives rise to an issue that cells cannot be effectively reduced at the region far away from the structure. The Cartesian method (Blazek, 2015) is to create simple uniform hexahedral grids parallel to Cartesian coordinate axes. Its mesh refinement is to simply halve the local hexahedral grids, which can greatly reduce grid consumption at the region away from the structure. Facing the separated flow near curve surfaces, hexahedral grids nearby have to cut part off to fit curve surfaces, resulting in the so-called 'cut cells'. The author (Wang, et al., 2020) numerically investigated wave and WEC (wave energy converter) models interaction, with the mesh strategy using 'cut cells' near the model and Cartesian cells in the external region. However, the so-called 'cut cells' might be irregular near curve surface, arising plenty of studies regarding 'embedded boundary issue' (Tucker & Pan, 2000; Berger, et al., 2003; Senecal, et al., 2007). Consequently, the hybrid grid method with the combination of Cartesian grids and structured grids unites the aforementioned advantages, namely body-fitted grids near the curve surface and massive grids reduction in the external region.
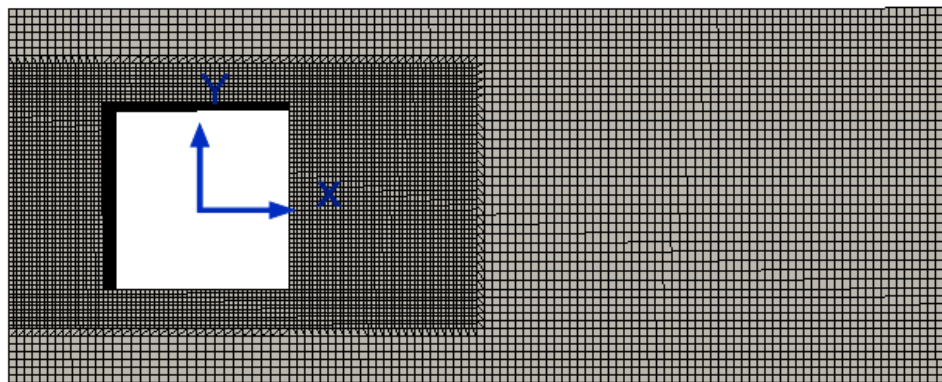
(a): front view;

(b): side view;

Figure 7.2 Grid topology (plain cylinders) of outer region.

(a): top view

(b): top view

(c): side view;
Large-diameter cylinder

(d): side view;
Small-diameter cylinder
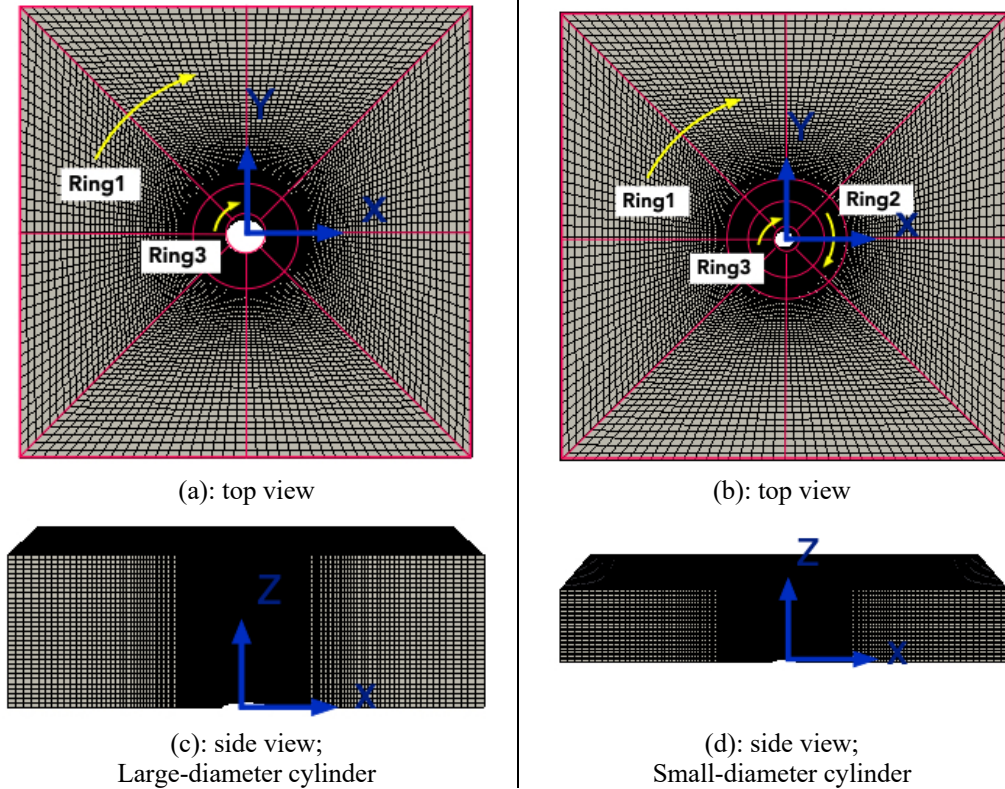
Figure 7.3 Grid topology (plain cylinders) of inner region.

Figure 7.2 and figure 7.3 demonstrate outer and inner grid topology regarding plain cylinders. Inner region being square-shaped is to allow the interface well connection between Cartesian grids and structured grids. The large-diameter cylinder and small-diameter cylinder share the same mesh layout in outer region (see figure 7.2), where one can clearly observe the multi-level refinement along X-Y plane and X-Z plane namely, two-time refinement and three-time refinement. Besides, the application of Cartesian grids in figure 7.2 exhibits the superb orthogonality. The inner region in figure 7.3 employs a few layers of block to encircle cylinders namely, Ring 1 / Ring 3 for the large cylinder, Ring 1 / Ring 2 / Ring 3 for the small cylinder. In order to meet demands on DES turbulence model, mesh layout along X-Y plane and X-Z plane is in agreement with that assigned by Nishino, et al. (2008). The thickness of the first cell approaching the cylinder surface is determined by constraining the averaged y plus (y^+) approximately at 0.6. The DES solution being a combination of RANS and LES must guarantee 'the attached boundary' enveloped under RANS mode (Strelets, 2001) contains adequate nodes. Nishino, et al. (2008) suggested 30 nodes within the attached boundary for implementing RANS mode. Stringer, et al. (2014) applied the 30-layer body fitted grids around the cylinder to carry out two-dimensional pure RANS simulation, indicating that 30 nodes are enough for resolving RANS part. The spanwise mesh layout is determined by testing different resolutions, as summarized in section 7.3.

(a): *S step*   (b): *R step*

Figure 7.4 Schematic sketch of mesh block arrangement.

(a): side view (*S step*)   (b) : side view (*R step*)

(c): 3D view (*S step*)   (d): 3D view (*R step*)

(e): close-up (*S step*)   (f): close-up (*R step*)

Figure 7.5 Grid topology near sharp / round step cylinder.

Subsequently, grid establishment regarding step cylinders can be implemented on the basis of grids for plain cylinders in figure 7.2 and 7.3. Considering the fact that step cylinders feature geometrical variation near the step junction, multi-blocks are assigned around step cylinders and the planar layout parallel to the cylinder axis is presented in figure 7.4 where each block represents four identical blocks round the cylinder. The sharp step cylinder and the round step cylinder share the similar block arrangement but differ in blocks near the step corner (R2, R3, M1, M4). For regions far away from step junctions, i.e., L1, L2, L3, L4 and S1, S2, S3, S4, M3, M6, mesh layout at X-Y plane resembles that near plain cylinders (see figure 7.3). The extra mesh refinement is implemented within block R2, M1, R3, M4, to simulate more flow details near the step corner; the additional mesh refinement in block R1 and R4 is to gain a smooth transition from outer region to the step corner. Block R9 -R12, Block R5 -R8, M2 and M5 subject to spanwise refinement are responsible for the spanwise transition from step corner to top boundary and bottom boundary. Figure 7.5(a) to (f) give an exhibition about the ultimate grids for sharp step cylinder and round step cylinder. Structured grids in the inner region (marked with purple colour) are connected with Cartesian grids in the outer region by applying the 'node to node' mode. One can clearly observe an extra mesh refinement near the step junction, to precisely model complicated flow fields near the step.

7.3 Convergence and Verification

Convergence study for plain cylinders

Table 7.3 and table 7.4 summarize outcome of convergence study on large-diameter cylinder and small-diameter cylinder with the emphasis on grid resolution at X-Y plane and X-Z plane. A total of eighteen testing cases are implemented, ten of which is for large-diameter cylinder. It should be noted that all cases excluding Case c9 apply DES turbulence model, and meanwhile Case c2 is treated as the benchmark due to the superb performance (Nishino, et al., 2008). Reference experimental results are captured from trend lines of C_d vs. Re, C_l vs. Re and S_t vs. Re (Zdravkovich, 1990; Massey, 1998; Norberg, 2003) being cited by Stringer, et al. (2014). Different mesh resolution is recognised using three parameters, i.e., $N_{x,y}$ (inner), N_z (inner) and N_{total}. The first two parameters describe structured grid part, denoting cell number at X-Y plane and along the span. The last variable N_{total} is cell number of the entire computational domain.

Table 7.3 Summary of results of convergence tests (Large cylinder, Re = 1.6e+4).

Case No.	$N_{x,y}$,inner	N_z, inner	N_{total}	$\Delta t U_0/D$	mean C_d	rms C_l	S_t
General size							
c1 coarse	21600	24	518400	0.001	1.33	0.780	0.212
c2 medium	25920	32	829440	0.001	1.17	0.451	0.212
c3 fine	30240	48	1451520	0.001	1.19	0.474	0.212
Impact of Plane X-Y							
c4	21600	32	691200	0.001	1.21	0.525	0.212
c2	25920	32	829440	0.001	1.17	0.451	0.212
c5	30240	32	967680	0.001	1.19	0.478	0.212
Impact of Plane X-Z							
c6	25920	16	414720	0.001	1.31	0.752	0.203
c2	25920	32	829440	0.001	1.17	0.451	0.212
c7	25920	48	1244160	0.001	1.21	0.497	0.212
Impact of time resolution							
c2	25920	32	829440	0.001	1.17	0.451	0.212
c8	25920	32	829440	0.0005	1.18	0.469	0.212
Impact of turbulence Model*							
c2	$k-\omega$ SST-DES (DES)				1.17	0.451	0.212
c9	$k-\omega$ SST (RANS)				1.36	0.873	0.212
Reference experimental results							
mean C_d: 1.152 (Zdravkovich, 1990), 1.171 (Massey & Ward-Smith, 1998)							
rms C_l: 0.462 (Norberg, 2003); S_t: 0.196 (Norberg, 2003)							
Note: * The only variation between case c2 and case c9 is turbulence model.							

Table 7.4 Summary of results of convergence tests (Small cylinder, Re = 0.8e+4).

Case No.	$N_{x,y}$,inner	N_z, inner	N_{total}	$\Delta t U_0/d$	mean C_d	rms C_l	S_t
General size							
c1 coarse	24000	24	576000	0.002	1.27	0.676	0.208
c2 medium	28800	32	921600	0.002	1.05	0.238	0.216
c3 fine	33600	48	1612800	0.002	1.04	0.229	0.212
Impact of Plane X-Y							
c4	24000	32	768000	0.002	1.09	0.311	0.220
c2	28800	32	921600	0.002	1.05	0.238	0.216
c5	33600	32	1075200	0.002	1.01	0.169	0.220
Impact of Plane X-Z							
c6	28800	16	460800	0.002	1.28	0.707	0.208
c2	28800	32	921600	0.002	1.05	0.238	0.216
c7	28800	48	1382400	0.002	1.09	0.313	0.212
Impact of time interval							
c2	28800	32	921600	0.002	1.05	0.238	0.216
c8	28800	32	921600	0.001	1.04	0.217	0.220
Reference experimental results							
mean C_d: 1.133 (Zdravkovich, 1990), 1.067 (Massey, 1998)							
rms C_l: 0.370 (Norberg, 2003); S_t: 0.203 (Norberg, 2003)							

For a comprehensive evaluation, three cases varying grid resolution in X-Y plane and X-Z plane namely, Case c1, c2, c3, are considered, corresponding to coarse mesh, medium mesh and fine mesh. Results regarding mean C_d and rms C_l exhibit a significant difference between Case c1 and Case c2 indicating a remarkable influence from the grid resolution. And meanwhile, the outcome from Case c2 and Case c3 is comparable with each other suggesting the acceptable grid convergence at X-Y plane and X-Z plane. Consequently, on the basis of results from Case c2, another two groups of testing case are designed to study grid resolution at X-Y plane and X-Z plane separately. By comparing results with that from Case c2, Case c4 to c7 excluding c6 are independent from grid resolution. The reasonable hypothesis for Case c6 is that grid resolution along the span is more sensitive than that at X-Y plane and results could be reliable only when the corresponding mesh is fine enough, for instance, $32 < N_z$ (inner) < 48. Results from Case c2 and c8 confirm the selected two time intervals are reasonable. The present numerical results are in great agreement with reference from previous publications evidencing the reliability of the present simulations.

a: coarse mesh (c1); b: medium mesh (c2);
c: fine mesh (c3);
Large-diameter cylinder (Re = 1.6e+4)

d: coarse mesh (c1); e: medium mesh (c2);
f: fine mesh (c3);
Small-diameter cylinder (Re = 0.8e+4)
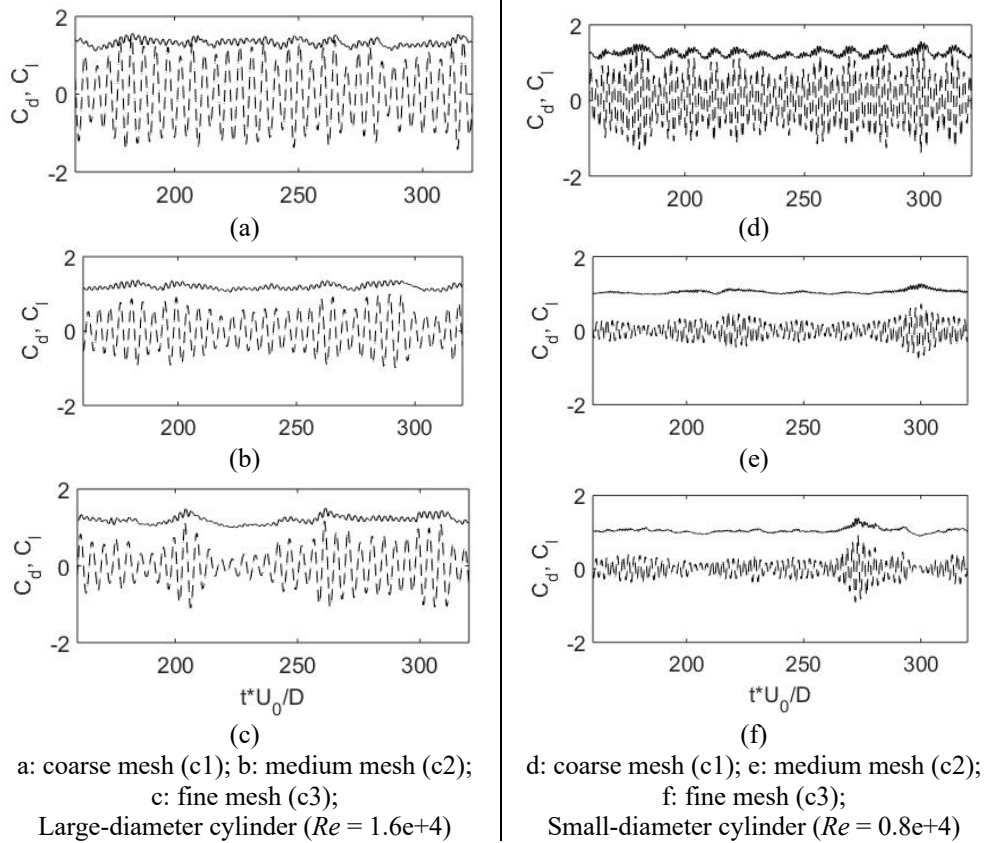
Figure 7.6 Time series of drag / lift coefficient.

(a): Case c3 (large-diameter cylinder)

(b): Case c3 (small-diameter cylinder)
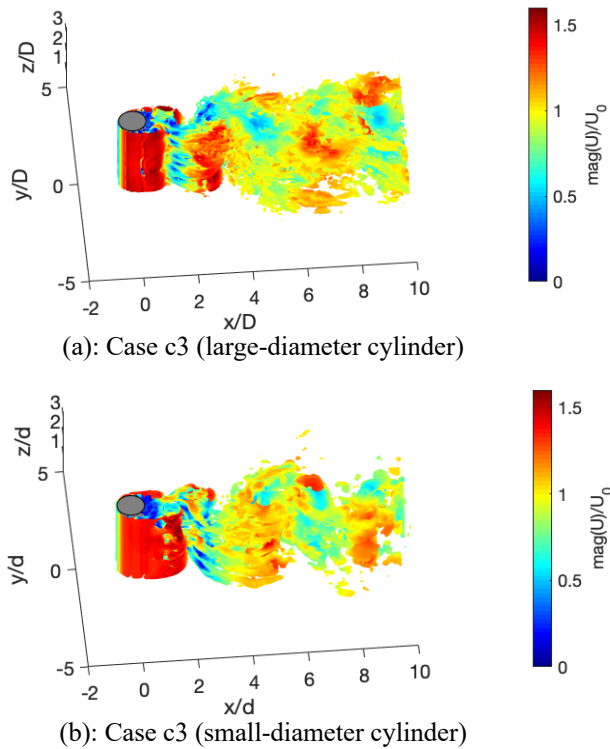
Figure 7.7 Q-isosurface behind large cylinder (a) and small cylinder (b).

Note: (a): Q-isosurface (fine mesh, $Q=0.2*U_0^2/D^2$) -large cylinder (coloured by velocity magnitude);

(b): Q-isosurface (fine mesh, $Q=0.2*U_0^2/D^2$) -small cylinder (coloured by velocity magnitude).

In order to illustrate the coefficient fluctuation, time series of drag coefficient and lift coefficient from testing cases with coarse mesh (c1), medium mesh (c2) and fine mesh (c3) of large-diameter cylinder and small-diameter cylinder are presented in figure 7.6(a) to (f). Solid lines and dash lines denote drag coefficient variation and lift coefficient variation respectively. For the outcome from coarse meshes, higher averaged drag coefficient (C_d) and stronger lift coefficient (C_l) fluctuation directly prove that the adopted grid resolution is not fine enough. Similar scale of the coefficient fluctuation for medium mesh and fine mesh indicates the acceptable convergence. Besides, the instantaneous isosurface ($Q=0.2*U_0^2/D^2$) for large-diameter cylinder and small-diameter cylinder in figure 7.7(a) & (b) enables vortices well displayed. It could also be found from figure 7.7 that the instantaneous isosurface exhibits detailed three-dimensional vortex shedding in the wake, involving small-scale vortices.

Apart from that, impact of turbulence model is briefly discussed via the comparative study of Case c2 & c9. The mean C_d and rms C_l from Case c9 shows significantly larger than that from Case c2 indicating DES turbulence model is robust in simulating turbulent flow around a cylinder. In order to check the performance of OpenFOAM parallel computing, an additional simulation case for large cylinder has been implemented with the usage of 1.5 times processors than that for Case c2 (large cylinder). The mean drag coefficient & the Strouhal number of the additional case being 1.17 & 0.212 shows great consistency with Case c2 which proves that statistic outcome from the present numerical simulation in parallel is acceptable and reliable.

Verification for step cylinders

The acceptable mesh layout for simulating plain cylinders is obtained via the above-mentioned convergence study, providing the step cylinders' simulation with the reliable reference. For gaining sufficient confidence towards the forthcoming result analysis on step cylinders' simulation in Chapter 8, time-averaged surface pressure distribution near the sharp step junction is compared to results from previous publications. The reference surface pressure distribution is from Ko & Chan (1984) and Morton, et al. (2009), corresponding to the Reynolds number of 80000 and 2000 respectively. More specifically, reference surface pressure distribution at Re = 80000 and 2000 exhibits similar variation near the step (see figure 7.8) giving rise to the deduction that time-averaged surface pressure distribution near the step junction is stable at the Reynolds number range from 2000 to 80000. Consequently, the comparison between the present numerical surface pressure distribution (Re = 1.6e+4) and the reference is shown in figure 7.8. One can conclude that the result from the present numerical simulation is in agreement with the reference. For regions away from the step junction, surface pressure coefficient keeps stable at z/D > 0.5 and z/D < -0.5. The steady value at large cylinder side are 1, 0.68, -0.2, -0.66 and -1, corresponding to 0°, 20°, 40°, 50° and 65°, and the pressure coefficient at small cylinder side are 1, 0.64, -0.3, -0.85 and -1.2. With it gradually reaching the step junction, the pressure coefficient at the front surface (0°, 20°) decreases from both sides. And meanwhile, the consequent positions (40°, 50° and 65°) encounter the notable fluctuation on pressure coefficient near the step junction at both sides.
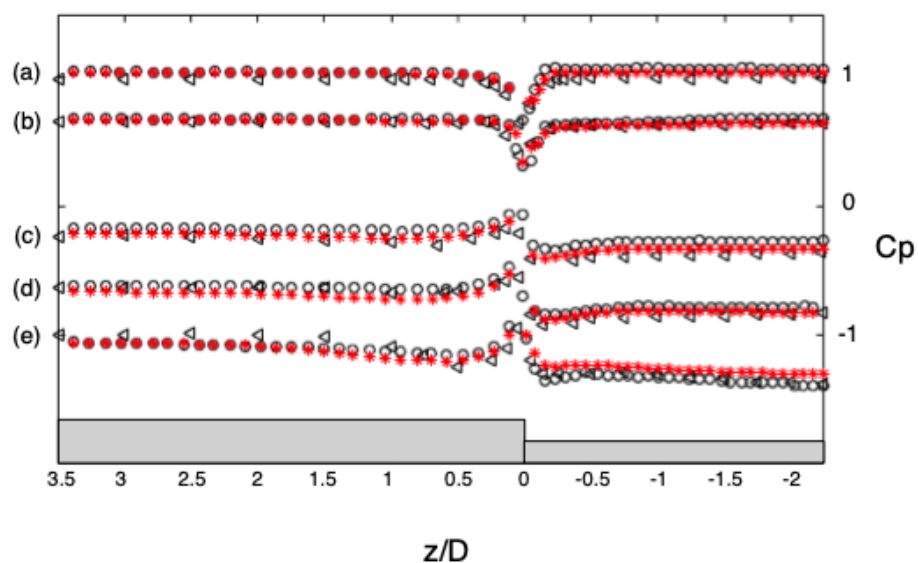
Arc angle: 0° (a); 20° (b); 40° (c); 50° (d); 65° (e);

△ ---Ko & Chan (1984); ○ ---Morton, et al. (2009); * ---Present study (numerical, Re = 1.6e+4).

Figure 7.8 Surface pressure coefficient verification for sharp step cylinder.

Subsequently, the averaged flow fields behind sharp step cylinder and round step cylinder are compared with the present experimental results in Chapter 6. It has been demonstrated via the experimental discussion about figure 6.7, that the flow within two regions behind the step junction is significant namely, the 'NSV' region for the streamwise velocity and the 'PSV' region for the spanwise velocity. The above-mentioned two regions are selected as the ideal location for velocity validation. As a result, six reference lines near these two regions are selected as shown in figure 7.9, three of which (z/D = 1.25, 2.5, 3.75) are to capture the streamwise velocity (u). And the other three (x/D = 1.25, 2.5, 3.75) are to capture the spanwise velocity (v). The comparison of time-averaged velocities between the present numerical results and the present experimental results are shown in figure 7.10 and figure 7.11. The streamwise velocity profiles (u) obtained from the present numerical simulation are comparable with that obtained from the present experiments, sharing the similar trend that the u profile variation mitigates at the cross-section away from the step junction, for instance z/D = 3.75. As for the spanwise velocity profile (v), the similarity between numerical results and experimental results is acceptable, more specifically, the detected velocity peak shifts upwards when the reference line moves downwards.
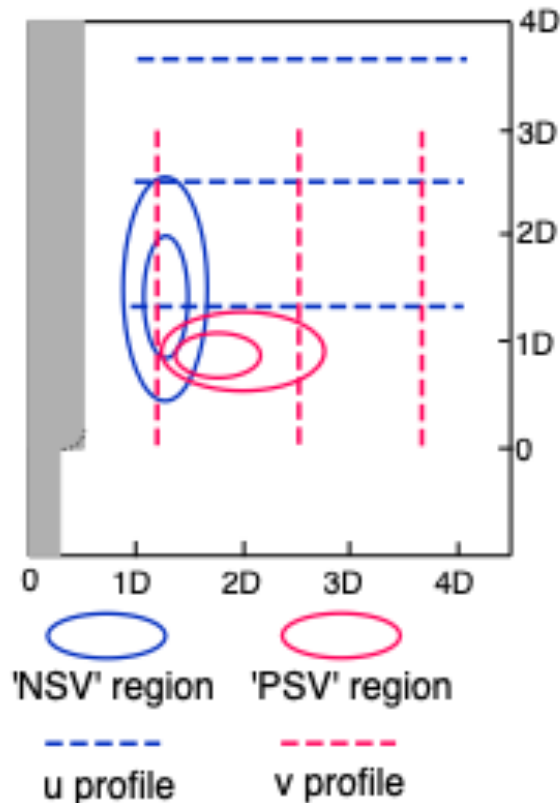
Figure 7.9 Illustration of velocity verification behind sharp / round step cylinder.

u profile
z/*D* = 1.25(a), 2.5(b), 3.75(c);
circles: experimental data (1st case, *S step*);
squares: numerical data (*S step*);
Re = 1.6e+4;

v profile
x/*D* = 1.25(d), 2.5(e), 3.75(f);
circles: experimental data (1st case, *S step*);
squares: numerical data (*S step*);
Re = 1.6e+4;
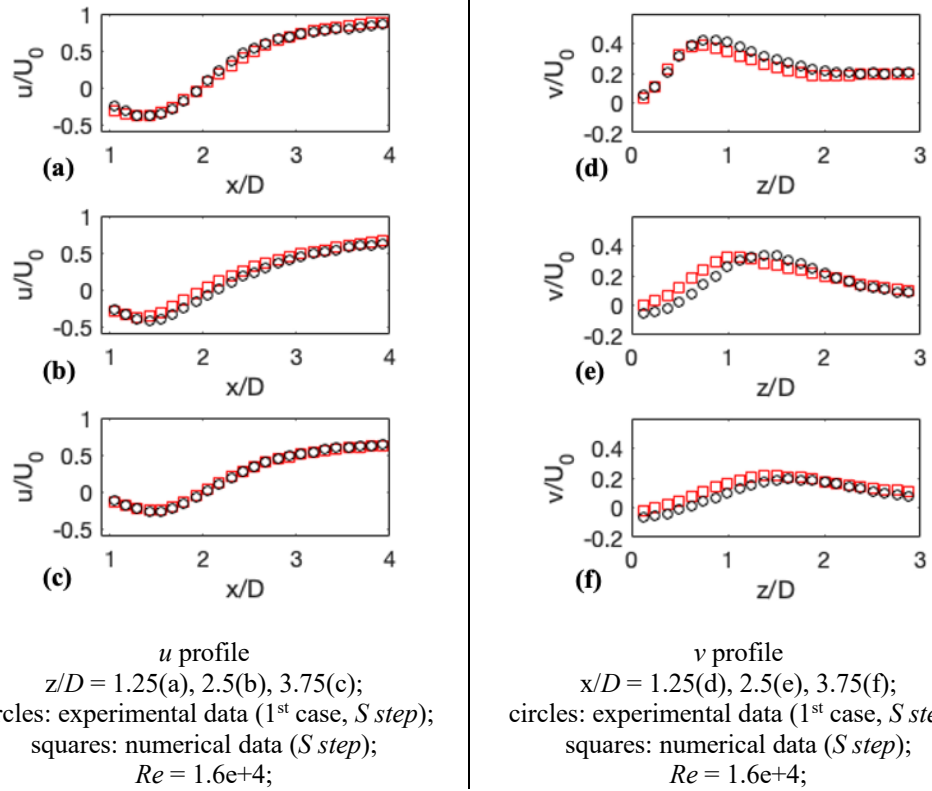
Figure 7.10 Velocity profile verification with the present experimental results (sharp step cylinder).

u profile
z/*D* = 1.25(a), 2.5(b), 3.75(c);
circles: experimental data (3rd case, *R step*);
squares: numerical data (*R step*);
Re = 1.6e+4;

v profile
x/*D* = 1.25(d), 2.5(e), 3.75(f);
circles: experimental data (3rd case, *R step*);
squares: numerical data (*R step*);
Re = 1.6e+4;
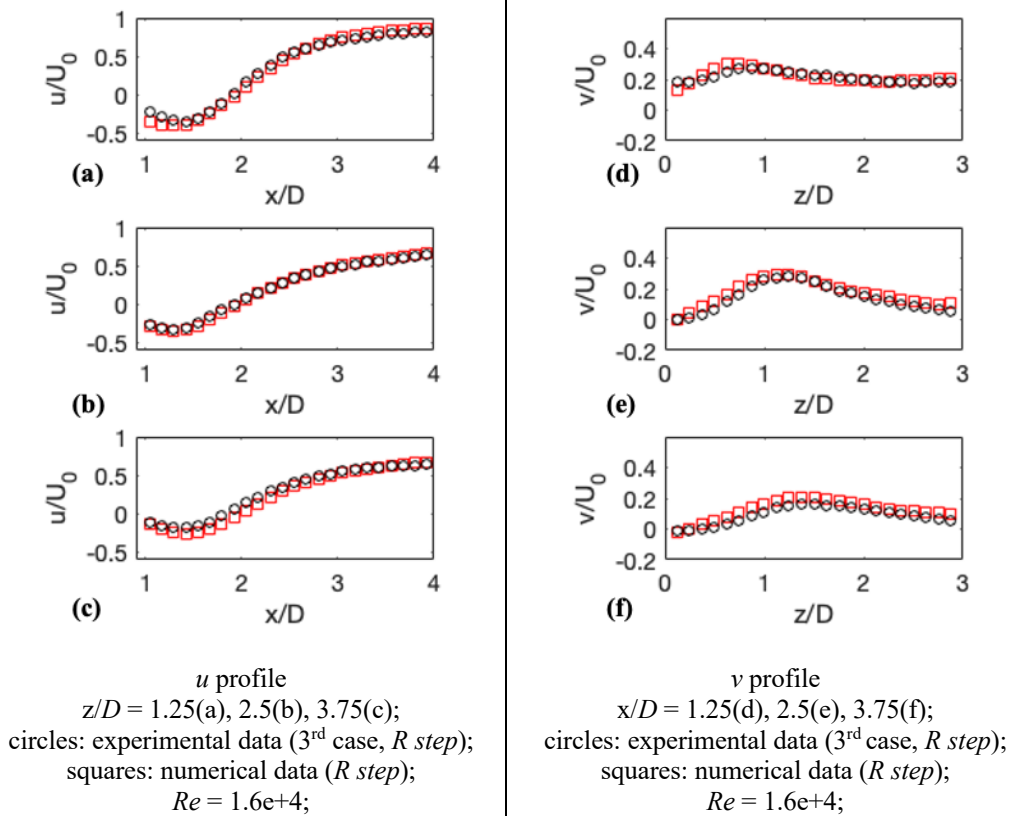
Figure 7.11 Velocity profile verification with the present experimental results (round step cylinder).

7.4 Brief Summary for Numerical Setup and Verification

This chapter presents numerical setup, convergence tests and the related verification. Followed by related numerical configurations, the hybrid grid typology with the combination of structured grids near cylinders and Cartesian grids in the outer region is introduced and adopted. The consequent part illustrates the design about grid typology around step cylinders. Convergence study on flow around plain cylinders figures out the reliable mesh layout at X-Y plane and grid resolution along the span. As for the verification part, surface pressure distribution (the present numerical outcome) near the sharp step cylinder is in agreement with the reference results (Ko & Chan, 1984; Morton, et al., 2009). Besides, velocity profiles (the present numerical outcome) regarding two velocity components near the selected regions ('NSV' region, 'PSV' region) behind sharp / round step cylinder are compared with that from the present experiments, indicating the good consistency.

Chapter 8
NUMERICAL RESULTS

This chapter presents numerical simulation results about complicated three-dimensional flow fields near the steps under the Reynolds number (*Re*) of 1.6e+4, with the emphasis on shape of step junction, i.e., sharp step junction (*S step*) and round step junction (*R step*). To be specific, this chapter successfully observes and compares streamwise vortices near sharp step junction and round step junction. In addition, qualitative and quantitative study near two types of step junction are followed, for instance, flow fields, surface pressure distribution and loading variation.

8.1 Streamlines near and behind Steps

Detailed discussion on the present experimental results has been given in Chapter 4 to Chapter 6, whereas all related flow fields being obtained from two measuring planes cannot fully characterise the three-dimensionality regarding complicated flow and vortices near the step junction. For instance, the 'downwash' denotes a branch of flow emanating from the rear side of step junction into the near wake region of large-diameter cylinder, which was used to clarify the mechanism of N-cell loop (Dunn & Tavoularis, 2006), and the occurrence of 'NSV' & 'PSV' region (section 6.1). However, the only strong proof to identify the 'downwash' from the present experimental study is the averaged two-dimensional velocity vector field behind step cylinders along Plane Y = 0*D* in figure 6.7, which cannot directly reflect the complicated three-dimensional activity near the step. Consequently, this subsection attempts to establish the relationship between two-dimensional 'downwash' observation from experimental results and corresponding numerical simulations, furthermore, to enrich more details about 'downwash', especially its three-dimensional description.
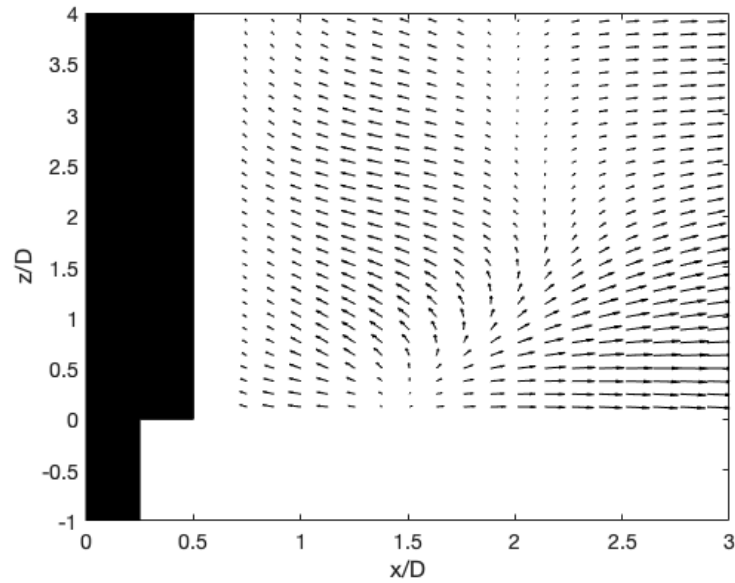
(a): experimental results, 1st case, *S step, Re* = 1.6e+4;
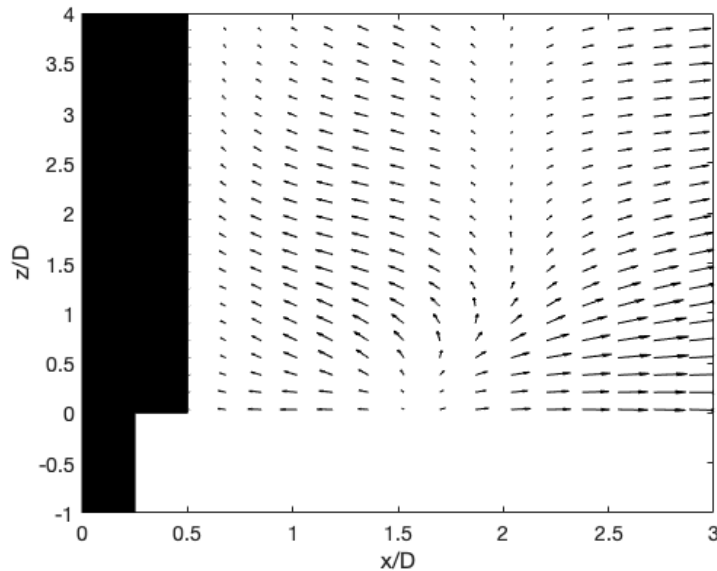
(b): numerical results, *S step, Re* = 1.6e+4;
Figure 8.1 Averaged velocity vector fields behind sharp step cylinder at Plane Y = 0*D*.

Figure 8.1 presents the comparison of averaged velocity vector field along the plane (Y = 0*D*) behind the sharp step cylinder at *Re* = 1.6e+4 between the present numerical simulation and experimental test. The notable spanwise flow behind the large-diameter cylinder termed as the 'downwash' is experimentally demonstrated in figure 8.1(a), from where one could clearly observe more details about its development. The 'downwash' starts near the position of x/*D* = 1.5, z/*D* = 0, travelling upwards along the span and subsequently splitting into two branches of flow towards two opposite directions, one branch of which goes downstream and the other branch of which turns back towards the rear side of large-diameter cylinder. The corresponding numerical results in figure 8.1(b) successfully reproduce the similar 'downwash' phenomenon and its evolution takes place

143

at the similar region suggesting the reliability of the present numerical simulation. It can be inferred that the three-dimensional 'downwash' obtained from the identical numerical simulation is acceptable. As a result, the forthcoming part extends the above-mentioned 'downwash' to three-dimensional version and presents the numerical results regarding streamlines near the sharp / round step junction in figure 8.2 (three-dimensional view) and figure 8.3 (top / side view).

(a): *S step*, *Re* = 1.6e+4;　　　　　　　(b): *R step*, *Re* = 1.6e+4;
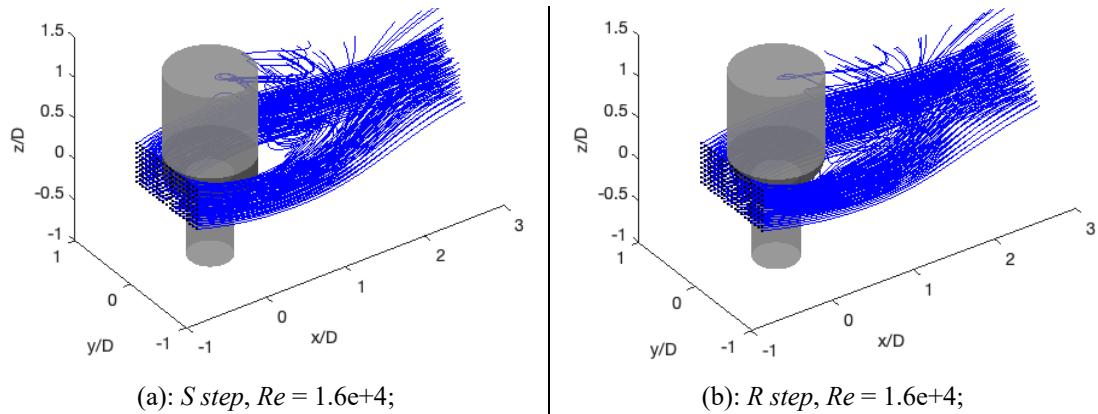
Figure 8.2 Three-dimensional view of numerical streamlines near the steps.

(a): top view, *S step*, *Re* = 1.6e+4;　　　(b): top view, *R step*, *Re* = 1.6e+4;

(c): side view, *S step*, *Re* = 1.6e+4;　　　(d): side view, *R step*, *Re* = 1.6e+4;
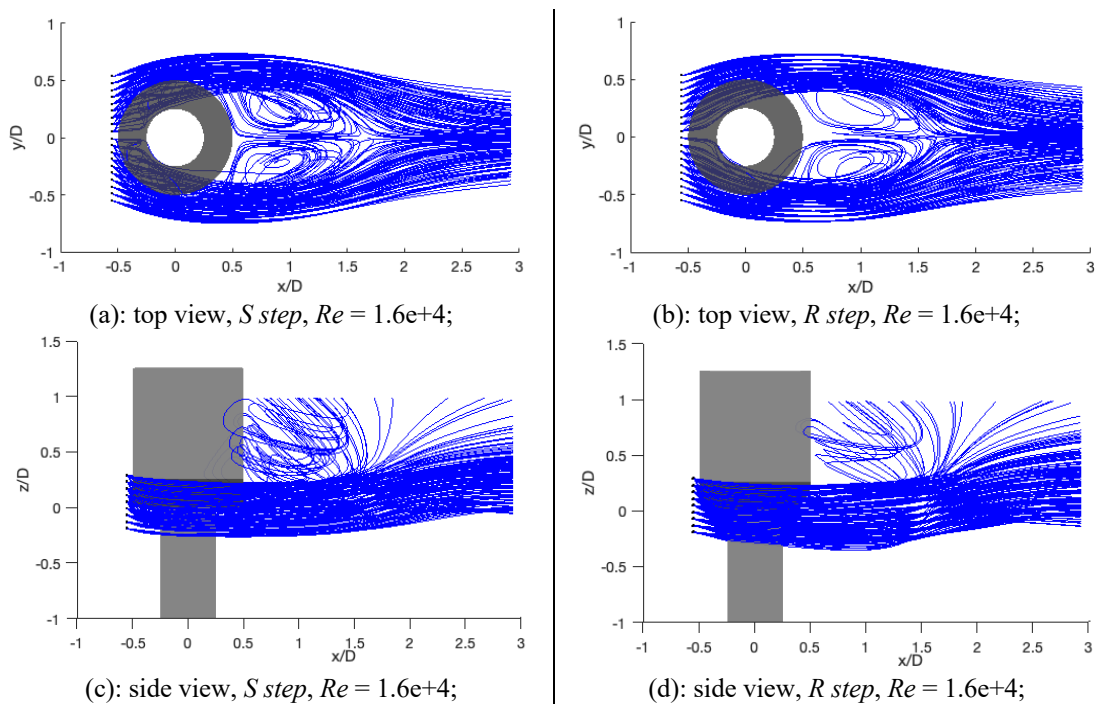
Figure 8.3 Diverse views of numerical streamlines near and behind the steps.

Streamlines in figure 8.2 and 8.3 clearly describe the three-dimensional flow development near and behind the sharp / round step junction. Firstly, considering the shared streamline trend regarding two types of step cylinder, the free stream travelling along the positive direction of X axis from left side hits the front side of step junction, and then horizontally splits into two branches moving downstream along the surface (see figure 8.3(a), (b)). Subsequently, a portion flow emanating from the rear side of step junction towards the

wake of large-diameter cylinder vertically splits into two branches (see figure 8.3(c), (d)), corresponding to the above-mentioned experimental phenomenon, namely two-dimensional 'downwash'. Considering the difference of streamlines near *S step* and *R step*, it could be obviously found that one branch of the spanwise flow being close to the back of large-diameter cylinder is weaker behind *R step* (round step junction). In addition, the front-view results and the close-up results are given in figure 8.4. Comparing figure 8.4(c) with figure 8.4(d), one could figure out apparent vortices near the step surface of *S step* (sharp step junction), whereas streamlines near the step surface of *R step* (round step junction) go parallel to round corner.

(a): front view, *S step*, *Re* = 1.6e+4;

(b): front view, *R step*, *Re* = 1.6e+4;

(c): close-up, *S step*, *Re* = 1.6e+4;

(d) : close-up, *R step*, *Re* = 1.6e+4;
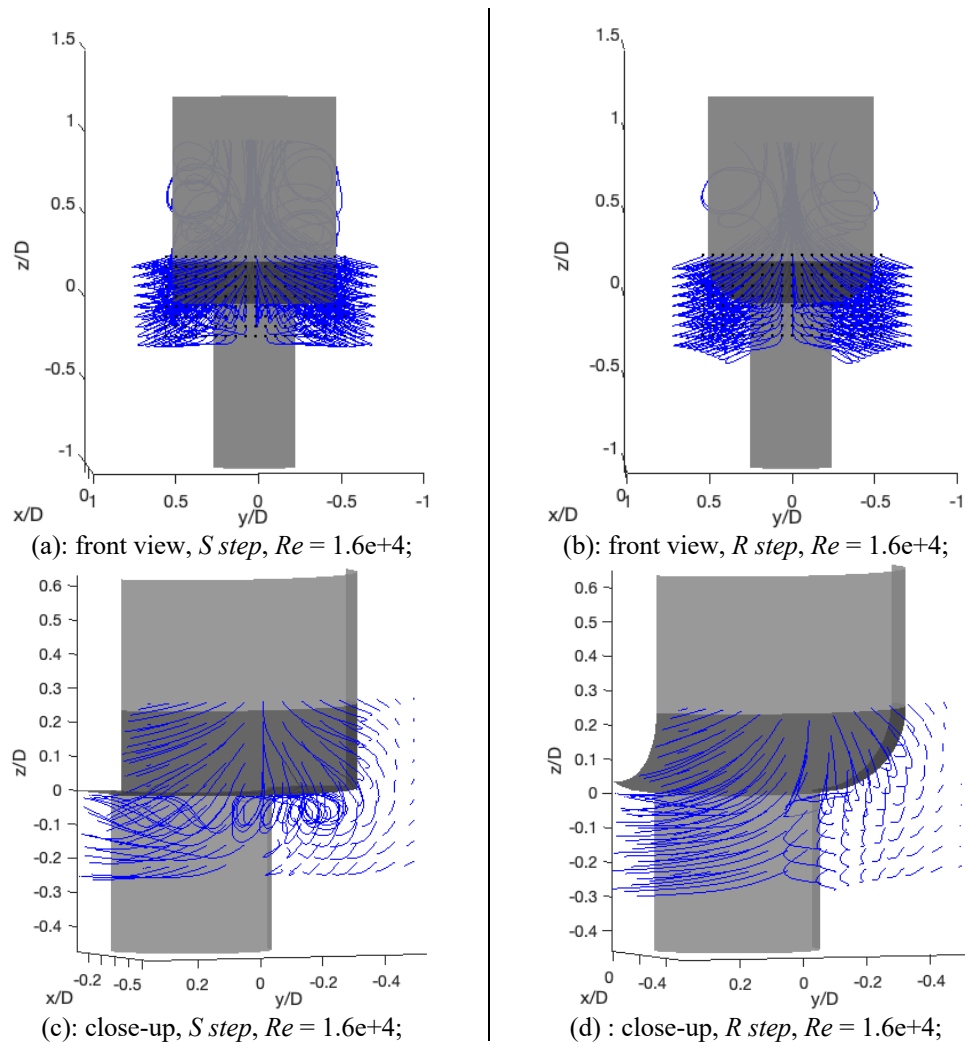
Figure 8.4 Diverse views of numerical streamlines near the steps.

145

8.2 Streamwise Vortices near Steps

Streamlines in figure 8.4(a) to (d) clearly exhibit the existence of vortices near sharp step junction, instead of near round step junction, highlighting the impact of shape of step junction. According to the reference (Dunn & Tavoularis, 2006; Morton, et al., 2009), the observed vortices near the step are termed as 'junction vortices' and 'edge vortices'. The incident flow hits the base of small cylinder at step; a portion flow turns back forming the 'reverse flow'. The 'reverse flow' merging with the consequent free stream, eventually rolls up and forms 'junction vortices'. Meanwhile, another portion flow going along the step junction surface forms 'edge vortices' at the rear edge of large-diameter cylinder. These two pairs of streamwise vortex move downwards at opposite directions, i.e., clockwise direction and anti-clockwise direction respectively. It should be noted that the 'edge vortices' stay closer to the step surface than 'junction vortices'. As a result, on the basis of the discussion of figure 8.4, this subsection numerically compares the streamwise vortices near the sharp step junction and the round step junction.

(a): side view;   (b): bottom view;
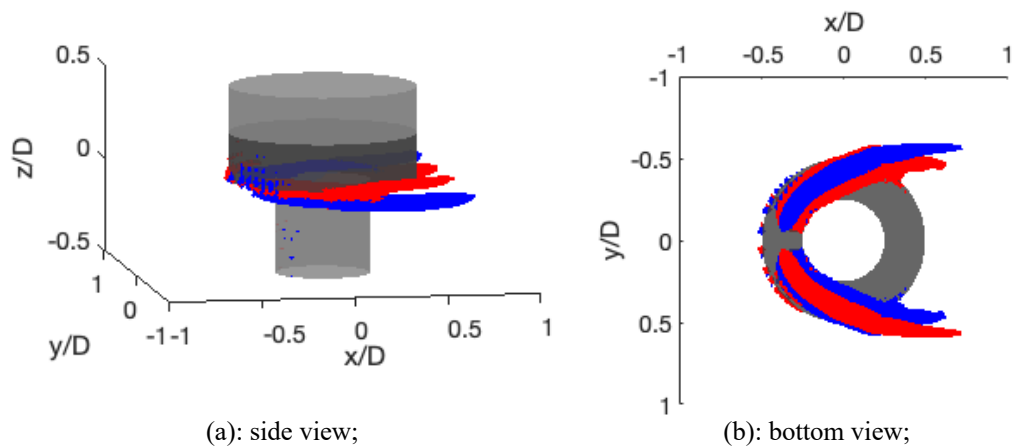
Figure 8.5 Streamwise vortex near step junction (sharp step cylinder, $Re = 1.6e+4$, $w^* = 0.02$).

(a): side view;   (b): bottom view;
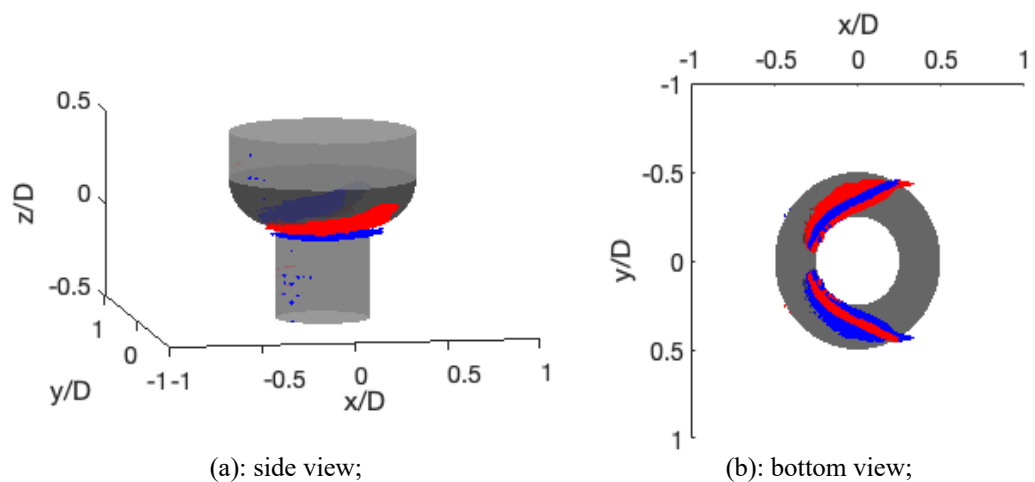
Figure 8.6 Streamwise vortex near step junction (round step cylinder, $Re = 1.6e+4$, $w^* = 0.02$).

Figure 8.5 and 8.6 depict streamwise vortices isosurface of $w^* = w_x \times D/U_0 = 0.02$ (the normalized vorticity at x direction) near sharp step junction and round step junction, where different colours denote different directions. One can observe two 'U-shaped' vortices near two steps are piled along spanwise direction. Besides, the vortex scale near round step junction being much weaker than that near sharp step junction is of interest, suggesting that the round step junction with the smooth geometric transition displays robust performance in mitigating streamwise vortices.

Figure 8.7 and 8.8 discuss the changing of streamwise vortices near sharp / round step junction at different isosurface values, i.e., 0.04 and 0.052. As it is mentioned above, junction vortices are at the base of small cylinder and edge vortices are at the edge of large cylinder. In other words, a pair of junction vortices are on top of a pair of edge vortices if looking at the step junction from the small-diameter cylinder side (see figure 8.7(a)). When it comes to the same isosurface value (0.04) for round step junction (see figure 8.7(b)), the junction vortices almost vanish, and only edge vortices are left, indicating that edge vortices near round step junction are more notable than junction vortices. As for the isosurface value of 0.052, nearly all streamwise vortices disappear near round step junction (see figure 8.8(b)), in contrast to that near sharp step junction, where junction vortices and edge vortices are still 'alive' (see figure 8.8(a)) and junction vortices are more notable than edge vortices. Consequently, compared with the sharp step junction, it can be inferred that the round step junction not only can mitigate the streamwise vortices near step junction, but also make edge vortices more outstanding than junction vortices.
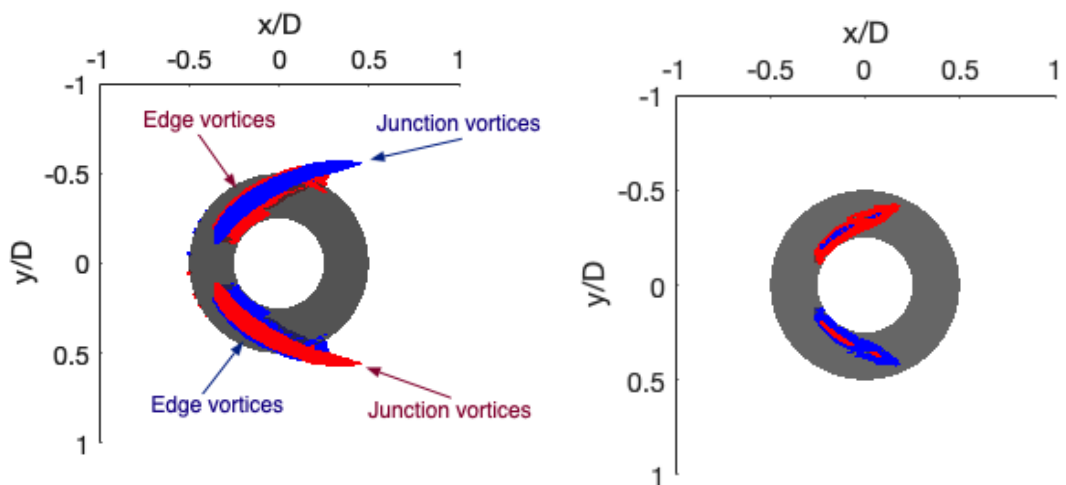
(a): sharp step cylinder, *Re* = 1.6e+4;   (b): round step cylinder, *Re* = 1.6e+4;
Figure 8.7 Streamwise vortex ($w^* = 0.04$) near step junction (bottom view).

(a): sharp step cylinder, *Re* = 1.6e+4;   (b): round step cylinder, *Re* = 1.6e+4;
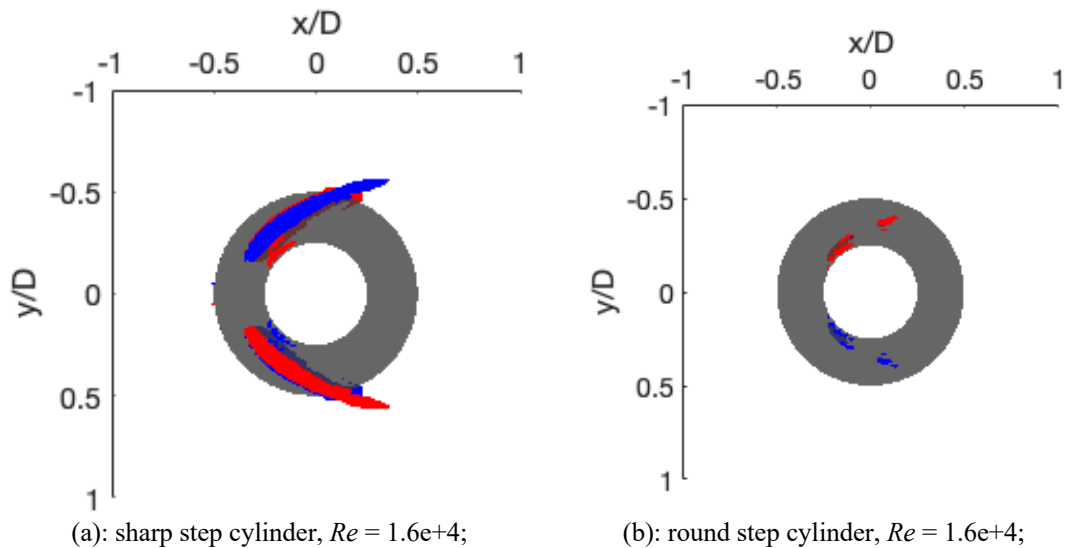
Figure 8.8 Streamwise vortex ($w^* = 0.052$) near step junction (bottom view).

8.3 Flow Fields near Steps

This section focuses on the comparison on flow fields near sharp step junction and round step junction. Figure 8.9 and 8.10 depict time-averaged flow fields at Plane Y = 0*D* near step junctions, together with the streamwise vortices isosurface at $w^* = 0.02$. The colormap is ratio of total local velocity to the incident velocity. Subsequently, time-averaged flow fields at other planes (Y = 0.2*D*, 0.4*D* and 0.55*D*) are plotted and presented in figure 8.11 to 8.13.
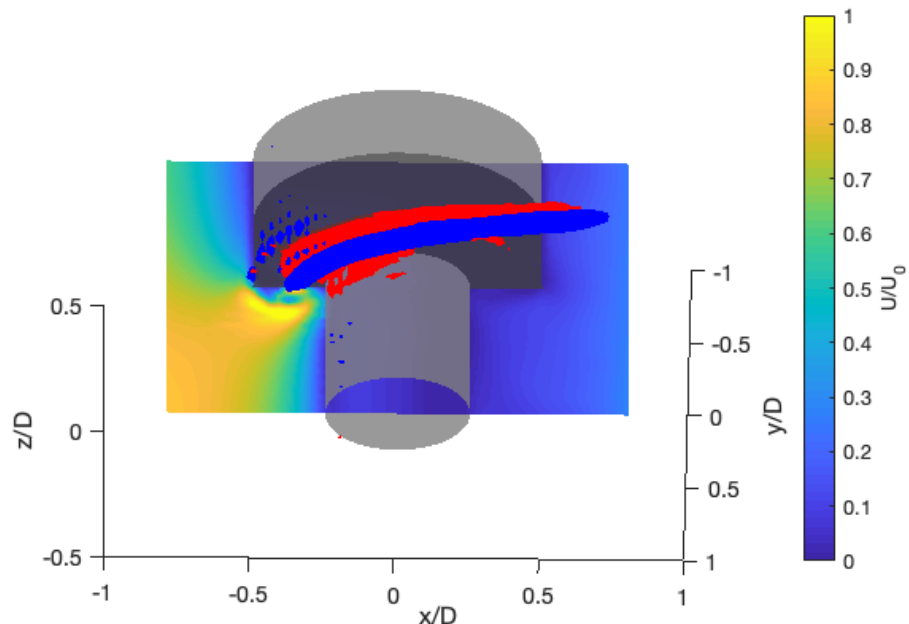
Figure 8.9 Streamwise vortex & velocity contour at the front (*Re* = 1.6e+4, sharp step cylinder).
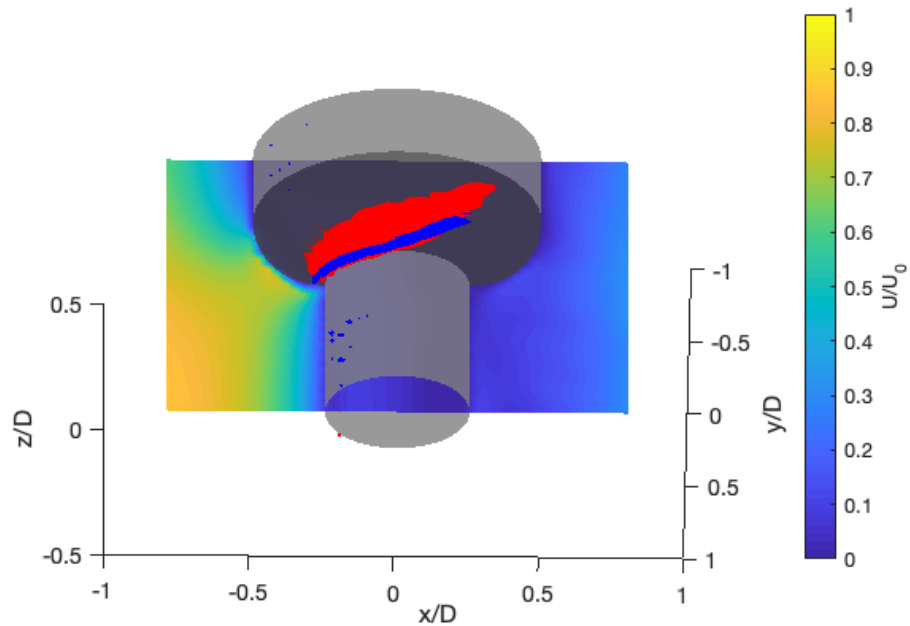
Figure 8.10 Streamwise vortex & velocity contour at the front (*Re* = 1.6e+4, round step cylinder).

The averaged flow field around sharp step junction and round step junction (figure 8.9 & 8.10) share similarities, that is, the incoming flow hitting the front side drops its velocity nearly till '0', except for the region near step surface where the velocity still retains a certain magnitude. More specifically, the velocity magnitude at front side of the sharp step is significantly stronger than that of the round step. For the region near the sharp step surface, one can observe a distinct 'roll-up', which is a symbol of the occurrence of a significant vortex. It was observed by Dunn & Tavoularis (2006) and was termed as 'recirculation bubble', and subsequently was numerically validated by Morton, et al. (2009). On the contrary, this so-called 'roll-up' disappears in front of round step junction, which can be inferred that the round step surface can smooth the flow field in front of the step junction.
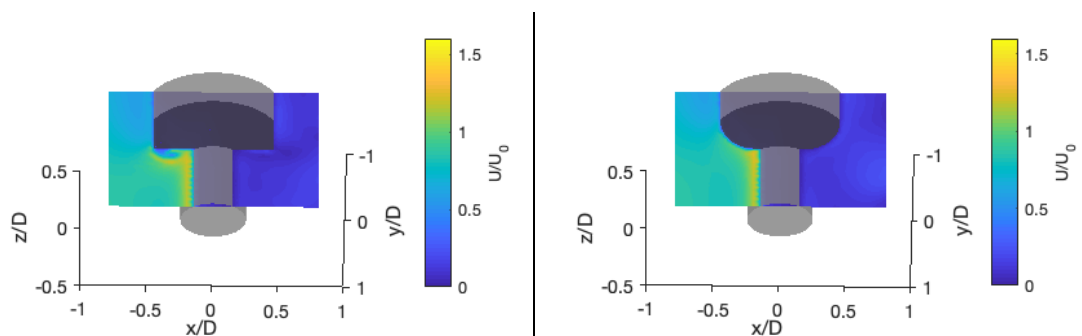
(a): sharp step cylinder, *Re* = 1.6e+4;   (b): round step cylinder, *Re* = 1.6e+4;

Figure 8.11 Streamwise vortex & velocity contour at the side (Plane Y = 0.2*D*).

(a): sharp step cylinder, *Re* = 1.6e+4;   (b): round step cylinder, *Re* = 1.6e+4;
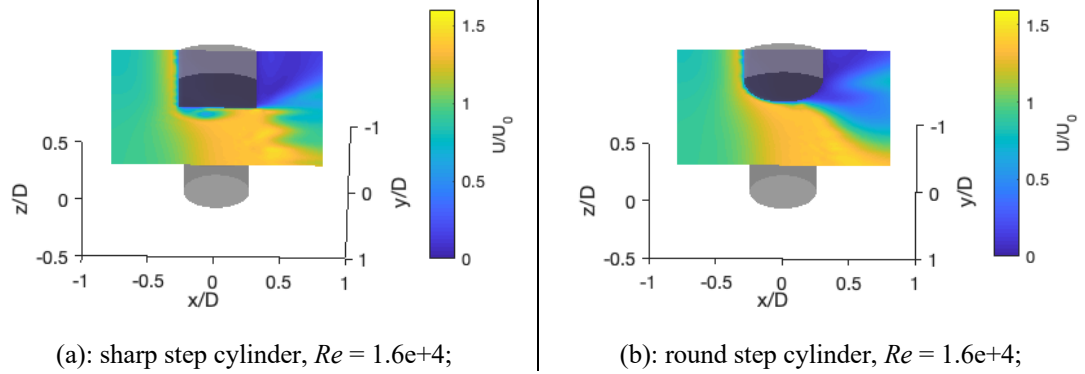
Figure 8.12 Streamwise vortex & velocity contour at the side (Plane Y = 0.4*D*).

(a): sharp step cylinder, *Re* = 1.6e+4;   (b): round step cylinder, *Re* = 1.6e+4;
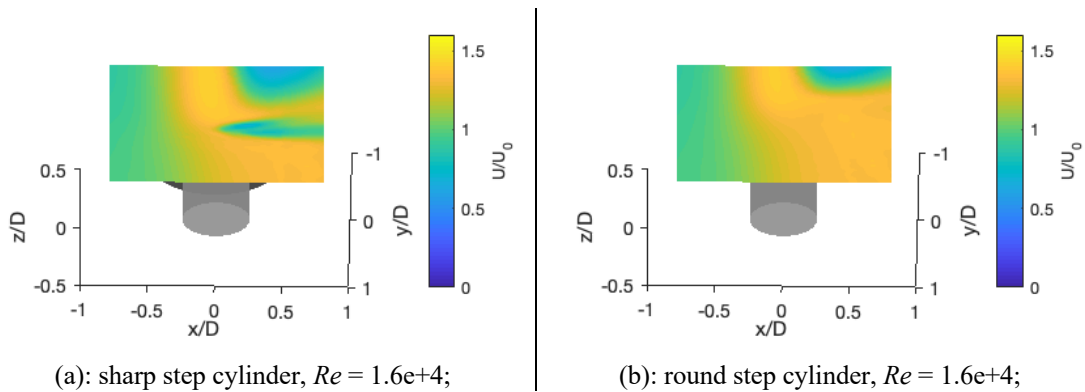
Figure 8.13 Streamwise vortex & velocity contour at the side (Plane Y = 0.55*D*).

Similarly, averaged velocity contours along three other different slices (Plane Y = 0.2*D*, Plane Y = 0.4*D* and Plane Y = 0.55*D*) are plotted and presented in figure 8.11 to 8.13. The phenomenon of 'roll-up' can be perceived evidently near the sharp step surface at Plane Y = 0.2*D* (figure 8.11(a)) and Plane Y = 0.4*D* (figure 8.12(a)). Besides, compared with that shown in figure 8.9, one can observe the 'roll-up' gradually moves downstream (figure 8.11(a), 8.12(a)), accompanied with reducing its thickness and extending its horizontal scope. However, the 'roll-up' activity disappears all the time near round step junction in figure 8.11(b), 8.12(b), 8.13(b). In summary, velocity contours along various planes near step junctions firmly prove that round step surface can help relief three-dimensional flow motion near the step junction.

sharp step cylinder;
Plane X = 0*D*, 0.0625*D*, 0.125*D*,
0.1875*D*, 0.25*D*, 0.3125*D*, 0.375*D*,
0.4375*D*;

round step cylinder;
Plane X = 0*D*, 0.0625*D*, 0.125*D*, 0.1875*D*,
0.25*D*, 0.3125*D*, 0.375*D*, 0.4375*D*;
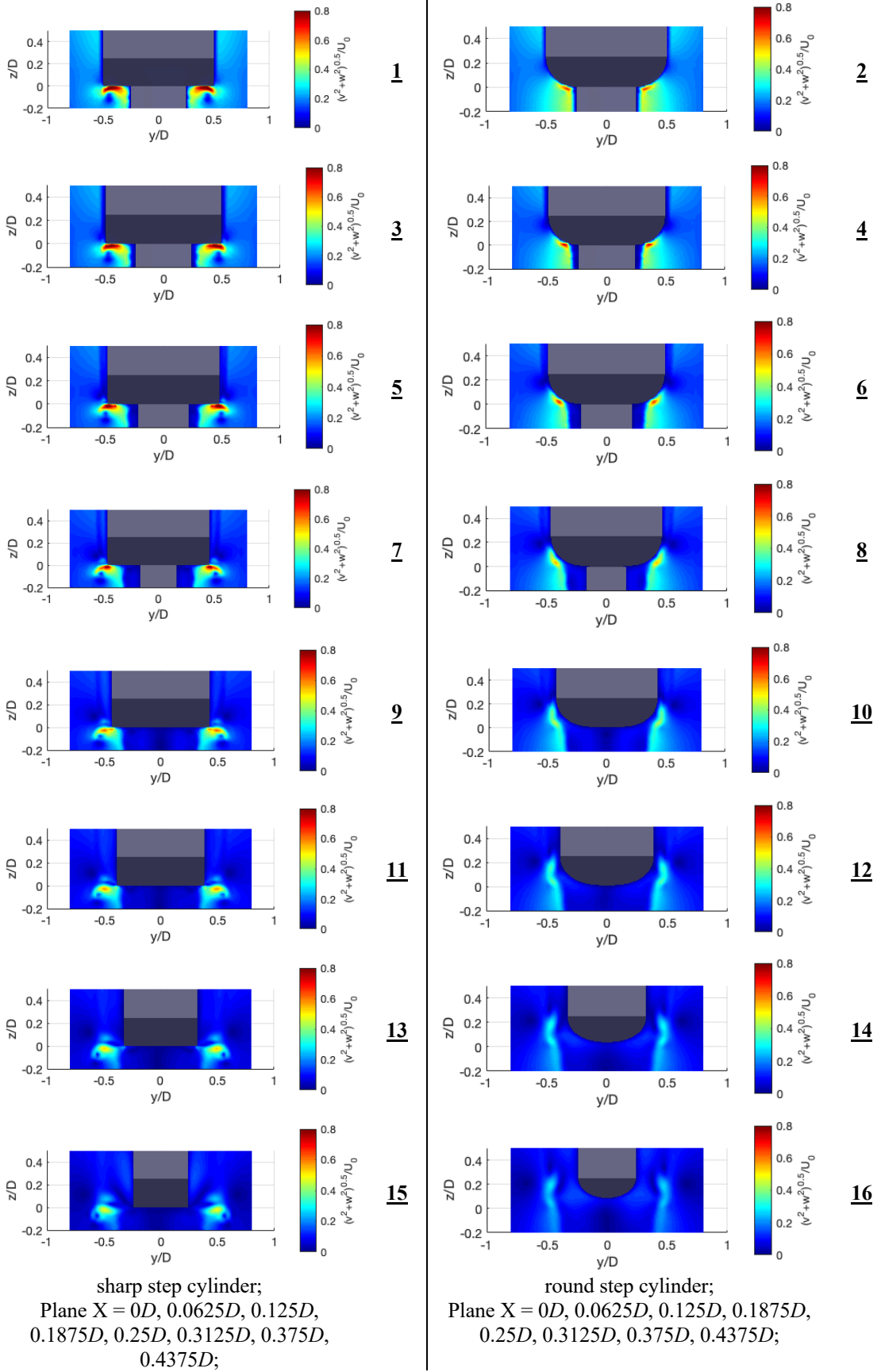
Figure 8.14 Velocity contour at back side (*Re* = 1.6e+4).

In addition, consider time-averaged velocity fields along various transverse planes, i.e., Plane X = 0*D*, 0.0625*D*, 0.125*D*, 0.1875*D*, 0.25*D*, 0.3125*D*, 0.375*D*, 0.4357*D*, 0.5*D*, 0.5625*D* and plot corresponding velocity contours in Figure 8.14 and 8.15. It should be noted that the colormap stands for the combination of crossflow velocity (*w*) and spanwise velocity (*v*). By comparing velocity contours along diverse planes near sharp step cylinder and round step cylinder, one can figure out the similar trend that velocity magnitude near sharp step junction is larger than that near round step junction. The left column of graphs in figure 8.14 & 8.15 depicts flow development along a sequence of planes near the sharp step junction. The flow near the sharp step junction weakens downstream, accompanied by the identical velocity magnitude core moving off the cylinder axis and eventually jumping over the step edge upwards (figure 8.15(1), (3)). As for the round step junction shown in the right column of figure 8.14 & 8.15, the significant velocity region displays a clear upward displacement along the round step surface ultimately giving rise to the velocity magnitude core being located at a higher position.

sharp step cylinder;
Plane X = 0.5*D*, 0.5625*D*;

round step cylinder;
Plane X = 0.5*D*, 0.5625*D*;
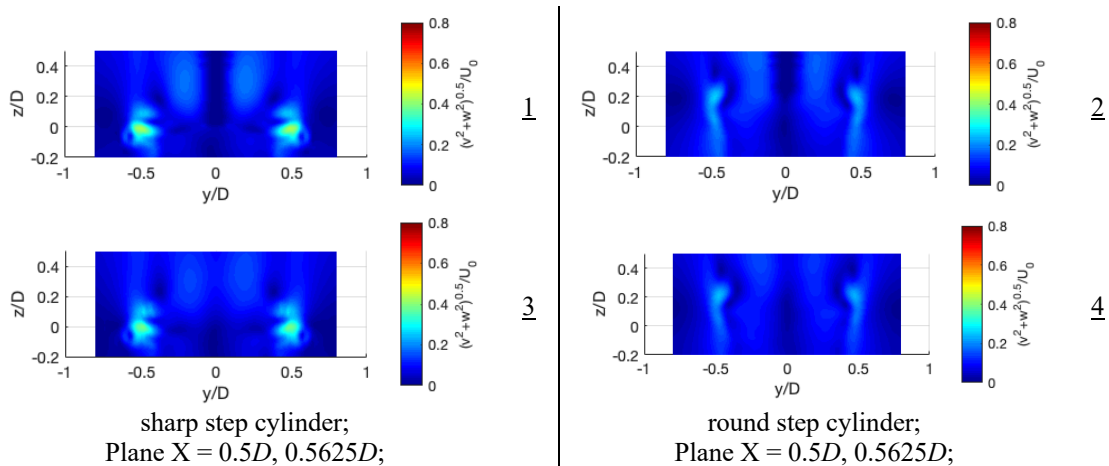
Figure 8.15 Velocity contour at back side (*Re* = 1.6e+4).

8.4 Surface Loading near Steps

This section focuses on surface pressure distribution and force coefficient variation from two regions namely region near step junction and region approaching step junction. The former region comprises the step surface (ring-shaped surface for sharp step, and round surface for round step), the surface at the span of $0D \sim 0.25D$; the latter region comprises a portion of large cylinder surface within the span of $0.25D \sim 2D$, a portion of small cylinder surface within the span of $-0.5D \sim 0D$. The surface pressure distribution from the above-mentioned two regions is considered, whereas analysis about the loading variation is only applied to region near step junction. Figure 8.16 and 8.17 compare the surface pressure distribution near two types of step junction. Two notable high-pressure areas from sharp step junction are exposed, namely one near the front edge of large-diameter cylinder and one near the front base of small-diameter cylinder; the surface pressure distribution displays a huge difference at two sides of the front edge of large-diameter cylinder from sharp step junction. Whilst the pressure distribution regarding round step surface has a smooth transition, and the pressure coefficient at the front base of small-diameter cylinder is lower than that from sharp step junction.
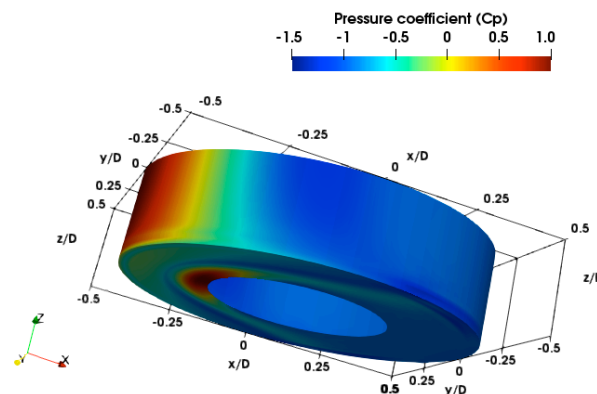
Figure 8.16 Surface pressure distribution near sharp step junction (Re = 1.6e+4).
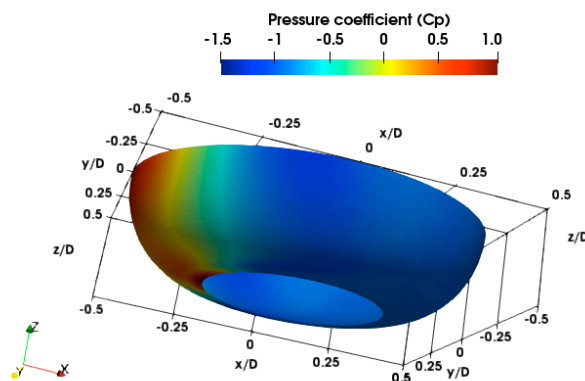
Figure 8.17 Surface pressure distribution near round step junction (Re = 1.6e+4).

In order to present a direct comparison, the surface pressure data is given a further processing by projecting the data to the identical round corner (figure 8.18). Side view and top view of the step cylinder are given in figure 8.18(a), (e), where sharp step junction and round step junction are highlighted and coloured by blue and red. Figure 8.18(b) and (c) explain how to project the step surface (the sharp one marked as blue solid line; the round one marked as red solid line) onto the identical round corner (marked as blue / red dash line). Subsequently, the identical round corner is applied another projection, to unite the content from sharp step and round step onto a flat ring (marked by orange colour), slightly larger than the original ring (marked as black dash circle).
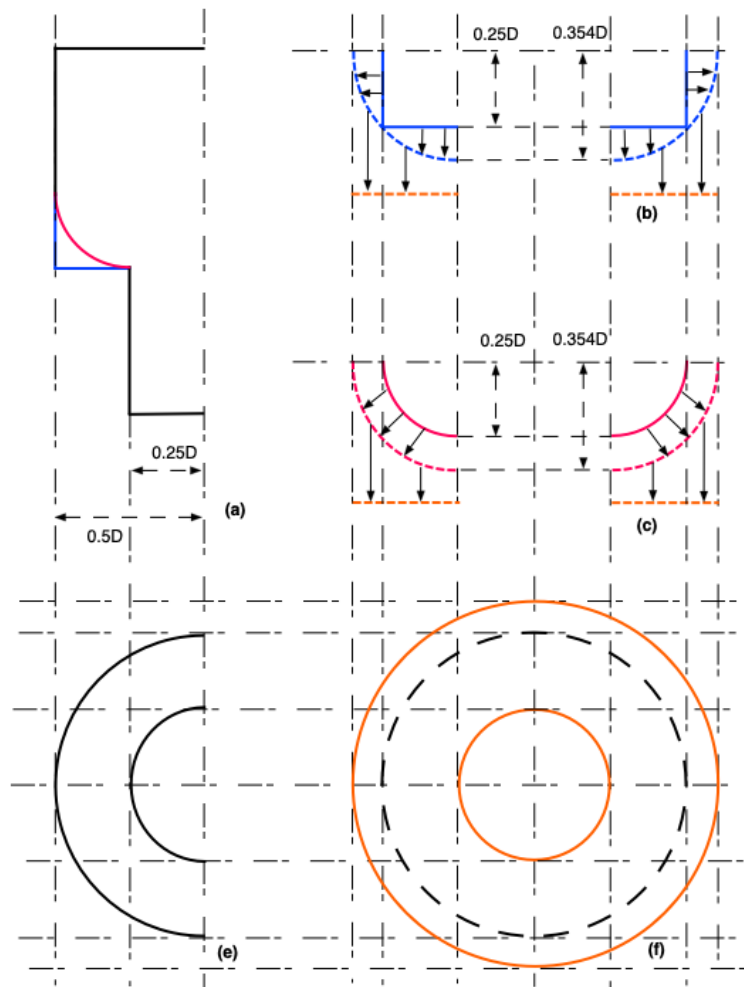
Figure 8.18 Explanation about surface pressure projection.

Note: (a): side view of step cylinder models; (b), (c): side view of surface pressure projection; (e): top view of step cylinders; (f): top view of surface pressure projection; Blue solid line: sharp corner; Red solid line: round corner; Blue dash line / Red dash line: large round corner; Orange dash / solid line: the outline of large round corner.

Followed by the operation in figure 8.18, the time-averaged surface pressure (Cp) layout near sharp / round step junction are compared in figure 8.19 & 8.20. High pressure coefficient is detected at the base of small cylinder (x/D = -0.25, y/D = 0) for sharp step cylinder and round step cylinder, the former of which is higher. By focusing on the pressure coefficient transition near the step corner (marked as black dash circles in figure 8.19 and figure 8.20), one can observe a smooth changing for the round step corner, in contrast to a significant jump for the sharp step corner.
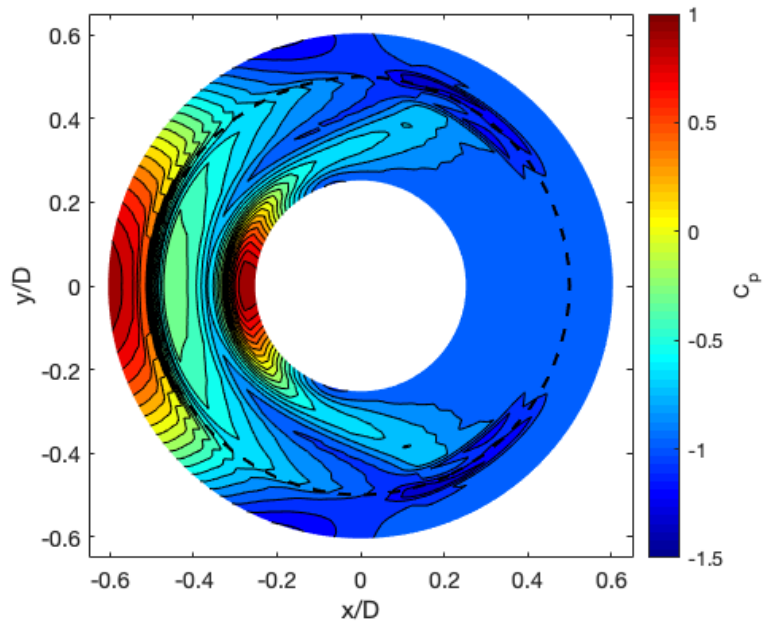
Figure 8.19 Surface pressure of sharp step junction at the identical round corner (Re = 1.6e+4).
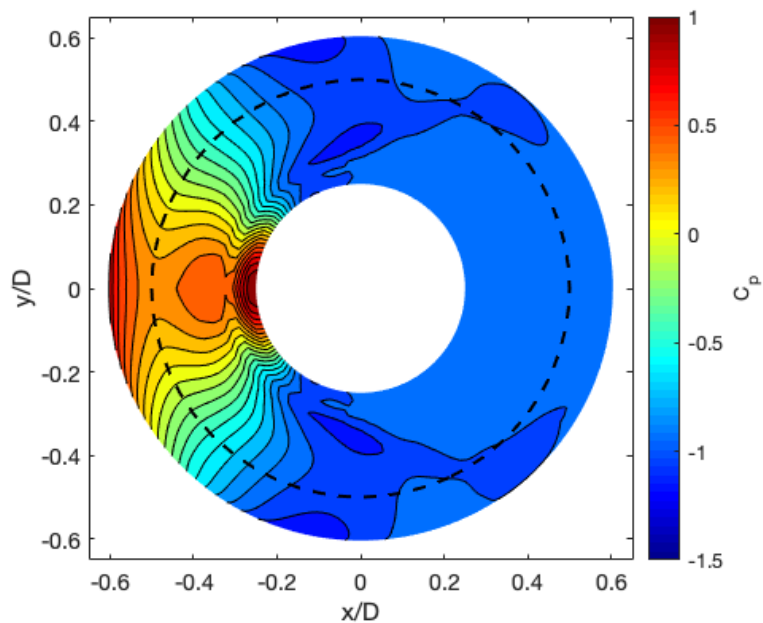
Figure 8.20 Surface pressure of round step junction at the identical round corner (Re = 1.6e+4).

Figure 8.21 and Figure 8.22 give a description about surface pressure distribution at the region approaching the step junction from large-diameter cylinder side ($0.25 < z/D < 2$) and small-diameter cylinder side ($-0.5 < z/D < 0$), where the arc angle of '0' degree stands for the stagnation point. Looking at the large cylinder side ($0.25 < z/D < 2$) in figure 8.21 and figure 8.22, pressure contour lines in the front side ($0 \sim 50°$) roughly keeps parallel to the cylinder axis along the span range of $z/D = 1 \sim 2$ and exhibit slightly bending within $z/D = 0.25 \sim 1$. As for the pressure distribution on small cylinder surface ($-0.5 < z/D < 0$), the pressure coefficient keeps stable along the span range of $-0.5 < z/D < -0.2$, whereas at $-0.2 < z/D < 0$, the pressure distribution is affected by the step junction. More specifically, the influence from sharp step junction is more significant than that from round step junction. Take the contour line '0.8' near 20° as an example, it has a big 'turn around' between $z/D = -0.1$ and $z/D = 0$ near sharp step junction, whilst just gives a slightly bending at the similar location near round step junction.
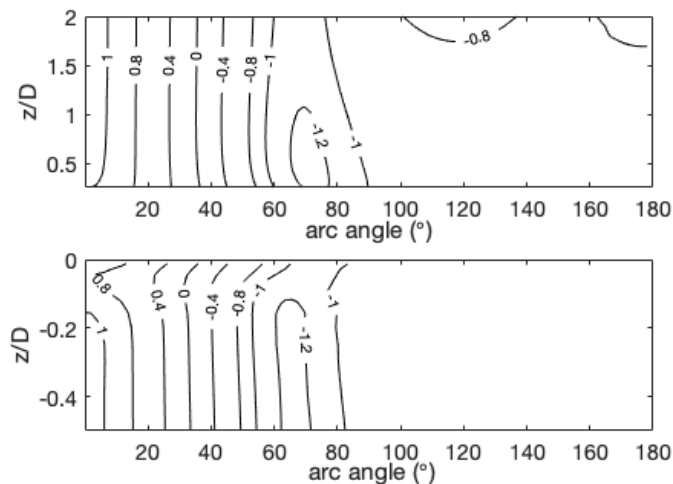
Figure 8.21 Surface pressure distribution out of sharp step junction ($Re = 1.6e+4$).
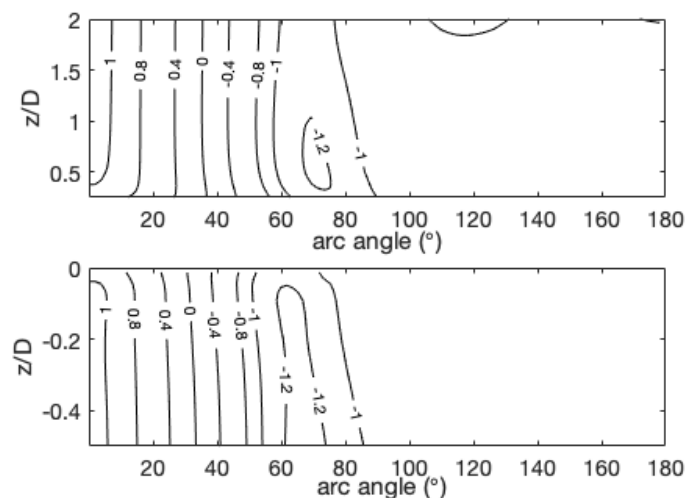
Figure 8.22 Surface pressure distribution out of round step junction ($Re = 1.6e+4$).

The loading variation over time ($t^* = t \times U_0/D$) at region near sharp / round step junctions is presented in figure 8.23. According to equation 2.3, force coefficients are calculated using the product of large diameter (D) multiplied by spanwise length ($0.25D$) as the 'reference area'; the involved loading components at three directions are drag coefficient, lift coefficient and span coefficient (loading along span direction). In figure 8.23, one could perceive force along span direction (span coefficient) is more significant than drag force (drag coefficient) near two types of step junction (*S step* and *R step*). By comparing results between *S step* and *R step*, it is apparent that loading along three directions is suppressed near *R step*; the corresponding statistic outcome is summarized in table 8.1.
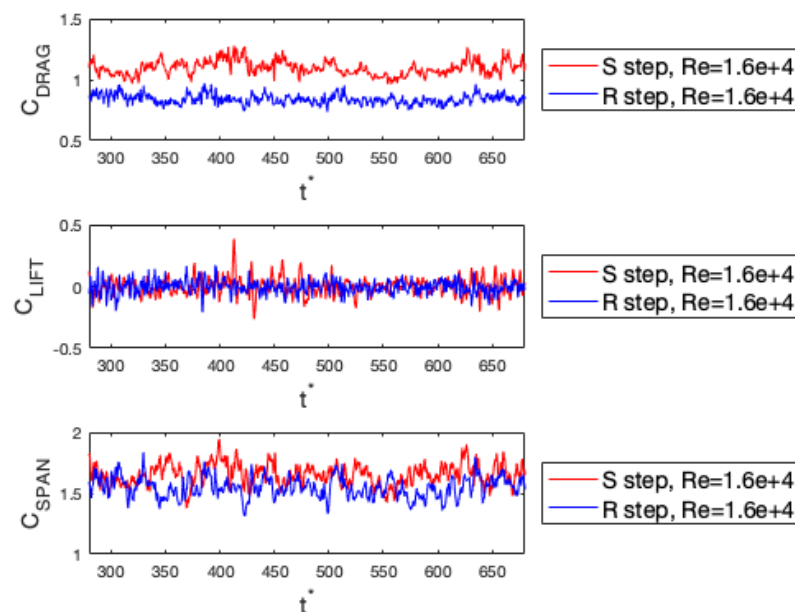
Figure 8.23 Variation of force coefficients (drag, lift, span) over time.

Note: the direction of 'span coefficient' for *S step* and *R step* is constant and identical; related content of C_{SPAN} in figure 8.23 and table 8.1 reflects the absolute value.

Table 8.1 Summary of statistical results of force coefficients.

	S step, Re = 1.6e+4	*R step*, Re = 1.6e+4
Mean drag coefficient (C_{DRAG})	1.107	0.824
Mean span coefficient (C_{SPAN})	1.652	1.549
RMS lift coefficient (C_{LIFT})	0.0727	0.0528

8.5 Brief Summary for Numerical Results

This chapter analyses related numerical results in terms of sharp step cylinder and round step cylinder at Re = 1.6e+4, and the major work focuses on the comparison of streamwise vortices, averaged flow fields, surface pressure coefficient and loading variation. Firstly, this chapter reproduces two-dimensional 'downwash' at Plane Y = 0D and successfully extends it into three-dimensional version via the exhibition of numerical streamlines near step junctions. Discussion about three-dimensional streamlines confirms the 'downwash' is weaker behind the round step cylinder. Subsequently, the observed discrepancy of streamlines near sharp step surface and round step surface introduces the discussion about streamwise vortices namely 'junction vortices' and 'edge vortices', revealing they are weaker near the round step surface. Besides, junction vortices are stronger than edge vortices near sharp step surface, whereas the former is weaker than the latter near round step surface. After that, this chapter performs analysis on flow fields at diverse planes near step junctions and discovers flow fields near round step junction are more smooth but weaker. Discussion on surface pressure coefficient distribution gives a smooth layout on round step surface, in contrast to that on sharp step surface. In addition, loading at round step junction is apparently suppressed, compared with that of sharp step junction.

Chapter 9
CONCLUSIONS AND RECOMMENDATIONS

9.1 Conclusions

This thesis performs investigation regarding complicated flow structures behind step cylinders, with the emphasis on the impact of shape of step junction (*S step*, *R step*) and Reynolds number (*Re* = 1.6e+4, 3.3e+4). To be more specific, apart from the normal step cylinder (*S step*, sharp step cylinder), a modified type is tested, i.e., *R step* (round step cylinder). The only discrepancy between these two models, is way of transition between large-diameter cylinder and small-diameter cylinder. By launching experimental tests in relation to sharp step cylinder under high Reynolds number (1.6e+4), quantitative velocity fields, as well as vortex shedding characteristics, provide precious data for the repository of study on 'sharp step cylinder' for the specific Reynolds number. The subsequent experimental investigation in terms of the round step cylinder at *Re* = 1.6e+4, 3.3e+4, promotes to gain a deeper insight of the impact of shape of step junction towards flow structures in the wake zone. Apart from that, related numerical simulations give rise to results about three-dimensional flow fields, surface loading variation, etc., which could be treated as the supplement of the present experimental study. More details about valuable conclusions can be listed as follows.

1) Experiments in terms of the sharp step cylinder are carried out by applying a variety of analysis methods, for instance, time-averaged / instantaneous velocity fields analysis, spectral-based analysis, wavelet-based analysis, POD-based analysis; corresponding conclusions are summarized as follows.

I.   Three vortex-shedding cells, i.e., L-cell, N-cell and S-cell, are well recognised in the wake under high Reynolds number by identifying 'velocity valleys'. According to spectral analysis, the frequency ratio (f_L / f_N) and averaged N-cell extent (length) are comprehensively studied within a large Reynolds number range. On the basis of linear fit outcome, a critical Reynolds number region $672 < Re < 836$ is put forward. The variation of frequency ratio and averaged N-cell length changes their linear trend before and after this critical Reynolds number. Dominant frequency transits smoothly between neighbouring vortex cells, and fluctuation of dynamic local frequency shows larger amplitude than that under lower Reynolds number.

II. According to velocity spectra (energy related), averaged spatial energy fields behind sharp step cylinder regarding three vortex cells are constructed, followed by the concept of 'averaged energy decay' being put forward and discussed. Two parameters ('energy decay rate' and 'energy decay shift') being extracted from the linear fit of 'averaged energy decay' are proved to be inherent features of vortex shedding. Besides, the 'energy decay rate' of N-cell is significantly bigger than that of the other two cells (L-cell, S-cell). Similar energy decay rate of L-cell, S-cell and that behind plain cylinders proves that L-cell and S-cell belong to Karman vortex shedding.

III. With the assistance of POD-based analysis, three pairs of POD mode corresponding to three distinctive 'principle components' can be clearly recognized. By comparing frequency information, one can figure out S-cell is an independent 'principle component', whereas N-cell and L-cell prefer to stay in the wake by forming two basic connections (Type A and Type B). Besides, instantaneous velocity fields can be reconstructed by taking S-cell, N-cell and L-cell related components into account, evidencing that notable dynamic vortex interactions in the wake feature the random characteristic, which differs from that under low Reynolds number.

2) Studies on the round step cylinder are carried out by means of experiments with the same setting as that for the sharp step cylinder. Similarly, identical 'data processing' is implemented, revealing notable influence about the shape of step junction which can be summarized as follows.

I. Three distinct vortex-shedding cells can also be successfully spotted in the wake, whereas N-cell features unique properties which differs from that behind the sharp step cylinder. For instance, its frequency (f_N) is lower and two averaged boundaries (N-L boundary, N-S boundary) exhibits slight shift along the span towards the step junction. The dynamic frequency outcome describes more significant signal with stronger fluctuation near round step junction.

II. With regard to the 'averaged energy decay' analysis and POD-based analysis, similar trend with that behind the sharp step cylinder is exposed, validating that the 'averaged energy decay' can be treated as the inherent feature regarding normal vortex shedding. As for the POD-based analysis, the POD

modes which 'N-cell' dominates behind the round step cylinder takes more contribution than that behind the sharp step cylinder.

III.   Time-averaged velocity fields at Plane Y = 0D reveals different phenomenon between *S step* and *R step*. Two highlighted velocity regions are observed behind step junctions and termed as 'NSV' region and 'PSV' region. By associating with velocity vector field, the 'downwash' can be spotted, which shows strong link with 'NSV' region and 'PSV' region. Consequently, based on study about 'NSV' region size and 'PSV' region size, the 'downwash' is proved to become weaker behind round step junction.

3) The objective of corresponding numerical simulation is to compare flow-related information near sharp step cylinder and round step cylinder at *Re* = 1.6e+4, for instance, streamwise vortices, averaged flow fields, surface pressure coefficient distribution and surface loading variation between. It is appreciated that the present numerical simulation successfully reproduces the 'downwash' phenomenon and extend it to three-dimensional version via the exhibition of streamlines. Streamwise vortices near step junctions demonstrate a significant difference between two types of step junctions; weaker streamwise vortices are discerned near round step junction. Besides, flow fields near round step junction are weaker. Surface pressure coefficient distribution is smoother and loading variation is suppressed, compared with that near the sharp step junction.

9.2 Recommendations for Future Work

In order to gain deep insight on complicated the flow field near the riser (with buoyancy modules) and the loading variation near the step surface, the present study carries out a series of wind tunnel experiments and relevant numerical simulations to investigate the simplified models (viz. sharp step cylinder and round step cylinder) with the Reynolds number of 1.6e+4, 3.3e+4. The present results together with final conclusions clearly characterise diverse types of vortex shedding, flow fields behind sharp / round step cylinders and surface pressure / loading distribution near the step junction. Nevertheless, there is still a plenty of 'unknown' behind step cylinders which needs to be revealed. The following content can be a brief extension which will be the reliable guidance for the author's future work.

The riser with buoyance modules is always placed in arch shape in deep ocean environment, which obviously induces to slanting riser-buoyance components with diverse angles against the incident flow. Besides, the interaction between the incident flow and flexible riser makes 'Vortex-induced Vibration' (VIV) prevalent in practical ocean engineering, which greatly causes fatigue and threatens the 'service time'. As a result, the author will focus on flow around inclined step cylinders, and VIV of sharp / round step cylinders. As for the vortex investigation, the author will do relevant theoretical and methodological research on vortex dynamics and vortex identification.

REFERENCE

Adrian, R. J., Christensen, K. T. & Liu, Z. C., 2000. Analysis and interpretation of instantaneous turbulent velocity fields. *Experiments in Fluids,* 29(3), pp. 275-290.

Ahmed, A. & Bays-Muchmore, B., 1992. Transverse flow over a wavy cylinder. *Physics of Fluids A: Fluid Dynamics,* 4(9), pp. 1959-1967.

Šidlof, P., Antoš, P., Šimurda, D. & Štěpán, M., 2017. Turbulence intensity measurement in the wind tunnel used for airfoil flutter investigation. *EPJ Web of Conferences,* Volume 143, p. 02107.

Alderton, N. & Thethi, R., 1998. Choosing the most appropriate rigid catenary riser design for various deepwater and harsh environments. *Advances in Riser Systems & Subsea Technologies for Deepwater Euroforum.*

Aseyev, A. S., 2015. *Vortex identification in the wake of a wind turbine array.* Portland State University: Master's thesis.

Ayoub, A. & Karamcheti, K., 1982. An experiment on the flow past a finite circular cylinder at high subcritical and supercritical Reynolds numbers. *Journal of Fluid Mechanics,* Volume 118, pp. 1-26.

Baban, F. & So, R. M. C., 1991. Recirculating flow behind and unsteady forces on finite-span circular cylinders in a cross-flow. *Journal of Fluids and Structures,* 5(2), pp. 185-206.

Bearman, P. W. & OWen, J. C., 1998. Reduction of bluff-body drag and suppression of vortex shedding by the introduction of wavy separation lines. *Journal of Fluids and Structures,* 12(1), pp. 123-130.

Berger, E. & Wille, R., 1972. Periodic flow phenomena. *Annual Review of Fluid Mechanics,* 4(1), pp. 313-340.

Berger, M. J., Helzel, C. & LeVeque, R. J., 2003. H-box methods for the approximation of hyperbolic conservation laws on irregular grids. *SIAM Journal on Numerical Analysis,* 41(3), pp. 893-918.

Berkooz, G., Holmes, P. & Lumley, J. L., 1993. The proper orthogonal decomposition in the analysis of turbulent flows. *Annual Review of Fluid Mechanics,* 25(1), pp. 539-575.

Bjørkli, R., 2012. *Numerical Simulations of Viscous Flow Around Stepped Circular Cylinder.* Institutt for marin teknikk: Master's thesis.

Blazek, J., 2015. *Computational fluid dynamics: principles and applications.* Oxford: Elsevier.

Breuer, M., 2000. A challenging test case for large eddy simulation: high Reynolds number circular cylinder flow. *International Journal of Heat and Fluid Flow,* 21(5), pp. 648-654.

Catalano, P., Wang, M., Iaccarino, G. & Moin, P., 2003. Numerical simulation of the flow around a circular cylinder at high Reynolds numbers. *International journal of heat and fluid flow,* 24(4), pp. 463-469.

Chen, Z. & Martinuzzi, R., 2018. Shedding of dual structures in the wake of a surface-mounted low aspect ratio cone. *Physics of Fluids,* 30(4), p. 045107.

Chua, L. P., Liu, C. Y. & Chan, W. K., 1998. Measurements of a step cylinder. *International Communications in Heat and Mass Transfer,* 25(2), pp. 205-215.

Cohen, M. X., 2019. A better way to define and describe Morlet wavelets for time-frequency analysis. *NeuroImage,* Volume 199, pp. 81-86.

Daubechies, I., 1992. *Ten lectures on wavelets.* Philadelphia: Society for industrial and applied mathematics.

Davidson, L., 2015. *An introduction to turbulence models,* Sweden: Chalmers university of technology.

Davidson, P. A., 2015. *Turbulence: an introduction for scientists and engineers.* Oxford: Oxford university press.

Deardorff, J. W., 1970. A numerical study of three-dimensional turbulent channel flow at large Reynolds numbers. *Journal of Fluid Mechanics,* 41(2), pp. 453-480.

De, A. & Sarkar, S., 2020. Three-dimensional wake dynamics behind a tapered cylinder with large taper ratio.. *Physics of Fluids,* 32(6), p. 063604.

Demartino, C. & Ricciardelli, F., 2017. Aerodynamics of nominally circular cylinders: A review of experimental results for Civil Engineering applications. *Engineering Structures,* Volume 137, pp. 76-114.

D'Alessandro, V., Montelpare, S. & Ricci, R., 2016. Detached–eddy simulations of the flow over a cylinder at Re= 3900 using OpenFOAM. *Computers & Fluids,* Volume 136, pp. 152-169.

Ding, L. et al., 2015. Flow induced motion and energy harvesting of bluff bodies with different cross sections. *Energy Conversion and Management,* Volume 91, pp. 416-426.

Dunn, W., 2004. *Vortex shedding from cylinders with step-changes in diameter in uniform and shear flows.* University of Ottawa: Doctoral dissertation.

Dunn, W. & Tavoularis, S., 2006. Experimental studies of vortices shed from cylinders with a step-change in diameter. *Journal of Fluid Mechanics,* Volume 555, pp. 409-437.

Dunn, W. & Tavoularis, S., 2011. Vortex shedding from a step-cylinder in spanwise sheared flow. *Physics of Fluids,* 23(3), p. 035109.

Etzold, F. & Fiedler, H., 1976. The near-wake structure of a cantilevered cylinder in a cross-flow. *Zeitschrift fur Flugwissenschaften,* Volume 24, pp. 77-82.

Falkovich, G. & Sreenivasan, K. R., 2006. Lessons from hydrodynamic turbulence. *Physics Today,* 59(4), pp. 43-49.

Farge, M., 1992. Wavelet transforms and their applications to turbulence. *Annual Review of Fluid Mechanics,* 24(1), pp. 395-458.

Farivar, D. J., 1981. Turbulent uniform flow around cylinders of finite length. *AIAA journal,* 19(3), pp. 275-281.

Fincham, A. & Delerce, G., 2000. Advanced optimization of correlation imaging velocimetry algorithms. *Experiments in Fluids,* 29(1), pp. S013-S022.

Fox, T. A. & West, G. S., 1993. Fluid-induced loading of cantilevered circular cylinders in a low-turbulence uniform flow. Part 1: Mean loading with aspect ratios in the range 4 to 30. *Journal of Fluids and Structures,* 7(1), pp. 1-14.

Franke, J. & Frank, W., 2002. Large eddy simulation of the flow past a circular cylinder at ReD= 3900. *Journal of Wind Engineering and Industrial Aerodynamics,* 90(10), pp. 1191-1206.

Gaster, M., 1969. Vortex shedding from slender cones at low Reynolds numbers. *Journal of Fluid Mechanics,* 38(3), pp. 565-576.

Gaster, M., 1971. Vortex shedding from circular cylinders at low Reynolds numbers. *Journal of Fluid Mechanics,* 46(4), pp. 749-756.

Gerrard, J. H., 1978. The wakes of cylindrical bluff bodies at low Reynolds number. *Philosophical Transactions of the Royal Society of London. Series A, Mathematical and Physical Sciences,* 288(1354), pp. 351-382.

Gould, R. W. F., Ponsford, P. J. & Raymer, W. G., 1968. Wind tunnel tests on chimneys of circular section at high Reynolds numbers. *Proc Symp Wind Effects on Buildings and Structures, Loughborough,* Volume 2, p. 10.

Grant, I., 1997. Particle image velocimetry: a review. *Proceedings of the Institution of Mechanical Engineers, Part C: Journal of Mechanical Engineering Science,* 211(1), pp. 55-76.

Harris, F. J., 1978. On the use of windows for harmonic analysis with the discrete Fourier transform. *Proceedings of the IEEE,* 66(1), pp. 51-83.

Hatton, S. A., 1995. Rigid Risers for Tanker FPSOs. *FPSO World Congress, Aberdeen October.*

Hsiao, F. B. & Chiang, C. H., 1998. Experimental study of cellular shedding vortices behind a tapered circular cylinder. *Experimental Thermal and Fluid Science,* 17(3), pp. 179-188.

Hussain, A. K. M. F., 1986. Coherent structures and turbulence. *Journal of Fluid Mechanics,* Volume 173, pp. 303-356.

Hussain, A. K. M. F. & Reynolds, W. C., 1970. The mechanics of an organized wave in turbulent shear flow. *Journal of Fluid Mechanics,* 41(2), pp. 241-258.

Jagadeesh, C., 2009. *Dynamics of vortex shedding from slender cones.* Queen Mary University of London: Doctoral dissertation.

Ji, C. et al., 2019. Vortex-induced vibrations of dual-step cylinders with different diameter ratios in laminar flows. *Physics of Fluids,* 31(7), p. 073602.

Ji, C. et al., 2020. Numerical simulations of flows around a dual step cylinder with different diameter ratios at low Reynolds number. *European Journal of Mechanics-B/Fluids,* Volume 79, pp. 332-344.

Jolliffe, I. T. & Cadima, J., 2016. Principal component analysis: a review and recent developments. *Philosophical Transactions of the Royal Society A: Mathematical, Physical and Engineering Sciences,* 374(2065), p. 20150202.

Kıymık, M. K., Güler, İ., Dizibüyük, A. & Akın, M., 2005. Comparison of STFT and wavelet transform methods in determining epileptic seizure activity in EEG signals for real-time application. *Computers in Biology and Medicine,* 35(7), pp. 603-616.

Kawamura, T. et al., 1984. Flow around a finite circular cylinder on a flat plate: Cylinder height greater than turbulent boundary layer thickness. *Bulletin of JSME,* 27(232), pp. 2142-2151.

Kim, Y. M. & You, K. P., 2002. Dynamic responses of a tapered tall building to wind loads. *Journal of Wind Engineering and Industrial Aerodynamics,* 90(12-15), pp. 1771-1782.

Ko, N. W. M. & Chan, A. S. K., 1984. Pressure distributions on circular cylinders with stepwise change of the diameter. *American Society of Mechanical Engineers (Paper).*

Ko, N. W. M. & Chan, A. S. K., 1990. In the intermixing region behind circular cylinders with stepwise change of the diameter. *Experiments in Fluids,* 9(4), pp. 213-221.

Ko, N. W. M. & Chan, A. S. K., 1992. Wakes behind circular cylinders with stepwise change of diameter. *Experimental Thermal and Fluid Science,* 5(2), pp. 182-187.

Ko, N. W. M., Leung, W. L. & Au, H., 1982. Flow behind two coaxial circular cylinders.

Lam, K., Wang, F. H., Li, J. Y. & So, R. M. C., 2004b. Experimental investigation of the mean and fluctuating forces of wavy (varicose) cylinders in a cross-flow. *Journal of Fluids and Structures,* 19(3), pp. 321-334.

Lam, K., Wang, F. H. & So, R. M. C., 2004a. Three-dimensional nature of vortices in the near wake of a wavy cylinder. *Journal of Fluids and Structures,* 19(6), pp. 815-833.

Lewis, C. G. & Gharib, M., 1992. An exploration of the wake three dimensionalities caused by a local discontinuity in cylinder diameter. *Physics of Fluids A: Fluid Dynamics,* 4(1), pp. 104-117.

Liang, Y. C. et al., 2002. Proper orthogonal decomposition and its applications—Part I: Theory. *Journal of Sound and Vibration,* 252(3), pp. 527-544.

Luo, S. C., Gan, T. L. & Chew, Y. T., 1996. Uniform flow past one (or two in tandem) finite length circular cylinder (s). *Journal of Wind Engineering and Industrial Aerodynamics,* 59(1), pp. 69-93.

Lysenko, D. A., Ertesvåg, I. S. & Rian, K. E., 2012. Large-eddy simulation of the flow over a circular cylinder at Reynolds number 3900 using the OpenFOAM toolbox. *Flow, Turbulence and Combustion,* 89(4), pp. 491-518.

Mair, W. A. & Stansby, P. K., 1975. Vortex wakes of bluff cylinders in shear flow. *SIAM Journal on Applied Mathematics,* 28(2), pp. 519-540.

Mallat, S., 1999. *A wavelet tour of signal processing.* San Diego: Academic press.

Massey, B. S., 1998. *Mechanics of fluids.* London: Van Nostrand Reinhold.

McClure, J., Morton, C. & Yarusevych, S., 2015. Flow development and structural loading on dual step cylinders in laminar shedding regime. *Physics of Fluids,* 27(6), p. 063602.

Menter, F. R., 1994. Two-equation eddy-viscosity turbulence models for engineering applications. *AIAA journal,* 32(8), pp. 1598-1605.

Meyer, K. E., Pedersen, J. M. & Özcan, O., 2007. A turbulent jet in crossflow analysed with proper orthogonal decomposition. *Journal of Fluid Mechanics,* Volume 583, pp. 199-227.

Morton, C., 2014. *Three-dimensional wake development and structural loading on dual step cylinders in cross-flow.* University of Waterloo: Doctoral dissertation.

Morton, C. & Yarusevych, S., 2009. Modeling flow over a circular cylinder with a stepwise discontinuity. *39th AIAA Fluid Dynamics Conference,* p. 3703.

Morton, C. & Yarusevych, S., 2010a. A combined experimental and numerical study of flow past a single step cylinder. *Fluids Engineering Division Summer Meeting,* Volume 49484, pp. 1209-1220.

Morton, C. & Yarusevych, S., 2010b. Vortex shedding in the wake of a step cylinder. *Physics of Fluids,* 22(8), p. 083602.

Morton, C. & Yarusevych, S., 2011. Cross flow over cylinders with two stepwise discontinuities in diameter. *Seventh International Symposium on Turbulence and Shear Flow Phenomena.*

Morton, C. & Yarusevych, S., 2012a. An experimental investigation of flow past a dual step cylinder. *Experiments in Fluids,* 52(1), pp. 69-83.

Morton, C. & Yarusevych, S., 2012b. Vortex Shedding in the Wake of a Dual Step Cylinder. *arXiv preprint arXiv:1210.3588.*

Morton, C. & Yarusevych, S., 2014a. Vortex dynamics in the turbulent wake of a single step cylinder. *Journal of Fluids Engineering,* 136(3), p. 031204.

Morton, C. & Yarusevych, S., 2014b. Analyzing three-dimensional wake vortex dynamics using time-resolved planar PIV. *17th International Symposium on Applications of Laser Techniques to Fluid Mechanics, Lisbon, Portugal.*

Morton, C. & Yarusevych, S., 2014c. On vortex shedding from low aspect ratio dual step cylinders. *Journal of Fluids and Structures,* Volume 44, pp. 251-269.

Morton, C. & Yarusevych, S., 2015. Three-dimensional flow and surface visualization using hydrogen bubble technique. *Journal of Visualization,* 18(1), pp. 47-58.

Morton, C. & Yarusevych, S., 2016. Reconstructing three-dimensional wake topology based on planar PIV measurements and pattern recognition analysis. *Experiments in Fluids,* 57(10), pp. 1-13.

Morton, C. & Yarusevych, S., 2020. Vortex shedding from cylinders with two step discontinuities in diameter. *Journal of Fluid Mechanics,* Volume 902.

Morton, C., Yarusevych, S. & Carvajal-Mariscal, I., 2009. Study of flow over a step cylinder. *Applied Mechanics and Materials,* Volume 15, pp. 9-14.

Morton, C., Yarusevych, S. & Scarano, F., 2016. A tomographic particle image velocimetry investigation of the flow development over dual step cylinders. *Physics of Fluids,* 28(2), p. 025104.

Nishino, T., Roberts, G. T. & Zhang, X., 2008. Unsteady RANS and detached-eddy simulations of flow around a circular cylinder in ground effect. *Journal of Fluids and Structures,* 24(1), pp. 18-33.

Norberg, C., 1992. An experimental study of the flow around cylinders joined with a step in the diameter. *Proceedings of the 11th Australasian fluid mechanics conference, Hobart, Australia,* Volume 1, pp. 507-510.

Norberg, C., 2003. Fluctuating lift on a circular cylinder: review and new measurements. *Journal of Fluids and Structures,* 17(1), pp. 57-96.

Okamoto, S. & Sunabashiri, Y., 1992. Vortex shedding from a circular cylinder of finite length placed on a ground plane. *Journal of Fluids Engineering,* 114(4), pp. 512-521.

Papangelou, A., 1992. Vortex shedding from slender cones at low Reynolds numbers. *Journal of Fluid Mechanics,* Volume 242, pp. 299-321.

Papangelou, A., 1993. A "robust" vortex-shedding anemometer. *Experiments in Fluids,* 14(3), pp. 208-210.

Park, C. W. & Lee, S. J., 2000. Free end effects on the near wake flow structure behind a finite circular cylinder. *Journal of Wind Engineering and Industrial Aerodynamics,* 88(2-3), pp. 231-246.

Parnaudeau, P., Carlier, J., Heitz, D. & Lamballais, E., 2008. Experimental and numerical studies of the flow over a circular cylinder at Reynolds number 3900. *Physics of Fluids,* 20(8), p. 085101.

Perrin, R. et al., 2006. Phase averaged turbulence properties in the near wake of a circular cylinder at high Reynolds number using POD. *Proc. 13th Int. Symp. Applications of Laser Techniques to Fluid Mechanics, Lisbon, Portugal.*

Piccirillo, P. S. & Van Atta, C. W., 1993. An experimental study of vortex shedding behind linearly tapered cylinders at low Reynolds number. *Journal of Fluid Mechanics,* Volume 246, pp. 163-195.

Rafati, S., 2014. *Investigating Step Cylinder Wake Topology with Tomographic PIV.* Delft University of Technology: Master's thesis.

Rashidi, S., Hayatdavoodi, M. & Esfahani, J. A., 2016. Vortex shedding suppression and wake control: A review. *Ocean Engineering,* Volume 126, pp. 57-80.

Reinders, F., Sadarjoen, I. A., Vrolijk, B. & Post, F. H., 2002. Vortex tracking and visualisation in a flow past a tapered cylinder. *Computer Graphics Forum,* 21(4), pp. 675-682.

Roshko, A., 1961. Experiments on the flow past a circular cylinder at very high Reynolds number. *Journal of Fluid Mechanics,* 10(3), pp. 345-356.

Saric, W. S., Reed, H. L. & Kerschen, E. J., 2002. Boundary-layer receptivity to freestream disturbances. *Annual Review of Fluid Mechanics,* 34(1), pp. 291-319.

Sarode, R. S., Gai, S. L. & Ramesh, C. K., 1981. Flow around circular-and square-section models of finite height in a turbulent shear flow. *Journal of Wind Engineering and Industrial Aerodynamics,* 8(3), pp. 223-230.

Schmitt, F. G., 2007. About Boussinesq's turbulent viscosity hypothesis: historical remarks and a direct evaluation of its validity. *Comptes Rendus Mécanique,* 335(9-10), pp. 617-627.

Senecal, P. K. et al., 2007. *A new parallel cut-cell Cartesian CFD code for rapid grid generation applied to in-cylinder diesel engine simulations,* United States: SAE International.

Shin, J., Rahai, H., Taherian, S. & Ferris, R. J., 2018. Numerical Investigations of Flow Past a Rotating Stepped Cylinder. *Fluids Engineering Division Summer Meeting,* Volume 51562, p. V002T09A002.

Sinha, S., Routh, P. S., Anno, P. D. & Castagna, J. P., 2005. Spectral decomposition of seismic data with continuous-wavelet transform. *Geophysics,* 70(6), pp. P19-P25.

Smagorinsky, J., 1963. General circulation experiments with the primitive equations: I. The basic experiment. *Monthly Weather Review,* 91(3), pp. 99-164.

Spalart, P. R., 2009. Detached-eddy simulation. *Annual Review of Fluid Mechanics,* Volume 41, pp. 181-202.

Stickland, M. et al., 2013. Measurement and simulation of the flow field around a triangular lattice meteorological mast. *Energy and Power Engineering,* 5(10).

Strelets, M., 2001. Detached eddy simulation of massively separated flows. *39th Aerospace Sciences Meeting and Exhibit,* p. 879.

Stringer, R. M., Zang, J. & Hillis, A. J., 2014. Unsteady RANS computations of flow around a circular cylinder for a wide range of Reynolds numbers. *Ocean Engineering,* Volume 87, pp. 1-9.

Sumner, D., Heseltine, J. L. & Dansereau, O. J. P., 2004. Wake structure of a finite circular cylinder of small aspect ratio. *Experiments in Fluids,* 37(5), pp. 720-730.

Sykes, D. M., 1962. The supersonic and low-speed flows past circular cylinders of finite length supported at one end. *Journal of Fluid Mechanics,* 12(3), pp. 367-387.

Talboys, E. & Brücker, C., 2018. Upstream shear-layer stabilisation via self-oscillating trailing edge flaplets. *Experiments in Fluids,* 59(10), p. 145.

Tanaka, S. & Murata, S., 1999. An investigation of the wake structure and aerodynamic characteristics of a finite circular cylinder: time-averaged wake structures behind circular cylinders with various aspect ratios. *JSME International Journal Series B Fluids and Thermal Engineering,* 42(2), pp. 178-187.

Teutsch, I., 2012. *Investigation of the Wake Flow behind a stepped circular Cylinder using Particle Image Velocimetry.* Institutt for marin teknikk: Master's thesis.

Tian, C., Jiang, F., Pettersen, B. & Andersson, H., 2021. Vortex system around a step cylinder in a turbulent flow field. *Physics of Fluids,* 33(4), p. 045112.

Tian, C., Jiang, F., Pettersen, B. & Andersson, H. I., 2017a. Antisymmetric vortex interactions in the wake behind a step cylinder. *Physics of Fluids,* 29(10), p. 101704.

Tian, C., Jiang, F., Pettersen, B. & Andersson, H. I., 2017b. Numerical investigation of flow around a step cylinder. *Proceedings of 9th National Conference on Computational Mechanics,* pp. 369-384.

Tian, C., Jiang, F., Pettersen, B. & Andersson, H. I., 2019. The long periodicity of vortex dislocations in the wake behind a step cylinder. *Proceedings of 10th National Conference on Computational Mechanics,* pp. 3-4.

Tian, C., Jiang, F., Pettersen, B. & Andersson, H. I., 2020a. Diameter ratio effects in the wake flow of single step cylinders. *Physics of Fluids,* 32(9), p. 093603.

Tian, C., Jiang, F., Pettersen, B. & Andersson, H. I., 2020b. Vortex dislocation mechanisms in the near wake of a step cylinder. *Journal of Fluid Mechanics,* Volume 891.

Torrence, C. & Compo, G. P., 1998. A practical guide to wavelet analysis. *Bulletin of the American Meteorological Society,* 79(1), pp. 61-78.

Tucker, P. G. & Pan, Z., 2000. A Cartesian cut cell method for incompressible viscous flow. *Applied Mathematical Modelling,* 24(8-9), pp. 591-606.

Uematsu, Y. & Yamada, M., 1994. Aerodynamic forces on circular cylinders of finite height. *Journal of Wind Engineering and Industrial Aerodynamics,* 51(2), pp. 249-265.

Vallès, B., Andersson, H. I. & Jenssen, C. B., 2002a. Oblique vortex shedding behind tapered cylinders. *Journal of Fluids and Structures,* 16(4), pp. 453-463.

Vallès, B., Andersson, H. I. & Jenssen, C. B., 2002b. Direct-mode interactions in the wake behind a stepped cylinder. *Physics of Fluids,* 14(4), pp. 1548-1551.

Van Oudheusden, B. W., Scarano, F., Van Hinsberg, N. P. & Watt, D. W., 2005. Phase-resolved characterization of vortex shedding in the near wake of a square-section cylinder at incidence. *Experiments in Fluids,* 39(1), pp. 86-98.

Wang, J., Ma, Q., Wan, D. & Yan, S., 2018. Numerical study on flow evolution after dual stepped cylinder at low Reynolds number. *28th International Ocean and Polar Engineering Conference, Sapporo, Japan.*

Wang, J., Ma, Q. & Yan, S., 2019. *Numerical study on secondary flow characteristics after dual stepped cylinder at low Reynolds number.* Singapore, Springer, pp. 559-572.

Wang, J. et al., 2020. Numerical simulation of focused wave interaction with WEC models using qaleFOAM. *Proceedings of the ICE - Engineering and Computational Mechanics,* 173(3), pp. 100-118.

Weiselsberger, C., 1921. New data on the law of hydro and aerodynamic resistance. *Physikalische Zeitschrift,* Volume 22, pp. 321-328.

Willert, C. E. & Gharib, M., 1991. Digital particle image velocimetry. *Experiments in Fluids,* 10(4), pp. 181-193.

Williamson, C., 206. Oblique and parallel modes of vortex shedding in the wake of a circular cylinder at low Reynolds numbers. *Journal of Fluid Mechanics,* pp. 579-627.

Williamson, C. H. K., 1996. Vortex dynamics in the cylinder wake. *Annual Review of Fluid Mechanics,* 28(1), pp. 477-539.

Yagita, M., Kojima, Y. & Matsuzaki, K., 1984. On vortex shedding from circular cylinder with step. *Bulletin of JSME,* 27(225), pp. 426-431.

Yan, Y., Ji, C. & Srinil, . N., 2020. Three-dimensional flip-flopping flow around a pair of dual-stepped circular cylinders in a side-by-side arrangement. *Physics of Fluids,* 32(12), p. 123608.

Zdravkovich, M. M., 1990. Conceptual overview of laminar and turbulent flows past smooth and rough circular cylinders. *Journal of Wind Engineering and Industrial Aerodynamics,* 33(1-2), pp. 53-62.

Zdravkovich, M. M., 1997. *Flow around circular cylinders-volume 1: fundamentals.* Oxford: Oxford University Press.

Zdravkovich, M. M., Brand, V. P., Mathew, G. & Weston, A., 1989. Flow past short circular cylinders with two free ends. *Journal of Fluid Mechanics,* Volume 203, pp. 557-575.